# Deep Controlled Source Electromagnetics for Mineral Exploration: A Multidimensional Validation Study in Time and Frequency Domain

**Inaugural-Dissertation**

zur Erlangung des Doktorgrades
der Mathematisch-Naturwissenschaftlichen Fakultät
der Universität zu Köln

vorgelegt von

**Wiebke Mörbe**

aus Freiburg im Breisgau

Köln, 2020

1. Gutachter: Prof. Dr. B. Tezkan
2. Gutachter: Prof. Dr. A. Hördt

Tag der mündlichen Prüfung: 25.11.2019

# Abstract

The focus of this thesis is the derivation of an independent multidimensional resistivity model utilising land based controlled source electromagnetics (CSEM) with resolution to conductive structures down to 1 km depth. Data is evaluated in both, time and frequency domain. Since the resistivity distribution is strongly multidimensional, besides conventional 1D inversion methods, 2D inversion techniques are applied to the dataset.

The objective of the BMBF funded DESMEX (Deep Electromagnetic Sounding for Mineral Exploration) project is the development of an electromagnetic exploration system which can be used for the detection and assessment of deep mineral resources. In order to obtain a high data coverage as well as a high spatial and depth resolution, airborne and ground based methods are combined in a semi-airborne concept. In the framework of the DESMEX project, the University of Cologne conducted large scale ground based long offset transient electromagnetic (LOTEM) measurements along an 8.5 km long transect in a former mining area in eastern Thuringia, Germany. Within the LOTEM validation study, an independent multidimensional resistivity model of the survey area was derived, which serves as a reference model for the semi-airborne concept developed within DESMEX and is eventually integrated into a final mineral deposition model. Utilising in total 6 transmitters in broadside configuration, data at 170 electric field stations were recorded during two large scale LOTEM surveys. In addition, a full component magnetic field dataset was acquired with SQUID sensors using a dense station spacing along the transect. For a preliminary evaluation, conventional 1D techniques are applied to the dataset. The individual switch on transients of the electric field can be explained by a 1D approach, the obtained models however indicate a strong multidimensional subsurface with rather large variations in resistivity. For further interpretation, the LOTEM data is analysed in frequency domain. Obtained 1D and 2D inversion models of the electric field component in frequency domain are in a good agreement with the time domain results. Subsequently, a joint multidimensional inversion of the full dataset in frequency domain was carried out, including electric and magnetic field data. Derived 2D inversion models are discussed in terms of sensitivities and resolution capabilities. Shallow high conductive structures are well comparable to inversion results from other conducted reconnaissance surveys and the semi-airborne CSEM model. The dominant conductivity structures can be linked to the occurrence of Silurian graptolite shales.

# Kurzzusammenfassung

Ziel dieser Arbeit ist die Ableitung eines unabhängigen Leitfähigkeitsmodells mit Hilfe von bodengebundenen Controlled Source Electromagnetic (CSEM) Messungen, welches Leitfähigkeitsstrukturen bis in 1 km Tiefe auflösen kann. Gemessene Daten werden sowohl im Frequenzbereich als auch im Zeitbereich ausgewertet. Da die Leitfähigkeitsverteilung deutliche Eigenschaften von Mehrdimensionalität aufweist, werden neben 1D Auswertemethoden auch 2D Inversionsalgorithmen angewandt.

Ziel des BMBF geförderten DESMEX Projektes (Deep Electromagnetic Sounding for Mineral Exploration) ist die Entwicklung eines elektromagnetischen Explorationsverfahrens, welches für die Detektion und Bewertung tiefer mineralischer Lagerstätten eingesetzt werden kann. Um sowohl eine hohe flächenhafte Datenabdeckung als auch eine hohe räumliche und vertikale Auflösung zur ermöglichen, werden bodengebundene und luftgestützte Systeme in einem Semi Airborne Konzept kombiniert. Im Rahmen des DESMEX Projektes führte die Universität zu Köln bodengebundene Long Offset Transiente Elektromagnetische (LOTEM) Messungenen entlang eines 8.5 km langen Profils in einem ehemaligen Abbaugebiet in Ostthüringen, Deutschland durch. Im Rahmen der LOTEM Validierungsstudie soll ein mehrdimensionales Leitfähigkeitsmodell abgeleitet werden, das als Referenzmodell für das neue Semi Airborne Konzept dient und in ein gemeinsames Lagerstättenmodell eingebunden wird. Im Rahmen von zwei großskaligen LOTEM Messkampagnen wurden unter Nutzung von 6 Sendern in Broadside Konfiguration Daten an 170 elektrischen Feld Stationen aufgezeichnet. Zusätzlich wurden die 3 Komponenten des Magnetfeldes mit dichtem Stationsabstand entlang des Profils mit einem SQUID Magnetometer aufgenommen. Als ersten Auswerteansatz wurden konventionelle 1D Inversionsroutinen auf den Datensatz angewendet. Die aufgezeichneten Switch-On Transienten des elektrischen Feldes können mit einer 1D Leitfähigkeitsverteilung erklärt werden. Die abgeleiteten 1D Leitfähigkeitsmodelle deuten allerdings auf eine deutlich mehrdimensionale Leitfähigkeitsverteilung mit starken Kontrasten entlang des Profils hin. Für eine weiterführende Interpretation wurde der Datensatz im Frequenzbereich ausgewertet. Die abgeleiteten 1D und 2D Inversionsmodelle im Frequenzbereich stimmen gut mit den Ergebnissen im Zeitbereich überein. Daher wurden im Anschluss eine gemeinsame, mehrdimensionale Inversion des elektrischen und magnetischen Datensatzes durchgeführt. Sensitivitäten und Auflösungseigenschaften der abgeleitete 2D Modelle in Zeit- und Frequenzbereich werden diskutiert. Oberflächennahe Leitfähigkeitsstrukturen stimmen gut mit den Inversionsergebnissen von luftgestützten Voruntersuchungen und dem Semi Airborne Modell überein und korrelieren mit dem Auftreten silurischer Schwarzschiefer.

# Contents

# List of Figures

# List of Tables

# CHAPTER 1

# Introduction

The focus of this thesis is the derivation of an independent multidimensional resistivity model utilizing land based controlled source electromagnetics (CSEM) for the validation of a newly developed semi-airborne concept for deep mineral exploration applications. Hereby, acquired CSEM data is analysed in both, time domain (TD) and frequency domain (FD) with the focus on deep conductive structures.

Ore mineralisation can increase the electrical conductivity in the subsurface significantly (e.g. Airo (2015); Spagnoli et al. (2016)). Electromagnetic methods, which gain information about the electrical conductivity properties of the subsurface, play an essential role for mineral exploration. There exists multiple electromagnetic studies successfully applied to mineral exploration applications in the last decades, either airborne (Witherly, 2000) or ground based (Strack et al., 1990), and EM is nowadays an established tool for mineral exploration. The depth extension of economic mineral deposits in Germany is poorly known. On the other hand, the exploitation of strategic important minerals is nowadays feasible for depth larger than 1 km. Therefore an efficient method is needed to evaluate the depth extension of the deposits. In the framework of the joint DESMEX project (Deep electromagnetic sounding for mineral exploration), funded by the German Federal Ministry of Education and Research (BMBF), a novel concept is developed (Smirnova et al., 2019b; Nittinger et al., 2017; Schiffler et al., 2017), where airborne and ground based EM methods are combined. The semi-airborne technique aims at deep electromagnetic exploration down to 1 km. Having the advantage, that airborne electromagnetic measurements can cover a large area rapidly, whereas ground based methods deliver complimentary information, a combination of both techniques provide a powerful tool to explore the depth extension of potential deposits for strategic resources. Within the validation study, long offset transient electromagnetic (LOTEM) measurements were performed in the survey area with the aim to derive an independent multidimensional resistivity model, which serves as a reference model for the semi-airborne concept and is eventually integrated in a final mineral deposition model.

The LOTEM method is a controlled source electromagnetic method in time domain and was predominantly advanced by Strack et al. (1990) and further developed at the University of Cologne (UoC) in the last decades. A theoretical description of LOTEM and CSEM methods in general can be found in various textbooks (e.g. Kaufman and Keller (1983); Nabighian and Macnae (1991)). LOTEM utilizes typically a horizontal electrical dipole (HED) with cable length between 1-2 km as transmitter and multi-component EM receiver stations at offsets ranging from 1 km up to several km from the source. As source signal, a square wave with alternating polarisation is used. Switching times and corresponding transient length used for LOTEM applications range typically between $10^{-4}$ s up to few decades of seconds. Depending on the geometry, the time range and the resistivity distribution of the subsurface, investigation depth between several tens of meters up to several decades of km can be reached (Ziolkowski et al., 2007; Haroon et al., 2015).

Recent applications of time domain CSEM at the UoC comprise e.g. applications of LOTEM in a marine environment for the detection of a groundwater aquifer (Lippert, 2015). Haroon (2016) developed a novel differential electrical dipole method for marine applications. Resistivity distributions were reconstructed typically by the application of 1D inversion routines and large scale 2D forward modelling studies. However, if the geology is rather complex, the electrical resistivity distribution can be strongly multidimensional. Trial and error forward modelling studies are time consuming and not efficient for the deviation of complex large scale models.

Multidimensional time domain modelling algorithms were presented by few authors, e.g. Martin (2009); Commer (2003); Oldenburg et al. (2012). However, open source inversion tools for time domain land based CSEM suitable for long offset applications are still not commonly available and not routinely utilized. Yogeshwar (2014) applied the 2D inversion algorithm `SINV` developed by Martin (2009) to an in-loop TEM dataset for shallow geomorphological applications. However, for the given LOTEM dataset presented in this thesis, the application of the `SINV` algorithm did not lead to satisfying results due to convergence and stability issues for large resistivity contrasts. In addition, for finite difference algorithms like `SINV`, the implementation of topography is not straight forward and results in a higher demand of computational resources.

On the other hand, for frequency domain CSEM applications, a range of open source frequency domain codes exists, which are tested for onshore galvanic dipole configurations (Key and Ovall, 2011; Grayver et al., 2013). From a theoretical point of view, the time domain and frequency domain approach is related over a Fourier transformation (Streich, 2016). However, advantages of the CSEM time domain methods in contrary with the conventional CSEM frequency domain method were advertised by several authors, e.g. Zhdanov (2010) and Strack (1992). One of the main reasons is the possibility to measure the transient step response of the earth in absence of the primary field (Streich, 2016), i.e. after the transmitter is switched off and in the case of land based application after the arrival of the air wave. The measurement setup is for both, time and frequency domain CSEM methods similar. Typically a HED is utilized as a source and a rectangular shaped signal is transmitted. For time domain applications the transient response after current switch off or switch on is evaluated. In frequency domain, transfer functions between the source current and the measured EM field responses for the transmitted fundamental frequency and its odd harmonics are evaluated. If an analysis of the data in frequency and time domain is possible, depends therefore mainly on the capabilities of the used instrumentation.

The application of 1D inversion algorithms are not suitable for the collected LOTEM dataset and the time domain transients are distorted by induced polarization effects. Hence, for the derivation of a deep subsurface model a more methodological aspect of CSEM application is investigated. In the framework of this thesis, the LOTEM dataset was evaluated in both, time and frequency domain. As the measurement equipment of the University of Cologne was so far only validated for time domain applications, both, transmitter and receiver systems were tested for an evaluation in frequency domain. Resolution studies for different data representations with the focus on deep conductive layers were performed. Haroon (2016) studied differences in the resolution capabilities of switch on and switch off transients. In the framework of this thesis, sensitivities towards deep conductors (and resistors) are studied in both domains and for different data representations. Whereas for an isotropic earth (Kaufman and Keller, 1983) no physical difference regarding the inductive response is present between those data representations, the relative contribution of the inductive earth response and time independent background DC field may vary. Under consideration of an absolute and relative noise floor, this results in different resolution capabilities of time domain switch on and switch off transients as well as frequency domain transfer functions. Additionally, induced polarization is affecting the electromagnetic response in both domains differently. This thesis therefore aims not for a general recommendation of the advantages and disadvantages of one method over the other. However, it is demonstrated that under the given circumstances with respect to the survey design, depth of investigation and instrumentation, an interpretation of data in both domains is feasible and leads to comparable results.

As a test area for the new semi-airborne method within DESMEX, a former antimony mining area in the Thuringian Slate Mountains, Germany was chosen. Due to its rather high resistivity (Costabel and Martin, 2019) and restricted extension (Schlegel and Wiefel, 1998), the antimony mineralisation itself can not be detected with electromagnetic methods. However, in the survey area graphitised black shales are present, which exhibit a high electrical conductivity contrast to the surrounding host rock material and therefore deliver an applicative target for electromagnetic induction methods. Located in a heavily faulted and deformed Antiform structure, the geological setting of the survey area is rather complex. Where the resistivity distribution of the shallow subsurface can be constrained by either geological and available borehole information or shallow geophysical investigation methods (e.g. airborne electromagnetics, radio-magnetotellurics), the deep structures remain unknown. In order to validate the newly developed semi-airborne concept down to depth of 1 km, a large scale ground based LOTEM survey along an 8.5 km long transect was carried out. To facilitate fast data acquisition in the framework of the LOTEM validation study and evaluate potential additional equipment resources for future time domain CSEM applications, magnetotelluric data loggers provided by the geophysical instrument pool Potsdam (GIPP) were tested for time domain applications. Next to the acquisition of electric field data, the full magnetic field response was measured at a dense spacing utilizing low temperature SQUID magnetometers (Chwala et al., 2011) by the Leibniz IPHT Jena. A large dataset in a broadband time/frequency range with approximately 20000 data points was obtained. The resulting inversion models deliver a robust image of the subsurface in terms of electrical resistivity.

Derived 1D inversion results in time and frequency domain exhibit a strongly heterogeneous lateral resistivity distribution. For subsequent 2D forward modelling studies and 2D inversion of the dataset in frequency domain, the open source algorithm `MARE2DEM` is utilized. During the studies performed for this thesis, Haroon et al. (2018) implemented a time domain solution in the open source code `MARE2DEM`. In the framework of this thesis, the code was applied to land based LOTEM field data for the first time.

**Structure of this thesis**

In Chapter 2 and 3, the theoretical background of the CSEM method is described for both, time and frequency domain and the basic theory of data inversion is introduced. Within Chapter 4, the objectives of the DESMEX project are formulated and the survey area of the DESMEX main experiment with its regional and local geology is discussed. This includes an overview over petrophysical and geophysical (pre-)investigation carried out in the survey area by the UoC and project partners involved in the DESMEX project. Chapter 5 gives insights in the performed LOTEM measurements in 2016 and 2017. An overview of the survey design is given and the utilised transmitter function, the receiver systems and sensors are discussed. Data acquired with the typical equipment used for LOTEM data acquisition was evaluated for the first time in frequency domain. Therefore, a detailed description of the processing applied to the dataset, in both, time and frequency domain, as well as an overview over the obtained transients and transfer functions is given in Chapter 6. As first step of evaluation of the dataset, a 1D inversion is carried out. 1D results are discussed in Chapter 7. A comparison of 1D inversion result in both domains and subsequent resolution studies are utilized to validate the frequency domain approach for subsequent 2D inversion. Furthermore, the distortions by multidimensional resistivity structures to the 1D inversion approach is studied. Since induced polarization arises due to graphitised black shales present in the survey area, effects on the EM dataset are estimated in both domains. Considering the multidimensionality of resistivity structures in the investigation area, a subsequent multidimensional inversion is inevitable. Chapter 8 introduces the open source 2.5D CSEM inversion algorithm `MARE2DEM`. Suitable forward and inversion parameters for the evaluation of the LOTEM dataset are derived and 2D sensitivities for different data representations in both domains are analysed. Subsequent inversion models of LOTEM field data are presented in Chapter 9, presenting a final model for the resistivity distribution of the subsurface. In Chapter 10, the final LOTEM validation model is compared with inversion results from the semi-airborne dataset, 1D airborne electromagnetics and direct current resistivity measurements. Integrating geological and petrophysical information, derived structures and resistivity distributions are evaluated. In Chapter 11, the main findings and results of this thesis are summarized. Conclusions are drawn and an outlook for future work is presented.

# CHAPTER 2

# The LOTEM Method

Long offset transient electromagnetics (LOTEM) is an active method utilizing the principle of electromagnetic induction by transmitting an alternating current using a grounded dipole and measuring the earth response in distances of typically 1-10 km. As source, a galvanically coupled electrical dipole is utilized, transmitting commonly a rectangular shaped signal in either a 50 % or 100% duty cycle. Since the source moment is proportional to the transmitter length and the current, one aims to install long transmitter cables and high currents. Note that the first is restricted by the accessibility, increased installation time and effort, while the second depends on the resistance of electrodes and cables. Measuring the transient response of the electric and magnetic field components at offsets up to several times the target depth, the method is typically applied to retrieve information of deep structures with a depth of investigation reaching several km (e.g Ziolkowski et al. (2007); Haroon et al. (2015)). The two common setups are either in broadside configuration or inline configuration. In Figure 2.1 a typical setup for the broadside configuration is displayed, having the receivers aligned along a profile located in the middle of the transmitter dipole, running perpendicular to it. In the inline configuration, the receivers would be located on a line in elongation of the transmitter dipole (cp. Figure 2.1, x-direction).

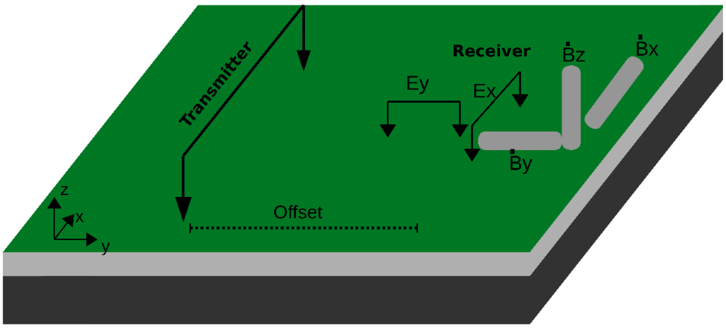

**Figure 2.1:** Schematic of a typical LOTEM setup in broadside configuration (after Strack (1992)). The transmitter is coupled galvanically to the ground. The EM field response is measured in offsets ranging from a few hundred meters to several kilometres.

At the receiver station up to 5 components are measured, consisting of the two horizontal electric and magnetic and the vertical magnetic field component. For typical LOTEM application, the magnetic field is not measured directly, but its time derivative $dB_{x,y,z}/dt$ (Strack, 1992). However, if low noise, high resolution magnetometers (e.g. SQUID magnetometers, cp. Section 5.2) are available, the measurement of the magnetic field (or the magnetic flux density $B$) directly exhibits several advantages (Asten and Duncan, 2012)), e.g. an earlier target response due to the slower decay of the B-Field.

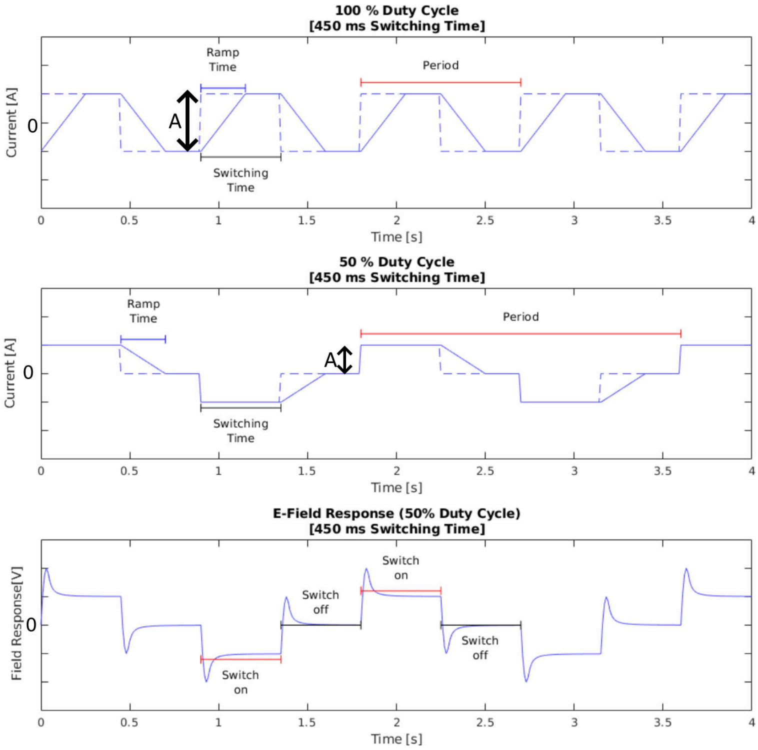

**Figure 2.2:** Exemplary 100% and 50% duty cycle transmitter wave function for a switching time of 450 ms. The switching time defines the time range for the transient response. One period consists of 2 current switches for a 100 % duty cycle and four current switches for a 50 % duty cycle. The transmitter amplitude A is twice as high for a 100 % duty cycle. When utilizing a 50% duty cycle one has to differentiate between electric field switch on and switch off response.

Operating the transmitter in a 50 % duty cycle, one has to differentiate between times with current being off and on (cp. Figure 2.2). For the latter, the measured transient $E_{on}$ is superimposed by the DC level of the transmitter. Different resolution capabilities of transients measured during off and on times of the transmitter for marine CSEM applications were studied by Haroon (2016). As discussed in this thesis, data acquired in a typical LOTEM survey can also be evaluated in frequency domain, which is somewhat similar to the well known CSEM techniques in frequency domain (Ziolkowski and Slob, 2019). In the framework of this thesis, resolution capabilities of transients during switch on and switch off are compared with the resolution properties of the transformed data in frequency domain. Note, that for frequency domain CSEM, not the transient behaviour is evaluated directly, but the relationship between measured field components and transmitter current in frequency domain. Therefore the term LOTEM would be misleading for the dataset when evaluated in frequency domain, and the more general term CSEM is utilized within this thesis. An overview on the LOTEM method regarding its theory and practical applications can be found in Kaufman and Keller (1983) and Strack (1992). An overview over CSEM applications in general is given in e.g. Ziolkowski and Slob (2019). Table 2.1 shows the variables and constants used in this thesis.

**Table 2.1.:** List of variables and constants. Bold characters represent vectors.

| Variable | Symbol | Units |
|---|---|---|
| Electric Field Strength | $\mathbf{E}$ | V/m |
| Electric Displacement | $\mathbf{D}$ | $\mathrm{As/m^2}$ |
| Magnetic Flux Density | $\mathbf{B}$ | $\mathrm{T = Vs/m^2}$ |
| Magnetic Field Strength | $\mathbf{H}$ | A/m |
| Electric Charge Density | $\varrho$ | $\mathrm{As/m^3}$ |
| Current Denisty | $\mathbf{j}$ | $\mathrm{A/m^2}$ |
| Current | $I$ | A |
| Electrical Permittivity | $\varepsilon = \varepsilon_0\varepsilon_r$ | As/(Vm) |
| Relative Dielectric Permittivity | $\varepsilon_r$ | 1 |
| Electrical Free Space Permittivity | $\varepsilon_0$ | As/(Vm) |
| Magnetic Permeability | $\mu = \mu_0\mu_r$ | Vs/(Am) |
| Relative Magnetic Permeability | $\mu_r$ | 1 |
| Permeability of Free Space | $\mu_0$ | Vs/(Am) |
| Electrical Conductivity | $\sigma$ | $\mathrm{S/m = 1/(\Omega m)}$ |
| Electrical Resistivity | $\rho$ | $\Omega$m |
| Angular Frequency | $\omega$ | 1/s |
| Frequency | $f$ | Hz |
| Wavenumber | $k$ | 1/m |
| Noise Level | $\eta_v$ | $\mathrm{V/m^2}$ |

## 2.1. Electrical Conduction Mechanisms

The physical property analysed in electromagnetic methods is the electrical conductivity $\sigma$ or its inverse, the electrical resistivity $\rho$. The electrical conductivity is the capability of material to conduct electrical current, which can be influenced by three different mechanisms: Electronic, electrolytic and dielectric conduction (Telford et al., 1990). The effect of dielectric conduction can be neglected for the resistivities and the frequencies typically used in electromagnetics, and the relative electric permittivity $\epsilon_r$ is not further considered. Since most of the rocks are poor electronic conductors, the prominent mechanism is the one of electrolytic conduction. It is dependent on the porosity $\theta$ of the rocks, the arrangement and volume of its pores and the conductivity $\rho_w$ and saturation $S$ of the fluid inside the pores and can be expressed with the empirical formula of Archie et al. (1942) for the effective resistivity $\rho_e$

$$\rho_e = \alpha\theta^{-m}S^{-n}\rho_w \tag{2.1}$$

with $n \approx 2$ and the constants $0.5 <= \alpha <= 2.5$ and $1.3 <= m <= 2.5$. Note that Equation 2.1, Archie's law, only applies for rocks without clay or metallic minerals. When current is applied, chemical energy is stored in the material due to variations in the mobility of ions in the fluid throughout the rock structure (Telford et al., 1990). If clay particles are present, so called membrane polarisation effects are arising (Ward, 1990). After the current is switched on, depending on the size of the rock pores, ions will accumulate at one end of the rock fluid interface which decreases current flow. After switching off the current, the ions will return to their original position, which will lead to a time dependent decay of voltage. Another source of induced polarization is electrode polarization, which occurs if metallic material is present in the rocks and next to electrolytic conduction, metallic conduction appears. This will lead to an accumulation of ions in the electrolyte adjacent to the mineral particle. When the current is switched off, ions diffuse back to their original condition, which results in a transient decay of the residual voltage. For example, graphite minerals can produce strong electronic polarization effects (Telford et al., 1990). Both, electronic and membrane polarization effects can be measured by the so called induced polarization (IP) method. Since in EM time (or frequency) dependent voltages are measured utilizing an alternating current signal, time and frequency dependent polarization effects can superimpose the induction response. In order to describe a frequency dependent resistivity $\rho_{rock}(\omega)$, the Cole-Cole model (Cole and Cole, 1941) is utilized, where the induced polarization is expressed in terms of chargeability $m$, relaxation time $\tau$, the dispersion coefficient $c$ and the time/frequency independent resistivity $\rho_0$.

$$\rho(\omega) = \rho_0 \left(1 - m \left(1 - \frac{1}{1 + (i\omega\tau)^c}\right)\right) \tag{2.2}$$

Since Graphite is present in the survey area, effects of induced polarization might superimpose the inductive response. Next to the frequency dependence, resistivity can depend on the direction of current flow. Then the resistivity is considered to be anisotropic, which typically occurs in stratified rocks such as slates or shales. Although anisotropy might occur in the area of study, in this thesis only isotropic resistivity is considered. Note that magnetic permeability $\mu_r$ leads to an increased current induced into the ground (Telford et al., 1990), and therefore would affect the measured EM response. However, for most rocks, the magnetic permeability is around one. The basic principles of electromagnetic induction and measured field responses in time and frequency domain are given in the next chapter.

## 2.2. Maxwell Equations

The principal of electromagnetic induction is based on the Maxwell equations which describe the behaviour of electromagnetic fields.

$$\nabla \times \mathbf{E} = -\frac{\partial \mathbf{B}}{\partial t} \tag{2.3}$$

$$\nabla \times \mathbf{H} = \frac{\partial \mathbf{D}}{\partial t} + \mathbf{j} \tag{2.4}$$

$$\nabla \cdot \mathbf{D} = \varrho \tag{2.5}$$

$$\nabla \cdot \mathbf{B} = 0 \tag{2.6}$$

where **B** is the magnetic induction, **H** is the magnetic field, **D** is the electric displacement, **E** is the electric field, **j** is the electric current density and $\varrho$ is the electric charge density. Bold characters denote non-scalars. Additionally the quantities are linked by their constitutive relationships for a linear isotropic medium

$$\mathbf{B} = \mu_o \mu_r \mathbf{H} = \mu \mathbf{H} \tag{2.7}$$

$$\mathbf{D} = \varepsilon_o \varepsilon_r \mathbf{E} = \varepsilon \mathbf{E} \tag{2.8}$$

$$\mathbf{j} = \sigma \mathbf{E} \tag{2.9}$$

where $\varepsilon_0$ is the permittivity of the free space, $\varepsilon_r$ the relative permittivity, $\mu_0$ the permeability of the free space and $\mu_r$ the relative permeability. Ohms law (2.9) describes the relationship between the total electric current density and the electrical conductivity $\sigma$ for an isotropic conductor. For investigating the subsurface with CSEM, the relative permeability $\mu_r$ and permittivity $\varepsilon_r$ can be considered as scalar and frequency independent quantities and will be neglected, following that $\mu = \mu_0$ and $\varepsilon = \varepsilon_0$. Furthermore, we assume that there are no free charges inside the earth, i.e. $\varrho = 0$. This leads to Equation (2.10)

$$\nabla \cdot \mathbf{j} = 0 \tag{2.10}$$

stating that there are no sources of current in the subsurface. Using these simplifications and Ohm's law (2.9) as well as the constitutional relation (2.7) and (2.8), we can perform a transformation of the Maxwell Equations into the Telegrapher's equations. If we multiply Equations (2.3) and (2.4) with $\nabla\times$, we obtain Equation (2.11).

$$\nabla \times (\nabla \times \mathbf{H}) = -\mu_0 \sigma \frac{\partial \mathbf{H}}{\partial t} - \mu_0 \epsilon \frac{\partial^2 \mathbf{H}}{\partial t^2} \tag{2.11}$$

With the vector identity $\nabla \times (\nabla \times \mathbf{F}) = \nabla(\nabla \cdot \mathbf{F}) - \Delta \mathbf{F}$ and $\nabla \cdot \mathbf{F} = 0$, concluding $\nabla \times (\nabla \times \mathbf{F}) = -\Delta \mathbf{F}$ we can derive the telegraphers equation.

$$\Delta \mathbf{F} = \mu_0 \sigma \frac{\partial \mathbf{F}}{\partial t} + \mu_0 \epsilon \frac{\partial^2 \mathbf{F}}{\partial t^2} \tag{2.12}$$

whereas $\mathbf{F}$ can either be $\mathbf{E}$ or $\mathbf{H}$. The telegraphers equation can be transformed into frequency domain via Fourier transformation, rewriting the time derivative as $\partial \mathbf{F}/\partial t = i\omega \mathbf{F}$. This leads to the Helmholtz equation

$$\Delta \mathbf{F} = i\omega \mu_0 \sigma \mathbf{F} - \mu_0 \epsilon \omega^2 \mathbf{F} \tag{2.13}$$

In the period range used in CSEM applications $\sigma \gg \omega\varepsilon$. Therefore, the second term of Equation 2.12 and 2.13 can be neglected and the equations utilizing the quasi static approximation (MT-Approximation) can be further simplified to

$$\Delta \mathbf{F} = \mu_0 \sigma \frac{\partial \mathbf{F}}{\partial t} \tag{2.14}$$

$$\Delta \mathbf{F} = i\omega \mu_0 \sigma \mathbf{F} \tag{2.15}$$

which is known as the diffusion equation in time and frequency domain.

### 2.2.1. Plane Wave Solution for a Uniform Conducting Halfspace

For plane electromagnetic waves the following equations applies

$$\mathbf{F} = \mathbf{F}_0 e^{i(\omega t - \mathbf{kr})} \tag{2.16}$$

where $\mathbf{F}_0$ is the amplitude, $\omega$ is the angular frequency and the wave number $\mathbf{k} = 1/\lambda \mathbf{e}_r$ is reciprocal to the wave length $\lambda$ and points in the moving direction of the wave. Using

Equation (2.16), the spatial derivative can also be rewritten as $\Delta\mathbf{F} = -k^2\mathbf{F}$. Together with (2.15) this leads to

$$k = \sqrt{-i\omega\mu\sigma} = \frac{1-i}{\sqrt{2}}\sqrt{\omega\mu_0\sigma} \tag{2.17}$$

With Equation (2.16) and (2.17) we can define the skin depth (2.18) that characterizes the penetration depth in which the amplitude of the electromagnetic wave is decayed to a 1/e of the initial surface value in case of a homogeneous subsurface.

$$\delta_{FD} = \sqrt{\frac{2}{\mu_0\omega\sigma}} \qquad \text{or} \qquad \delta_{FD}[\text{km}] \approx 0.5 \cdot \sqrt{\rho[\Omega\text{m}] \cdot T[\text{s}]} \tag{2.18}$$

### 2.2.2. Step Excitation Solution for a Uniform Conducting Halfspace

Ward and Hohmann (1988) give the impulse solution for EM Fields F at $z = 0$ in time domain as

$$\mathbf{F} = \mathbf{F}_0 \frac{\sqrt{\mu\sigma}z}{2\sqrt{\pi t^3}} e^{-\frac{\mu\sigma z^2}{4t}} \tag{2.19}$$

Setting the derivative of Equation 2.19 to zero, the diffusion depth

$$\delta_{TD} = \sqrt{\frac{2t}{\mu\sigma}} \tag{2.20}$$

can be derived. It described the depth for a fixed $t$, at which the EM fields reach their maximum and is somewhat similar to the skin depth (Eq. 2.18) obtained in frequency domain. By forming the time derivative of the diffusion depth, one can obtain the velocity $v_{TD}$, at which the maximum of the EM-fields is propagating (Ward and Hohmann, 1988).

$$v_{TD} = \frac{1}{\sqrt{2\mu\sigma t}} \tag{2.21}$$

## 2.3. HED Solution for a Uniform Conducting Halfspace

In order to get insights in the behaviour of the EM field components in time and frequency domain for their corresponding data representations, we focus in the following on the solution of a horizontal electrical dipole (HED) as utilized for LOTEM/CSEM applications on the surface of a homogeneous halfspace. Equations and conclusion are summarized from Kaufman and Keller (1983). The solution for both time and frequency domain for a 1D layered or 2D case is somewhat more elaborate and the properties of the different EM components are more in-transparent. For derivations of the EM field solutions regarding a 1D layer case we refer to Kaufman and Keller (1983) or Ward and Hohmann (1988). Weidelt (1986) approaches the solution over the separation of the EM fields in TE and TM Mode. An analytical solution for a 1D case is not possible, since it involves an iterative Bessel integral from a multiple number of layers, where the Hankel transformation must be carried out numerically. For the problem formulation in 3D, refer to Section 8.1.

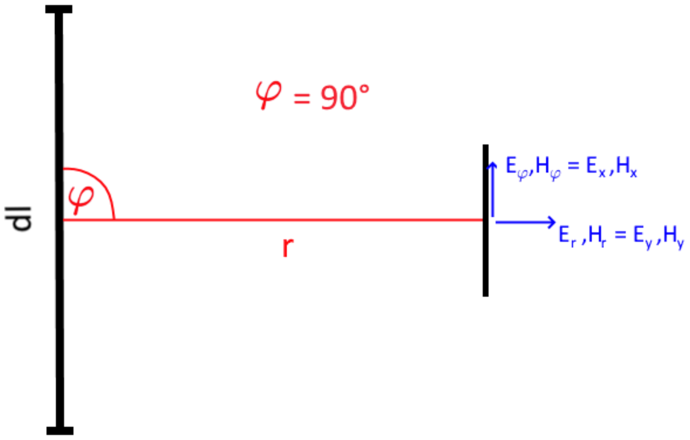

**Figure 2.3:** Definitions of field components utilized during the survey. Having a broadside configuration, the EM field components reduce to $E_x$, $B_y$, and $B_z$ in case of a homogeneous halfspace or a 1D layer case. Therefore, subsequent formulas were simplified. The direction of $r$ coincides with the y-direction, the direction of x coincides with $\varphi$.

Field data is discussed as real and imaginary part in frequency domain and step on and step off transients in time domain in the subsequent sections. In order to get an understanding for the behaviour of the collected field data, we differentiate between the solution for the named data representations in both domains. A HED excites always a combination of tangential electric (TE) and tangential magnetic (TM) fields. However, for the broadside configuration utilized during field measurements (Figure 2.3), the TE Mode dominates the response at the receiver locations. Therefore, the sensitivity towards resistive structures is low. Only $E_x$, $B_y$ and $B_z$ components are $\neq 0$. Next to the components of the TE-mode, during field measurements, $B_x$ was measured. $B_x$ deviating from 0 gives us therefore insights, if the conductivity distribution of the subsurface can be approximated as 2D. However, being 0 for a homogeneous halfspace and our measurement configuration, it will not be discussed further in this section. Since we utilized the electric fields as validation for the frequency domain approach of the LOTEM dataset and studied different resolution behaviours in 1D and 2D for time and frequency domain, we focus on the electric field component in the following part, especially for the comparison between time and frequency domain. However, since a dense full component SQUID dataset was evaluated in frequency domain, the solution for the magnetic field is given for the sake of completeness. In the utilized 1D and 2D algorithms the forward solution is calculated in frequency domain and subsequently transformed into time domain via Fourier transformation. The following solutions are given for a point dipole. For an extended dipole, typically the solution of 10-20 single dipoles distributed along the transmitter wire is superimposed (cp. Section 8.2.1).

### 2.3.1. HED Solution in Frequency Domain

Under the assumptions given in Section 2.2, the EM Fields in frequency domain for a horizontal electrical dipole (HED) can be written as

$$E_r = \frac{\sigma I dl}{2\pi\sigma r^3}\cos(\varphi)\left[1 + e^{kr}(1 - kr)\right] \tag{2.22}$$

$$E_\varphi = \frac{I dl}{2\pi\sigma r^3}\sin(\varphi)\left[2 - e^{kr}(1 - kr)\right] \tag{2.23}$$

Note that the $E_z$ component due to boundary conditions equals 0 at the surface and is therefore not further discussed.

$$p_{FD} = \frac{r}{\delta} = \sqrt{\frac{\sigma\mu\omega}{2}}r \tag{2.24}$$

$$H_r = -\frac{Idl}{4\pi r^2}\sin(\varphi)h_r(p) \tag{2.25}$$

$$H_\varphi = -\frac{Idl}{4\pi r^2}\cos(\varphi)h_\varphi(p) \tag{2.26}$$

$$H_z = \frac{Idl}{4\pi r^2}\sin(\varphi)h_z(p) \tag{2.27}$$

The Equations 2.25-2.27 reflects the geometry dependency of the magnetic field. The factors $h_\varphi, h_r, h_z$ are dependent on the induction number $p$. For the full expression of the magnetic field components, refer to (Kaufman and Keller, 1983). Given the geometry depicted in Figure 2.3, for $\varphi = 90°$ it follows $E_\varphi = E_x$, $E_r = E_y = 0$ and $H_\varphi = H_x = 0$ and $H_r = H_y$. Equations 2.22-2.23 and 2.25-2.27 simplify, if we considering low and high induction numbers separately.

### 2.3.2. Near Field Approximation FD

First we consider the near field zone of the transmitter, which is given for low induction numbers $p_{FD} \ll 1$, i.e. for small offsets and/or low frequencies. In order to differentiate the field solutions as real and imaginary parts, the term $e^{kr}$ is developed with a Taylor expansion, resulting in field solutions for real and imaginary part for the $E_x$ component.

$$\Re E_x \approx -\frac{Idl}{2\pi\sigma r^3}\left[1 + \frac{1}{3\sqrt{2}}(\sigma\mu\omega)^{3/2}r^3\right] \tag{2.28}$$

$$\Im E_x \approx \frac{Idl}{2\pi\sigma r^3}\left[\frac{\sigma\mu\omega r^2}{2} - \frac{1}{3\sqrt{2}}(\sigma\mu\omega)^{3/2}r^3\right] \tag{2.29}$$

From Equation 2.28-2.29 we can conclude the following (after Kaufman and Keller (1983)):

- The first term of the real part can be thought as frequency independent galvanic term and depends on the resistivity of the medium. The second term is purely inductive, independent of the transmitter-receiver offset and is a function of $\sigma$ and $\omega$.

- The imaginary part is purely inductive. The first term is independent of conductivity but depends on the offset. It arises due to the change over time of the stationary magnetic field. The second term depends on the conductivity. Both terms are frequency dependent.

- For low frequencies (DC level) the imaginary part approaches zero. The real part approaches the galvanic term, i.e. the stationary field which is proportional to the resistivity.

For the magnetic field component it follows for $H_z$ and $H_y$

$$\Re H_z \approx \frac{Idl}{4\pi r^2}\left[1 - \frac{\sqrt{2}}{15}(\sigma\mu\omega)^{3/2}r^3\right] \tag{2.30}$$

$$\Im H_z \approx \frac{Idl}{4\pi r^2}\left[\frac{1}{4}\sigma\mu\omega r^2 - \frac{\sqrt{2}}{15}(\sigma\mu\omega)^{3/2}r^3\right] \tag{2.31}$$

$$\Re H_y \approx \frac{Idl}{4\pi r^2}\left[1 - \frac{3\pi}{64}\sigma\mu\omega r^2\right] \tag{2.32}$$

$$\Im H_y \approx \frac{Idl}{4\pi r^2}(\sigma\mu\omega r^2)\left[\frac{3}{32} + \frac{1}{8}\ln\left(\frac{\sqrt{\sigma\mu\omega}r}{2}\right)\right] \tag{2.33}$$

From Equation 2.30-2.33 we can conclude the following:

- Similar to the equations for the electric field, the real part of $H_z$ and $H_y$ consisting of the stationary magnetic field and a second inductive term, which is dependent on the frequency and conductivity. Note that the stationary part of the magnetic field is independent on the resistivity of the medium, unlike to the electric stationary field. Note that this holds also for a horizontally layered case. Therefore, there is lower sensitivity of the magnetic field components towards the background resistivity.
- The frequency dependent second term of the real part for the $H_z$ component is more sensitive towards the conductivity than the respective terms in the $E_x$ and $H_y$ components. Furthermore, the imaginary parts of the magnetic fields have a higher sensitivity to conductivity than the imaginary part of the $E_x$ component.

### 2.3.3. Far Field Approximation FD

In the next step, the behaviour for the far-field, i.e. large induction numbers (and therefore large values for $k$) is analysed, i.e. for large offsets and/or high frequencies. For the electric field holds

$$E_x = -\frac{Idl}{\pi\sigma r^3} \tag{2.34}$$

which follows directly from Equation 2.23, since $k$ is a complex value. For the magnetic field, one can write

$$H_y = -\frac{Idl}{\pi k r^3} \tag{2.35}$$

$$H_z = \frac{3Idl}{2\pi k^2 r^4}. \tag{2.36}$$

The derivation for $H_y$ and $H_z$ in terms of $H_r$ and $H_z$ can be found in Kaufman and Keller (1983). We can summarize some conclusions:

- $E_x$ is real valued, frequency independent and coincides with the stationary field (*2). Therefore, $E_x$ does not exhibit an inductive term for large induction numbers but is sensitive to the background resistivity.
- The magnetic field components are frequency dependent. Both are smaller than the stationary magnetic fields. The $H_z$ component decreases faster than $H_y$ with increasing offset to the source, however exhibits a higher sensitivity towards conductivity ($1/k^2$ vs. $1/k$).

### 2.3.4. HED Solution in Time Domain

The EM solutions in frequency domain are connected to the solutions in TD by a unique Fourier transformation. In order to retrieve the time domain solution, the frequency domain response is transformed into time domain utilizing a sine or cosine transformation.

$$\mathbf{F_{off}}(\mathbf{r}, t) = -\frac{2}{\pi} \int\limits_0^\infty \frac{\Im(\mathbf{F}(\mathbf{r}, \omega))}{\omega} \cos(\omega t) d\omega \tag{2.37}$$

$$\mathbf{F_{on}}(\mathbf{r}, t) = \frac{2}{\pi} \int\limits_0^\infty \frac{\Re(\mathbf{F}(\mathbf{r}, \omega))}{\omega} \sin(\omega t) d\omega \tag{2.38}$$

where $\mathbf{r} = (x, y, z)$ and $\mathbf{F}(r, t)$ the EM fields in space-time domain and $\mathbf{F}(r, \omega)$ the EM fields in space-frequency domain. Equations 2.37-2.38 giving the transformations as implemented in the recently developed time domain solution (Haroon et al., 2018) of the 2D code `MARE2DEM`. Theoretically, the step off response can subsequently be calculated by subtracting the step on response from the DC response, following equation (Kaufman and Keller, 1983)

$$E_{off} = E_{DC} - E_{on}, \tag{2.39}$$

where $E_{DC}$ is the stationary electric field corresponding to direct current conditions ($\omega = 0$) and can be written for a homogeneous halfspace as

$$E_{DC} = -\frac{Idl}{2\pi\sigma r^3}. \tag{2.40}$$

This approach is implemented in the utilized time domain 1D algorithms `EMUPLUS` and `MARTIN`. Note that in order to solve the integrals given in 2.37-2.38, the solution must be calculated for a large number of frequencies in order to gain a stable forward solution (cp. Section 8.2.10), which makes the solution in time domain computationally more expensive than in frequency domain. In the following, magnetic fields in time domain, $H_y$ and $H_z$ (e.g. measured by SQUID magnetometer) or its time derivative $dB_{y,z}/dt$ (measured by induction coils) refer to the corresponding component after switch off. We give the solution for early and late time approximation for high and low induction numbers in analogy to Section 2.3.1 for a homogeneous halfspace. For the general formulation for EM fields in time domain on the surface of a conductor we refer to (Kaufman and Keller, 1983) or Ward and Hohmann (1988). Similar to the frequency domain response for $H_\varphi(90°) = H_x = 0$ and $E_r(90°) = E_y = 0$. Solutions taken from Kaufman and Keller (1983) were simplified for an isotropic case in the following. Note, that throughout this thesis, the terms switch on and switch off response is utilized synonymously with the terms step on and step off response.

### 2.3.5. Near Field Approximation TD

The near field or late time approximation holds for small induction numbers $p_{TD} = \frac{r}{\delta_{TD}}$, i.e. for small offsets and/or late times.

$$H_y = \frac{Idl\sigma\mu}{64\pi t} \tag{2.41}$$

$$H_z = \frac{Idlr}{60}\left(\frac{\sigma\mu}{\pi t}\right)^{3/2} \tag{2.42}$$

In time domain typically the time derivative of the magnetic field is measured, when induction coils are utilized.

$$\frac{\partial B_y}{\partial t} = -\frac{Idl\sigma\mu^2}{64\pi t^2} \tag{2.43}$$

$$\frac{\partial B_z}{\partial t}(\varphi = 90°) = -\frac{Idl\sigma^{3/2}\mu^{5/2}r}{40\pi^{3/2}t^{5/2}} \tag{2.44}$$

For electric fields we obtain:

$$E_{off} = -\frac{Idl}{12\pi^{3/2}}\sqrt{\frac{\sigma\mu^3}{t^3}} \tag{2.45}$$

Therefore after current switch off, the electric fields approach zero for late times. Following Equation 2.39, electrical switch on and switch off response deviating only by the DC term 2.40 at any time t.

$$E_{on} = -\frac{Idl}{2\pi\sigma r^3} + \frac{Idl}{12\pi^{3/2}}\sqrt{\frac{\sigma\mu^3}{t^3}} \tag{2.46}$$

For large values of $t$, the electric field after switch on approaches the DC level. If one compares the field solution in time domain to the fields in frequency domain for small induction numbers, we notice, that the switch on solution for the near field approximation exhibits the same dependencies as the real part given in Equation 2.28. The switch off shows the same dependencies as the vortex term, i.e., the second term of the real part (cp. Eq. 2.28) and imaginary part (cp. Eq. 2.29) except for a constant factor. In the near field, the electric field component shows a dependency of $\sqrt{\frac{\sigma}{t^3}}$ in time and $\sqrt{\sigma\omega^3}$ in frequency domain respectively. We conclude:

- For small induction numbers, the switch on electric field response is comparable to the real part of the electric field component in frequency domain
- The switch off response is comparable to the inductive term present in both, imaginary and real part. It is not superimposed by any additional term.

### 2.3.6. Far Field Approximation TD

The far field or early time approximation holds for large induction numbers $p_{TD} = \frac{r}{\delta_{TD}}$, i.e. for large offsets and/or early times. For the magnetic fields, one obtains

$$H_y = -\frac{Idl}{4\pi r^2}\left[1 - \frac{8\sqrt{t}}{r\sqrt{\pi\sigma\mu}}\right] \tag{2.47}$$

$$H_z = -\frac{Idl}{4\pi r^2}\left[\frac{6t}{r^2\mu\sigma} - 1\right] \tag{2.48}$$

In time domain typically the time derivative of the magnetic field is measured, when induction coils are utilized.

$$\frac{\partial B_y}{\partial t}(\varphi = 90°) = \frac{Idl}{r^3}\sqrt{\frac{\mu}{\pi^3\sigma t}} \tag{2.49}$$

$$\frac{\partial B_z}{\partial t} = -\frac{3Idl}{2\pi\sigma r^4} \tag{2.50}$$

For the electric fields, again one needs to differentiate between fields after switch off $E_{off}$ and switch on $E_{on}$

$$E_{off} = \frac{Idl}{2\pi\sigma r^3} \tag{2.51}$$

$$E_{on} = -\frac{Idl}{\pi\sigma r^3}. \tag{2.52}$$

When we compare the solution for high induction numbers in frequency domain for the electric field given in Equation 2.34 with the time domain solution in Equation 2.52, one can observe, that the solution is the same in both domains. The solution between switch off and switch on for early times differs by the DC level giving in Equation 2.40. This holds also for the $E_y$ component not shown here. Note that the factor of 2 between switch on (2.52) and switch off (2.51) is only valid, if we consider an isotropic conductivity distribution (Kaufman and Keller, 1983).

## 2.4. Practical Exploration Depth

The skin depth in frequency domain and the diffusion depth in time domain can be taken as a measure of exploration depth, if the source field can be approximated as planar. For example Spies (1989) defines for magnetotelluric soundings a depth of investigation of 1.5 $\delta_{FD}$ as reasonable. However, for CSEM applications, the geometry of the transmitter-receiver offset must be taken into account for any estimations of exploration depth, since the measured field responses are offset dependent and a strong primary field might superimpose the inductive field response, if a relative error floor is considered. Spies (1989) gives an approximation of the exploration depth dependent on the transmitter-receiver offset for HED in time domain. The exploration depth reflects a more practical value dependent on the dipole moment, the conductivity and the estimated noise level. He defines for the far-field approximation

$$\delta_{S_{PET}} = 0.48 \left( \frac{Irdl}{\sigma \eta_\nu} \right)^{1/5} \tag{2.53}$$

For the near field he defines

$$\delta_{S_{PLT}} = 0.28 \left( \frac{Idl}{\sigma \eta_\nu} \right)^{1/4} \tag{2.54}$$

The given equations were utilized in order to estimate the required dipole moment and transient length with regards to the estimated noise level before the survey. Theoretically the given equations can also be used for the estimation of the exploration depth for a 1D case, if one iteratively integrates over the conductivity of each layer (Yogeshwar, 2014). For a 2D conductivity distribution, the equations are not applicable. Therefore, as described in Sections 3.5 ,3.6.3,& 8.1.1 the DOI was estimated via the analysis of different sensitivity parameters obtained during forward calculation. This approach does not only give insights about the maximal exploration depth but also on the resolution of individual layers or model cells. For 2D, sensitivity studies and forward calculations are carried out to estimate the resolution of certain model structures.

## 2.5. Summary

The LOTEM method utilizes a horizontal electrical dipole as transmitter, which is galvanically coupled to the ground and a superposition of transmitted EM-Fields and the secondary earth response is measured at receiver stations within certain offset. If the dataset is further interpreted in time domain, typically the transient response of the EM field directly after switch on or switch off is evaluated. The latter allows the measurement of the earth response in absence of a primary field. In frequency domain (CSEM), the earth response is achieved by the analysis of the the ratio between the measured field response and the transmitter signal.

LOTEM/CSEM is a diffusive method and displacement currents can be neglected. For the assumption of plane EM waves, the skin depth (FD) of the diffusion depth (TD) can be taken as an approximate measure of frequency or time dependent penetration depth. However, for an active (CSEM) source, the planar wave approximation does not hold and maximal penetration depth are geometry dependent. As a simple measure of maximal depth of investigations, different approaches must be applied for the near and the far zone, which are not only dependent by the conductivity, time or frequency, but additionally on the geometry and take field values into account. However, in order to study the resolution characteristics of model parameters, different inversion and sensitivity parameters must be evaluated.

A HED excites always a combination of tangential electric (TE) and tangential magnetic (TM) fields. However, for the broadside configuration utilized during field measurements, the TE Mode is dominating. Therefore, the sensitivity towards resistive structures is low and only $E_x$, $B_y$ and $B_z$ components are $\neq 0$.

Solutions for the HED on the surface of a uniform conductor are given in frequency domain and its transform in time domain. In frequency domain one can differentiate between the solution for real and imaginary part. Where the real part of the $E_x$ component contains a superposition of galvanically and inductive terms for the near field approximation, the imaginary part is purely inductive, however exhibits next to the vortex term an additional frequency and offset dependent, but conductivity independent term.

The time domain transform can be obtained from the frequency domain solution via Fourier transformation. For time domain electric fields, one can differentiate between step on and step off solution. Where the step on solution is superimposed by the DC field and shows similar characteristics to the real part in frequency domain for both, far and near field approximations, the step off solution is purely inductive for late times.

# CHAPTER 3

# Inversion Theory

The forward problem describes the prediction of data based on a certain physical model. The theory of the LOTEM/CSEM forward problem for a homogeneous halfspace was presented in Section 2.3. In this chapter the inverse problem in geophysics will be discussed. The inverse problem deals with the reverse problem: A dataset was measured and by calculating the forward solution, the model parameters are determined (Menke, 2018). Considering that in 2D problems the number of unknown parameters exceeds the number of data, the problem is strongly ill-posed and non-unique. Therefore, constrains must be defined in order to find the in a geological sense most reasonable result explaining the data sufficiently. In the first step, the formulation of the inverse problem and its solutions will be discussed. An overview of the general inverse problem is based on descriptions of Menke (2018), Meju (1994) and Chave and Jones (2012). In more detail, the inversion schemes which are implemented in the utilized 1D algorithms `EMUPLUS` (Scholl, 2005), `MARTIN` (Scholl and Edwards, 2007) and `EM1DW` (personal communication M. Becken) and the 2D code `MARE2DEM` (Key, 2016) are explained. In all of the named inversion algorithms an Occam Gauss-Newton style inversion approach is implemented. Additionally the 1D algorithms `MARTIN` and `EMUPLUS` utilize a Marquardt and Marquardt-Monte-Carlo scheme.

## 3.1. The Inverse Problem

The inversion of geophysical data aims to determine the subsurface structure of the earth (Meju, 1994). Therefore, a parametrisation of the subsurface with a numerical function $\mathbf{m}(\mathbf{r})$ must be carried out, whereas $\mathbf{r} = $ (x,z) consists of one horizontal direction and the vertical depth for a 2D interpretation. In the obtained dataset, i.e. the induced voltages at a certain location and time or frequency can be stored as components in a N-dimensional data vector $\mathbf{d}$ and the corresponding data errors in an error vector $\mathbf{e}$ (Chave and Jones, 2012),

$$\mathbf{d} = (d_1, d_2, ..., d_n)^T \tag{3.1}$$

$$\mathbf{e} = (e_1, e_2, ..., e_n)^T \tag{3.2}$$

where T denotes the transpose operator. The model parameters $\mathbf{m}$ can be stored in the same way as components in a M-dimensional model vector $\mathbf{m}$

$$\mathbf{m} = (m_1, m_2, ..., m_M)^T \tag{3.3}$$

and can be parametrised for the EM inverse problem as $\mathbf{m} = \rho$ or $\mathbf{m} = log(\rho)$. In the latter, positive values for the resistivities are guaranteed. According to this notation the inverse Problem can be written as

$$\mathbf{d} = \mathbf{F}(\mathbf{m}) + \mathbf{e} \tag{3.4}$$

where $\mathbf{F}$ denotes the transformation from model space to data space and is given by $\mathbf{F}(\mathbf{m}) = (F_1(\mathbf{m}), F_2(\mathbf{m}), ..., F_n(\mathbf{m}))$ with the model vector as its argument. It comprises the solution of the Helmholtz equation for the electric and magnetic field given in Section 2.2. If we assume that the inverse of $\mathbf{F}$ exists and $\mathbf{e} = 0$, the solution of the forward problem is simply given by $\mathbf{m} = \mathbf{F}^{-1}(\mathbf{d})$, and the model parameters can be found by finding the inverse of $\mathbf{F}$. However, in most cases this solution does not exist and an estimation for $\mathbf{m}$ has to be made.

## 3.2. Well and Ill Posed Problems

If exactly enough information, i.e. data $(N)$ is present to determine the model parameters $(M)$, the solution can be uniquely determined and is referred to as even-determined. Often when facing 2D or 3D EM inverse problems where more unknown model parameters exists than data, the inverse problem is underdetermined (M>N). If there is more information than unknowns, the problem is overdetermined. If the inverse problem is to a certain degree overdetermined and to another degree underdetermined, i.e. some parameters are better resolved than others, the problem is called mixed-determined. For such ill posed problems, the least square method can be applied to find the best fitting estimation of $\mathbf{m}$. Additionally, a priori information can be utilized to constrain the problem. In order to solve an ill posed problem, one usually tries to find the model parameter $\mathbf{m}$ which minimizes the distance $\mathbf{e} = \mathbf{d} - \mathbf{F}(\mathbf{m})$ between observed $(\mathbf{d})$ and predicted $(\mathbf{F}(\mathbf{m}))$ data. There are different measures of length for the distance, commonly calculated as sum of the power n of the elements i of a vector $\mathbf{e}$, e.g.:

$$L_1\text{norm:} \|\mathbf{e}\|_1 = \left[\sum_i |e_i|^1\right] \tag{3.5}$$

$$L_2\text{norm:} \|\mathbf{e}\|_2 = \left[\sum_i |e_i|^2\right]^{1/2} \tag{3.6}$$

$$L_n\text{norm:} \|\mathbf{e}\|_n = \left[\sum_i |e_i|^n\right]^{1/n} \tag{3.7}$$

For scattered data, typically low order norms are utilized, since they give equal weights to errors with different sizes (Menke, 2018). For high order norms, larger errors are weighted more. Most commonly in geophysics and also in the algorithms utilized in this thesis, a least square method ($L_2$ norm) is used, since most datasets follow Gaussian statistics and therefore it seems appropriate to put a higher weight on data with high prediction error. However, when utilizing the $L_2$ norm, outliers can lead to erroneous results. Therefore for more scattered data the $L_1$ norm or the application of a robust scheme which is insensitive to a certain amount of outliers could improve the results.

In this thesis, the error ($\sigma$) weighted root mean square (RMS), here denoted as $\chi$ (Eq. 3.8) is used as measure of the data fit.

$$\chi = \sqrt{\frac{1}{N}\sum_{i=1}^{N}\frac{(d_i - F_i(\mathbf{m}))^2}{\sigma_i^2}}. \tag{3.8}$$

Note, that in this thesis, the notations $\chi$, error weighted RMS and RMS are used equivalently and always denote the error weighted root mean square. This means, that the best fit model parameter $\mathbf{m}$ minimizes the RMS, which can be described as a minimization of a data misfit functional or cost function

$$\Phi(\mathbf{m}) = (\mathbf{d} - \mathbf{F}(\mathbf{m}))^T \mathbf{W}^2 (\mathbf{d} - \mathbf{F}(\mathbf{m})) \tag{3.9}$$

where $\mathbf{W}$ denotes the positive definite error weighting matrix $\mathbf{W} = diag(\sigma_1^{-1}, \ldots, \sigma_N^{-1})$, which contains the reciprocal of the data errors.

## 3.3. The Unconstrained Linearised Problem

For EM problems the data is connected to the forward response in a non linear way. In order to still utilize the linear least square technique, the problem is approximated as linear by expanding the functional $\mathbf{F}(\mathbf{m})$ using Taylor series about an initial guess $\mathbf{m}_0$ of the model parameters. For the initial guess we assume, that $\mathbf{F}(\mathbf{m}_0)$ is linear around $\mathbf{m}_0$ in a way, that a small perturbation of model responses can be expressed as

$$\mathbf{F}(\mathbf{m}) = \mathbf{F}(\mathbf{m}_0) + \mathbf{J}_{\mathbf{m}_0}(\mathbf{m} - \mathbf{m}_0) + \mathcal{O}(\|\mathbf{m} - \mathbf{m}_0\|^2) \tag{3.10}$$

where $\mathcal{O}$ denotes the Landau operator and where $\mathbf{J}_{\mathbf{m}_0}$ denotes the Frechet derivative (Meju, 1994)

$$[\mathbf{J}_{\mathbf{m}_0}]_{ij} = \left.\frac{\partial F_i(\mathbf{m})}{\partial m_j}\right|_{\mathbf{m}=\mathbf{m}_0}. \tag{3.11}$$

containing the partial derivatives of $\mathbf{F}$ with respect to each model parameter $\mathbf{m}_j$, also known as the Jacobian or sensitivity matrix in geophysics. The Jacobian matrix can be utilized as a measure of resolution. Well resolved parameters have high valued entries in the Jacobian matrix, meaning that the Forward operator is sensitive to small perturbations. For poor resolved parameters the entries of the Jacobian matrix tend to zero. The size of the Jacobian matrix will be $(N \times M)$ for $N$ data and $M$ model parameters (Meju, 1994). Note that high order terms of the Taylor expansion are neglected here under the assumption that the series is converging, i.e. $\Delta\mathbf{m}_j$ is small for all $j$. Therefore, we can restate our non-linear inverse problem in a linearised inverse problem by

$$\mathbf{F}(\mathbf{m}) = \mathbf{F}(\mathbf{m}_0) + \mathbf{J}_{\mathbf{m}_0}(\mathbf{m} - \mathbf{m}_0). \tag{3.12}$$

$\mathbf{F}(\mathbf{m})$ denotes an affine transformation, a linear transformation plus a constant. Replacing the model function $\mathbf{F}(\mathbf{m})$ from Equation (3.9) with the linearised approximation, the updated cost function yields

$$\Phi(\Delta\mathbf{m}_k) = (\underbrace{\mathbf{d} - \mathbf{F}(\mathbf{m}_k)}_{:=\mathbf{y}} - \mathbf{J}\Delta\mathbf{m}_k)^T \mathbf{W}^2 (\underbrace{\mathbf{d} - \mathbf{F}(\mathbf{m}_k)}_{:=\mathbf{y}} - \mathbf{J}\Delta\mathbf{m}_k). \tag{3.13}$$

The term $\mathbf{d} - \mathbf{F}(\mathbf{m}_k)$ is constant and for brevity substituted by $\mathbf{y}$.

## 3.4. Gauss Newton and Steepest Descent Method

In order to find the model parameter which minimizes the linearised cost function, the derivative of $\Phi$ with respect to $\Delta\mathbf{m}_k$ is equated to zero (Equation 3.14).

$$\frac{\partial\Phi}{\partial\Delta\mathbf{m}_k} = \frac{\partial(\mathbf{y}^T\mathbf{W}^2\mathbf{y} - \Delta\mathbf{m}_k^T\mathbf{J}^T\mathbf{W}^2\mathbf{y} - \mathbf{y}^T\mathbf{W}^2\mathbf{J}\Delta\mathbf{m}_k + \Delta\mathbf{m}_k^T\mathbf{J}^T\mathbf{W}^2\mathbf{J}\Delta\mathbf{m}_k)}{\partial\Delta\mathbf{m}_k} = 0 \tag{3.14}$$

giving

$$-2\mathbf{J}^T\mathbf{W}^2\mathbf{y} + 2\mathbf{J}^T\mathbf{W}^2\mathbf{J}\Delta\mathbf{m}_k = 0. \tag{3.15}$$

Rearranging yields for the model perturbation

$$\Delta\mathbf{m}_k = (\mathbf{J}^T\mathbf{W}^2\mathbf{J})^{-1}\mathbf{J}^T\mathbf{W}^2\mathbf{y}. \tag{3.16}$$

In order to achieve the updated model $\mathbf{m}_{k+1}$, the model perturbation is added to the model from the previous step $k$, e.g. the starting model $k = 0$.

$$\mathbf{m}_{k+1} = \mathbf{m}_k + \Delta\mathbf{m}_k \tag{3.17}$$

This process is repeated until a model is found which adequately fits the data and typically referred to as the unconstrained iterative least square fitting or Gauss Newton method. A drawback of this method is the strong dependency on the starting model. If the starting model is too far from the global best fit model, the method may converge to a local minimum (Compare Figure 3.1). Additionally, if the eigenvalues are close to zero, $\mathbf{J}^T\mathbf{J}$ is ill conditioned and the solution overshoots the linear range (Meju, 1994). Therefore, the Gauss Newton algorithm typically is adapted including a constraining bound to the step length.

Another way to find the model update is the steepest descent method. Here, the model is corrected in the direction of the negative gradient of the non linear objective function, where $\gamma$ is a constant and denotes the step size of the model correction (Meju, 1994). The method has good initial convergence property, however the rate of convergence decreases during inversion when the step size decreases.

$$\Delta\mathbf{m}_k = -\gamma\frac{\partial\Phi}{\partial\mathbf{m}_k} \tag{3.18}$$

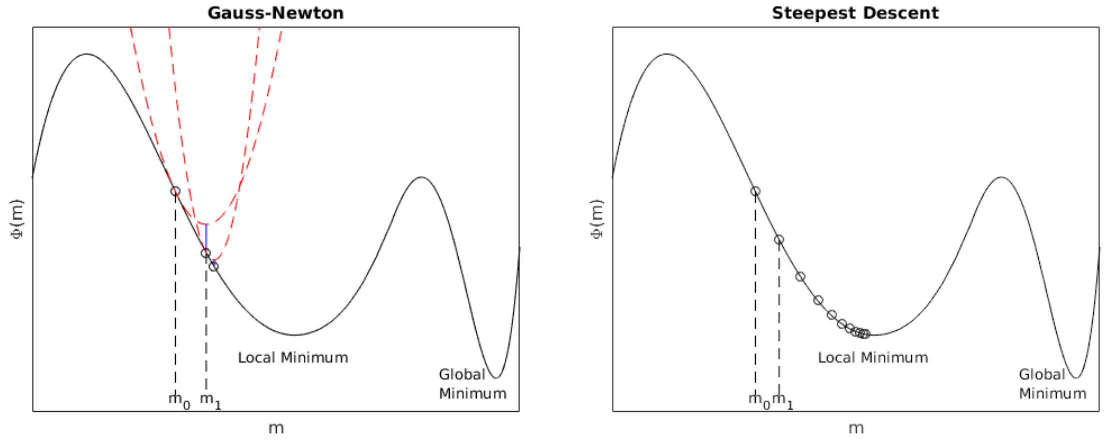

**Figure 3.1.:** The Gauss Newton method tries to localize the minimum of the error function $\Phi(\mathbf{m})$ by finding the minimum of the linearised function (red line, paraboloid) which is tangent to the trial solution $\mathbf{m}_k$. The new model estimate is then the minimum of this paraboloid. The gradient method tries to minimize the non linear cost function directly, going in the direction of the steepest descent. Here, as starting estimate $\mathbf{m}_0$ a model was chosen which is too far from the best fit model solution. Therefore, both minimization algorithms minimize towards a local minimum and not the global minimum of the cost function.

The derivative of the non linear cost function with respect to the model parameter writes

$$\frac{\partial\Phi}{\partial\mathbf{m}_k} = -2\mathbf{J}^T\mathbf{W}^2(\mathbf{d}-\mathbf{F}(\mathbf{m}_k)) \tag{3.19}$$

and after equating it to zero, we yield for the model update

$$\Delta\mathbf{m}_k = -2\gamma\mathbf{J}^T\mathbf{W}^2(\mathbf{d}-\mathbf{F}(\mathbf{m}_k)). \tag{3.20}$$

The step size must be determined carefully, since a small step size leads to a slow convergence characteristic. For large step sizes, the minimum might be skipped over. Usually during inversion, a large value of $\gamma$ is chosen,resulting in a rapid convergence in the beginning of the inversion process (compare Figure 3.1). During later stages of the inversion $\gamma$ decreases. The optimum value of $\gamma$ is determined by a line search finding the value for which the updated cost function $\Phi(\mathbf{m}_k + \Delta\mathbf{m}_k)$ is minimized. Note that the solution for $\mathbf{m}$ does not involve any inverse matrix. Compared with the Gauss Newton algorithm, the steepest descent method has the advantage, that the scheme can not diverge. However, the rate of convergence decreases for later stages in the inversion. Since the Gauss Newton method and the method of the steepest descent exhibit different convergence speeds during different stages of inversion, often both methods are combined.

## 3.5. Constrained Occam Inversion

In general, the EM inverse problem is not well-defined. To define still a well-posed solution for the inverse problem the linearised least square approach can be extended with a second so-called stabilizing parameter $\Omega$ leading to the damped least square solution after Tikhonov and Arsenin (1977).

$$\Psi(\mathbf{m}) = \Phi(\mathbf{m}) + \mu\Omega(\mathbf{m}) \tag{3.21}$$

where $\Omega$ is the stabilization functional $\mu$ is the regularization parameter. Constable et al. (1987) introduced as stabilization term a measure of the model roughness R. Equation (3.21) can be rewritten as (3.22) considering a linearised inverse problem.

$$\Psi(\mathbf{m}_k) = (\mathbf{d} - (\mathbf{F}(\mathbf{m}_k) + \mathbf{J}\Delta\mathbf{m}_k))^T\mathbf{W}^2(\mathbf{d} - (\mathbf{F}(\mathbf{m}) + \mathbf{J}\Delta\mathbf{m}_k)) + \mu\mathbf{m}^T\mathbf{R}^T\mathbf{R}\mathbf{m} \tag{3.22}$$

where $\mathbf{R}$ contains the roughness formulation with $R_1$ and $R_2$ as different measures of roughness

$$R_1 = \sum_{i=2}^{M}(\rho_i - \rho_{i-1})^2 \qquad \text{and} \qquad R_2 = \sum_{i=2}^{M-1}(\rho_{i+1} - 2\rho_i + \rho_{i-1})^2 \tag{3.23}$$

Occam R1, or first order roughness corresponds hereby to the first derivative of $\rho$ with respect to the depth z and therefore correlates to the difference between neighbouring model parameters. Occam R2 is the second order derivative and penalizes the change of the gradient between model parameters. In other words, utilizing the roughness parameter $R_1$, the model aims to minimize the gradient of $\rho(z)$ directly, whereas with $R_2$ the curvature is minimized. This hinders sudden jumps of resistivity and therefore also suppresses thin layers with large conductivity contrasts to the surrounding.

For a 1D case, the Roughness formulations can be rewritten in matrix notation as $\mathbf{R}_1$, $\mathbf{R}_2 \in \mathbb{Z}^{M\times M}$

$$\mathbf{R}_1 = \begin{bmatrix} 0 & 0 & 0 & \dots & 0 & 0 \\ -1 & 1 & 0 & \dots & 0 & 0 \\ 0 & -1 & 1 & \dots & 0 & 0 \\ \vdots & & \ddots & \ddots & & \vdots \\ 0 & 0 & 0 & \dots & -1 & 1 \end{bmatrix} \tag{3.24}$$

and $\mathbf{R}_2 = \mathbf{R}_1^T\mathbf{R}_1$. In the utilized 1D inversion algorithm `EMUPLUS`, `EMTS` and `MARTIN`, both inversion schemes, using the roughness Parameters $\mathbf{R}_1$ and $\mathbf{R}_2$ are implemented.

For the model update after derivation of (3.22) with respect to the model parameters one gets for the linearised problem

$$\Delta\mathbf{m}_k = (\mathbf{J}^T\mathbf{W}^2\mathbf{J} + \mu\mathbf{R}_{1,2}^T\mathbf{R}_{1,2})^{-1}[\mathbf{J}^T\mathbf{W}^2(\mathbf{d} - \mathbf{F}(\mathbf{m}_k))) - \mu\mathbf{R}_{1,2}^T\mathbf{R}_{1,2}\mathbf{m}_k]. \tag{3.25}$$

The Occam approach is usually performed with a high amount of model parameters M. For example, considering a 1D inversion case, the 1D inversion is performed for fixed thickness which is logarithmically increasing with depth utilizing around 20-50 layers. As starting model routinely a homogeneous halfspace is assumed. Therefore resistivity changes are only introduced if they are necessary to explain the data. As rough guess of the depth of investigation (DOI), Occam inversions using the first and second order derivative of smoothness constraints can be compared. For regions where both obtained models deliver similar structures, the corresponding model parameters are well resolved. If the inversion results from Occam R1 and Occam R2 are diverging, the resolution of the model parameter is poor (e.g. Yogeshwar et al. (2013), Cai et al. (2018)).

### 3.5.1. The Regularization Parameter

The regularization, or smoothing parameter $\mu$ weights between the data misfit and the model roughness. Having small values of $\mu$, the roughness will be more penalized and the inversion model is smooth on the expanse of high data misfit. For small $\mu$, the inversion problem tends to the unconstrained inverse problem without considering the roughness of the model. In the utilised inversion algorithms in this thesis, the starting value of $\mu$ is high, resulting in smooth inversion models in the first iterations. For later stations in the convergence process, $\mu$ is decreased and the resulting model gets more and more rough. The best trade off between data fit and roughness of the model is determined for every iteration during inversion process using a L-curve criterion (Hansen and O'Leary, 1993). Values of $\mu$ with the highest curvature when plotted as a function of misfit and curvature give corresponds to the best trade off.

## 3.6. Marquardt-Levenberg Algorithm

Levenberg (1944) proposed a damped least square to reduce instability and non-convergence of the ill posed problem. As stabilization functional the length of the model update is added. $\beta$ acts hereby as trade off parameter or damping parameter between the data residual and the step length. For very small values of $\beta$, the solution approximates the Gauss Newton solution. Setting a bound to the size of the perturbation, the step length is constrained.

$$\Phi = (\mathbf{d} - (\mathbf{F}(\mathbf{m}_k) + \mathbf{J}\Delta\mathbf{m}_k))^T \mathbf{W}^2 (\mathbf{d} - (\mathbf{F}(\mathbf{m}_k) + \mathbf{J}\Delta\mathbf{m}_k)) + \beta(\Delta\mathbf{m}_k^T \Delta\mathbf{m}_k) \tag{3.26}$$

For minimization, the extended cost function is derived with respect to $\Delta\mathbf{m}_k$, equated to zero and subsequently solved for the model update.

$$\Delta\mathbf{m}_k = (\mathbf{J}^T\mathbf{W}^2\mathbf{J} + \beta\mathbf{I})^{-1}\mathbf{J}^T\mathbf{W}^T\mathbf{W}(\mathbf{d} - \mathbf{F}(\mathbf{m}_k)) \tag{3.27}$$

Typically for Marquardt inversion, only a few layers are introduced (e.g. 5) which can vary in resistivity and thickness during inversion. In the beginning when the model is far from the real solution the steepest descend method dominates. Close to the solution, the Gauss Newton method overtakes. Since the Marquardt inversion scheme strongly depends on the initial model guess, often the Occam approach is carried out beforehand. The resulting smooth inversion model is then used to constrain the resistivities and the amount of layers and corresponding thickness of the Marquardt starting model.

### 3.6.1. SVD

In order to calculate the inverse of the weighted Jacobian matrix $\mathbf{WJ}$ , a singular value decomposition can be carried out. Any $N \times M$ matrix with $N$ data entries and $M$ model parameters can be factorized in the product of three other matrices.

$$\mathbf{WJ} = \mathbf{USV}^T \tag{3.28}$$

$\mathbf{U} \in \mathbb{R}^{N \times N}$ is an orthogonal matrix which spans the data space, giving information, how much a change of a data point will change the model. The columns of $\mathbf{U}$ contain the individual eigenvectors of $\mathbf{WJ}(\mathbf{WJ})^T$. The orthogonal matrix $\mathbf{V} \in \mathbb{R}^{M\times M}$ spans the model space and contains the eigenvectors of $(\mathbf{WJ})^T\mathbf{WJ}$, which reflect linear combinations of the independently resolved model parameters and is subject of the Eigenvalue analysis as discussed in the next Section. $\mathbf{S}$ is an $N \times M$ diagonal matrix, containing the non zero eigenvalues $(\lambda_1, \ldots, \lambda_N)$, or singular values of $\mathbf{WJ}$, which are the square roots of the eigenvalues of $(\mathbf{WJ})^T\mathbf{WJ}$. Typically they are sorted in decreasing order, weighting the influence of the linear combinations to the model result (Hördt, 1992). The factorization can be applied to the normal equation given in (3.27).

$$\Delta\mathbf{m}_k = \mathbf{V}\,\underbrace{(\mathbf{S}^2+\beta^2\mathbf{I})^{-1}\mathbf{S}^T\mathbf{S}}_{:=\mathbf{T}}\,\mathbf{S}^{-1}\mathbf{U}^T\mathbf{W}(\mathbf{d}-\mathbf{F}(\mathbf{m}_k)) \tag{3.29}$$

The damping matrix $\mathbf{T}$ is a diagonal matrix and contains the damping terms. Therefore, small Eigenvalues will be damped in order to stabilize the calculation of the inverse and prevent an overshooting of the linear range.

$$T_{ii} = \frac{S_{ii}^2}{S_{ii}^2+\beta^2} \tag{3.30}$$

By normalizing the damping matrix by the maximum singular value $S_{11}$, we obtain

$$T_{ii} = \frac{\lambda_i^2}{\lambda_i^2+\nu^2} \tag{3.31}$$

$\nu = \beta/S_{11}$ is hereby the relative singular value threshold (Hördt, 1992). A typical value for $\nu$ is 0.1, meaning that only singular values larger than 10 percent are changed during inversion. For LOTEM, typically a Marquardt Levenberg method of second order is applied, where $C$ equals 2.

$$T_{ii} = \frac{\lambda_i^{2C}}{\lambda_i^{2C}+\nu^{2C}} \tag{3.32}$$

A more detailed description of the SVD method can be found in e.g. Zhdanov (2002).

### 3.6.2. Eigenvalue Analysis

An Eigenvalue analysis can be performed by studying the eigenparameters (EP) which are contained in the $\mathbf{V}$ matrix and the corresponding Eigenvalues stored in the diagonal matrix $\mathbf{S}$, which are a measure of importance of each EP. Each EP consists of an independent linear combination of model parameters. The higher the corresponding eigenvalue, the better is the resolution of the eigenparameter. The result of the eigenparameter analysis can be displayed after Scholl and Edwards (2007), where the relative weights of the logarithm of the original parameters (e.g. resistivity and thickness) contained in each eigenparameter are displayed as circles. The radius of each circle is relative to the magnitude of each contribution to the eigenparameter. The colour of the circle represents positive and negative values. After Edwards (1997) the standard error in an eigenparameter is the reciprocal of its eigenvalue.

$$\Delta EP = S^{-1} \tag{3.33}$$

Values of the standard error $\Delta EP$ are displayed along the x-axis and refer to the relevance of the EP. $\Delta_{max}$ expresses the fractional errors of the logarithmic model parameters and gives a coarse upper estimation, whether the original model parameter is resolved. It contains the ratio between the **V** matrix and the eigenvalues **S**.

$$\Delta_{max}(m_j) = \sum_{k=1}^{M} \left| \frac{V_{jk}}{S_{kk}} \right| \tag{3.34}$$

### 3.6.3. Importance and BTSV

Another measure of resolution are the importances **L** of model parameters, utilizing the V-matrix and the damping term T

$$\mathbf{L} = \mathbf{VT} \tag{3.35}$$

The importances contain information about the resolution of the model parameters, ranging between 0 (poor resolved) and 1 (high resolved). For high values, the influence of the model parameter to the data fit is high. However, a drawback of the importances is the large dependency on the damping matrix and therefore also from the starting model. The value of the damping term is selected by the user and is changing during the inversion process.

$$\mathrm{Imp}_i = L_{ii} \qquad \text{with} \quad 0 \leq \mathrm{Imp}_i \leq 1 \tag{3.36}$$

Therefore in this thesis an additional measure of the resolution of a model parameter is used, following the approach of Hördt (1992). Back Transformed Singular Values (BTSV) can be calculated, which contain the eigenvalues of the eigenparameters, related over

$$\mathbf{Q} = \sqrt{\mathbf{VE}(\mathbf{VE})^T} \tag{3.37}$$

where **E** corresponds to the normalized eigenvalues of the parameter space eigenvector matrix **V**, containing values between 0 and 1. The highest value exhibits the best resolution of the corresponding model parameter.

$$\mathrm{BTSV}_i = Q_{ii} \qquad \text{with} \quad 0 \leq \mathrm{BTSV}_i \leq 1 \tag{3.38}$$

### 3.6.4. Equivalent Models

If two models have an identical response within their errors bounds, they are defined as equivalent. If model parameters are poorly resolved, large changes of those model parameters will not affect the data fit strongly. In order to investigate, how much one can alter obtained model parameters within the error bounds, for the utilized 1D algorithms, a Hybrid Marquardt Monte Carlo scheme is implemented (Scholl, 2005). Typically model parameters are randomly disturbed within a predefined percentage range and equivalent results are compared. The outcome results in a number of Marquardt inversion models, which all show a sufficient low data misfit. If the resulting models show large variations in resistivity or model thickness, the corresponding model parameter is poorly resolved. If the variations are only small, the model parameter is well resolved.

## 3.7. Calibration Factor

In the utilized 1D inversion algorithms `MARTIN` and `EMUPLUS`, a calibration factor (CF) can be included. If static errors affect the data, e.g. by shifts in amplitude of the transmitter current, receiver-transmitter offsets or dipole length, a calibration factor can be adapted during the inversion. It is a non physical time independent factor, which is multiplied with the forward calculated transient response during each forward call in order to best fit the modelled transient with the measured transient. If one do not account for static errors, typically the CF is fixed and set to 1. If the calibration factor is freed, it can be adapted during each inversion step to find a best fit model. However, since for electric fields, the integrated area of $\mathbf{E}(t)$ is dependent on the resistivity distribution of the earth, a free calibration factor increases the ambiguity greatly. Therefore the CF is kept fixed to one for the presented 1D inversion models.

## 3.8. Parameter Transformation

Often the dependency between model parameters $\mathbf{m}$ and the model response $F_i(\mathbf{m})$ are not close to linearity (Scholl and Edwards, 2007). In order to achieve a better approximation, both the data and model parameters can be transformed into log space, e.g. by $\mathbf{F}(\mathbf{m}) \rightarrow \log_{10}(\mathbf{F}(\mathbf{m}))$ and $\mathbf{m} \rightarrow \log_{10}(\mathbf{m})$. Additionally the error weighting matrix $\mathbf{W}$ must be adapted accordingly. For the error weighted difference between forward calculated response $\mathbf{F}(\mathbf{m})$ and measured data $\mathbf{d}$ in log space one can write

$$\begin{aligned}\log_{10}(F_i(\mathbf{m})) - \log_{10}(d_i) &= \log_{10}(1 + c_i)\\ &\approx \frac{c_i}{\log(10)}\\ \delta &= \left|\frac{\log_{10}(d_i) - \log_{10}(F_i(\mathbf{m}))}{p/\log(10)}\right|\end{aligned}$$

Here, $p_i = \frac{\sigma_i}{d_i}$ denotes the relative error of the data and $c_i = \frac{F_i(\mathbf{m})}{d_i} - 1$ is the relative difference between the forward calculated data and the measured data. This helps on the one hand not to overestimate the misfit, when $F_i(\mathbf{m})$ is very small compared to $d_i$, i.e. $|c| \gg 1$. On the other hand, we get a more accurate description of the relative misfit between the two values. Basically this means that we treat $c \ll 1$, and therefore $\log(1 + c) \approx c$.

However, if sign reversals are present in the data, which is often the case for time domain switch off transients or frequency domain real and imaginary part, a log transform will be erroneous. Then an area sinus hyperbolicus (arsinh) transformation can be applied to the dataset (Eq. 3.40). The arsinh transformation as described in Scholl and Edwards (2007) is implemented in the 1D time domain implementation of `MARTIN`, `EMUPLUS` and the 2D time domain implementation of `MARE2DEM`.

$$\tilde{F}_i(\mathbf{m}) = \operatorname{asinh}\left(\frac{F_i(\mathbf{m})}{s}\right) = \ln\left(\frac{F_i(\mathbf{m})}{s} + \sqrt{\left(\frac{F_i(\mathbf{m})}{s}\right)^2 + 1}\right) \tag{3.40}$$

The scaling factor $s$ is typically set to 0.01 of the maximum value of the transient respectively. For large values of $d_i$ compared with $s$ or small values of $d_i$ compared to $-s$ the dependency is rather logarithmically. For values close to $s$, the dependency is linear. Additionally the sensitivities must be adjusted. For the adapted sensitivities after arsinh transformation one can write

$$\tilde{\mathbf{J}}_{ij} = \frac{\partial \tilde{F}_i(\mathbf{m})}{\partial \log(m_j)} = \left(\frac{\partial \log(m_j)}{\partial m_j}\right)^{-1} \frac{\partial \tilde{F}_i(\mathbf{m})}{\partial F_i(\mathbf{m})} \frac{\partial F_i(\mathbf{m})}{\partial m_j} = \frac{m_j}{\sqrt{F_i(\mathbf{m})^2 + s^2}} \mathbf{J}_{ij} \tag{3.41}$$

and accordingly for the log transformation, the sensitivities yield

$$\tilde{\mathbf{J}}_{ij} = \frac{\partial \tilde{F}_i(\mathbf{m})}{\partial \log(m_j)} = \left(\frac{\partial \log(m_j)}{\partial m_j}\right)^{-1} \frac{\partial \log(F_i(\mathbf{m}))}{\partial F_i(\mathbf{m})} \frac{\partial F_i(\mathbf{m})}{\partial m_j} = \frac{m_j}{F_i(\mathbf{m})} \mathbf{J}_{ij} \tag{3.42}$$

In order to compare the Jacobian matrices with each other, the transformed Jacobian matrix need to be divided by the calculated prefactor $p_{ij}$

$$p_{ij} = \left(\frac{\partial \log(m_j)}{\partial m_j}\right)^{-1} \frac{\partial \log(F_i(\mathbf{m}))}{\partial F_i(\mathbf{m})} \tag{3.43}$$

For time domain data, in this thesis typically a log transformation is utilized for switch on voltages and an arsinh transformation for switch off voltages and the induced voltages for the time derivative of the magnetic field. For frequency domain, real and imaginary part of the transfer function are calculated. However, as discussed in Section 8.2.9, it might be advantageous to transform the data in amplitude and phase values. Considering that amplitude and phase do not exhibit sign changes, a log transform of the data is utilized for inversion.

# CHAPTER 4

# The DESMEX Project

Since strategically important minerals often exhibit high electrical conductivities, (e.g. Airo (2015), Spagnoli et al. (2016)), electromagnetic methods are an important tool for mineral exploration. Where the depth extension of existing mineral deposits is mostly unknown, methods are required to obtain deep information, not only to delineate the depth extension of the mineral deposit, but also to understand the geological structures of the host rocks. In order to combine a large penetration depth with a fast and dense area coverage, a semi-airborne method is developed within the BMBF funded DESMEX (Deep Electromagnetic Sounding for Mineral Exploration) project (Smirnova et al., 2019b; Nittinger et al., 2017; Schiffler et al., 2017), utilising a ground based transmitter and airborne receivers. Additionally installed ground based electric field receivers ensure a high penetration depth and deliver complimentary information about the resistivity distribution of the subsurface. The measurement principal is illustrated in Figure 4.1. Compared with grounded receivers, an airborne receiver system allows a fast data coverage over a large spatial area and is applicable in rough terrain. Challenges consists hereby of the minimization of high motion induced noise levels and a limited amount of data for subsequent stacking due to the high flight velocity during data acquisition.

In the framework of the project, two different receiver systems were evaluated. One system utilizing commercially available fluxgate magnetometers and induction coils (Smirnova et al., 2019b; Nittinger et al., 2017), developed by University of Münster (WWU), the German Federal Institute of Geosciences and Natural Resources (BGR), and Metronix GmbH. The second system was developed by Leibniz Institute of Photonic Technologies (IPHT) and the Supracon AG and utilizes a superconducting quantum interference device magnetometer (Schiffler et al., 2017) for three-component magnetic field measurements. Additionally to the airborne magnetic field receiver system, ground based receiver stations deliver complementary information, if the electric field is measured.

In order to validate the newly developed semi-airborne method and to delineate parameters for the derivation of a final subsurface model, in the framework of DESMEX numerous geological, mineralogical (cp. Müller (2018), Krolop et al. (2019)) petrophysical (Costabel and Martin, 2019) and geophysical (Steuer et al., 2015; Rochlitz et al., 2017; Martin et al., 2018; Preugschat, 2019) studies were performed, and new modelling routines for EM data evaluation (Rochlitz et al., 2019) were developed. Within the DESMEX study long offset transient electromagnetic measurements aim to provide a validation to the developed semi-airborne method, with focus towards deep structures, and deliver a 2D subsurface model, which will be integrated into a final deposit model. In the following section, the motivation for LOTEM measurements as validation method in the framework of the joint DESMEX project is shortly highlighted, the geology of the survey area is delineated and existing petrophysical and geophysical investigations are outlined.

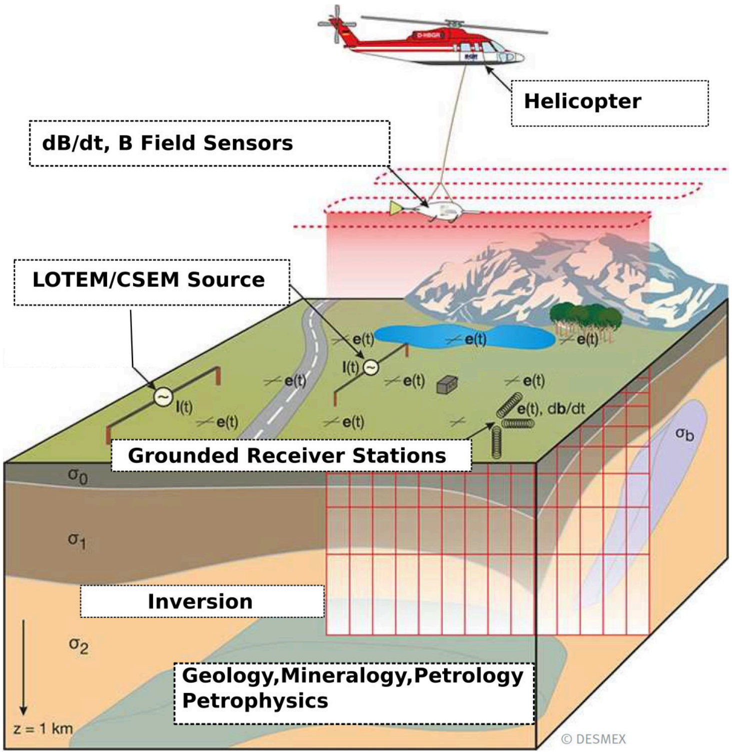

**Figure 4.1:** The semi-airborne method consists of galvanically coupled dipole transmitters installed at the ground, which produce a strong source signal, allowing data acquisition at larger offsets and reaching larger penetration depths compared to airborne systems. Airborne receivers measure the magnetic response. Additional ground based stations deliver complementary information. New modelling and inversion routines are developed to evaluate the acquired data. Geophysical data and additionally information from geology, mineralogy, petrology and petrophysics will be integrated in a final mineral deposition model.

## 4.1. Detecting Deep Structures with LOTEM

Land based CSEM methods like LOTEM exhibit a high resolution as well as a high penetration depth and are therefore an adequate tool to bring insights into deep geological subsurface structures. The LOTEM validation study aims to derive an independent multidimensional resistivity model of the survey area, which serves as a reference model for the semi-airborne concept and will eventually be integrated in a final mineral deposition model.

Ground based CSEM methods deliver several advantages and disadvantages compared with semi-airborne measurements. The installation is more time consuming and slower than airborne measurements. Additionally one is restricted in terms of accessibility. However, the advantage of land based measurements is the possibility to measure the electric field response additionally to the magnetic field response, which delivers complementary information. Most importantly it exhibits an increased sensitivity towards poor conductors. Moreover, utilizing stationary receivers, longer measurement duration and therefore larger offsets and an increased exploration depth can be realized. The LOTEM validation study aims to resolve high conductive targets within depths of 1 km. Survey parameters, e.g. measurement duration, transmitter periods and therefore the time range for evaluation, which is one of the constrains of the maximal penetration depth, as well as the resolution and utilized offsets are determined in order to resolve deep conductors. An example of the applicability of LOTEM towards deep conductors is illustrated in Figure 4.2. The target response assuming a conductive layer in 1 km depth in a homogeneous halfspace is up to 70 %. Therefore, under consideration of typical relative data errors in the range of 5%, the conductor is well detectable.

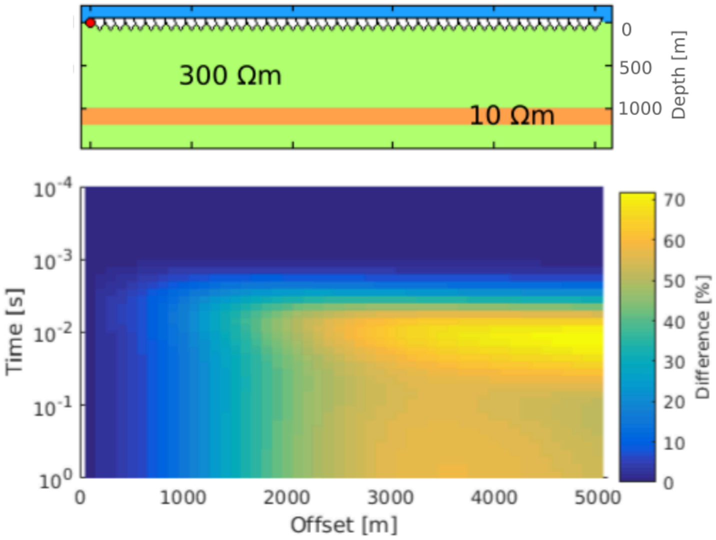

**Figure 4.2:** Upper Panel: 1D Model with conductive layer of 200 m thickness in 1 km depth. Lower Panel: Target response for the broadside $E_x$ switch on component. Shown is the rel. difference between the forward response calculated for the 1D model vs. a homogeneous halfspace of 300 Ωm. Offsets between receiver (triangles) and transmitter (red circle) are ranging between 0 and 5000 m. Forward response calculated with `MARE2DEM`.

However, since mineral deposits are often not located in a 1D environment in terms of conductivity, the installation of multiple transmitter-receiver configurations and a combined measurement of electric and magnetic field components delivers complementary information of the subsurface and constrain the ill-posedness (cp. Section 3.2) of the problem. Even more, as discussed in the next section, the geology in the survey area is rather complex and induced polarization and anisotropy effects might influence acquired EM results. Therefore several transmitters and a dense recording of both, magnetic and electric fields were realized in the survey area. In order to get information about shallow and deep targets, the transient fields over a broad time range are measured. Details about the field setup and survey parameters of the LOTEM validation study are discussed in Chapter 5.

## 4.2. Geology of the Survey Area

As a test area for the DESMEX semi-airborne experiment and the LOTEM validation study, a former antimony mining area located in the Thuringian Slate mountains on the border to Saxony, Germany, was chosen, which is part of the Berga Antiform located in the central part of the Saxo-Thuringian Zone. It can be assigned to the wrench and thrust zone of the Saxo-Thuringian Zone (Krolop et al., 2019; Kroner et al., 2007) and was formed by a regional deformation event during the Variscian Orogenese. The regional geological strike direction follows the dominant Variscian strike from northeast to southwest. The Berga Antiform consists out of several shale and quartzite units from Ordovician age

(Dill, 1993), partly covered by thin layers of Silurian to Middle Devonian black shales. Several faults and thrust zones running traversely to the Berga saddle (cp. Figure 4.3), the main faults being the Vogtland thrust fault and the Mühltroffer cross zone. At the survey area, in the Schleiz region, the Ordovician rocks from the Phycoden group form thick sequences of sandy and silty schists, overlain by organic clay slates (Griffel slates) which often contain pyrite, followed by quartzite and sandy silt slates (Leder Slates) of the Gräfenthal Group, cut through by steep Metabasalt from the Devonian (Krolop et al., 2019).

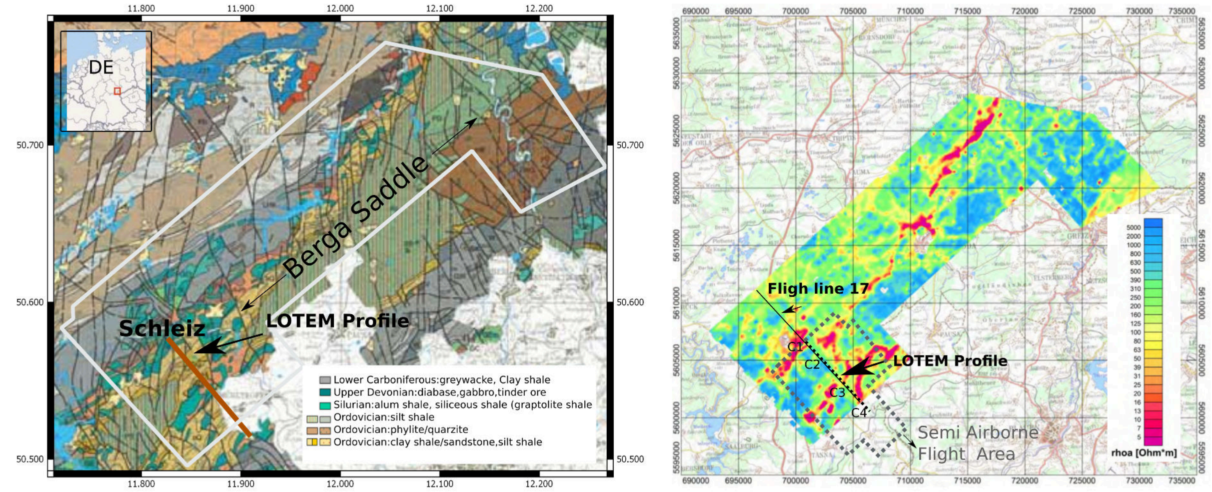

**Figure 4.3.:** a) Geological overview of the survey area located in the Berga Anticline at the border of Thuringia, Saxony, DE. Geological map based on the digital geological map (Liebe et al., 1912; Gräbe et al., 1996) of Thuringia (Germany). The white line outlines the flight area for HEM measurements. b) Apparent resistivities at a frequency of 1.8 kHz from HEM measurements. The dotted black line denotes the location of the LOTEM profile. The dotted grey line denotes the location of the complete semi-airborne flight area from 2016 and 2017. Modified after Steuer et al. (2015).

Until the 1950s, antimony was mined down to approximately 200 m depth at the mine "Halber Mond" (Dill, 1993), located in the DESMEX survey area close to the district town Schleiz. Figure 4.4b shows a cross section of the formations at the former antimony mine. The extension of the cross section is marked in the geological map in Figure 4.4a. As shown in Figure 4.4b, in the northwest of the LOTEM profile, close to the former antimony mine "Halber Mond", sequences building up the lower part of a reverted horizontal fold. The antimony containing ore veins are bound to NW-SE Variscian fault zones, crossing their host rocks discordantly.

However, due to the local restriction of antimony to lenticular sectioned ore bodies with a high restricted extension reaching from several decimetres to max. 3 m (Schlegel and Wiefel, 1998) and a resistivity larger than 100 Ωm of antimony ore (Costabel and Martin, 2019), the antimony mineralisation itself can not be resolved with electromagnetic methods. Additionally, the alteration of the host rocks is very weak (Krolop et al., 2019) and is probable not detectable with EM. Since the DESMEX experiment is not aiming for the detection of exploitable minerals in the first stage, but aims for an evaluation of the newly developed method, strategic important minerals as target are not essential. A high conductive target, which can be correlated to a geological sequence is sufficient for validation. As illustrated in the following section, the Silurian black shale exhibits low

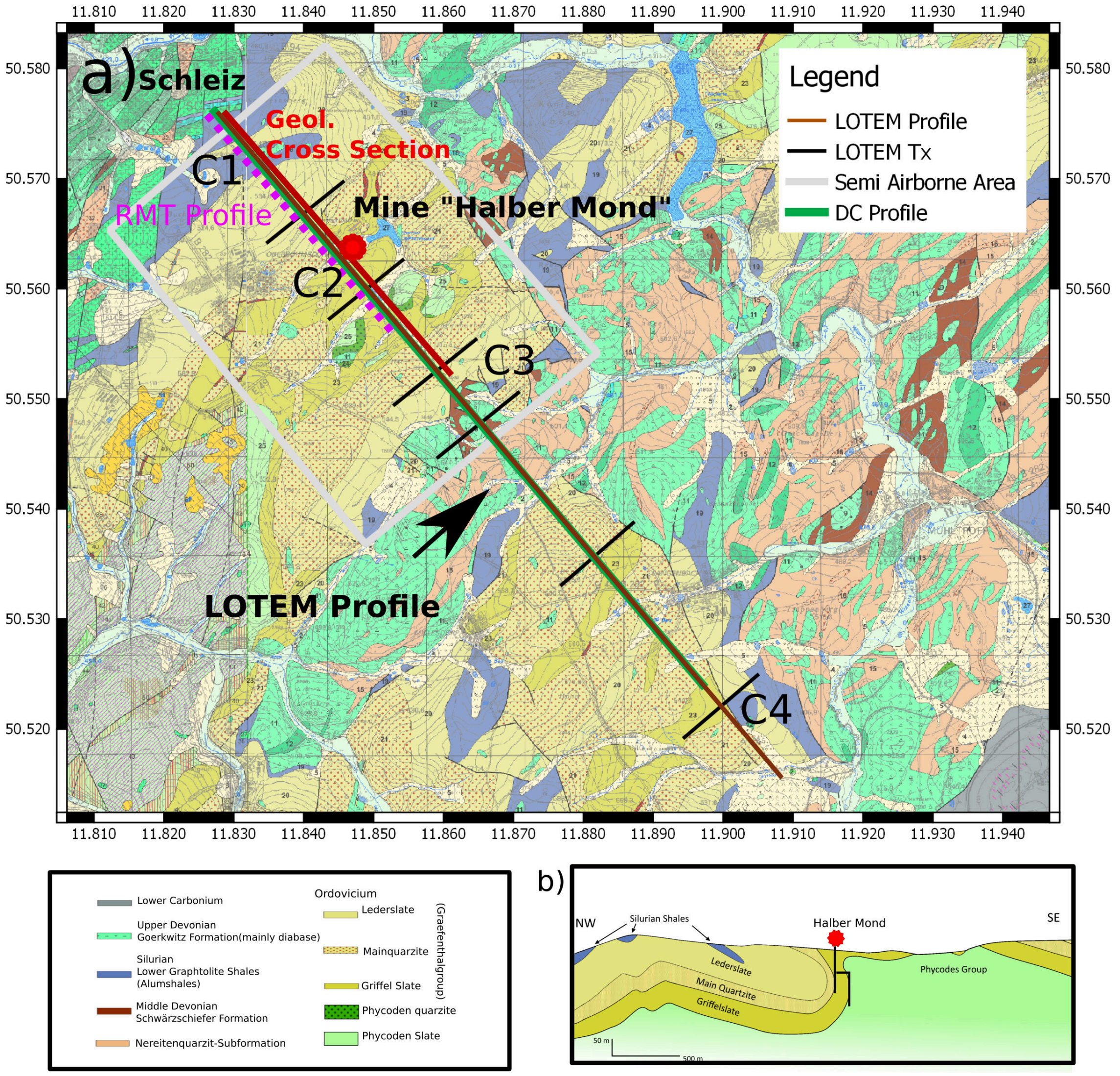

**Figure 4.4.:** a) Geological outcrop map based on the digital geological map (Liebe et al., 1912; Gräbe et al., 1996) of Thuringia (Germany) and location of the DC Profile (green) and the LOTEM Profile (brown), the semi-airborne flight area 2016 (white), the approx. location of the cross section (red), the former antimony mine "Halber Mond" (red star) and the RMT profile (purple). Note, that the LOTEM profile runs parallel to the DC Profile and extended in the NW. Locations of the most prominent Siluraian black shale formations along the LOTEM profile are marked with C1-C3. b) Cross section, modified after Wagenbreth (1946).

electrical resistivities and is therefore an applicative target for validation studies, even though it is not directly correlated to the antimony ore veins or its host rocks.

## 4.3. Petrophysical Measurements

Costabel and Martin (2019) performed petrophysical measurements from samples collected in the survey area. They investigated the density $\rho_{dens}$, the magnetic susceptibility $\kappa$ and the specific electrical resistance $\rho$ utilizing spectral induced polarization methods in laboratory environment. Figure 4.5 lists measured $\rho$ for the investigated rock samples. For the Silurian black (alum) shales, low resistivity values down to 2 $\Omega$m were measured, which they related to pyrite and graphite occurrence in the black shales. For the other rock types, $\rho$ scatters over a wide range from 100 and 10000 $\Omega$m. However, they found, that the limited scale of rock samples utilized for laboratory measurements leads to an increased $\rho$ value. Therefore they conclude, that samples which exhibit resistivity values above 100 $\Omega$m can not directly be linked to resistivity values derived from EM field measurements. Utilizing next to laboratory measurements statistical values for $\rho$ derived from borehole logs (Geophysica, 2019) from the survey area, two most reliable lithological units in terms of geophysical measurable parameters were defined: The Devonian diabase with an averaged resistivity of approx. 500 $\Omega$m and Silurian black shales with an averaged resistivity of 20 $\Omega$m. All other investigated rock types exhibited resistivities above 100 $\Omega$m. Therefore the authors conclude, that conductive anomalies with $\rho < 100$ $\Omega$m can most probable be related to the occurrence of black shales.

Due to the layered structure of the black shales coupled with the occurrence of highly (electronic) conductive minerals as graphite (cp. Section 2.1), anisotropy and induced polarization effects are expected (Costabel and Martin, 2019). However parameters derived from laboratory measurements were varying over large scales for different probes. The large range was explained with different concentrations of graphite and pyrite in the black shales, which are responsible for induced polarization effects as well as the inaccuracy of the measurement method. Therefore, a quantitative value for the Cole-Cole parameters (cp. Equation 2.2) and anisotropy factor was not derived for the evaluation of EM field data. However they found, that induced polarization effects inherently occur for black shales, independent of their water saturation grade or the absolute electrical resistivity and therefore must be inevitably considered for interpretation of EM field measurements.

Martin et al. (2018) performed shallow dipole-dipole induced polarization measurements in time domain in the survey area to characterize the geometry and properties of the shales. They revealed strong polarization effects with chargeabilities in the order of 250 mV/V in the survey area which the authors related to the occurrence of the Silurian graptolite shales.

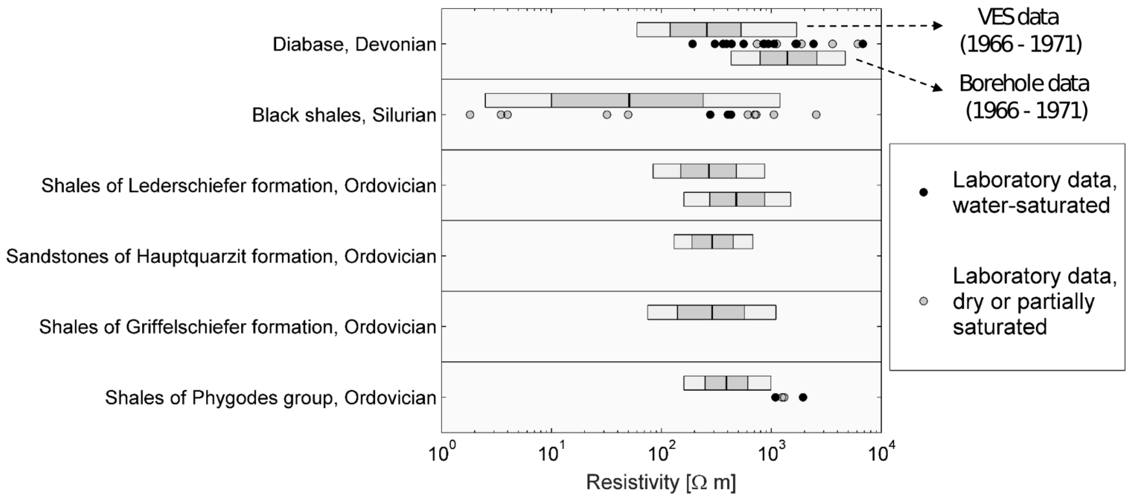

**Figure 4.5.:** Results from petrophysical measurements in Schleiz: $\rho$ values from laboratory data for 10 Hz. The upper bar in each line contains data from vertical electrical sounding, the lower bar, if present, shows data from borehole geoelectric (Costabel and Martin, 2019).

## 4.4. Further Geophysical Investigations

The University of Cologne (UoC) conducted two geophysical pre-investigations in the survey area in 2015. In-Loop transient electromagnetic (TEM) measurements (Ossen, 2017) were conducted in order to get information about the conductivity distribution in the upper 300-400 m and to define suitable locations exhibiting resistivity contrasts for the semi-airborne flight area and the LOTEM validation profile. Measurements were conducted in the northwest and southeast of Schleiz along several parallel profiles, partly overlapping with the LOTEM profile. The acquired dataset showed strong influence of 2D effects, e.g. $dB_z/dt$ transients exhibited sign reversals, which do not occur for a 1D conductivity distribution utilizing TEM in-loop configuration. Partly, a high conductive overburden related to the occurrence of black shale was found, however the data fit utilizing 1D inversion schemes was poor for most stations. In addition, radio magnetotelluric measurements (Hauser et al., 2016) were conducted parallel to the LOTEM Profile in order to to derive a 2D conductivity model for the shallow subsurface, covering exploration depth between 20-60m. High conductive structures below 10 Ωm correlated with the black shale structure (marked with C1 in the Figure 4.4) could be clearly separated from the more resistive surrounding Ordovician slates.

Next to airborne magnetics and radiometric measurements, BGR carried out frequency domain airborne electromagnetic measurements (HEM) in the flight area as pre-investigation for suitable areas of the main semi-airborne experiment in the framework of DESMEX (Steuer et al., 2015). Figure 4.3b shows an area map of apparent resistivities for one exemplary transmitter frequency. Utilizing frequencies between 387 Hz and 133 kHz, the system detects the shallow subsurface and reaches penetration depth down to approx. 150 m. Due to the small foot print of the airborne system, 1D routines are applicable for inversion (Steuer et al., 2015). The 1D inversion result of the HEM flight line 17, marked in Figure 4.3b, is compared with the derived LOTEM Model in Chapter 10. Based on the petrophysical investigations and combined with geological outcrop maps, the prominent high conductive anomalies shown in the HEM result could be related to the occurrence of

Silurian black shales. Considering the resistivity area map in the investigation area of the LOTEM study, the shallow subsurface resistivity distribution can not be considered as 1D.

As additional pre-investigation survey for the semi-airborne Main experiment, the Leibniz Institute for Applied Geophysics (LIAG) performed direct current (DC) dipole-dipole measurements parallel to the LOTEM profile. The spacing between electrodes was fixed to 125 m. Having a maximal separation between electrodes of 4375 m, a maximal exploration depth of approx. 1000 m can be reached. Results of DC measurements, with its profile location marked in Figure 4.4, will be discussed in comparison with the LOTEM inversion model in Chapter 10.

For the DESMEX main experiment, two semi-airborne surveys were carried out in in the survey area in the years 2016 and 2017. The total extend of the flight area of both years is marked in Figure 4.3. As transmitters, the LOTEM Source from the University of Cologne (cp. Section 5.1) and a high current source from LIAG was utilized. In order to reach a large penetration depth, a low fundamental frequency of approx. 10 Hz was transmitted and odd harmonics up to 6 kHz were evaluated. Detailed information about the semi-airborne flight experiment and the utilized airborne receiver systems can be found in Smirnova et al. (2019b) and Schiffler et al. (2017). Models taken for comparison with the derived LOTEM Model in Chapter 10, are from a subset of data located in the area indicated in Figure 4.4.

## 4.5. Summary

The joint DESMEX project aims for the development of a novel semi-airborne electromagnetic exploration method, which can detect deep mineral resources. As validation method, LOTEM is an applicative tool. Realising large offsets and a low signal to noise ratio compared with airborne measurements, it is a suitable method to image deep geological structures. Additional ground based electric field measurements deliver complementary information.

In the presented survey area no strategically important minerals are present which can be detected by semi-airborne methods. However, exploration for subsequent exploitation is not the aim of the DESMEX project, but the development and validation of a new system. In order to acquire first information about the subsurface resistivity distribution and to locate a suitable area for the semi-airborne experiment, which exhibits electrical conductivity contrasts and is accessible in order to install and operate the grounded transmitters, extensive geophysical pre-investigations were carried out by the UoC, BGR and LIAG. Based on geophysical and petrophysical investigations in the survey area (Steuer et al., 2015; Costabel and Martin, 2019) within the DESMEX project combined with geological information (cp. Figure 4.4), the occurrence of shallow Silurian alum (graptolite) shales in the survey area can be tracked. The shales exhibit resistivities down to 2 Ωm, which display a large electrical conductivity contrast to the surrounding material, exhibiting resistivities above 100 Ωm. Hence, it is an applicative target in order to demonstrate the newly developed semi-airborne technology.

Therefore, the LOTEM study presented here will aim to reach a maximum penetration depth as well as a high resolution in parts of the survey area which are dominated by conductive graptolite shales. Due to the high complexity of the geological/geoelectrical setting of the surroundings located in a heavily faulted geological setting and possible anisotropy effects and induced polarisation effects of the graptolite shales, information from the geophysical investigations as well as from geology and petrophysics is mandatory for a full interpretation of the electrical subsurface image. However, LOTEM measurements can deliver a low noise, deep reaching data base for subsequent interpretation.

# CHAPTER 5

# Field Setup

For the LOTEM validation study, an extensive survey was carried out in the Thuringian Slate Mountains, Germany, during summer 2016 and 2017. In total 6 transmitter positions in broadside configuration running along the regional geological strike direction (x-direction) as well as 52 E-field receiver stations along an 8.5 km long profile (y-direction) were set up (Figure 5.1). Using multiple transmitter locations for most of the receiver stations, in total 170 $E_x$-field datasets were measured. Offsets between transmitter and corresponding receiver station were ranging between 300 m and 4921 m. Vertical magnetic field induction coil data was obtained roughly every 300 m along the profile, however due to the time costly setup, induction coil measurements were skipped 2017. Further more, during the survey 2016, measurements utilizing a Low Temperature Superconducting Quantum Interference Device (LT-SQUID) were performed for the first time for LOTEM application. The system was provided and operated in field by IPHT Jena. Since the measurements proved to be superior to induction coil measurements in terms of data quality and acquisition time, the SQUID profile was extended in 2017, providing a dense three component magnetic LOTEM dataset.

In order to achieve information of the geological transition zones, the profile was set up perpendicular to the geological strike direction. Having the transmitters set up in broadside configuration, and under the assumption that the 2D electrical conductivity distribution follows the regional Variscian strike direction running northeast to southwest, mainly tangential electric (TE) fields are excited, which result in a strong vertical magnetic field component. Hence, the $E_x$ component running parallel to the broadside transmitter, the magnetic $B_y$ field component and the vertical magnetic field component $B_z$ show the highest signal to noise ratio. Therefore, next to the full component magnetic measurement, the $E_x$ component was measured. Note that the survey area is located close to the district town Schleiz, being a potential source of anthropogenic noise. In addition, a gas pipeline was running along the road close to the LOTEM profile, which is an active EM noise source due to its cathodic corrosion protection. Unfortunately pipelines were elongated towards Mühltroff between 2016 and 2017 (cp. Figure 5.1), crossing the LOTEM profile. However, since cathodic noise protection usually exhibit a rather long periodic signal of 15 s (Streich et al., 2011) compared with the measured transient length, no distortion due to the cathodic corrosion protection is evident for the range of interest in the time series and its spectral representation. Not avoidable in industrialised area, the LOTEM profile crossed several power lines, which is usually the strongest source of anthropogenic noise. The sampling time at electric field stations close to power lines was increased and a minimum distance of approx. 100 m kept.

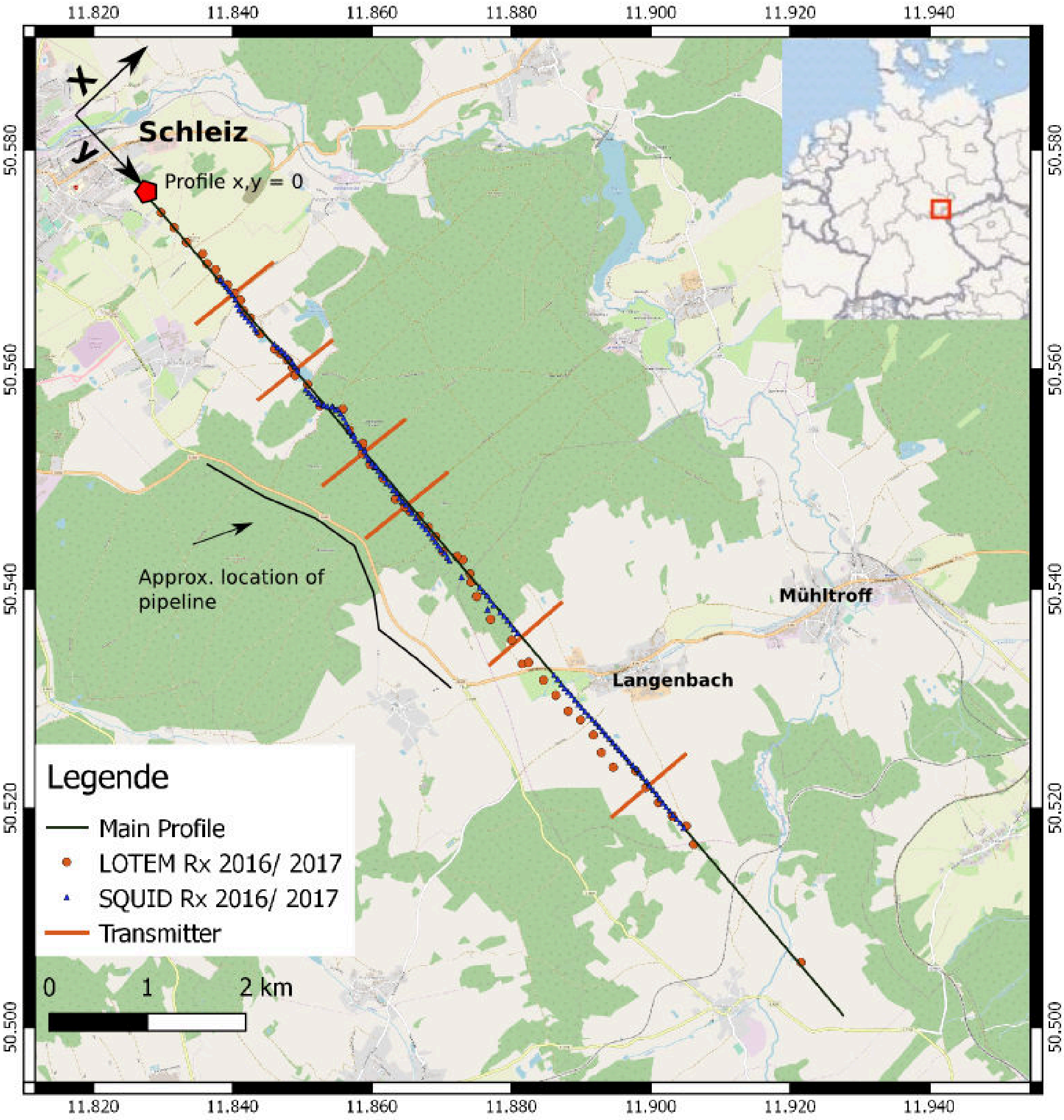

**Figure 5.1.:** Location of the LOTEM transmitters and receivers deployed during the field campaigns 2016 and 2017 along an 8.5 km long profile. Base Map: Open Street View. The direction of the profile lies perpendicular to the geological strike direction of the area. In total, 52 receiver stations using multiple sources were deployed, focussing on the E-field component parallel to the transmitter.

Transmitter amplitudes between 10 and 24 Ampere and a transmitter length of ∼1 km could be realised. The transmitter setup takes, depending mainly on the soil properties for electrode grounding in an optimum case around $\frac{1}{2} - 1$ day to install. However once transmitter sites were set up and if no additional problems occurred, up to two transmitter locations could be operated per day. In order to accelerate measurements, the transmitter cables and electrode fields were kept installed during the complete survey time. Receiver stations were set up mainly in the beginning of the survey. However, since not enough equipment was available to set up all stations at the same time, receiver sites were moved and reinstalled several times during the survey period. For each transmitter position, data at around 20 - 30 electric field stations were collected. Depending on the offset, the local noise level and the utilized switching time, at each station data was recorded between 30 min and up to 2 h in order to have a sufficient amount of stacks and subsequently a sufficiently high signal to noise ratio. Afterwards, the measuring equipment was moved to the next receiver site. Due to low internal noise of the LT-SQUID device, combined with a fast station setup, data acquisition for the full component magnetic field dataset took between 5 and 30 min.

The UoC had at the time of measurements four KMS-820 receiver units available. Since one acquisition unit is required for permanent current recording at the transmitter site, three receiver stations can run simultaneously. In order to accelerate data acquisition, several SPAM MK IV acquisition units and an additional set of receiver E-Field cables and Ag/AgCl non-polarisable electrodes were applied for and granted by the Geophysical Instrumental Pool Potsdam (GIPP). Since the devices were developed for frequency domain magnetotelluric application, they were validated for time domain application before the survey. Technical aspects of the transmitter setup and the utilized transmitter waveform are discussed in Section 5.1. Since the LOTEM dataset is subsequently processed and evaluated in time and frequency domain (cp. Chapter 6), effects of a distorted transmitter signal are investigated in both domains. Utilized receiver units and sensors are introduced in Section 5.2. An overview over all receiver transmitter combinations, utilized current functions, station positions and evaluations can be found in the Appendix A.

## 5.1. Transmitter System

As transmitter the high power and fast switching device GGT 30 (Zonge International) was used, which is powered by a 400 cycle alternator connected to a generator. The internal switch box of the GGT 30 regularises the pulse width of the transmitted signal. An accurate time synchronisation between transmitter and receiver sites was ensured by GPS synchronisation utilising a pulse per second (PPS) signal, where the trigger point, i.e. the switching point of the transmitted signal, is selected to be in phase with a common reference time (e.g. 06.00.00 AM UTC). However, due to a software malfunction in the GPS clocks, time shifts occurred between receiver and transmitter during the measurement in 2016. The problem was solved for the following survey. For problems due to synchronisation errors refer to Section 6.3.

Being a broad band transmitter, output base frequencies ranging from DC level up to 8 kHz. Output voltages $V$ can be regulated between 50 and 1000 V. The maximum Output current is restricted to $I = 45$ A. A permanent operation in field with output currents above 30 A is however not advisable with the currently implemented cooling system. During the field survey, the utilized current strength was varying between 10 and 22.5 A, since the maximum current output is restricted by the resistance ($R$) of the electrode cables and the grounding resistance of the electrodes. In field, combined electrode resistances for both electrode fields and transmitter cable in the range of 44 to 80 Ohm could be accomplished. Following Ohms Law $U = RI$, and considering a total resistance of 44 Ohm and the maximum output voltage of 1 kV, transmitter currents of up to 22.2 A could be realised.

Figure 5.2 shows an example of two of the electrode fields realised in the survey area. In order to minimise the grounding resistance, metal gratings with a high surface and steel electrodes were buried partly in to the ground and watered, with the addition of bentonite to keep humidity during the duration of transmission. In the forest, electrode grounding proved to be difficult due to dry and rooty soil conditions. If possible, advantage of suitable pre-existent spots was taken, e.g. grounding at water filled old tractor tracks along the forest road.

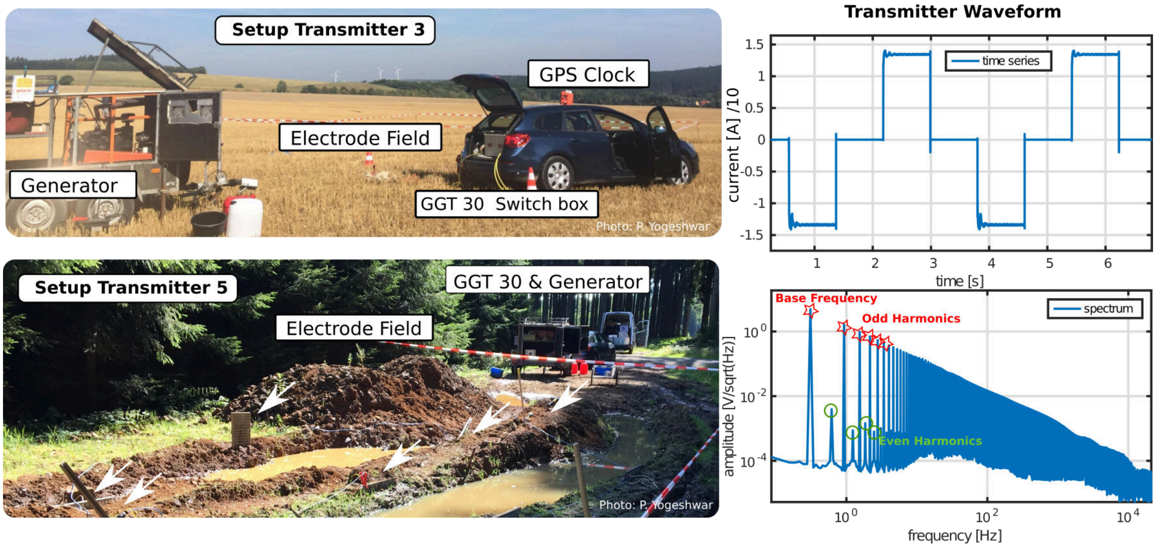

**Figure 5.2.:** Left Panel: Transmitter Setup for two of the transmitter sites. White arrows mark the position of partly buried electrodes. Right Panel: Utilized transmitter waveform as time series and as spectrum.

For safety reasons due to high voltages, the open electrode fields should be properly secured and guarded by at least one person. In order to achieve a high transmitter dipole moment $D = Idl$, which is the product of current $I$ and cable length $dl$, typically 1 km long transmitter cables were set up. The length was mainly restricted due limits in accessibility and an increased man power necessary to control and oversee the transmitter cables. The right panel in Figure 5.2 shows an exemplary transmitted waveform. A rectangular signal with switching times between 450 ms and 1050 ms was used, delivering an applicable transient length. A 50 % duty cycle was preferred over a 100 % duty cycle, since it delivered a cleaner signal, i.e. no distortion in the time, when the transmitter is switched off compared to a relatively noisy DC level. A relatively short ramp time of approximately 120 $\mu$s for a switch off procedure for a dipole length of 1000 m enables a data acquisition also in the early times (cp. Figure 5.3). Distortions after switch off is mainly produced by the overshoot of the transmitter signal and can be corrected with the measured system response (cp. Section 6.1.5).

The switch on signal exhibits more distortions produced by the transmitting device and has usually a longer ramp time. One of the critical points for time domain evaluation of

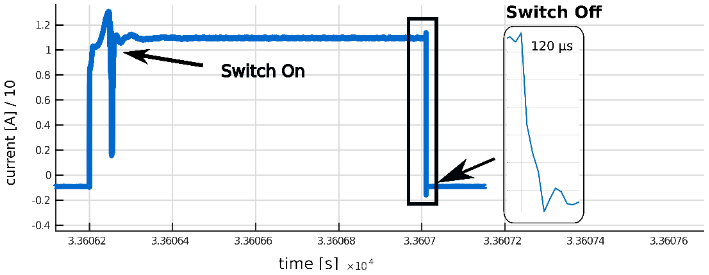

**Figure 5.3:** Ramp function of the transmitter measured by a current clamp. After current switch on, the transmitter signal exhibits strong distortions. The ramp time after switch off is approximately 120 $\mu$s long.

the dataset is the creation of a short ramp function. With regards of evaluation not only in time but also in frequency domain, the spectrum of the transmitted signal is analysed. The spectrum (cp. Figure 5.2, right panel) exhibits sharp peaks for the odd harmonics of the base frequency, which will be utilized as evaluation frequencies for processing in frequency domain. As shown in a synthetic modelling study in the Appendix A.1, issues due to a longer ramp time are not crucial for a frequency domain evaluation of the data. However in frequency domain a long ramp time would result in a reduced signal to noise ratio for high order odd frequencies. Additionally due to the deviation of the transmitter wave form from a perfectly periodic symmetry, even harmonics are visible in the spectrum, although their Signal to Noise ratio is considerably lower than for the odd harmonics, and they are therefore excluded from further processing. Therefore, a fast switching time is similar to time domain evaluation beneficial for frequency domain processing. As discussed in Section 6.2, the signal is well applicable for frequency domain processing, allowing an evaluation of odd harmonics up to 10 kHz with a base frequency ranging between 0.25-0.6 Hz.

For current recording, a current clamp was utilized. In order to sustain a secure position of the current clamp around the cable, it was placed in a pelicase and stabilized with Styrofoam. Since the survey 2016 was planned as a time domain LOTEM survey, continuously current recording necessary for subsequent processing in frequency domain was not always available. However, current amplitude and the waveform of the signal was checked throughout the survey, indicating a stable current over time. Hence, available short time current records utilized for a subsequent calculation of the transmitter system response, where synthetically prolonged over the complete measurement duration. In 2017, a continuous current recording was performed.

## 5.2. Receiver Systems and Sensors

As data logger at the receiver stations and for current recording, the KMS-820 acquisition units from KMS Technologies and the SPAM MK IV from the geophysical instrument pool Potsdam (GIPP) were utilized. The KMS-820 units were already tested for time domain application (Haroon, 2016). The SPAM MK IV was developed for frequency domain applications. Test measurements performed at the UoC utilizing a TEM Setup with fast switching times (in the range of 40 $\mu$s) produced distortions in the time series, which are probably caused by internal digital filter effects due to strong gradients after switch off. However, for longer ramp times (120 $\mu$s), oscillation effects are reduced. Additionally, oscillations are reduced, if higher sampling rates are utilized (cp. Appendix A.2).

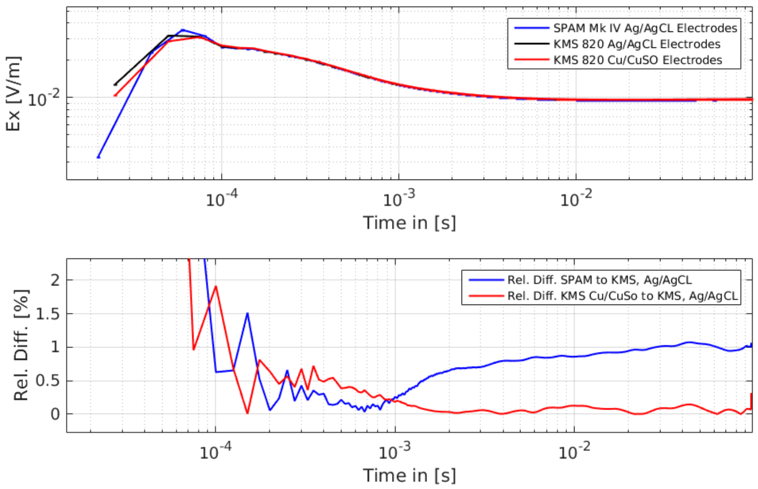

**Figure 5.4:** Comparison between the KMS-820 Logger systems (KMS-Technologies) and the SPAM MK IV Logger and Sensor Box (GIPP). The electric field response of both systems utilizing two different types of non-polarisable electrodes were tested.

Therefore, and in order to get transient information at very early times, high sampling frequencies of 40 kHz for the KMS-820 unit and 50 kHz for the SPAM MK IV system were chosen. Note, that due to the dependency of the time series distortion on the sampling frequency, for current recording and recording at the receiver stations, similar sampling frequencies should be applied. In order to validate the SPAM MK IV system for time domain application, repeated measurements were performed at the first day in the survey area with both data logger systems (cp. Figure 5.4). For the given switching times and setups, the KMS data logger and SPAM data logger deliver comparable results. For times $> 120\mu$ s, differences are smaller 1%. Since the data loggers differ in its internal delay by $50\mu$ s for the utilized sampling rates, the recorded time series of the data logger must be shifted according to the difference in delay, if different data logger systems ( SPAM MK IV and KMS-820 unit) are utilized at the receiver station and for current recording. In the comparison displayed in Figure 5.4 the transient recorded with the KMS-820 unit was shifted by -50 $\mu$s.

As E-Field sensors non-polarisable Cu/CuSO electrodes (UoC) and Ag/AgCl electrodes (GIPP) were used. Both electrode types were tested on the first day of measurement (Figure 5.4), but delivered comparable results. In order to ensure a small grounding resistance and hence a high quality of the signal over several subsequent days, the semi-permeable membrane of the electrodes were covered with bentonite, watered and buried 20-30 cm deep into the ground. The dipole length of the E-field receivers variates between 40 and 70 m depending on accessibility.

For the measurement of the time dependent change of the vertical magnetic field component, the TEM-3 coil from ZONGE with an effective induction area of 10500 $m^2$ and self constructed 40 × 40 $\mathrm{m}^2$ loops with an effective area of 84600 $m^2$ were utilized. The induction coils were partly buried for stabilisation and to minimise motion induced noise. Measurements with the large loop systems delivered high quality transients due to its large effective area, however the setup was time consuming. Additionally the loop system is only suitable for the measurement of the vertical component. In order to measure the full magnetic field tensor, a Low Temperature Superconducting Quantum Interference Device (LT-SQUID) was utilized for the first time for LOTEM measurements in the survey 2016. The device was developed (Chwala et al. (2015), Chwala et al. (2011)) by IPHT and Supracon AG in Jena, Germany, who provided and operated the system during the field survey. An overview over the technical aspects of the device for TEM applications can be found in Stolz (2015). For recent application of the system for Loop TEM in comparison with induction coil measurements, refer to Rochlitz et al. (2018). One of the main advantages is the direct measurement of the magnetic field instead of its time derivative, which exhibits a slower field decay, combined with a low intrinsic noise level of the SQUID magnetometer of $15\frac{\mathrm{fT}}{\sqrt{\mathrm{Hz}}}$ (Rochlitz et al., 2018). As logger system for the SQUID Device, the SMARTem24 (EMIT) was utilized. Having the advantage of a low intrinsic noise level and a high resolution, measurement times per site were ranging between 5-20 min, depending on the offset.

Figure 5.5 compares transient measurements of the time derivative of $B_z$ at neighbouring receiver stations utilizing the SQUID system and a Crone induction coil provided by IPHT Jena (receiver station 117) and the loop receiver station (receiver station 21). Distance between the stations are around 40 m within an offset of 1650 m to the transmitter site. For comparison, the time derivative of the SQUID response was taken. Note that the measurement for the loop lasted 1 h, whereas SQUID and induction coil measurements only lasted 10 minutes. The transient behaviour for all sensors is similar, except early times and the late time Crone coil response, which is reaching the noise level at around $7 \cdot 10^{-2}$ s. Both, SQUID and Loop TEM exhibit a stable transient response up to 1 s. Differences of early time responses up to $10^{-3}$ s can be explained by the high inertia of the loop sensor, resulting in a long influence of the system response to the transient response. The SQUID response for LOTEM proved to be comparable to conventional induction coil measurements. Due to the superior noise properties and resolution, together with a fast acquisition time, in 2017, only SQUID data was collected. The profile could be covered with a dense station spacing of 50 m. Therefore, the focus concerning magnetic field evaluation will lie on the SQUID dataset.

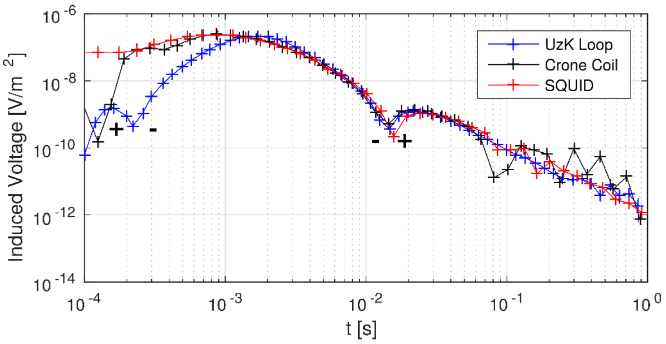

**Figure 5.5:** Comparison between the time derivative of $B_z$ measured by the SQUID Device, the Crone Induction coil and the large loop induction coil. Transient responses for the SQUID Device and the Crone coil was provided by IPHT Jena. For comparison the time derivative of the SQUID response was taken. Sign reversals are indicated with (+) and (-).

## 5.3. Summary

Utilizing 6 broadside transmitters, LOTEM data was collected for the electric field component $E_x$ and the horizontal and vertical magnetic field $B_x, B_y$ and $B_z$. Switching times of up to 1 s and high sampling frequencies between 40 and 50 kHz enable subsequent evaluation of transient data in the time range of between $2 \cdot 10^{-5}$ s to 1 s and between

0.25 Hz up to 25 kHz in frequency domain. Note, that the range of usable data might be smaller dependent on the signal to noise ratio of each station after data processing.

In the field survey, transmitter length of 1 km with current strength in the range of 8 to 22 A could be realized. Where the step off ramp function exhibit a rather short ramp length of approx. 120 $\mu$s, the step on signal is strongly distorted. Therefore, Section 6.4 will focus on the processing of step off transient data rather than step on data, however for subsequent inversion, the step off transient was recalculated to a switch on response. The transmitter signal in frequency domain exhibit strong high energy odd harmonics of the transmitted base frequency, making a further evaluation in frequency domain promising. Synchronisation errors between transmitter and receivers could be fixed for the survey in 2017.

In the framework of the survey, SQUID devices were successfully applied for the LOTEM application. In order to increase the data acquisition rate, the Magnetotelluric SPAM MK IV devices was validated for LOTEM applications. However, since oscillations at early times after switch off are dependent on the sampling frequency, similar acquisition rates should be utilized for both receiver units and for current recording.

# CHAPTER 6

# Data Processing

This chapter deals with the processing of data in both, time and frequency domain. Traditionally, LOTEM data is evaluated in time domain. However, for the collected dataset, as discussed in Section 7.3, the measured EM response in the survey area is superimposed by an induced polarization response (IP), which hinders the evaluation of the late time response in time domain. Furthermore, there exists a large range of frequency domain CSEM inversion algorithms (Key and Ovall, 2011; Grayver et al., 2013), whereas the availability of time domain codes is rather limited. Therefore in a novel approach, the acquired LOTEM data is not only evaluated in time but also in frequency domain. A comparison of obtained post-processed data and inversion models can deliver insights, if a frequency domain evaluation is suitable. Accordingly in this section, processing schemes for both domains are introduced.

Since EM noise is superimposing the field response, the collected raw dataset must be processed carefully to obtain a high quality input for subsequent inversion. Starting with the raw time series, several steps are performed during data processing, before a high quality transient in time domain, or a transfer function in frequency domain can be obtained for each station. A schematic depiction of the steps which are conducted, is illustrated in Figure 6.1. The terminology in this chapter follows the description in Figure 2.1. The period $T$ refers to one full period of the transmitted signal. The switching time refers to the duration between subsequent current switches and the ramp time refers to the time which it takes to switch the transmitter off.

If processing is performed in time domain, time segments are subdivided in segments with the length of one switching time. In order to increase the signal to noise ratio, the data is filtered and selective stacking and smoothing routines are applied. The resulting step on or step off transient reflects the decrease of EM fields over time. For frequency domain processing, the MT processing scheme `EMTS` from WWU Münster (personal communication M. Becken), was adapted to CSEM applications. The raw data of both, received and transmitted signal is Fourier transformed, and frequency dependent transfer functions between transmitted and received signal are calculated. A detailed description can be found in Section 6.1 for time domain processing and in Section 6.2 for frequency domain processing.

Next to the application of digital filter routines, coherent noise can be minimized by choosing adequate switching times beforehand, utilizing the advantage of evaluating a periodic signal (Section 6.1.1). The distortion by asynchronous data acquisition is illuminated in Chapter 6.3. For the evaluation of data in both domains it is important to acquire an accurate time synchronization between receiver and transmitter in order to pick the correct onset of the transient (time domain), or have a synchronous recorded receiver signal and transmitter signal (frequency domain) respectively. The transmitter is triggered by a GPS-clock, and must be synchronized with the GPS data of the data-loggers. In order to simplify the processing routine and prevent errors, the trigger point was set in phase with a common reference time (e.g. 06:00:00 AM UTC-time). An overview over the post-processed dataset in time and frequency domain in its different data representations can be found in Section 6.4.

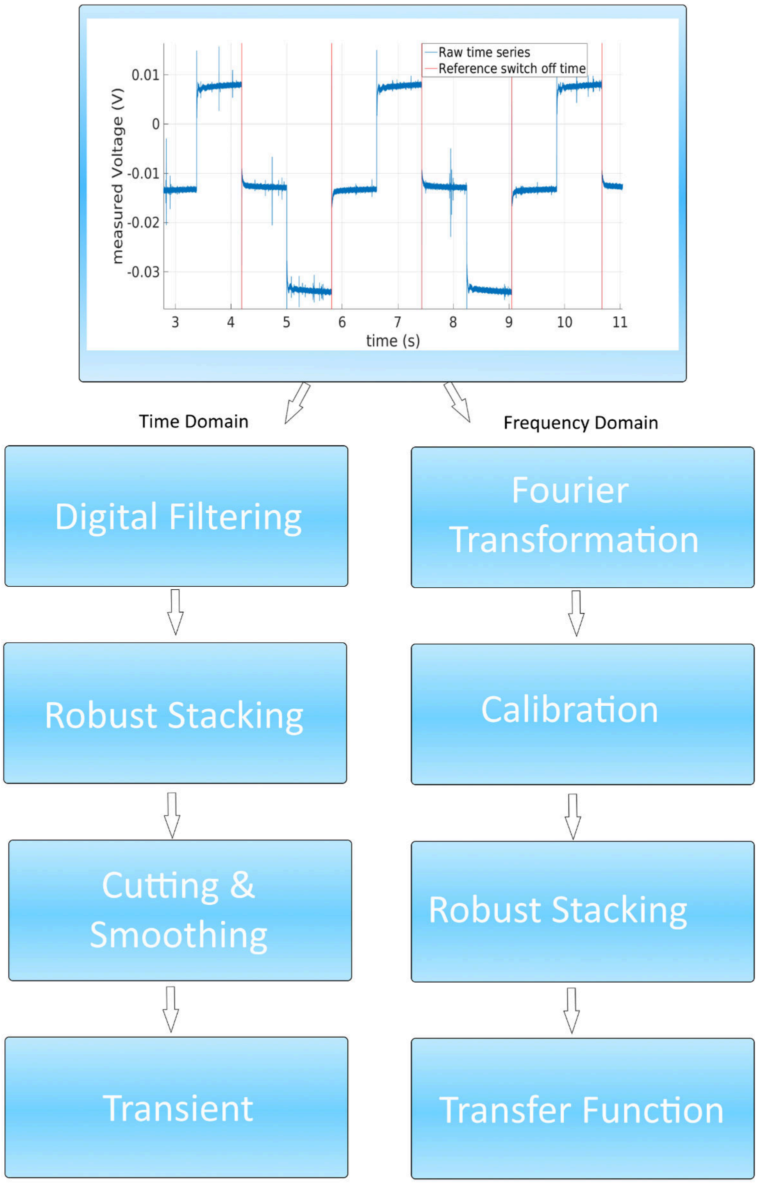

**Figure 6.1.:** Processing steps from raw data to post-processed data for an exemplary E-field station. Left side: Steps carried out for time domain evaluation: Starting from the raw time series, the transient is filtered, stacked, cut, and smoothed. Right side: Processing steps carried out for frequency domain evaluation: The raw data is transformed into frequency domain and the transfer function between measured field response and transmitted current is calculated. If frequency dependent system responses are present, a calibration function is applied.

## 6.1. Time Domain Processing

For a data evaluation in time domain, the transient response of the received electric and magnetic field component at the receiver location is evaluated in the time range between subsequent current switches. Figure 6.1 schematically shows the steps from the recorded raw data to the post processed transient. The single steps to obtain transients will be listed in the following section and displayed for one electric field station exemplarily, located with an relatively short offset of 630 m to the transmitter site. Processing routines hereby used are mainly based on Scholl (2005) and Haroon (2016).

During the processing one aims to minimize effects in the transient which are not created by the EM earth response due to the transmitted signal but are from anthropogenic sources, e.g. railways and power lines. Additionally non-correlated noise (over the time scales of the measurement), e.g. ionospheric spikes need to be reduced, commonly achieved by performing the measurements repeatedly and stacking the data. After the application of filter routines data might be still affected by correlated high frequency noise. Therefore additionally smoothing schemes are applied to the dataset. For time domain evaluation a full recording of the transmitted signal is not necessary. Only the current strength must be known in order to normalize the received signal to the transmitter amplitude. However, since the transmitter ramp, the utilised sensors and recording system will influence the measured signal, a system response is subsequently convoluted with the forward response during data modelling and inversion on base of the used transmitter waveform. For the calculation of the system response, routines analogue to the field data processing are applied.

### 6.1.1. Preprocessing: Switching Times

In the survey area several anthropogenic noise sources like pipelines, railways, and power lines are present. In order to increase the signal to noise ratio by minimising the Gaussian noise present in the data, transient measurements at one location are stacked between 1000 and 3000 times. By selecting appropriate switching times beforehand, the periodic reoccurrence of the most dominant noise sources can be utilised to minimise its influence during the stacking procedure. Considering a 50 % duty cycle and as main noise contributions 50 Hz (20 ms), 150 Hz (6.67 ms) and 16.7 Hz (60 ms), half a signal period (T/2) must fulfil the criterion

$$\frac{T}{2} = n \cdot 60\text{ms}. \tag{6.1}$$

Hence, after half a period, the noise is in phase. Considering the negative sign of the signal in the second half of the period, which will be multiplied by a factor of -1 during processing, the periodic noise contributions can be effectively reduced during stacking. Based on a-priori information about the resistivity in the survey area, 1D modelling studies were conducted to define an applicative transient length. Switching times of e.g. 450 ms ($T/2 = 900$ ms) or 810 ms ($T/2 = 1620$ ms) covered the time range of the target response and reduced the main noise contribution during the stacking procedure.

In Figure 6.2a the advantages of an appropriate transient length to minimise the periodic noise contribution in the observed electric field data are demonstrated. Without applying additional filter techniques during the processing of the data, the difference is remarkable. In the stacked data, the railway noise of 60 ms is clearly visibly in the 500 ms (light blue) long transient, whereas it is visibly reduced in the 450 ms (black, red) long transient. Even after the application of a digital three point filter, the 500 ms (dark blue) signal still contains periodic noise contributions. Hence, the 450 ms switching time is therefore clearly superior in noise suppression compared with the 500 ms switching time. Figure 6.2b lists the suitability of selected switching times regarding the property of periodic noise suppression by stacking.

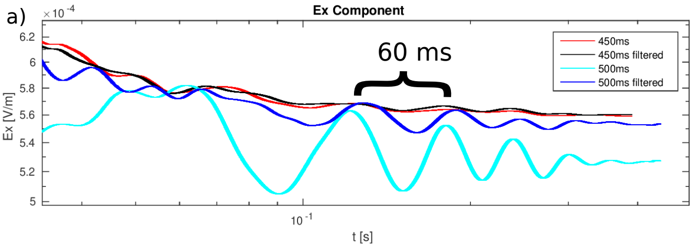

b)

| $T_{switch}$ | 50 Hz | 16.7 Hz |
|---|---|---|
| 450 ms | ✓ | ✓ |
| 500 ms | ✓ | X |
| 810 ms | ✓ | ✓ |
| 1000 ms | ✓ | X |
| 1050 ms | ✓ | ✓ |

**Figure 6.2.:** a) Distortion of transients by railway noises using two switching times. For all transients the same smoothing coefficients and number of stacks were used. b) Overview of switching times suitable for noise reduction by stacking. For the LOTEM Validation study, switching times of 450, 810 and 1050 ms were used.

## 6.1.2. Digital Filtering

In order to minimise correlated noise present in the data and remove DC offsets and possible linear drifts of the DC level, digital filter techniques are applied. In time series processing most commonly time domain digital filter techniques are applied. Additional filters tested in the framework of the thesis, e.g. notch filters worked for the spectral analysis of the data, but distorted the signal in time domain. Here, a three point filter (similar to e.g. Kingman et al. (2004) and Pankratov and Geraskin (2010)), is applied to the raw time series, which uses the periodicity of the transmitting signal in half periods. Each point in the time series $d_i$ is averaged with the point half a transmitting period later $d_{i+T/2}$, starting at the beginning of the time series. Reaching the last data point $M$, the filter moves backward in time, applying the average scheme in opposite direction until the start of the time series.

Forward Movement

$$\bar{d_i} = \frac{1}{2}(d_i - d_{i+T/2}) \qquad i = 1, 2, \ldots, M - T/2 \tag{6.2}$$

Backward Movement

$$\hat{d_j} = \frac{1}{2}(\bar{d_j} - \bar{d}_{j-T/2}) \qquad j = M, M-1, \ldots, T/2 \tag{6.3}$$

The Application of a three-point filter will affect the time series by the following:

- Removal of correlated noise: By averaging each time point with the time point in half a period distance, correlated noise can be minimised. If the period fulfils the criterion described in Section 6.1.1, correlated noise produced by a 50 Hz and 16.7 Hz base frequency are minimised in the most effective way. This process can be seen as a preliminary stacking.

- Levelling: An offset of the DC level is automatically removed, since positive and negative polarized data is summed up for the calculation of the new mean value. Note that the negative sign in Equation 6.2 compensates the different polarization of the time points half a period apart.
- Linear Drift removal: The three point filter acts two times on the time series, going one time in positive direction and at the end of the time series in negative direction. Therefore, linear drift effecting the time series can be removed.

Figure 6.3 a illustrates the effect of the three-point-filter. The blue line displays the power spectrum (a) and the time series (b) of the raw data, in orange the three point filtered dataset. In the spectral representation, the minimisation of the 16.7 Hz and 50 Hz signal is evident. The 50 Hz noise of the power line is overlaying the raw time series visibly with a period of 20 ms. After the application of the three point filter the 20 ms period overlying the signal is reduced. The mean value of the time series is shifted to zero and linear shifts present in the time series are removed. Therefore further application of a levelling algorithm between or after the last processing steps is not necessary. However, high frequency noise as well as random noise peaks are still present in the dataset. Therefore stacking and low pass filtering of the data is necessary.

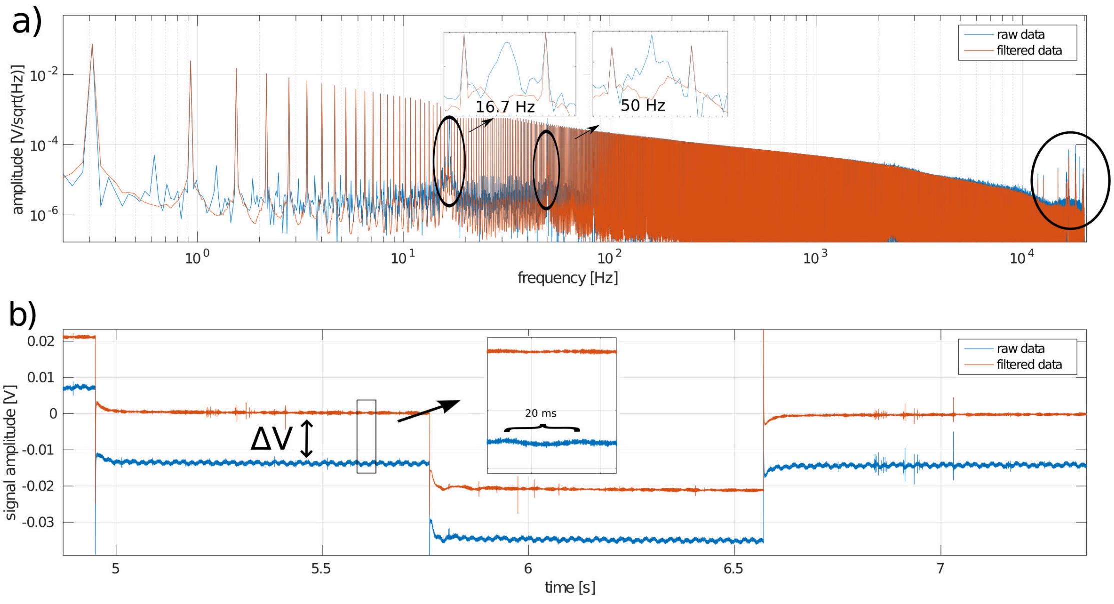

**Figure 6.3.:** Raw data (blue line) and three-point filtered filtered data (orange) displayed as spectral depiction over frequency (a) and over time (b). The dominant spikes in (a) represent the signal with odd harmonics as well as the noise frequencies of 50 Hz and 16.7 Hz as zoomed-in depiction. Correlated noise frequencies could be removed. In time domain (b), the 50 Hz noise represents as a sinus with a period of 20 ms is removed in the filtered series. Additionally, the dataset is levelled. High frequency noise (black circle) is still present after filter application.

### 6.1.3. Cutting and Stacking

Before the time series is stacked, the filtered time series is divided in time segments of a half signal period. Prior to stacking, each time segment is cut after half a signal period. Likewise to the procedure of three point filtering, the second half is multiplied by a factor of -1 to compensate the reversed polarity of the second half and shifted half a period in time in order to match the first half of the signal. Therefore the number of possible stacks is increased by a factor of two. Stacking is mainly performed to reduce non periodic noise from the data. If the dataset is normal distributed, stacking will increase the signal ($s$) to noise ($n$) ratio of the time series by a factor of $\sqrt{(N)}$, resulting in an increased signal to noise ratio $\frac{s0}{n0}$, where $N$ is the number of stacked time points.

$$\frac{s_0}{n_0} = \sqrt{N}\frac{s}{n} \tag{6.4}$$

The mean value for each data point $d_i$ over all time segments $N$ can be simply calculated by

$$\bar{d_i} = \frac{1}{N}\sum_{j=1}^{N} d_{ij} \qquad\qquad j = 1, 2, \ldots, N \tag{6.5}$$

The standard deviation of the data can therefore be calculated as

$$\sigma_i = \sqrt{\frac{1}{N-1}\sum_{j=1}^{N}(\bar{d_i} - d_{ij})^2} \tag{6.6}$$

Since LOTEM data is usually not normal distributed, the standard deviation can be strongly biased by outliers. Therefore, a form of selective stacking is applied as introduced in Hanstein et al. (1986). Selective stacking means hereby, that the data points at a certain time point for all time segments are sorted after amplitude and only values within a certain probability threshold are used for the further data evaluation. How many data points needs to be rejected in order to get a normal distributed dataset can be evaluated by the analysis of normal probability plots. In Figure 6.4 the probability is plotted against the sorted voltage values for one arbitrary time point $d_i$ for all time segments for the exemplary station 25 and as comparison station 18 with an offset of 2537 m. The probability of each data point reflects, how many measurement points have a value equal or smaller than the given data point.

The solid blue line connects the first and third quartile of the dataset and is extended to the lower and upper end. If the data is normal distributed, it will follow the blue line. Curvatures indicate a deviation of the dataset from normal distribution. For Station 25 the data is mainly normally distributed. For the station 18 recorded with a receiver-transmitter offset of 2537 m the data shows the behaviour of normally distributed data for about 80 % of the dataset. The lower 10 % and upper 10 % show a slight curvature, reflecting a deviation from a normal distribution and were excluded before stacking. Most of the recorded datasets are nearly normally distributed. Routinely, the upper and lower 10-15 % were excluded prior to stacking. The remaining dataset reflects a Gaussian distribution, therefore an adapted standard deviation can be calculated according to

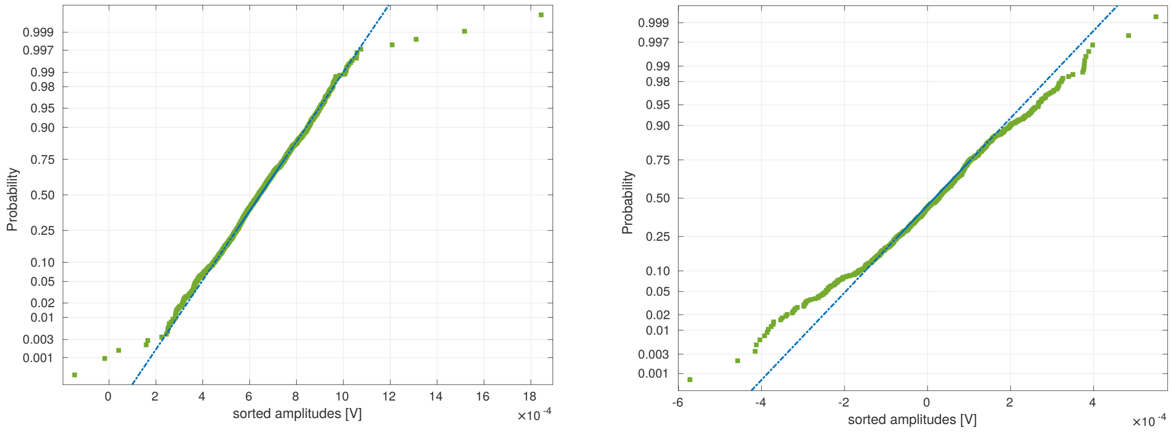

**Figure 6.4.:** a) QQ Plot for station 25 (Offset 630 m).(b) QQ Plot for station 18 (Offset 2537 m). In a) the data is close to a normal distribution. In b), the upper and lower 10 % of the sorted voltages show a deviation from the normal distribution. Both QQ Plots are displayed for one arbitrary data point at 6.25 ms after switch off.

$$\tilde{\sigma}_i = \frac{q_{3i} - q_{1i}}{1.35}. \tag{6.7}$$

In order to calculate the adapted standard deviation, the first and third quartile $q_1/q_3$ are utilized, since the inner 50 % of data points are usually normal distributed. The factor 1/1.35 correlates the number of rejected data points to the standard deviation. The adapted calculation of the standard deviation reflects the errors more accurately than the definition of the standard deviation following Equation 6.6, since it does not take outliers into account. The standard deviation describes the variation of a set of data points. Throughout this thesis, errors will be displayed and discussed as standard errors (SE), which measures the deviation from the mean of the dataset and therefore takes the number of stacks $N$ into account. In order to calculate the standard error from the standard deviation, one can calculate

$$SE_i = \frac{\sigma_i}{\sqrt{N}} \tag{6.8}$$

Note that for the calculation of the standard error only the number of actual stacks, i.e. the amount of re-occurring half periods is taken into account. Later application of filter techniques (Hanning Window) and averaging of logarithmically distributed time points is not included in the calculation for the standard errors. Since errors of neighbouring time points can be correlated, this would result in unreasonable small statistical errors, especially for late times. For the field dataset, averaging over 1000 stacks proved to be sufficient.

### 6.1.4. Application of Hanning Window

In order to minimize noise, which is still affecting the transient after digital filtering and stacking, a time variable Hanning Window as described in Hanstein et al. (1986) is applied to the post stacked transient as a weighting function. An averaged mean is calculated for data points in a successively increasing time window around a data point $d(t)$. Since

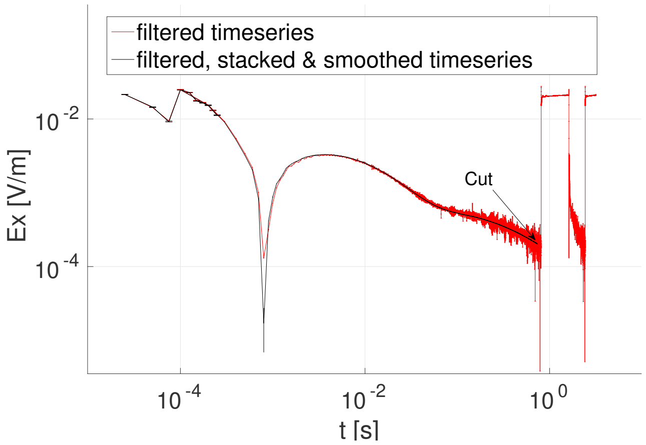

**Figure 6.5:** Stacked, cut and filtered time series in double logarithmic display. The influence of the ramp is clearly visible at early times. High frequency noise could be visibly reduced in the final transient. Displayed is the final step off transient for the electric field recorded at 630 m offset.

at early times after the switch off, high frequency signals are dominating the transient response (i.e. the transient shows the largest gradient) the size of the applied window is small directly after the switching. Therefore for early times only a few data points are incorporated in the calculation of the mean. For later times, the earth response is dominated by low frequency signals. Hence, high frequency parts in the signal are non-physical and most probable due to EM noise. Note, that correlated high frequency noise is present in the spectra (compare Figure 6.3, frequencies larger 10 kHz) which is found in all recorded field data in the survey area and can be related to VLF transmitters. Due to the increased window size at later times, more data points over a larger time scale are included in the interpolation and high frequency noise is minimised (compare Figure 6.5).

### 6.1.5. The System Response

The observed field data does not only consist of the earth response $x(t)$ but is influenced by the impulse response of the utilized measurement system. Those effects can be summarized as system response and can be a superposition of the following:

- The ramp function of the transmitter system: Dependent by the cable length, contact resistance of the electrode, the maximum current amplitude and the chosen transmitter function (Duty cycle, switching time, switch on/switch off/switch over). In most cases the ramp function is non linear (compare Figure 6.6).
- The data-logger: Especially the internal low pass filters can delay the recorded signal dependent on the sampling frequency. Additionally it can influence especially the early times, i.e. due to strong gradients after switching on/off/over the transmitter (compare Figure A.2 in the Appendix).
- The sensor system: Since the non-polarisable electrodes did not bias the recorded signal of the measured fields, this point is negligible for electric fields. The used induction coils for the magnetic field exhibit an inertia of the measured signal.

For the field survey and the used transmitter setup and 50 % duty cycle, the ramp time of the transmitter is approximately between 100 and 150 $\mu$s (Figure 6.6 a) long and shows a significant voltage overshoot at early times after switching off the signal. Since the switch on signal was heavily distorted and showed an influence of the ramp time of up

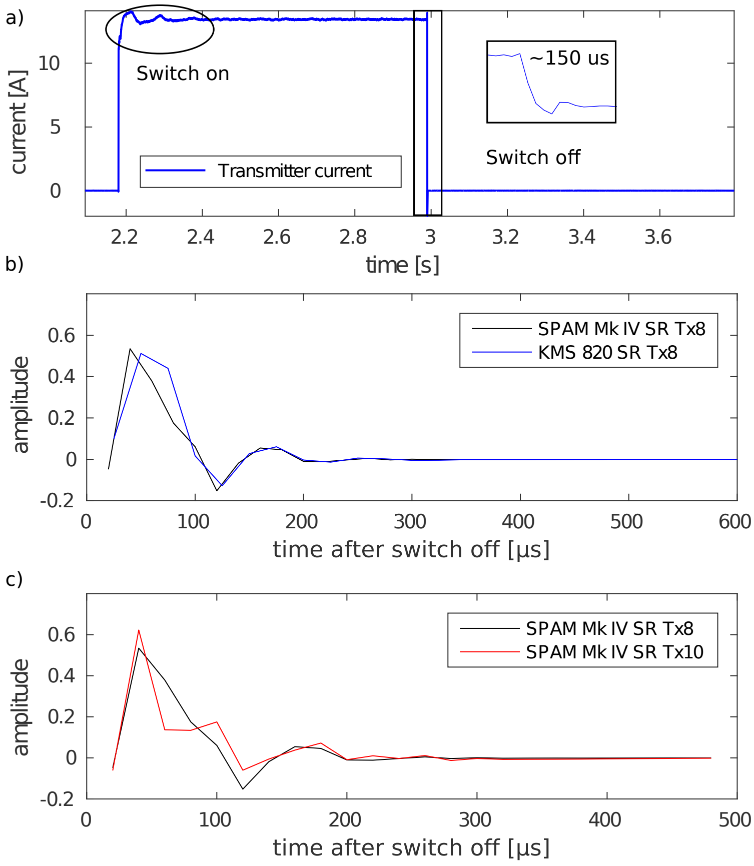

**Figure 6.6:** a) Transmitted switch on and switch off signal. The switch on signal shows distortions over a broad time range. The ramp time of the switch off signal is for most transmitter sites 100-150 $\mu$s long. b) System response for the switch off recorded at the transmitter site for the two different data-loggers. c) System response recorded at different transmitter sites.

to several ms, it was not used for further interpretation. In order to interpret the early times ($<150\ \mu$s) after switch off correctly, a system response must be recorded at the transmitter site additionally to the recorded signal at the receiver sites. The relationship between the measured field response $y(t)$ can be expressed as a convolution between the impulse response of the system $s(t)$ and the unaffected earth response $x(t)$(Strack, 1992).

$$y(t) = s(t) * x(t). \tag{6.9}$$

Therefore in order to achieve the ”true” earth response $x(t)$, the measured data must be deconvolved by the measured response of the system.

However, since a deconvolution of measured field data, which is biased by noise, proved to be numerical unstable (Scholl, 2001), the system response is convoluted with the forward modelled earth response during the inversion process (compare Section 7.1). For the E-fields a current clamp was used to record the transmitted current for approximately 5 minutes at each transmitter site with the SPAM Mk IV logger systems. Here we assume that the influence of the non-polarisable electrodes can be neglected and therefore only the transmitter ramp function and the distortion of the signal from the internal filters of the A/D converter of the logger-system needs to be considered. For the time derivatives of the magnetic field, since the inertia of the coils have an impact on the system response, stations located close to the transmitter site were used. Hence, we assume the influence of the earth response is negligible for short offsets and early times, which are the most affected by the system response (Scholl, 2001). Note, that the approach for measuring the magnetic field system response is only an approximation, since the recorded induced voltage created an over-voltage in the coil system and the data-logger system, when located to close to the transmitter. Therefore, receiver coils were located at least 100 m away from the transmitter site and hence the measured response consists of both, the earth and system response. The measured time series at or close to the transmitter site is processed likewise to the recorded EM transients, including filtering, stacking, cutting into transient length (i.e. time between current switches) and smoothing. Since the signal to noise ratio of the transmitter signal recorded directly or very close to it is significantly higher than for a recorded LOTEM transient, a very short recording time of e.g. 20 periods is sufficient.

The system response of the electric field still reflects a step response after the application of the listed LOTEM processing steps. Therefore, the time series must be deviated with respect to time to obtain an impulse response with the unit [V/s]. For the magnetic field response, recorded with a magnetic induction coil sensor, the measured system response reflects an impulse response. Therefore an additional derivation is not necessary. In order to not distort the amplitudes of the modelled transients after convolution, the impulse response is in a last step normalized to its area. The effects of the system response is mainly generated by the distortion due to the transmitter ramp. Therefore, transients directly after the switch are affected the most. Hence, usually only the early part of the measured system between the zero-point (switching point) and a time point $t_{max}$, which clearly show voltages deviating from zero, are normalized and subsequently convoluted with the forward modelled earth response $y(t)$ (cp. Equation 6.9) during the inversion process. The resulting system response after processing is unit-less.

In Figure 6.6 b a comparison between the system response utilizing data-logger systems at the same transmitter location is shown. Since the resulting system response only shows very small deviations, effects between the logger systems are rather small and can therefore be neglected. Subsequently current was only recorded by the SPAM MK IV system for most transmitter sites and used for subsequent interpretation of data sets recorded with both receiver systems. Note, that this proceeding is only applicable, if a similar high sampling rate with both data loggers is used, since the influence of the internal filters is stronger for lower sampling frequencies (compare Figure A.2 in Appendix) than for higher. Figure 6.6 c shows the comparison of the system response with the same logger system at two different transmitter locations. Deviations occur, since the system response depends on the different coupling resistances and current amplitudes. Therefore it is advisable to measure the system response at each transmitter location. Additionally, the system response should be measured again, if a different duty cycle, a new switching time or a much higher or lower amplitude is transmitted.

### 6.1.6. Data Representation

In order to reduce the number of data points suitable for inversion, the transient is interpolated to 10 logarithmic equidistant time points per decade. Additionally, the transient is normalized to the receiver length for E-fields [V/m] or to the area of the receiver coil for B fields respectively [V/m$^2$].

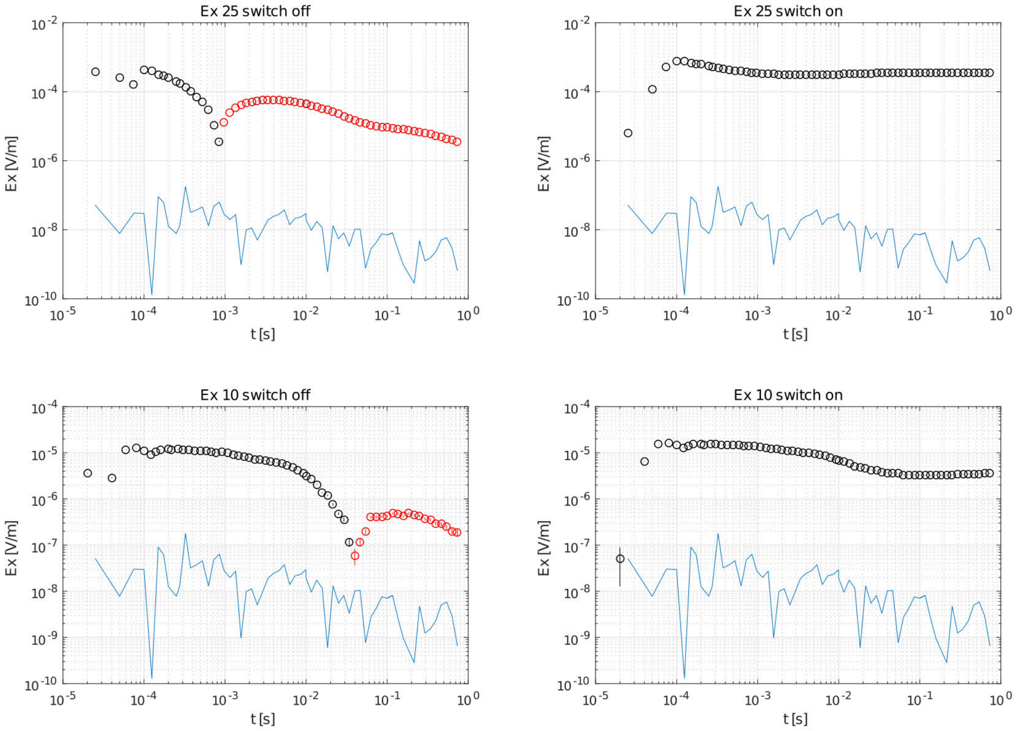

**Figure 6.7.:** Electric field data recorded at different offsets in step on and step off representation, normalized to the receiver length. Next to the data, the local noise level is shown (blue line). The black circles represent negative data points, the red circles positive data points.

Electric field data can be presented either in step on or step off representation. Step on and step off signal are simply related by the DC level (cp. Equation 2.39). Figure 6.7 shows the post-processed E-field transient of the exemplary station Tx8 25 in step off and step on representation. Additionally, the station 10 with the largest offset to Tx8 (Offset 3773 m) is displayed. For step on representation, the step off signal was levelled to the DC level of the late time step on data according to Equation 2.39. Note, that data represented as step on data is therefore only a recalculation of step off data. Recorded step on data was not further utilized, since the ramp time showed large distortions. Additionally the station with the largest offset to the same transmitter Tx8 is shown. For both datasets and both data representations, switch off and recalculated switch on, the transients exhibit low data errors over the complete time range. Both dataset are located well above the local noise level, which exhibits amplitudes in the order of $10^{-8}\frac{\mathrm{V}}{\mathrm{m}}$. Note, that the noise level was recorded during times, when the transmitter was switched off, and processed likewise to the field dataset, including stacking, smoothing and interpolation. For averaging, 1000 stacks were utilized, which is the standard value typically used for electric field processing in this survey. The influence of the system response is visible in the post processed transients for switch on and switch off, respectively. For the sake of completeness, exemplary magnetic field transients are shown for coil and loop measurements in the Appendix B.2. However, since most of the magnetic field data transients exhibit sign reversals and cannot be interpreted with a conventional 1D EM TD code and a dense multi component SQUID dataset in frequency domain is available, they will not be discussed in detail. In order to get a more quantitative view about the data quality of the post-processed transients, refer to Section 6.4.

## 6.2. Frequency Domain Processing

In order to perform a frequency domain interpretation of the LOTEM dataset, the raw time series was transformed and processed in frequency domain. Insights about robust processing of univariate transfer functions can be found in Egbert and Booker (1986). Other than for time domain processing, where often only the step on or the step off transient of the data is being processed and subsequently inverted individually, in frequency domain the complete period (and additional stacks to increase the S/N ratio) is analysed. Every periodic signal can be rewritten as a superposition of sinusoidal waves, which can be expressed as complex valued exponentials using Euler's formula and can be transformed into frequency domain utilising Fourier-series. The k-th complex valued Fourier-coefficient $C_k$ of the Fourier series can be obtained as follows from the measured time series $d(t_n)$

$$C_k = \frac{1}{N}\sum_{n=1}^{N} d(t_n) e^{2\pi i n k/N} \tag{6.10}$$

where $N$ is defined as $N = \frac{T}{\delta t}$ with $T$ as an integer period of the duty-cycle and $\delta t$ as sampling time. Since a rectangular signal typically utilized for LOTEM/CSEM applications consists of the weighted summation of odd sinusoidal signals, it contains next to the base frequency its odd harmonics as Fourier coefficients. Therefore the exponent $k$ only consists out of odd numbers, e.g. $k = 1, 3, 5, 7$. The amplitude of the odd harmonics is decreasing with higher order. Since due to technical aspects, the signal is not perfectly rectangular and symmetric, next to the odd harmonics, even harmonics and additional noise frequencies between the harmonics can appear in the Fourier-transformed signal. Nevertheless, since the odd harmonics of the transmitted signal exhibit by far the highest signal to noise ratio, only the odd harmonics are evaluated.

At the receiver stations the superposition of the transmitted signal and the earth response is measured. In order to extract the earth response $\mathcal{B}_{x,y,z}$ and $\mathcal{E}_{x,y}$ for the measured magnetic and electric field data in frequency domain, the transfer function between the frequency dependent measured field component $\mathbf{B}_{x,y,z}(\omega)$ and $\mathbf{E}_{x,y}(\omega)$ and the injected current $\mathbf{I}(\omega)$, here in form of a rectangular signal, is calculated,

$$\mathbf{B}_{x,y,z}(\omega) = \mathcal{B}_{x,y,z}(\omega)\mathbf{I}(\omega) \tag{6.11}$$

$$\mathbf{E}_{x,y}(\omega) = \mathcal{E}_{x,y}(\omega)\mathbf{I}(\omega) \tag{6.12}$$

where $\omega$ represents the angular frequency. Therefore, in frequency domain processing, additional to the recorded time series a full record of the transmitted signal must be obtained. Since a continuous time series using a constantly high sampling rate was acquired for the field data as well as the corresponding transmitter current for most of the survey days, a transformation of the data in frequency domain is possible. Note that the transfer function is due to the Fourier transform complex valued and can be either displayed as

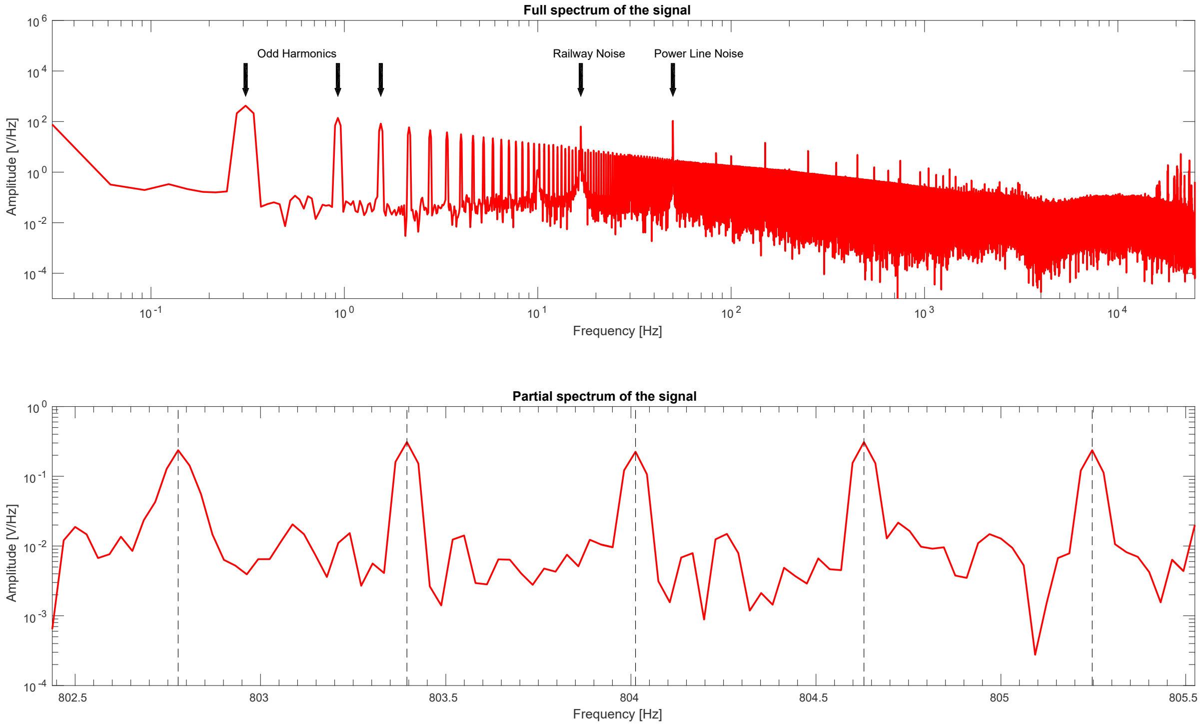

**Figure 6.8.:** Upper Panel: Exemplary power spectrum of an recorded E-Field station. Having a period length of 3.24 s, the base frequency lies at 0.3086 Hz. Odd harmonics are clearly visible in the raw spectrum. Lower Panel: Spectrum for frequencies of 802-805 Hz. High order odd harmonics are clearly visible in the raw data.

real part and imaginary part or amplitude and phase. Since the observed data is normalized by the source current, the resulting transfer function is independent from the source signal but only defined by the subsurface resistivity and the geometrical setup.
For the analysis of the dataset in frequency domain, the robust magnetotelluric processing scheme EMTS based on Egbert and Booker (1986) was adapted to the odd harmonics of the transmitter signal. Figure 6.1 shows next to the processing steps in time domain the steps required for frequency domain processing schematically. In this section, the single steps of the applied frequency domain processing routine will be explained in detail for one electric field recording exemplarily. Input data is likewise to time domain processing the recorded raw dataset. Output is the processed transfer function between the measured field component and the recorded current function.

## 6.2.1. Discrete Fourier Transform

In this thesis, transfer functions were evaluated by calculating Fourier coefficients utilizing the known frequency for the transmitter signal after Equation 6.10. Figure 6.8 shows an exemplary power spectrum of an electric field record. Next to the odd harmonics of the transmitted signal, the railway and power line noise is visible. Before the transformation of the data into frequency domain, an appropriate window function must be applied to the dataset. The window length must be an integer multiple of the transmitting period in order to match the Fourier coefficients exactly and to prevent spectral leakage effects. In order to prevent information loss, a 50 % overlap was used. To ensure, that every single window covers the same period extend of the signal, the window length should equal an integer of $2 \cdot T$. In order to determine a favourable window length beforehand, different integer pre-factors were tested. However, as displayed in Figure 6.9, the relative difference between the transfer functions is small for period length greater than $2 \cdot T$. Differences above 3% occur only for data points around the sign reversal, which are in any case excluded before subsequent inversion. In order to benefit from the robust calculation of the transfer function, the smallest window length of $2 \cdot T$ was utilized for the complete dataset, resulting in a large number of adjacent windows for subsequent stacking.

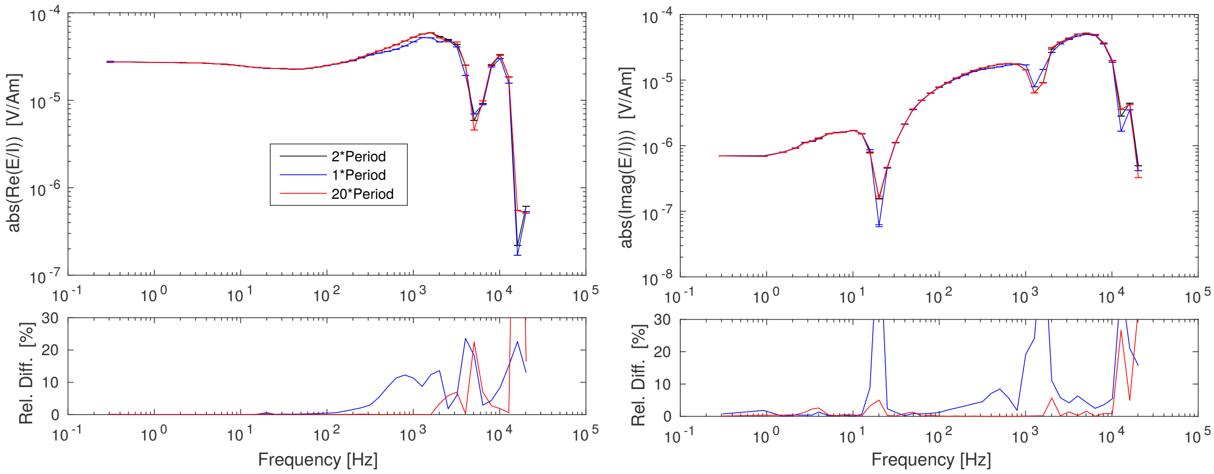

**Figure 6.9.:** Comparison of transfer functions displayed as real and imaginary part calculated utilizing a different window length. Window length must be an integer of the transmitted period. Relative differences are calculated with respect to the preferred window length of 2·Period. Note that for displayed transfer functions, all listed FD processing steps were applied.

Next to the varying window size, different window functions were tested. However, the difference in the resulting transfer functions is negligible (cp. Figure B.1 in Appendix). Since the exact period length of the CSEM signal is known, the window size needs to be adapted to it. Therefore no spectral leakage should be present in the data. The Hanning window has only a moderate impact on the spectral resolution and amplitude resolution and was therefore used in the routine. However, since a periodical signal is evaluated, a rectangular window leads to comparable results.

Most switching times were selected in a way (cp. Section 6.1.1), that the spectral distance to the main coherent noise, i.e. 50 Hz and 16.7 Hz is maximal. Therefore, if one would consider that noise frequencies are stable over time and only exhibit a short band signal in frequency domain, no further filter routines are required. However, anthropogenic noise sources are often not stable over time. Figure 6.10 exemplarily shows a power spectrum ranging from 448-452 Hz of a 10 min long section of the recorded time series. Having 450 Hz as an odd harmonic of the 50 Hz power line noise, the peak in the power spectrum at this frequency can be identified as unwanted noise frequency. Varying along 449 - 451 Hz over the 10 min recording time, frequencies of 450 Hz ±1 Hz were excluded from further processing. The same procedure was applied for all harmonics of known periodic noise

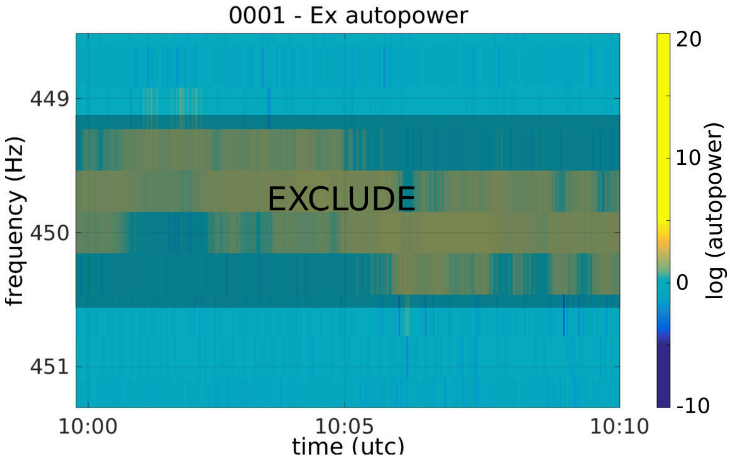

**Figure 6.10:** Autopower spectrum of an exemplary electric field station over a time period of 10 min. Regions of increased amplitude (yellow) are affected by the odd harmonic of the power line noise, which exhibits a higher amplitude than the odd harmonics of the transmitter signal. For this representation data is binned for Fourier calculations in windows of length $T$.

sources. Following settings for discrete Fourier transformation proved to be effective for the given dataset:

- Window function: Hanning
- Window length: $2 \cdot T$
- 50 % overlap
- Exclusion of Frequencies close to harmonic noise frequencies (e.g. 50 Hz)

Since the transfer function varies smoothly over frequency, the evaluation frequencies are averaged around a central frequency $F_c$ in a range of a frequency bandwidth of $F_c \cdot 2^{\pm 0.25}$.

## 6.2.2. Application of Calibration Functions

After the Fourier transformation, the spectra of the recorded field data needs to be multiplied by the frequency dependent transfer functions of the sensors. For E-Fields, having non polarisable Electrodes as sensors, the fields must be only normalized by the dipole length of the receiver. Hence, voltages are converted to $\frac{V}{m}$. As magnetic field sensors, next to the SQUID system, induction coils and large sized loops for the vertical magnetic fields were used. Figure 6.11 shows the frequency dependent transfer function of the TEM-3 coil as amplitude and phase. The instrumental magnetic transfer functions converts the measured voltage into $\frac{\mathrm{nT}}{\mathrm{m}^2}$. However for most of the conventional magnetic field measurements, the loop sensor was utilized, where no calibration function is currently available. Therefore, and under consideration of a dense full component SQUID dataset, we abstained from a further evaluation of the time derivative of the magnetic field components. Note, that the dense magnetic SQUID dataset has likewise to the electric field sensors only a frequency independent calibration factor, which was already applied to the raw time series before Fourier transformation. For the recording of the transmitter current a LEM current clamp with a high cut off frequency was utilized, therefore a frequency dependent gain function is not expected. A measurement of the amplitude (DC) was checked in laboratory beforehand. However, one should keep in mind that the calibration function can correlate with the clamps battery voltage. During this survey, the current clamp was not tested in dependency of time/voltage level, which should be considered in following surveys. However, batteries were replaced every day, to prevent that voltages dropping below a critical level.

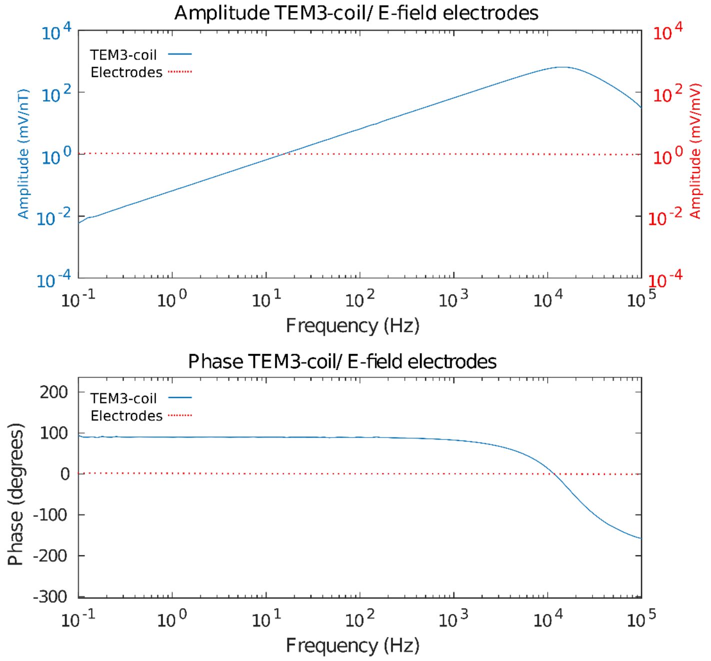

**Figure 6.11:** Frequency dependent calibration functions for TEM-3 coils (induction coil). The non-polarisable electrodes utilized for electric field recording do not have a frequency dependent behaviour. Calibration function for TEM-3 coil was measured at the Niemegk Geomagnetic Observatory, GeoForschungsZentrum Potsdam.

### 6.2.3. Calculation of Robust Transfer Functions

The linear relationship between the measured field and the transmitted current can be expressed as

$$\mathbf{Y}(\omega) = \mathcal{F}(\omega)\mathbf{X}(\omega) \tag{6.13}$$

where $X$ contains the Fourier coefficients of the transmitted current function and $Y$ the Fourier coefficients of recorded magnetic or electric field, multiplied with a system related calibration function. For each evaluation frequency, the centre frequency as well as neighbouring frequencies from $N$ adjacent windows are included in the robust linear regression estimate. In order to calculate the transfer function $\mathcal{F}$ between the electric or the magnetic field component and the current function respectively, the univariate regression problem needs to be solved, which can be expressed as

$$\mathcal{F}^{est}(f_C) = [\mathbf{X}^T\mathbf{X}]^{-1}\mathbf{X}^T\mathbf{Y} \tag{6.14}$$

Within an iteratively re-weighted least squares algorithm, a Hubers weighting function with a tuning constant of 1.345 is applied to the residuals from a previous iteration, which results in a down-weighting of outliers. From the variance-covariance matrix of the estimates of B, the standard error can be calculated, which anti-correlates with the number of utilized Fourier coefficient, i.e. with the number of neighbouring frequencies and the number of adjacent windows. Since neighbouring frequencies have correlated errors, the estimation of standard errors will result in unreasonable small errors. Therefore, for the error estimates, we take likewise to the time domain error calculation only the number of stacks, i.e. the number of $N$ adjacent windows into account.

### 6.2.4. Data Representation in FD

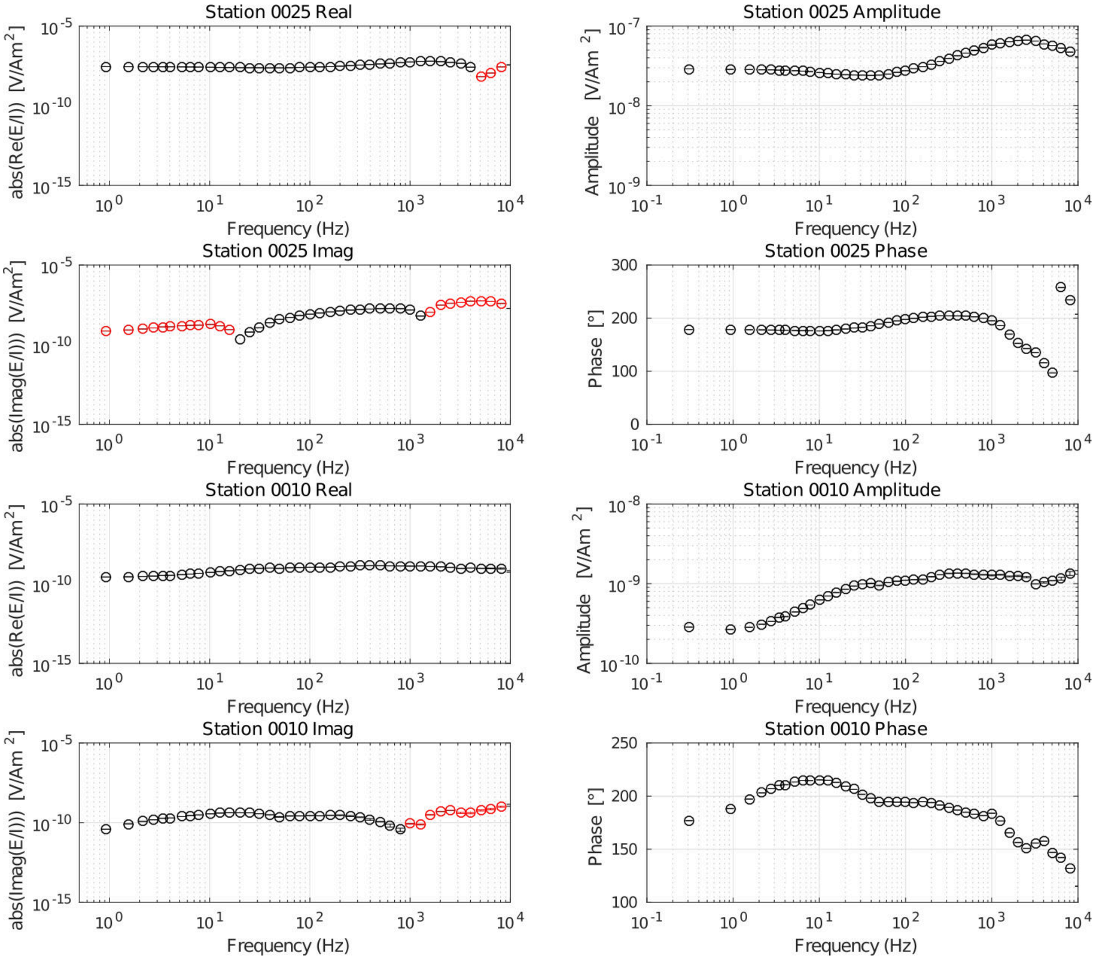

**Figure 6.12.:** $E_x$ Transfer function. Offset Rx25: 630 m. Offset Rx10: 3772 m. Displayed as real and imaginary part and amplitude and phase. In real and imaginary data representation, the black circles represent negative data points, the red circles positive data points. To better evaluate the smoothness of the transfer function between neighbouring frequencies, phases are displayed in the domain between 90° and 270°.

The resulting transfer function $\mathcal{F}$ is complex valued. A transformation of the dataset to phase and amplitude exhibits advanced inversion behaviour during (multidimensional) inversion, as discussed in Section 8.2.9. Therefore, resulting transfer functions are displayed as real and imaginary part as well as phase $\varphi$ and amplitude respectively in Figure 6.12-6.14. The transformation from real and imaginary part to amplitude and phase writes

$$A = \sqrt{\Re^2 + \Im^2} \tag{6.15}$$

$$\varphi = \tan^{-1}\left(\frac{\Im}{\Re}\right) \tag{6.16}$$

The corresponding data errors are calculated by estimating the sum of the contributing error sources and follow a non-Gaussian ($L_1$ norm) error propagation. The data errors displayed in Figure 6.12-6.14 were taken from data processing and for amplitude and phase following the error propagation in the Appendix B, where a full derivation of the error propagation for amplitude and phase can be found. However, since the low error levels obtained from data processing reflect only the statistical behaviour of the dataset, an error floor containing estimations of systematic errors (e.g. inaccuracy of receiver length, angular uncertainty, geological noise and correlated noise affecting the data) must be added to the dataset before inversion. Since static errors affect the real and imaginary part in the same way, the error floor is set to an identical value $\varepsilon$ for both, imaginary and real part. If $\Delta\Re/\Re = \Delta\Im/\Im = \varepsilon$ holds, the equation for the error in amplitudes simplifies to:

$$\frac{\Delta A}{A} = \varepsilon \tag{6.17}$$

and for the phase respectively, a frequency independent absolute error in radian is set to (cp. Appendix B)

$$\Delta\varphi = \varepsilon. \tag{6.18}$$

Figure 6.12 shows the transfer functions for the exemplary electric field component within a short offset (630 m) and additionally for a high offset (3773 m), represented as real and imaginary part and with data transforms to amplitude and phase. Note that the error levels are low over the complete frequency range for real and imaginary part. The imaginary part of the transfer function is typically lower than for the real part. The amplitude is therefore mainly dominated by the real part of the transfer function. The phase gives insight about the ratio between real and imaginary part.

The full component SQUID magnetic field dataset was processed likewise to the electric fields and displayed in Figure 6.13 and Figure 6.14. The shown transfer functions is with an offset of 650 m close to the presented electric field station in Figure 6.12. Both real part and imaginary part exhibit a similar magnitude, resulting in phase jumps of 180° in phase representation at the cross points of real and imaginary part. The high values of the $B_x$ component (parallel to the transmitter) are already indicating 3D effects, misalignment of sensors and/or deviation in x direction from the profile.

Unfortunately, noise measurements from the survey area are not available for SQUID devices. However, obtained statistical errors from processing are low over the complete frequency range except at data points around sign reversals, indicating high quality transfer functions. However, due to the strong dependency of the behaviour, i.e. amplitude and shape of the transfer function to the geometrical setting, one can not obtain much information from a single transfer function. Therefore, for a more quantitative view of obtained transfer functions and errors along the profile refer to Section 6.4.

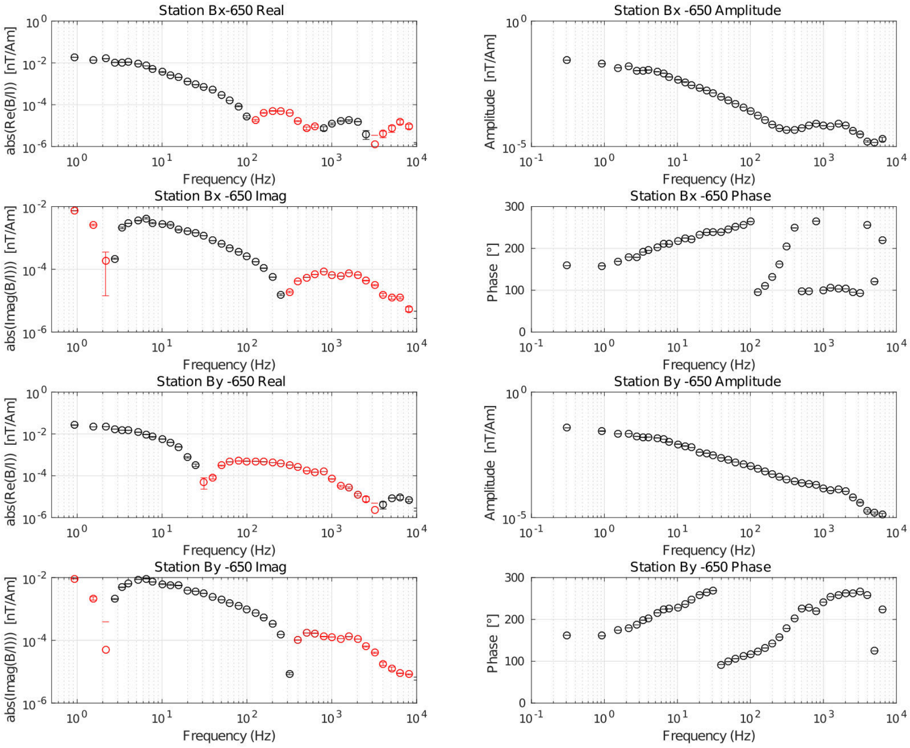

**Figure 6.13.:** Transfer functions for SQUID $B_x$ and $B_y$ component. Offset 650 m. Displayed as real and imaginary part and amplitude and phase. In real and imaginary part data representation, the black circles represent negative data points, the red circles positive data points. To better evaluate the smoothness of the transfer function between neighbouring frequencies, phases are displayed in the domain between 90 and 270°.

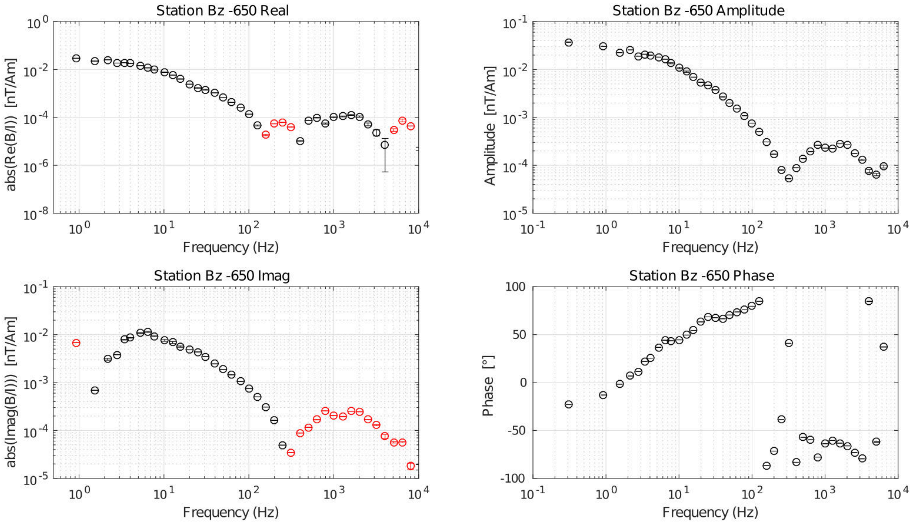

**Figure 6.14.:** Transfer functions for SQUID $B_z$ component. Offset 650 m. Displayed as real and imaginary part and amplitude and phase. In real and imaginary data representation, the black circles represent negative data points, the red circles positive data points. Phases are displayed in the domain between -90 and 90°.

## 6.3. Effects of Synchronisation Errors

There are different sources for synchronisation errors which effect the data. Either a constant data delay between the transmitted current and the received field component is present, as depicted in Figure 6.15 a, or a time dependent delay in the received data (cp. Figure 6.15 b), which can be linear or non-linear. The first can arise, if either different data logger systems for current recording and the receiver units are used (e.g. the KMS 820 unit and the SPAM Mk iV system) which have different, often frequency dependent internal delay times which need to be accounted for. Those differences can be measured in laboratory with a test signal and the shift can be determined up to one data sample exactly. Here a constant shift of 50 $\mu$s between the KMS-820 unit and the SPAM Mk4 data logger for the in field applied sampling rates of 40 kHz and 50 kHz, respectively was determined and included during time series processing.

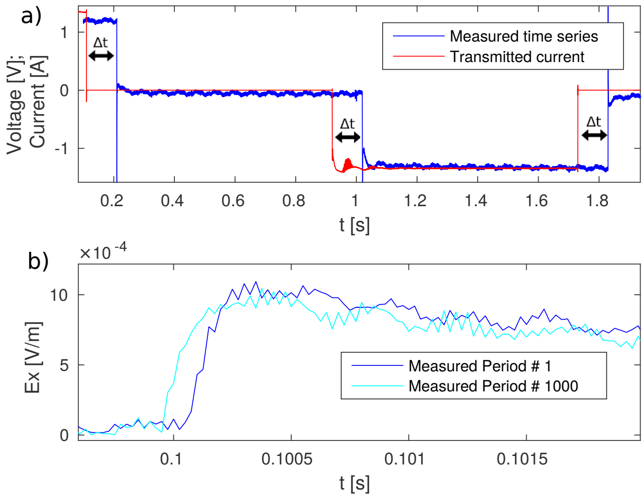

**Figure 6.15:** a) Constant delay $\Delta t$ between transmitter current (red) and field component (blue). For short offsets with a high signal to noise ratio, the offset can be evaluated visually. b) Depiction of a raw time series at the current switch for the first transmitted period, and after 1000 periods. Clearly a shift in time between both time series is visible. Before stacking of the data, this time shift must be corrected.

If the constant delay is produced by an erroneous GPS starting point of the data logger (e.g. if the GPS signal was not logged at the beginning of the measurement or during an automatic restart of the measurement device, which sometimes appeared) often the shift can be identified visually by comparing the starting point of the (processed) transient with the raw signal and/or the system response of the transmitter current. Since in both cases the determination of the starting point of the transient, i.e. the time point of the current switch is only exact to one data point, early time data between $2{\cdot}10^{-5}$ s to $10^{-4}$ s was down-weighted with an error floor of 5 % in order to deal with the time inaccuracy. For frequency domain data, where the full waveform of the transmitter current is recorded and used to normalize the received field data, a small shift between both time series can already result in a large shift in the real and in the imaginary part (cp. Figure 6.16), especially for high frequencies. A shift of 20 $\mu$s corresponds hereby to the inaccuracy of one data sample. Therefore, when different data logger systems for current recording and field component recording were used, frequencies higher than 1 kHz were excluded from data interpretation, since a higher data accuracy than one data sample cannot be assured. During the survey in 2016 problems with the GPS Clocks of some data loggers occurred which added up to create a time dependent delay during data recording. Since the GPS

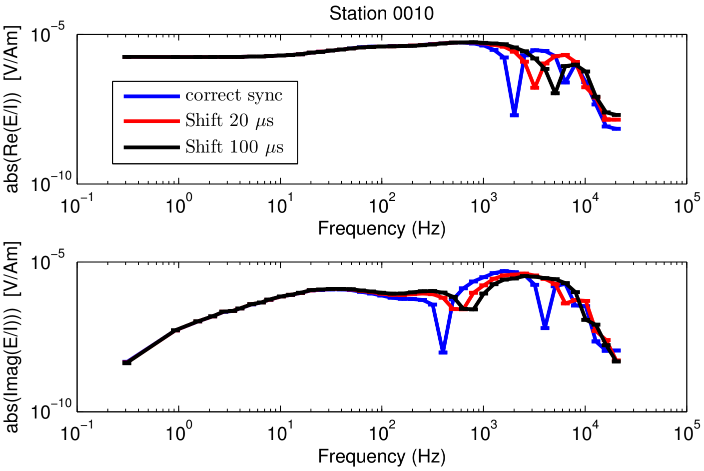

**Figure 6.16:** Effect of time shift between current data and received data in frequency domain. Real and imaginary part are affected for high frequencies to medium frequencies

connection was (partly) lost, the time recording of the data logger was solely dependent on the internal Quartz clock, which can shift over time due to e.g. temperature changes. The affected time series must be treated carefully in both domains. For time domain evaluation, even with a rather small shift of e.g. 1 data point per 100 periods/stacks, the influence to the early times of the transient is not negligible (compare Figure 6.17). Stacking and averaging over a shifted time series will result in a prolonged ramp form and the early parts of the transients cannot be fitted with the measured system response. For most receiver stations, the signal to noise ratio of the processed data was high enough to determine the shift per second. Missing data points were padded with dummy zero points in order to minimize the time shift in the data to below one data sample. Figure 6.17 illustrates the effect of the zero padding. The characteristic form of the transient directly after switching off could be restored. In the survey 2016 when using a 100 % duty cycle, additionally the triggering of the transmitter was affected. Due to programming errors the GPS clocks used for triggering showed an additional linear time shift. For stations with a short offset and therefore a high signal to noise ratio which were affected by both, transmitter clock drift and the drift of the internal master (Quartz) clock, the shift per second could be determined per data block.

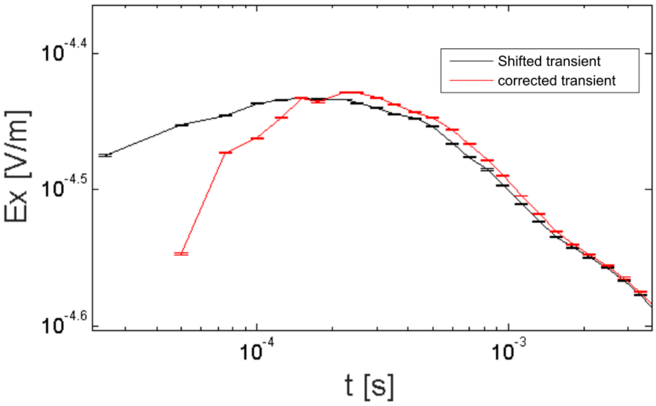

**Figure 6.17:** A time dependent shift in the raw data will result in a prolonged ramp of the processed transient (black). By removing the shift before stacking, the characteristic effect of the non-linear early time system response can be restored.

The few stations with large offsets and non linear time shifts were subsequently recorded again in 2017 or excluded from further evaluation. For frequency domain evaluation the error of a time depending shift between transmitter and receiver current is more crucial, because both time series are needed for further analysis and therefore the influence, similar to the effects of an constant delay is more prominent. Since the errors which would be produced by time shifts, affect even medium frequencies between $10^2$ and $10^3$, data of stations with a non constant data shift were excluded from further evaluation for now.

## 6.4. The Dataset

After application of the listed processing steps, transients or transfer functions, respectively, could be achieved in time and frequency domain. High quality data was obtained for 6 different transmitters, 157 E-field receiver stations, and 101 full component SQUID stations. Figure 6.18 shows the distribution of stations for each corresponding transmitter. Not all stations which were processed in time domain are included for frequency domain inversion and vice versa. Electric field data was processed in both, time and frequency domain. Induction coil $B_z$ data was only processed in time domain, since yet, no calibration function for the loop sensor exists. Since magnetic induction coil data exhibited a strong influence of multidimensional EM effects and a 2D inversion of the dataset is performed in frequency domain, magnetic SQUID data was processed in frequency domain only. For stations for which during data acquisition in 2016 both, data-loggers and the transmitter shifted in time due to insufficient GPS synchronization, only processing in time domain was applied. Since the effect of insufficiently shift-corrected data is not as obvious in the transfer functions as in the time domain transients, shifted frequency domain data must be analysed carefully. In order to reduce processing time, those stations were neglected for frequency domain processing. In addition, data was excluded from subsequent 2D inversion, if it exhibits behaviour indicating strong IP effects or three dimensional effects which hinder the inversion from convergence. An overview over all stations including Tx and Rx geometry, its evaluation domain and comments about the data quality can be found in the Appendix A.

In the following data is shown exemplarily for the Transmitter Tx 8 and Tx 10 (Figures 6.19-6.22). For the sake of completeness, the voltage depiction for all transmitter-receiver distributions is shown in the Appendix B. Since the time domain data was later on inverted as switch on transients ($E_{on}$), i.e. the post-processed switch off transients ($E_{off}$) were levelled to the DC field ($E_{DC}$) approached at late times by the previous switch on transient, the data is displayed as switch on data and switch off data, respectively. Note, that this is only a simple conversion of the dataset after Equation 2.39 and only relevant, if some relative error level (e.g. to account for geological noise, static errors, e.g. by geometrical errors, etc.) is applied to the dataset.

Figure 6.19 displays the processed dataset as recorded voltage, normalized to the transmitter current and the receiver length for the electric fields along the profile for Tx 8 in time domain. Red colours refer to a high voltage level, blue colours to a low voltage level. The acquired standard errors from the processing depicted in the lower panel of Figure 6.19 are small considering the switch on depiction. Only the two stations with the largest offset in the NW of the profile and one station at profile meter 4600 shows errors larger 2%. The derived standard errors for switch off data are higher, which is reasonable

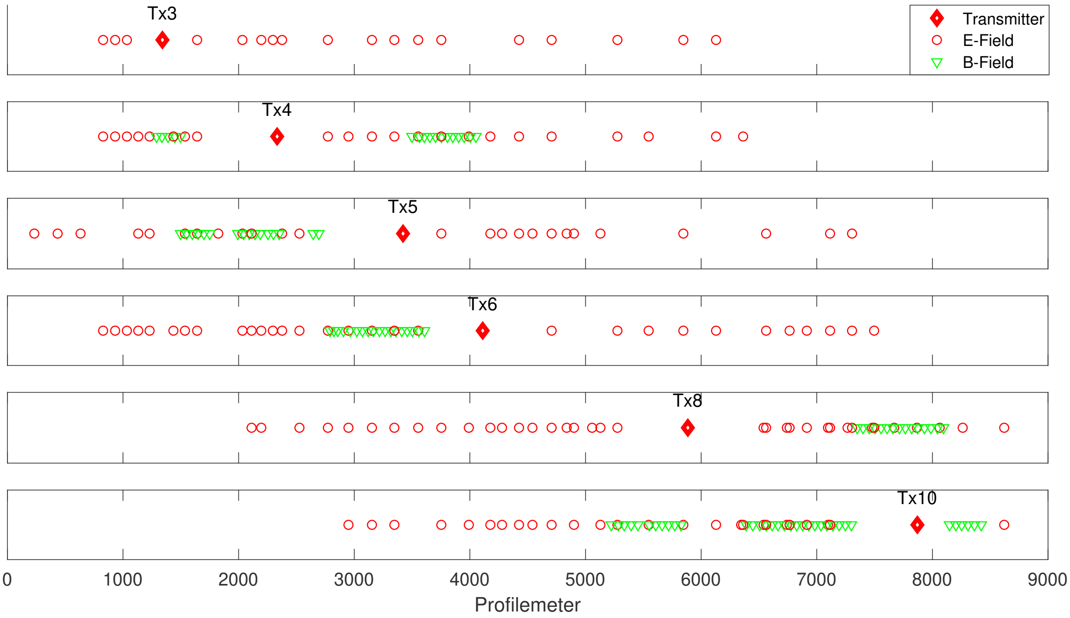

**Figure 6.18.:** Overview over high quality data transfer functions derived for each of the 6 transmitters. Green markers represent stations, at which SQUID data was recorded, red data displays electric field data. Note, that only electric field data was processed in time domain.

considering the inductive response tends to zero for late times and exhibits voltages up to 2-4 decades smaller than the DC level. By comparing the derived standard errors with the voltage levels, one can observe the strong correlation between measured voltages and statistical error level.

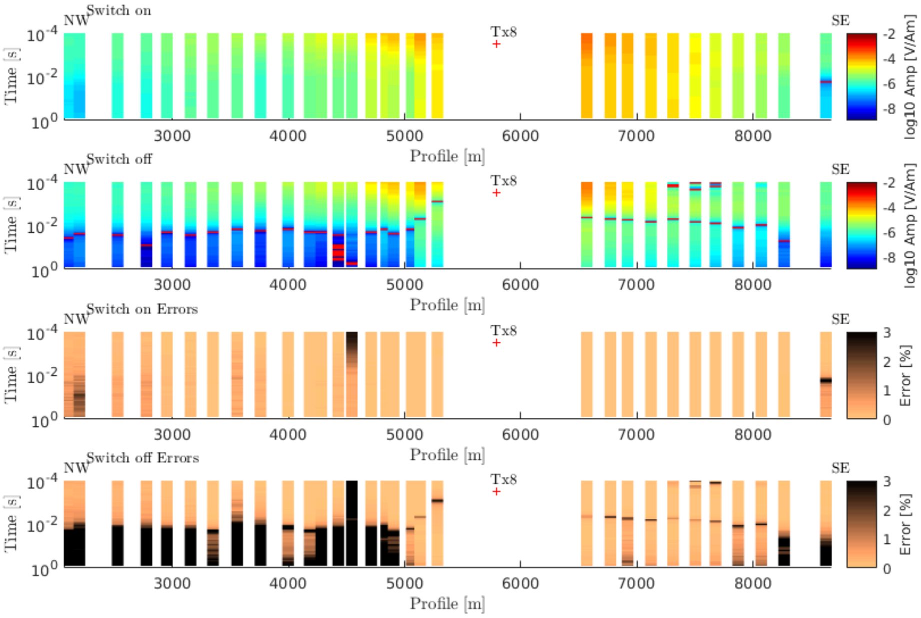

**Figure 6.19.:** Voltages measured along Tx 8 for switch on and switch off $E_x$ data plotted over time. The normalized voltages are plotted under the corresponding receiver station. The dataset is normalized to the current and receiver length. Red markers indicate the location of sign reversals. Below, the errors achieved from the robust processing routine are displayed for each data point.

Since in the switch on depiction of the data, the DC level is overprinting the inductive parts of the signal, the voltages are higher than in the switch off depiction. For the same reason, the dynamic range of the switch off transients is higher, reflecting the inductive signal decreasing over time (cp. Section 2.3.4). For late times, switch on data is tending to the static DC level, where switch off data reflects the decrease of the inductive signal to low voltages. As expected, close to the source, located at profile meter 5880, and for early times, the measured voltages are the highest and decreasing with increasing offset to the source. Note, that the decrease of the measured voltages is asymmetric for switch on data, with higher values in the southeast and lower values in the northwest of the transmitter. This is already an indication for a 2D distribution of electrical conductivity in the subsurface, suggesting higher resistivities in the southeastern part of the profile.

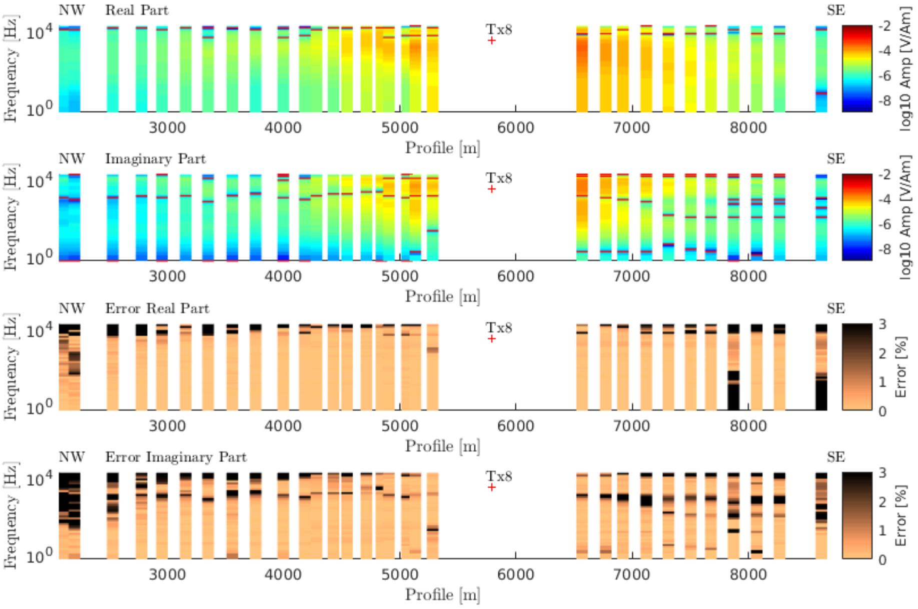

**Figure 6.20.:** Voltages measured along Tx 8 for real and imaginary part of $E_x$ plotted over frequency. The dataset is normalized to the current and receiver length. The normalized voltages are plotted under the corresponding receiver station. Red markers indicate the location of sign reversals. Below the errors achieved from the robust processing routine are displayed for each data point.

A similar behaviour can be observed in the post-processed transfer functions displayed as real and imaginary part respectively along the profile (cp. Figure 6.20). The real part, reflecting a combination of the primary field and the inductive signal similar to the switch on content of the data, exhibits a lower dynamic range than the imaginary part and is overprinted by the primary field. The imaginary part of the transfer function, containing only the inductive part of the signal, exhibits a higher dynamic range and decreases to zero for low frequencies (cp. Section 2.3.2). Sign reversals are present in the switch off representation of the dataset as well as in the frequency domain data. Under consideration of a reasonable fixed error floor, taking e.g. geometrical errors into account, an inversion of the switch off time domain dataset would be beneficial, since the inductive signal is not overprinted by the DC of the signal, which can be for late times up to 2-4 decades higher. Therefore, including the DC level in the inversion, the resolution of the inductive part of the signal decreases significantly, and especially late time inductive information is lost. When jointly interpreting data from both, real and imaginary part, the inductive information is decoupled from the galvanic term in the imaginary part.

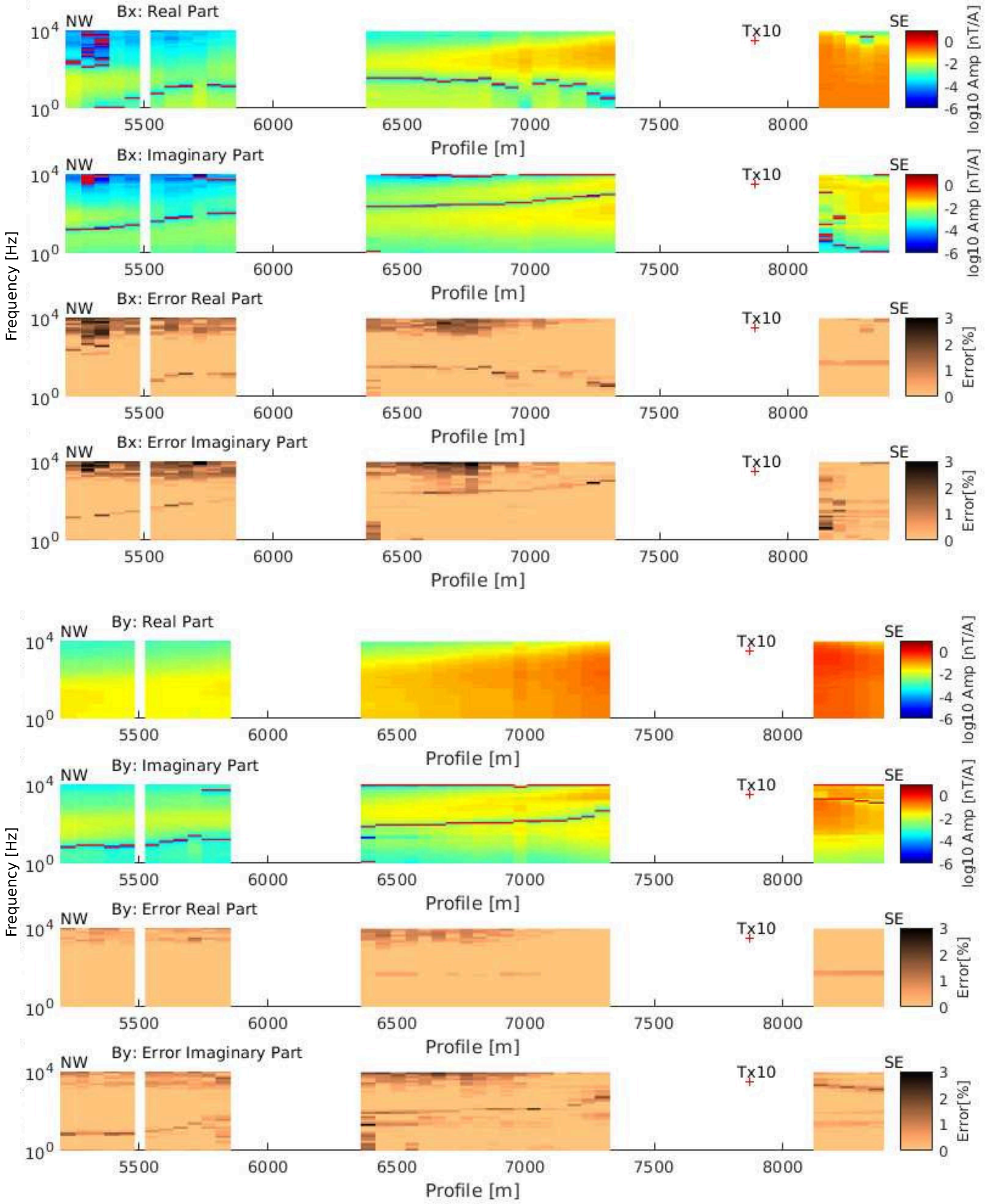

**Figure 6.21.:** The measured horizontal magnetic field components utilizing SQUID sensors for Tx 10 showing real and imaginary part plotted over frequency. The dataset is normalized to the current and receiver length. The normalized voltages are plotted under the corresponding receiver station. Red markers indicate the location of sign reversals. Below the errors achieved from the robust processing routine are displayed for each data point.

In Figure 6.21, the observed voltage levels for horizontal SQUID Data and the derived standard errors for Tx 10 are displayed. This transmitter was chosen for the demonstration of the distribution of the normalized magnetic field along the profile, since most stations utilized this transmitter. Having a denser station distribution, the observed SQUID voltages are very consistent along the profile. Similar to the recorded electric field data, the distribution of voltages over the profile is mainly driven by the receiver-transmitter offset. Sign reversals are present in both, real and imaginary data. We observe as expected higher voltages in the strong magnetic field component $B_y$, which is perpendicular to the electric dipole transmitter. Considering that the receiver array is on a transect perpendicular to the transmitter and approximately cutting the middle of the transmitter dipole, the $B_x$ component should be close to zero for a 1D or 2D conductivity distribution. However measured amplitudes are consistent along the profile and exhibit high values. Therefore, either strong 3D effects are present in the dataset or constant deviations from the $B_x$ field sensor from the actual x direction. This point will be discussed further in Section 9.1.2. Relative errors for the horizontal components are small for both components and also for high offsets, reaching errors in the range of 3 % only for frequencies above 1000 Hz and for data points around the sign reversal. Errors for the $B_y$ components are lower than for $B_x$, which is reasonable considering the higher measured voltages of the former. Even data was recorded only approximately 8-15 min per station, obtained transfer functions are exhibiting a high data quality with low statistical errors and a consistent voltage distribution along the profile.

In Figure 6.22 the vertical magnetic field recorded with the SQUID sensor is depicted for the same transmitter receiver setup. It shows as well a consistent behaviour along the profile. Only the stations located at approximate profile meter 7000 and 6500 deviating from the voltage decrease observed along the profile. Standard errors for high frequency data are higher for the vertical component as for the horizontal components, which correlates with the low voltages measured for high frequency data.

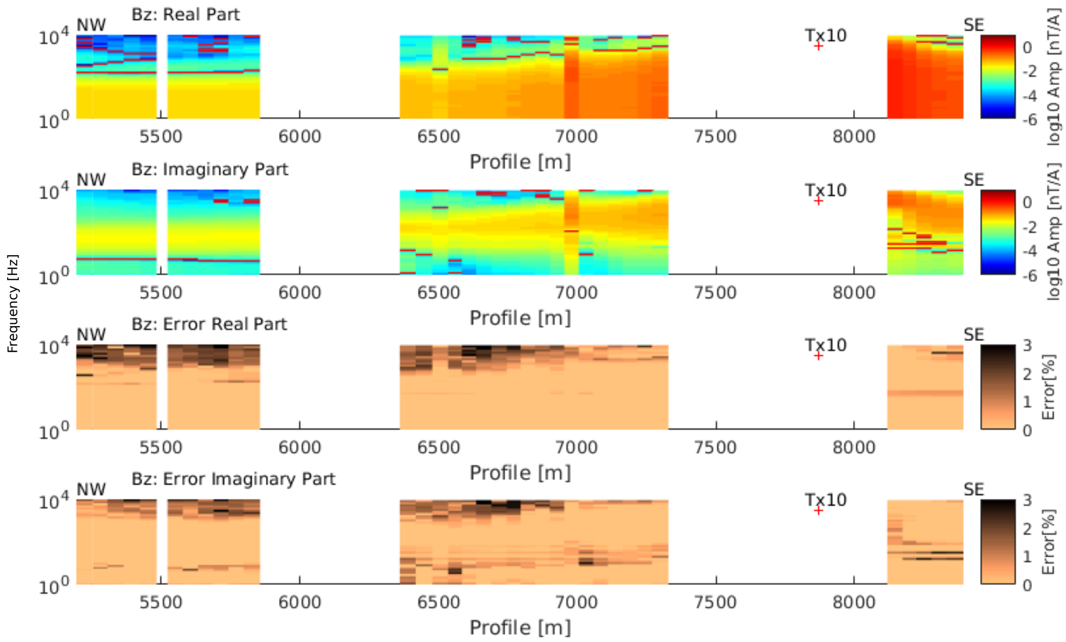

**Figure 6.22.:** The measured vertical magnetic field utilizing SQUID sensors for Tx 10 showing real and imaginary part plotted over frequency. The dataset is normalized to the current and receiver length. The normalized voltages are plotted under the corresponding receiver station. Red markers indicate the location of sign reversals. Below the errors achieved from the robust processing routine are displayed for each data point.

## 6.5. Summary

Obtained electric field data was processed in time and frequency domain. For magnetic measurements, data obtained by Loop Sensors and the TEM-3 coil system exhibit sign reversals for most stations. Since these sign reversals can not occur in a 1D resistivity distribution, and considering that multidimensional inversion is subsequently performed in frequency domain, SQUID data was evaluated in frequency domain only.

For time domain processing, a standard LOTEM processing scheme was applied, including filtering, stacking and smoothing routines. In order to improve the quality of the transients, switching times of the transmitter were adapted to favour an optimal noise suppression of the most common anthropogenic noise sources. Next to the processing of the dataset, system responses for each transmitter site were calculated and the step off transients were levelled to the DC amplitude for subsequent inversion. Step on transients are all well located above the local noise level and exhibit low errors throughout the complete time range. Late time step off transients exhibit typically higher relative errors due to the lower amplitude.

For frequency domain processing in the framework of this thesis, the magnetotelluric processing scheme EMTS (WWU Münster) was adapted for LOTEM-CSEM processing. The most important steps are hereby a correct definition of the evaluation frequencies and therefore the window length for subsequent inversion. Likewise to time domain processing, for the calculation of the standard error, the standard deviation is normalized to the number of stacks, i.e. adjacent windows. Stacks over neighbouring frequencies were excluded from the normalization, since the superposing noise between adjacent frequencies can be correlated and calculated errors tend to be unreasonable small.

Contrary to previous applications of the LOTEM method at the UoC, for synchronisation, GPS information of the transmitter and data-loggers was utilised. However, during the first survey, the GPS clock triggering the transmitter shifted in time due to a software malfunction. Where shifts in time domain can be easily corrected in a sufficient way during processing, leading only to deviations in the very early times, phases in frequency domain are more sensible and are affected over a larger frequency range. If the shift is non linear over time, the reconstruction of the time series is in need of more sophisticated methods. For now, if shifted data was non linear over time, the dataset was excluded from frequency domain data processing, which led to the loss of data at some receiver stations acquired during the first survey. The error of the GPS clocks was fixed in the second survey and allowed a rapid data processing.

For a more quantitative view, measured voltages are evaluated along the profile. The obtained transfer functions and transients show a consistent behaviour along the profile, exhibiting decreasing amplitudes over time and with distance to the transmitter site. Observed errors are in general low for frequency domain real part and step on data representation. For step off data and imaginary part, being both not superimposed by the galvanic field and therefore exhibiting typically lower amplitudes, error levels are higher, especially for step off TD data. When analysing the real part or switch on representation, an asymmetric voltage distribution can be observed, indicating higher resistivities in regions with relative high voltages.

# CHAPTER 7

# 1D Inversion of the Dataset

As first evaluation step, a 1D inversion, which considers only resistivity variation in z-direction, is conducted. It has the advantage of a small computational load compared with multidimensional modelling. However, especially for long offset TEM applications with typically large footprints, i.e. covering a large area of investigation, the resistivity of the subsurface can seldom be approximated as 1D. Moreover, the complex geological settings and lateral resistivity distributions derived from geophysical pre-investigations (e.g. TEM, HEM), suggest a 2D or 3D subsurface. Even if the data can be fitted, outcoming inversion models can be strongly influenced by 2D effects. However, 1D inversions is a suitable tool to get a first image about the resistivity distribution in the subsurface. Additionally, the influence of 2D, the effects of IP to the EM response and approximate depth of investigation can be estimated without a large computational effort.

In order to benefit from a range of open source multidimensional frequency domain CSEM codes, for subsequent multidimensional inversion, a frequency domain code is utilized. Therefore aim of this chapter is not the derivation of subsurface models which can be interpreted in a geological sense, but it should give a first idea over the resistivity distribution and multidimensionality of the subsurface as well as the effects of IP towards the measured data. Moreover, if frequency domain inversion results deliver models similar to the inversion of data in time domain, the transformed LOTEM dataset can be further evaluated by multidimensional frequency domain inversion algorithms.

## 7.1. 1D Inversion in Time Domain

For the inversion of the dataset in time domain, conventional Occam R1 and R2 routines as well as Marquardt inversion routines were applied to the dataset. For Occam inversions, routinely a homogeneous halfspace of 300 Ωm was used as starting model. The number of layers was fixed to 32, with a logarithmically increasing thickness from 5-10 m up to 5000 m. The earth was assumed to be isotropic and free from IP effects. Since the Marquardt inversion routine depends stronger on the starting model, typically in a first step, Occam inversion routines were applied. For Marquardt inversion, a starting model with only a few layers, here typically 5, was derived based on the resistivity distribution given in the inversion result of the Occam algorithm. In order to test the resolution for different layers and resistivities, equivalence models were calculated. A freed calibration factor can increase the data fit and account for 2D effects and setup errors. However, on the other side, it increases the ambiguity greatly. Therefore, it was set to 1 and fixed during inversion. Since the earth response for early times of the measured transients are superimposed by effects due to the system response, calculated forward models are convolved with the measured and processed system response during inversion.

### 7.1.1. Inversion of Switch Off Transients

Since the transmitted signal after switch on showed strong distortion over a large time range (cp. Section 5.1) due to technical reasons, only the switch off dataset could be evaluated. However, as shown in Figure 7.1 exemplarily for one electric field station, electric field switch off data could not be fitted by a 1D inversion approach. Most of the switch off data exhibited sign reversals. Note, that prior to inversion, data points around the sign reversal were removed and transformed via an arsinh-transformation in order to facilitate a reproduction of the sign reversal. Additionally several modelling studies including tests of different starting models for all inversion schemes (Occam R1, R2, Marquardt) were applied, however a sufficient data fit could not be obtained. Figure 7.1 shows next to the inversion result of the complete switch off transient the inversion of the transient utilizing only data points until $10^{-2}$ s. The outcoming inversion model is comparable to the inversion result of the switch on data dataset, which was recalculated to switch on by levelling to the DC value (cp. Section 2.3.4). This demonstrates that an sufficient data fit obtained for the full time length of the switch on transient does not result automatically in more information, e.g. for deep structures. On the opposite, it reflects more the downweighting of the inductive response due to the additional DC level, which is up to 2 decades higher at late times compared with the inductive response. Even when assuming a reasonable 1 % relative error floor for subsequent inversion, inductive response at late times is strongly downweighted. Therefore, if switch off data is available and can be fitted by the inversion routines, one should refrain from a recalculation to switch on for inversion. This hold especially, if relative error floors are considered. Then, in order to get a high information content for high and low conductive structures, one should rather aim for a joint interpretation of switch on and switch off data. For the given dataset however, switch off data could not be fitted by the EM 1D inversion algorithms. Therefore, in order to obtain stable inversion results and to include the additional information about the DC level compared with the inversion of early time switch off data, subsequent inversions were performed with recalculated switch on data.

### 7.1.2. Occam Inversion and Datafit for Tx 8

As a first interpretation of the data, an Occam smoothness constrained inversion was applied to the time domain E-field dataset. As rough guess of the depth of investigation (DOI), Occam inversions using the first (R1) and second order (R2) derivative of the smoothness constraints can be compared. For regions where both obtained models deliver similar structures, the corresponding model parameters are well resolved. If the

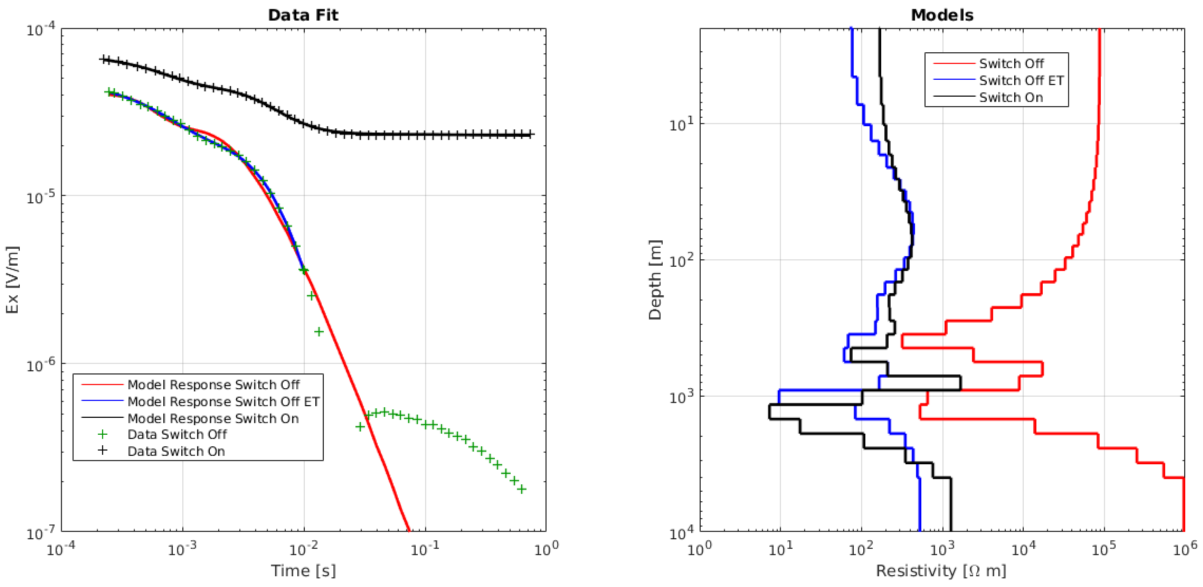

**Figure 7.1.:** Data, modelled data and Occam R1 models obtained by inversion of switch off electric field data (exemplarily for Tx 8, Rx 18), taking only early times (ET) into account vs the full transient length and the transient levelled to DC (= Switch On). In order to stabilize the inversion, data points around the sign reversal are removed. Plotted is the absolute value of voltage normalized to the receiver length. Data fit Switch On: $\chi = 1.0$; Switch Off: $\chi = 8.64$; Switch Off ET: $\chi = 1.08$

inversion results from Occam R1 and Occam R2 are diverging, the inversion is driven by the regularization parameters and the resolution of the model parameter is poor (e.g. Yogeshwar et al. (2013), Cai et al. (2018)).

The resulting Occam inversion models utilizing Occam R1 and R2 roughness constrains, exemplarily shown for Tx8, is plotted in Figure 7.2 in colour code. Note that the corresponding measured dataset at each station does not only exhibit subsurface information beneath the station, but for the area between transmitter and receiver. However, since sensitivity below the receiver (and transmitter) position is increased, stations are plotted under the corresponding receiver station. Additionally the relative difference for each station between modelled data and calculated data over time as well as the error weighted RMS ($\chi$-value) is shown. The approximated divergence point between Occam R1 and R2 is indicated for both inversion results. Exploration depth is depending on the offset and conductivity distribution, however most stations exhibit estimated depth of investigation over 1500 m. For structures located above the maximum DOI, inversion with both regularisation parameters deliver similar results. The relative difference between observed and modelled data is higher for the first few data points in the range of $10^{-4}$ s. In order to account for inaccuracies produced by the system response, which result in an increased misfit for early times, an error floor decreasing from 5 % to 1% for data points between 20 $\mu$s and 120 $\mu$s was set. Higher error levels are weakly correlated to late times. Since the error obtained from processing exhibited errors smaller 1% for all stations, for the stabilization of the inversion algorithm a minimum error of 1 % was set to all data points. For most stations the data is reasonable fitted showing an error weighted RMS value below 3.

Figure 7.3 exemplarily shows the inversion models and corresponding data fits for Occam R1, Occam R2, Marquardt and equivalence models. For Marquardt inversion, the 5-layer

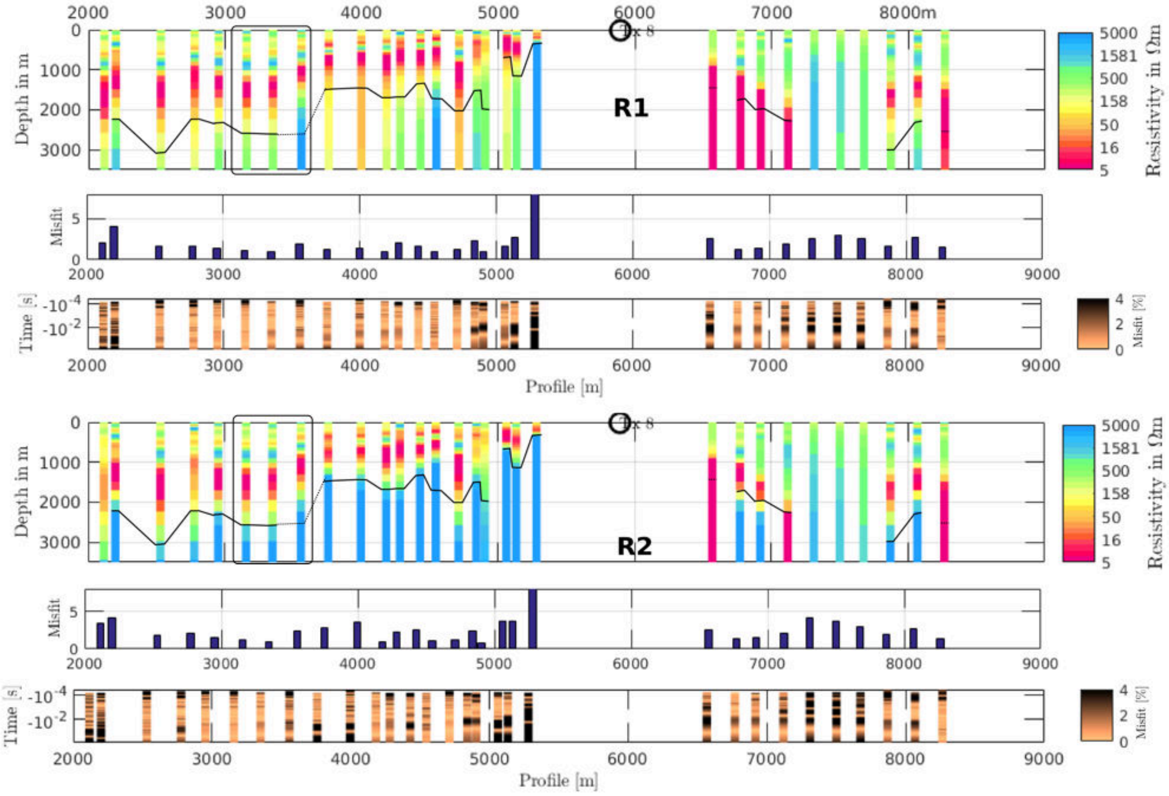

**Figure 7.2.:** Inversion Result of field data utilizing Tx 8 for different regularization parameters Occam R1 and R2. Estimated depth of investigation for divergence points between Occam R1 and R2 is indicated with a black line. Under each inversion model, the total misfit and the misfit over time is plotted per station in percent.

starting model was derived from the Occam inversion results. Modelled data from all three inversion routines can fit the data reasonably well. For station 17 and 18, the first data point at early times was removed from the dataset. Utilizing a larger error floor, the first 5 data points were downweighted for all three displayed stations. If the Marquardt models exhibit equivalence models which are strongly varying in terms of depth or resistivity, the corresponding layer is only poorly resolved. In all three shown cases, the upper three layers are well resolved, exhibiting only a few equivalence models with only weakly varying model parameters that can fit the data within a misfit range of 5%. Resistivity and thickness of the fourth layer of station 19 is reasonably well resolved, whereas the lower edge of the fourth layer is only poorly resolved for station 17 and 18. The fifth layer correspondingly is varying widely with respect to its upper edge and resistivity and is not resolved. However, for all three cases, both Occam inversion models do not diverge and indicated a more resistive layer in depth. Note that the prominent voltage jump at around $10^{-4}$s is present in all datasets and can be reasonably fitted within its errors, if the derived system response is convolved with the forward model.

### 7.1.3. 1D Inversion Results of E-Field Data

Figure 7.4 shows the Occam R1 inversion results of the electric field dataset for all transmitter receiver configurations. The length of the plotted model columns reflects the depth of investigation estimated by the above mentioned criteria. For most stations the estimated depth of investigation is larger than 1.5 km. The error-weighted RMS ($\chi$-value)

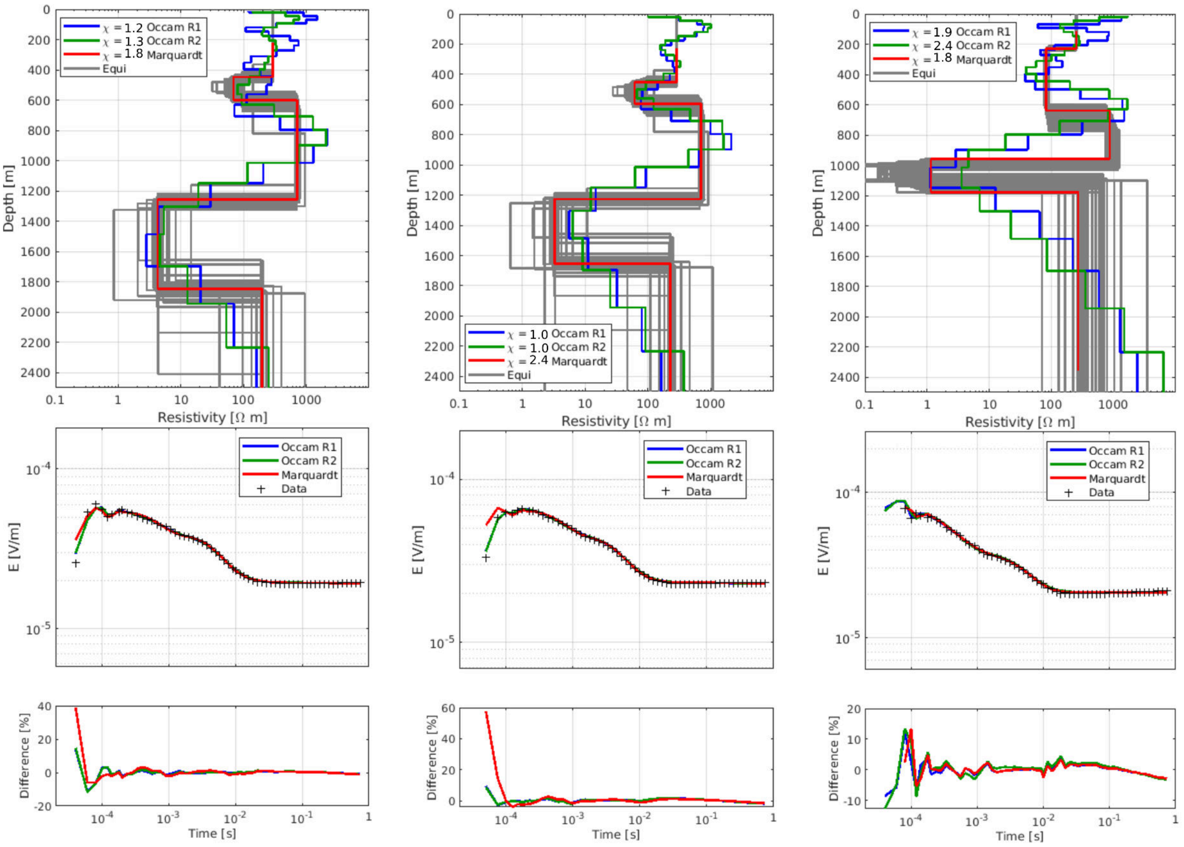

**Figure 7.3.:** Occam and Marquardt inversion results as well as equivalence models to the Marquardt inversion results for three neighbouring stations marked in Figure 7.2 with a grey box. The upper panel shows the inversion models. In the centre, data and modelled data is shown while in the lower panel the relative difference to the measured data over time is depicted.

between model and data ranges for most stations between an optimum value of 1 up to 2, meaning that the data is well explained by the model.

The stitched view of the 1D inversion results already exhibit a strongly 2D subsurface in terms of resistivity. The behaviour of the inversion results in terms of resistivity and layering, even when fitting the measured dataset reasonably well, is not consistent along the profile or for different transmitter-receiver geometries. In Figure 7.5, the 1D inversion models of receiver station 18 utilising two different transmitters (Tx3, Tx6) are compared. The inversion models, even if well fitted, deviate from each other, indicating a lateral conductivity variation of the subsurface along the profile. Given the multidimensional character of the subsurface, each of the six different Tx-Rx setups deliver complementary information for a subsequently multidimensional inversion.

### 7.1.4. Influence of 2D Conductivity Structures

Figure 7.6 demonstrates the bias using synthetic data obtained by a 2D conductive body in a resistive halfspace using a 1D inversion approach. Based on results of DC and semi-airborne data acquired in the survey area (Cherevatova et al., 2018), a simplified model of a good conducting (10 Ωm) block anomaly, resembling the black shales, in a more resistive halfspace (300 Ωm) was constructed (Figure 7.6 a) and synthetic E-field data and $\mathrm{d}B_z/\mathrm{d}t$ data were calculated. The receiver and transmitter geometry was taken from

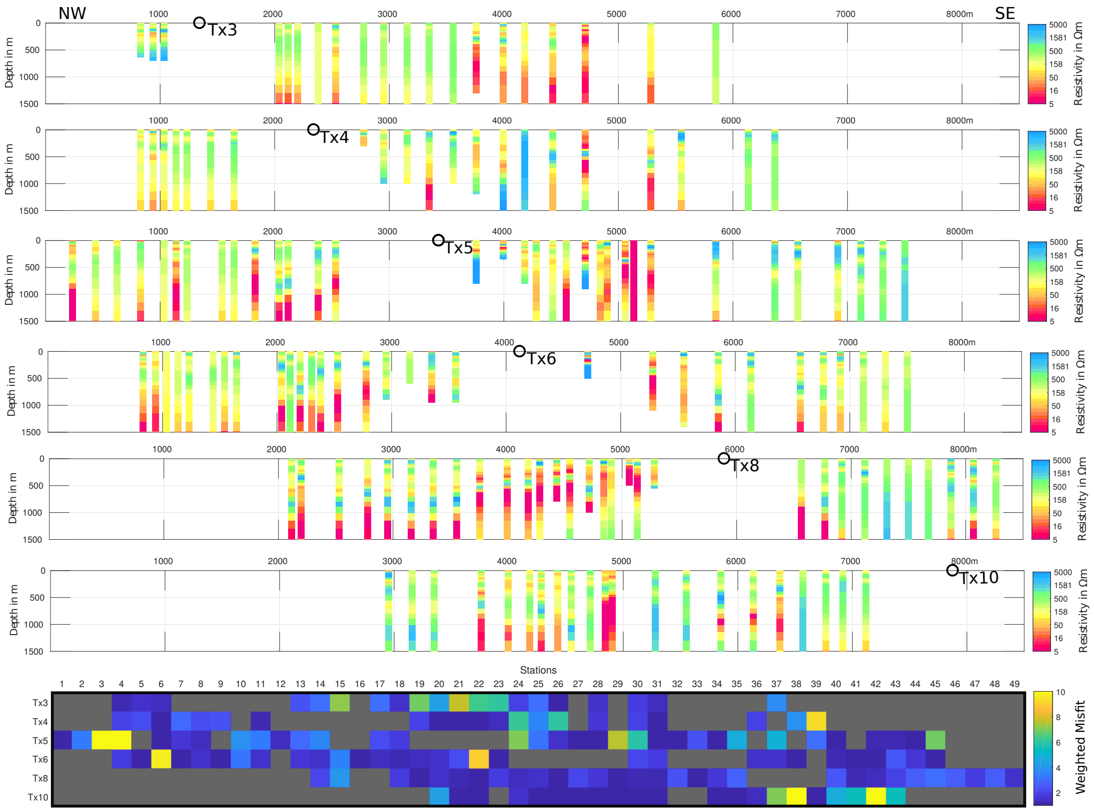

**Figure 7.4.:** 1D Occam inversion results using the regularisation parameter R1 for each transmitter location (black circle) are plotted under the corresponding receiver position. For short offsets (<1 km), the estimated DOI is rather shallow, whereas for longer offsets a DOI of >2 km is reached. Under the models, the misfit between modelled and observed data is displayed for each station.

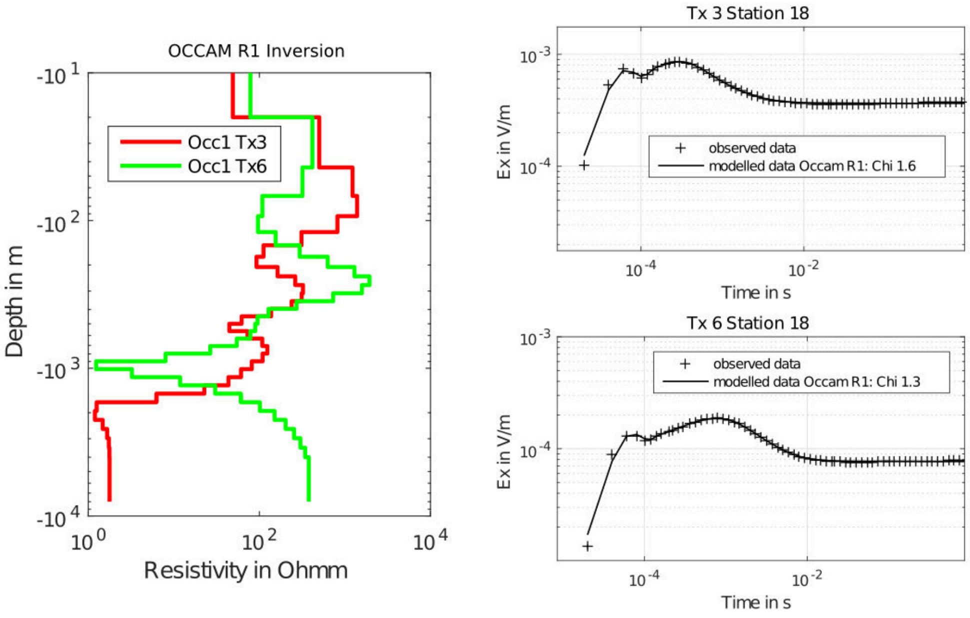

**Figure 7.5.:** Left Panel: Occam R1 inversion result for Station 18 using Transmitter 3 and 6. Right Panel: The data is well fitted by the modelled data for both stations along the complete time range.

the field setup as shown in e.g. Figure 7.2 for Tx 8. The block model and subsequent smooth Occam inversion of the electric field data is plotted in Figure 7.6b. Even in a distance of 3 km from the block anomaly, the influence of the conductive 2D structure is visible. In Figure 7.6c the transients for the electric field and the time derivative of the vertical magnetic field are displayed and compared with transients modelled for a homogeneous halfspace at profile meter -2100, located at one of the borders of the conductive anomaly. Similar to the field data, the time derivative of the vertical magnetic component exhibits sign reversals and can therefore not be interpreted using a 1D inversion approach.

A first interpretation in 1D will therefore only give a rough estimation about the resistivity distribution. In order to constrain the lateral extension of the complex geoelectrical structure and to utilize the complementary data interpreting different receiver-transmitter setups jointly a 1D inversion approach is not suitable. Therefore, in order to adequately interpret the data, a multidimensional inversion of the dataset must be carried out.

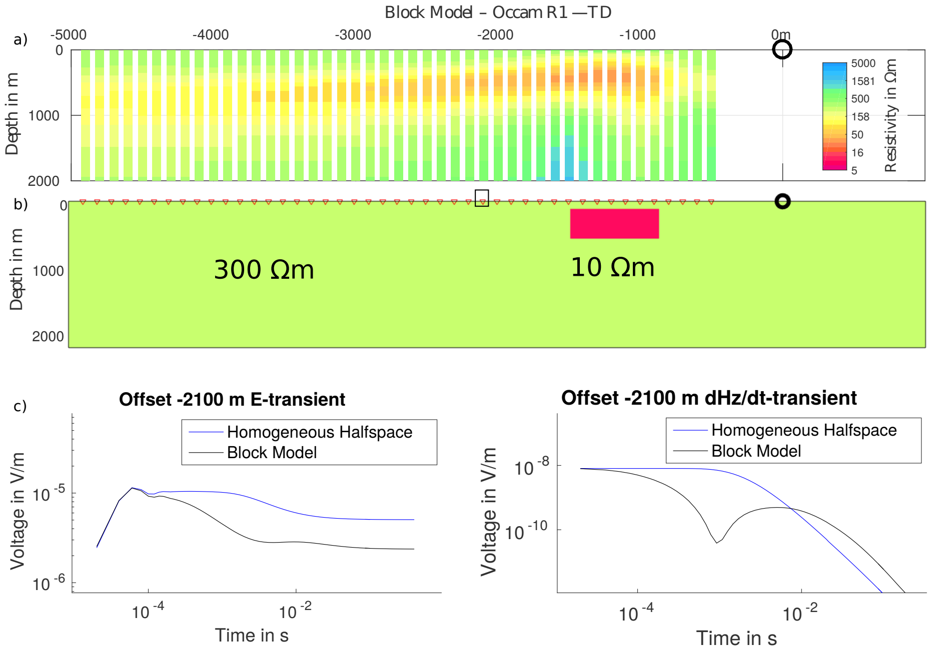

**Figure 7.6.:** Synthetic study inverting synthetic E-field data (a) obtained over a a 2D block anomaly (b) using a conventional 1D Occam R1 approach. The synthetic data was calculated using a 2D finite difference TD code (Druskin, 1988). c) Resulting transients for the E-field and the vertical dH/dt-field for the station at profile meter -2100 (marked with grey box).

## 7.1.5. Magnetic Field Data

The time derivative of the magnetic field exhibits sign reversals for most stations, which can only be produced by a multidimensional conductivity model (Hördt et al., 2000). Therefore, most of the stations were not evaluated with 1D inversion algorithms. However, for some stations, no, or only late time sign reversals occurred and data could be modelled utilizing a 1D approach.

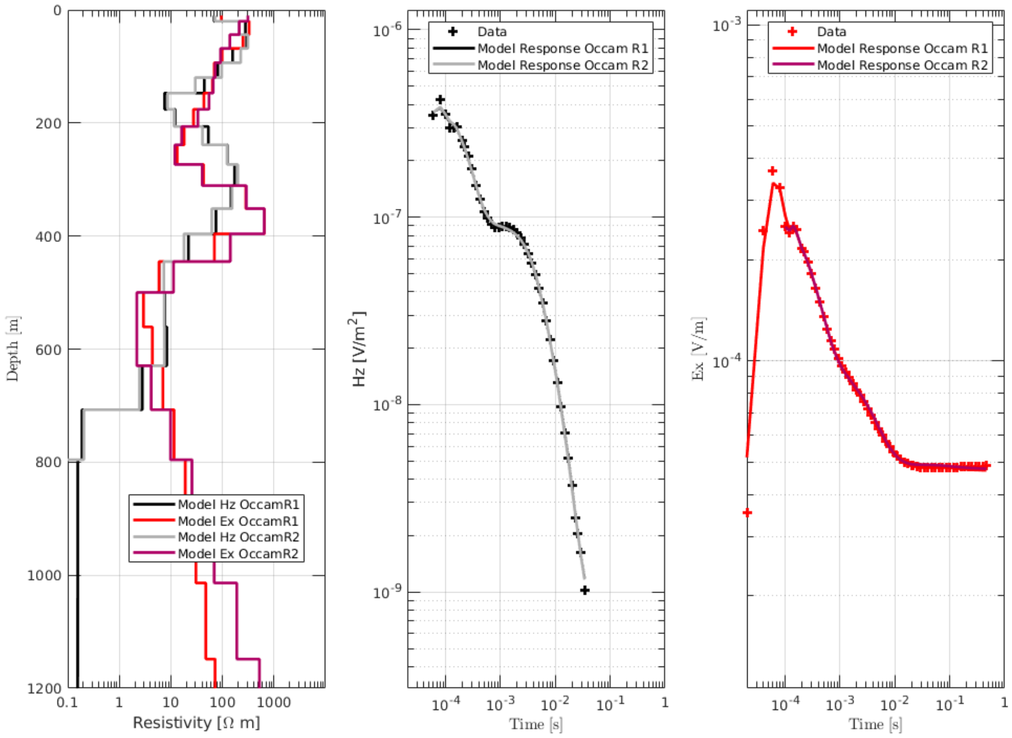

**Figure 7.7.:** Occam R1 and R2 inversion results and data fits for the $E_x$ and the time derivative of $B_z$. Data fit for $B_z$: Occam R1: 1.7, Occam R2: 1.8 Data fit for $E_x$: Occam R1: 1.8, Occam R2: 1.2

Figure 7.7 shows an exemplary receiver station, at which both datasets, the electric field dataset and the time derivative of the magnetic field could be individually fitted by a 1D inversion approach. Note, that for magnetic field data, data points for late times were removed due to high error levels. Both datasets could be well fitted with the 1D algorithm. For both datasets the same system response was convolved with the forward model, which resulted in a good data fit also for the early times. The models strongly diverging after 800 m, exhibiting a high conductive layer for the modelled magnetic field data and a more resistive layer for the electric fields. According to the divergence behaviour of the Occam R1 and R2 inversion models, the estimated depth of investigation is approx 1000 m for both datasets. A forward modelling study, taking the Occam R1 inversion model obtained from the electric field data as model for subsequent forward calculation for the $B_z$ component exhibited a $\chi$ value of 30. Therefore, both datasets cannot be explained by the same subsurface model. Note that even if no sign reversal is present in the magnetic field data, the dataset might be still strongly affected by 2D effects. Therefore, in order to interpret magnetic and electric field data jointly, a joint multidimensional inversion must be carried out.

## 7.2. 1D Inversion Models in TD and FD

In order to ensure that an interpretation of the LOTEM data in time and frequency domain delivers similar information regarding the subsurface structures, a comparison of 1D smooth Occam inversion models calculated for both domains is carried out. The resulting Occam inversion model is plotted exemplarily for Tx8 in Figure 7.8 colour coded under the corresponding receiver station.

Transfer functions were inverted using a frequency range between the base frequency, ranging between 0.24 Hz and 1 Hz and odd harmonics up to 1 kHz. Frequencies larger than 1 kHz were excluded prior to inversion. For time domain data, the complete time range of the transients starting from $10^{-4}$ s up to 1 s was used. In both domains, the same homogeneous halfspace of 300 Ωm was used as start model for inversion.

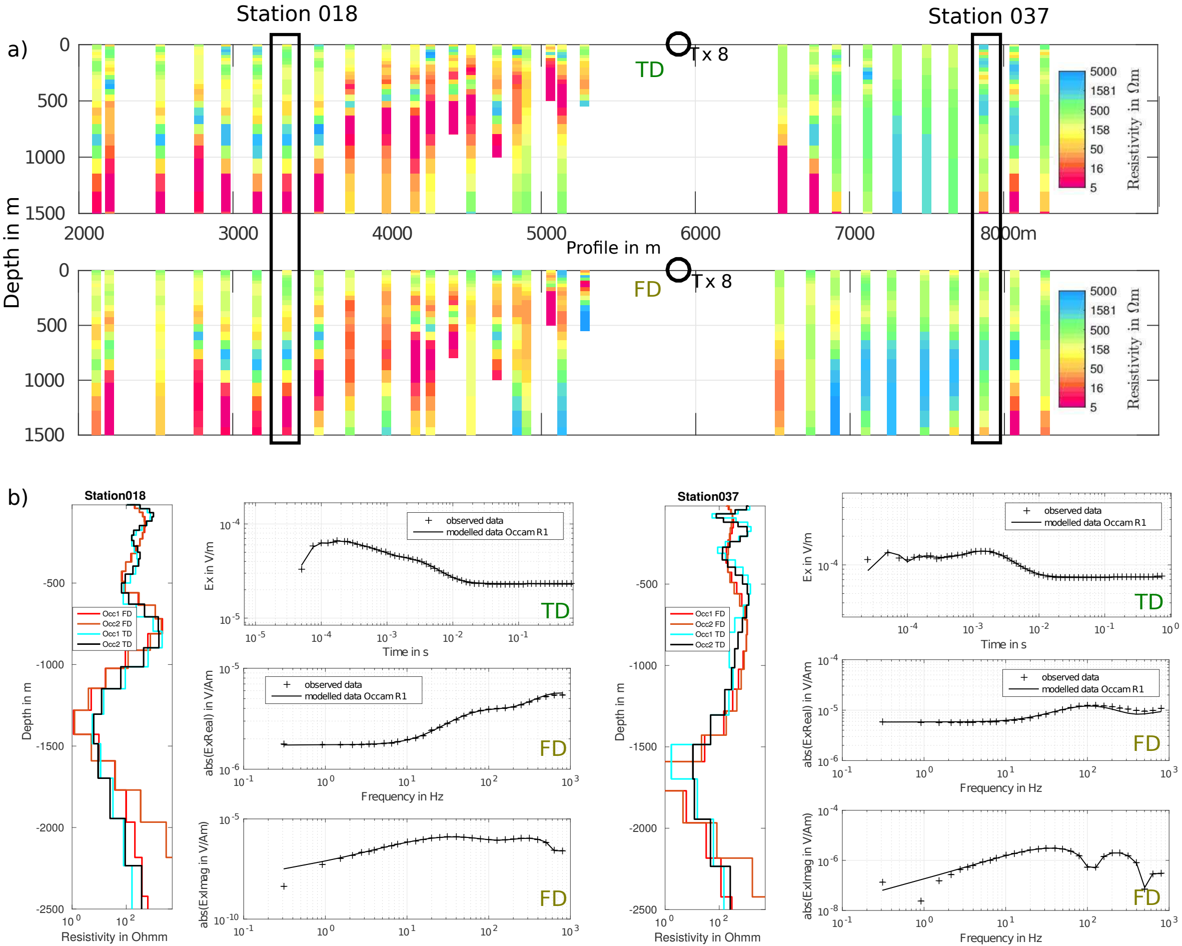

**Figure 7.8.:** a) Results of 1D time domain inversion and 1D frequency domain inversion, illustrated in colour code. The 1D Occam R1 inversion results for transmitter location Tx8 (black circle) are plotted under the corresponding receiver position. The lower panel shows the Occam R1 and Occam R2 results for time domain and frequency domain inversion and the data fit for stations 018 and 037 exemplarily.

The averaged weighted data fit of the LOTEM 1D inversion is 1.8, the overall misfit of the frequency domain data exhibits a higher weighted misfit of 3.2, where the overall misfit of the more resistive part of the profile in the southeast for both methods is higher than in the more structured part in the northwest. Note, that in both methods effects of IP are not included, which can bias the inversion results.

For most of the stations the Occam inversion result between both methods is comparable. As most prominent structure both inversion profiles exhibit a resistive layer on top of a more conductive structure in depth ranges of ∼1000 m between profile meter 2000 and 3500, rising up to 500 m at profile meter 4500. Figure 7.8b shows the Occam R1 and R2 models and the corresponding Occam R1 data fit for a station in the northwest part of the profile and one station exemplarily for the more resistive part of the profile located in the southeast. All 4 models for both stations show similar results until a depth of ∼2000 m. The observed data and model fit of the Occam R1 inversion for the frequency domain transfer function and the time domain transient demonstrates that both datasets are well explained by the model for station 018. For station 037 in the southeastern part of the profile the model shows more structure changes in the upper 500 m. This can be explained by the inclusion of early time transient data, whereas high frequencies over 1 kHz were excluded. The behaviour of Occam R1 and Occam R2 models suggests a depth of investigation of ∼2500 m for all models.

### 7.2.1. Synthetic Resolution Study

In order to give an expression of the resolution of the model parameters in 1D, a singular value decomposition was carried out and the set of Eigenparameters (EP) were calculated for a synthetic three layer case for frequency domain data and time domain step on data (cp. Section 3.6.2). The model was extracted from a simplified subsurface model derived from station 18. The synthetic model was preferred over the real inversion model to ensure comparability for the inversion statistics. Based on the inversion settings for the real data, an error floor of 1 % was set to the time domain data and an error floor of 3 % to the frequency domain data for modelling of the SVD parameters prior to inversion.

Transfer functions are ranging from 1 Hz to 1 kHz, transients from $10^{-4}$ s to 1 s respectively. The result of the Eigenparameter analysis is displayed after Scholl and Edwards (2007), where the relative weights of the logarithm of the original parameters contained in each Eigenparameter are displayed as circles (Figure 7.9). The radius of each circle is relative to the magnitude of each contribution to the Eigenparameter. The colour of the circle represents positive and negative values. After Edwards (1997) the standard error in an Eigenparameter is the reciprocal of its eigenvalue. Looking at the distributions of the model parameters to the eigenvalues, both domains exhibit a similar behaviour. Having the thickness $d_1$ as dominant contributor to the most relevant Eigenparameters with low upper error bounds, this model parameter is the best resolved parameter in frequency and time domain, also been represented by the highest BTSV. Both methods are able to resolve the resistivity and thickness of the first 2 layers. The last layer exhibits a considerably higher $\Delta_{max}$ as well as a higher error for the Eigenparameter most influenced by it, and is therefore less resolved than the other parameters. Note, that the absolute value of the BTSV between different models (i.e. domains) can not be compared directly to each other, since the values are normalised to the highest calculated value. However, one can observe, that the influence of the first layer on the modelled dataset is significantly higher in frequency than in time domain. Nevertheless, all layers exhibit a smaller $\Delta_{max}$ in frequency domain when compared with time domain. Therefore, all parameters are slightly better resolved in frequency domain, even when considering a higher error floor (3 %) for the synthetic frequency domain data. Note, that the assigned error floor scales directly with the fractional errors of the model parameters.

Next to the Eigenparameters and the BTSV, the synthetic model and the equivalence models of the best fit Marquardt model is plotted which show a $\chi$ below 1. Again, the first two layers are well constrained by the Marquardt model, since equivalence models show only a small deviation from the model parameters of the best fit model, whereas the resistivity of the last layer is poorly defined in both domains. For the second and the third layer, the variations in the equivalence models are smaller in frequency domain. One reason for the better resolution of frequency domain data compared with time domain step on data might be the joint inversion of real part and imaginary part of the former, with a higher relative response in the inductive imaginary part, compared with only considering a single inversion of step on data in time domain, superimposed by a high amplitude purely galvanic DC level. Note, that this advantage disappears, if step off data can be evaluated.

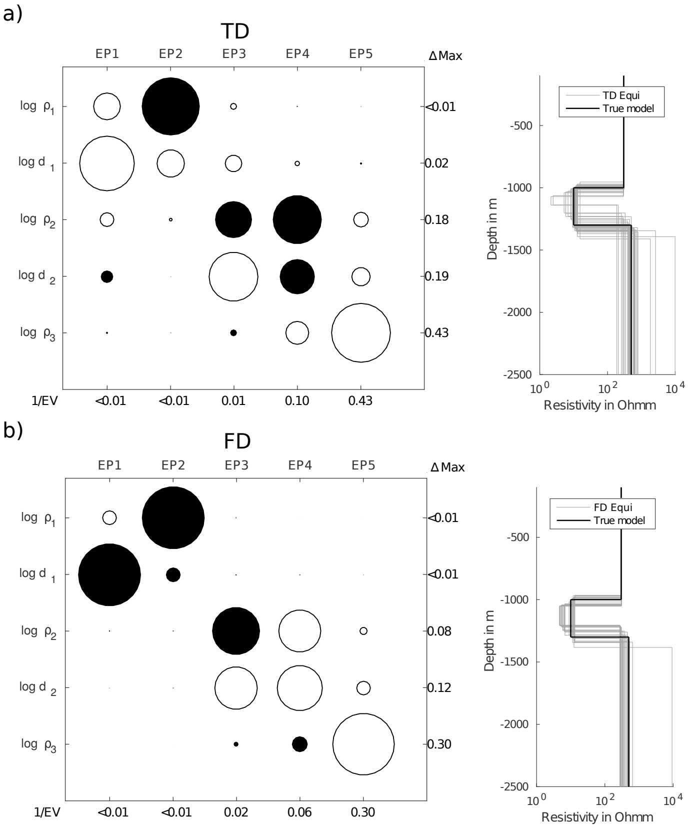

c)

| Parameter | Value | TD | FD |
|---|---|---|---|
| $\rho_1$ | 300 Ωm | 0.595 | 0.385 |
| $d_1$ | 1000 m | 0.884 | 0.979 |
| $\rho_2$ | 10 Ωm | 0.230 | 0.018 |
| $d_2$ | 300 m | 0.205 | 0.016 |
| $\rho_3$ | 500 Ωm | 0.024 | 0.002 |

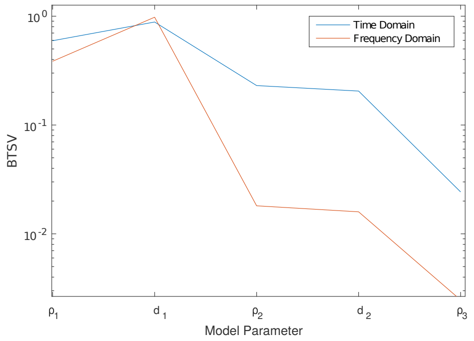

**Figure 7.9.:** a) Eigenvalue analysis for time domain data and (b) frequency domain data obtained by the inversion of forward calculated data from the true model. Next to the Eigenvalues, the synthetic model and equivalence models as obtained by inversion. c) Synthetic model and calculated BTSV for each model parameter.

Therefore, the study of the Eigenparameter and BTSV analysis for this simplified synthetic three layer model leads to two conclusions: First, the SVD for both domains exhibit a similar weighting of the model parameters to the corresponding Eigenparameters. Second, taking the error levels of the real field dataset into account, no loss of resolution for deep targets is expected, when inverting the LOTEM dataset in frequency instead of time domain. Both, the thickness and resistivity of the upper two layers are well resolved by the frequency and time domain inversion of the E-field LOTEM data.

## 7.3. The Influence of IP

Martin et al. (2018) performed shallow dipole-dipole time domain IP measurements in the survey area to characterize the geometry and properties of the conductive Graphtolite shales. They revealed strong polarization effects with chargeabilities in the order of 250 mV/V in the survey area which the authors related to the presence of the graphtolite shales. For broadside electric field data, as measured in the presented LOTEM dataset, the IP response exhibits the opposite sign to the inductive response (Hoheisel et al., 2004). Therefore, especially for late times, where the inductive effect decayed to small values and the IP effect is increasingly strong, the transient response is dominated by the latter and sign reversals in the step off transients can occur. For step on data, where the inductive response is overprinted by the DC level, the IP response will lead to a decrease of the measured amplitude.

Figure 7.10 illustrates effects of induced polarization on step off and step on data as well as real and imaginary part in time domain and frequency domain, for one given receiver-transmitter offset exemplarily. A station close to the transmitter site was selected as an exemplary station in order to interpret only a small induction volume and therefore relatively small 2D effects in the dataset can be assumed. The 1D forward study was performed using an IP+EM forward modelling algorithm (Hoheisel, 2000), where next to the modelling of EM transients, IP parameters for each layer can be included. For modelling of the IP parameters the Cole-Cole model (Cole and Cole, 1941) is utilized (cp. Equation 2.2), where the induced polarization is expressed in terms of chargeability $m$, relaxation time $\tau$, and the dispersion coefficient $c$. The depth and resistivity of the EM forward model given in Figure 7.10c is based on a Marquardt 1D inversion obtained by inverting step on data only.

Here, the conductive layer was assumed to be responsible for IP effects, therefore IP parameters were assigned to this layer only and the EM+IP response in time domain and frequency domain (Figure 7.10 a + b) was modelled. Additionally, the measured data for the given receiver transmitter offset is displayed. Note, that the presence of IP and an integration of IP effects in the inversion process would influence the thickness and conductivity of the out-coming inversion result and is therefore probably not the best fit model for the given dataset. However, with the modelling study, the relative influence of induced polarization on step on and step off data in time domain and respectively on real and imaginary data in frequency domain can be compared. The relative difference between the forward modelled EM response and the EM+IP response is plotted for each case over time and frequency respectively. In time domain, the IP response is most dominant for late times. As expected, the relative misfit and therefore the relative influence of the IP response is up to a decade larger for step off data than for step on data. In the real part of frequency domain data, the IP effects are, similar to the late times in time domain, the highest for low periods. The relative influence of IP is larger in the imaginary part, where the IP response is scattered over a large frequency band. Nevertheless, the relative difference between the IP model and the EM model is smaller than for the step off data. The real part is similar to the step on response overprinted by the DC level and therefore shows a small relative difference between the two modelled transfer function. Concluding from this modelling study and considering those strong IP parameters, step off data can

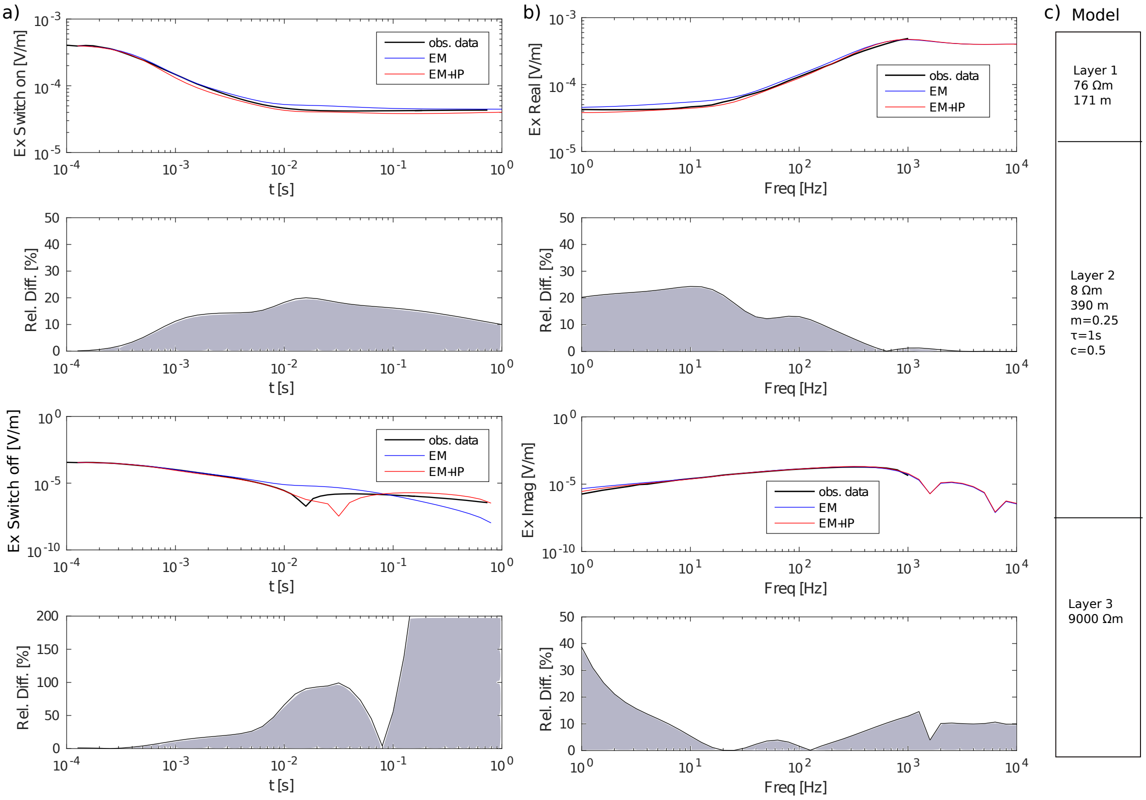

**Figure 7.10.:** a) Comparison of the model response in time domain without IP Parameters (blue) and with IP parameters (red). The model is based on the Marquardt inversion of data from station with an offset of 1000 m to Tx8. The observed data from the station is plotted in black. Data is shown with DC level (step on) and without DC level (step off). Additionally the relative difference between the model response with and without IP parameters is displayed. b) Modelled data in frequency domain and relative difference for the same model used in a). For the EM forward calculation, chargeabilities were set to 0 for all layers. Utilized Model parameters are listed in c).

not be inverted by an EM inversion algorithm. The influence on step on data, as well as on frequency domain data is less significant. When interpreting the dataset neglecting IP effects, either only early part information of step off data, step on data using considerate error floors or frequency domain data can be inverted. Note, that for cases where the IP response is the target parameter, one should invert time domain step off data with a joint inversion of IP and EM parameters, since the relative IP response is the largest in step off transients. Since here the data is interpreted considering EM response only, step off data could not be interpreted 1D. Therefore, being less influenced by the IP effects, step on data was inverted in time domain and subsequently compared to the frequency domain approach.

## 7.4. Summary

Electric field data in time domain was inverted utilizing 1D inversion routines. Since time domain switch off data could not sufficiently be modelled and the sign reversal present in the switch off dataset could not be reproduced, data was recalculated to switch on transients and subsequently inverted. The switch on data could be sufficiently explained by the modelled data over the complete time range for most stations, however a 1D inversion approach is clearly not suitable to obtain an interpretable image of the subsurface in terms of resistivity. The resistivity distribution showed strong lateral resistivity contrasts and the obtained models are not consistent along the profile and for different transmitter-receiver geometries. Moreover, the measured time derivative of $B_z$ showed sign reversals, which do not occur in a 1D subsurface distribution and are an indicator for multidimensional resistivity distribution. A block anomaly model study demonstrates, that 2D structures can strongly bias the 1D inversion models within a large distance to the 2D structure.

The LOTEM dataset was not only processed in time but also in frequency domain for the first time. The approach could be validated by comparing inversion results obtained in both domains, which delivered similar 1D inversion models. In order to prove, that an inversion of the dataset does not lead to an decreased resolution of a deep conductive target, resolution studies were carried out.

As shown in petrophysical studies and time domain IP measurements which were carried out in the framework of DESMEX, induced polarization effects are present in the survey area. Considering Cole-Cole parameters based on those results, the influence of induced polarization to the EM time and frequency domain response is studied. The relative effect of IP towards late time TD switch off data is by far the largest. Moreover, it can produce sign reversals which are present in switch off data. Due to the additional superposition of the DC field in switch on data, the relative effect towards the switch on transients is smaller. In frequency domain, effects on the real part of the transfer functions are comparable to effects on TD switch on data, whereas the relative influence of IP is larger in the imaginary part. However, IP effects are overall smaller in frequency domain. Considering that for a subsequent 2D inversion only electromagnetic effects are taken into account, an inversion of frequency domain data is even beneficial, since the relative influence of induced polarization is weaker.

## CHAPTER 8

# Synthetic 2D Modelling Studies

For modelling studies and subsequent 2D inversion in frequency domain, the goal oriented finite element open source Fortran code `MARE2DEM` (Key, 2016) was utilized. It supports (joint) inversion of MT and CSEM data, both onshore and offshore. Quadrilateral grids as well as unstructured triangular grids can be utilized, which gives a high geometric flexibility and allows for an easy implementation of topography. In the framework of this thesis, inversions are performed on an unstructured triangular grid. For efficiency, the algorithm has a dual grid approach, where the mesh for inversion is defined by the user, and triangles are adaptively refined at zones with high conductivity contrasts during forward calculation. In a first step the forward response is calculated on a rather coarse mesh. Afterwards, regions which exhibits the highest estimated error are refined until the errors of the forward solution are within a certain predefined tolerance, which is set to 1 % in the modelling presented here. Additionally, a minimum size for each element is set in order to prevent an over-refinement e.g. at locations close to the transmitter. As error estimator, the goal function proposed by Ovall (2006) is implemented, which approximates the errors at the discrete location of the receivers a posteriori, since only an accurate solution at a subdomain of the model, i.e. the receivers is necessary. In order to speed up the forward modelling and subsequent inversion, the algorithm is parallelised over frequency, wave number, transmitter and receiver, where meshes created for a certain wave number and frequency is shared with neighbouring frequencies and wave numbers in order to reduce the computational load. Since available clusters are seldom offer computational resources in the range of $10^4$ processors, the receivers are grouped and mesh sharing is introduced. Hereby, neighbouring frequencies and wave numbers are grouped together and solved for the same mesh, since the EM fields typically vary smoothly over those parameters. Additionally, receivers are subdivided in smaller groups, allowing the adaptive refinement task to find a suitable mesh in fewer iterations. Since for small offsets, the EM forward solution for a point source significantly deviates from the forward solution of a dipole source due to bipole effects, a CSEM dipole source is approximated by a calculation of point dipoles along a given dipole wire (Key et al., 2014; Haroon et al., 2018). The model space only varies in 2D, assuming conductivity is invariant in x-direction, with the receivers aligned at a profile going in y-direction. Per default wave numbers between $10^{-5}$ and $10^{-1}$ m are utilized in order to transform the fields back into the 3D spatial domain. For model boundaries zero Dirichlet conditions are applied. For an efficient solution of the linear system required by the goal oriented error estimator, the super-nodal sparse matrix factorization routine `superlu` is utilised. In the following section, the parameters concerning e.g. mesh generation and different roughness parameters, which are utilized during the inversion of field data and corresponding forward modelling tests are introduced. More details about the adaptive refinement method and parallel implementation details can be found in Key (2016). More recently, Haroon et al. (2018) implemented a solution of EM fields in time domain, which allows the evaluation of transient LOTEM data. The time domain transformation and subsequent synthetic tests in time domain are given in Section 8.2.10.

## 8.1. The MARE2DEM Algorithm

The description of the forward problem as implemented in `MARE2DEM` can be found in Key and Ovall (2011) and Key (2016). Since in this thesis only an isotropic earth is considered, we limit the problem formulation to an isotropic earth. The Maxwell equations described in Section 2.2 hold in frequency domain

$$\nabla \times \mathbf{E} - i\omega\mu\mathbf{H} = \mathbf{M}_s \tag{8.1}$$

$$\nabla \times \mathbf{H} - \sigma\mathbf{E} = \mathbf{j}_s \tag{8.2}$$

where $\mathbf{j}_s$ and $\mathbf{M}_s$ denotes the electric and magnetic source term. Both EM sources may depend on 3D field variations. The conductivity $\sigma(y,z)$ is 2D and constant in strike direction x. With help of a Fourier Transformation into wave domain, the 2D fields write

$$\hat{\mathbf{F}}(k_x, y, z) = \int_{-\infty}^{\infty} \mathbf{F}(x, y, z) e^{-ik_x x} dx, \tag{8.3}$$

where $k_x$ is the spatial wave number in strike direction and $\mathbf{F}$ stands for either $\mathbf{H}$ or $\mathbf{E}$. After Key and Ovall (2011), the coupled differential equations for the strike parallel EM components $u = (E_x, H_x)$ in wave domain can be simply written as

$$-\nabla \cdot (A\nabla\mathbf{u}) + C\mathbf{u} = \mathbf{f} \quad \text{in } \Omega \tag{8.4}$$

where $\Omega$ denotes the model domain and $\mathbf{u} = \mathbf{0}$ at the outer boundary $\delta\Omega$. $\mathbf{f} = (f_1, f_2)$ holding the source terms (Key and Ovall, 2011). The coefficients A and C for an isotropic earth write

$$R = \begin{pmatrix} 0 & -1 \\ 1 & 0 \end{pmatrix} \qquad A = \lambda \begin{pmatrix} \sigma I & ik_x R \\ ik_x R & i\omega\mu I \end{pmatrix} \qquad C = \begin{pmatrix} \sigma & 0 \\ 0 & i\omega\mu \end{pmatrix} \tag{8.5}$$

After solution of Equation 8.4, the EM fields in the transverse plane are obtained and transformed back into the 3D spatial domain with an inverse Fourier transformation. In order to solve the forward problem via finite elements, Equation 8.4 is reformulated for $\mathbf{u}$ being strike parallel EM fields at the element vertices. For a detailed description, refer to Key and Ovall (2011).

### 8.1.1. Calculation of Sensitivities

For the calculation of sensitivities within the `MARE2DEM` algorithm, the reciprocity of the problem is used rather than a direct calculation of the partial derivatives of the electric and magnetic field with respect to the model parameters. In the `MARE2DEM` algorithm, the adjoint reciprocity formula is implemented after Farquharson and Oldenburg (1996) for any EM field component $\mathbf{F}$ and extended for the triaxial anisotropy $\sigma_j$ (Key, 2016)

$$\frac{\partial \mathbf{F}}{\partial \sigma_j}(x, y, z) = \frac{1}{2\pi} \int\limits_{-\infty}^{\infty} \hat{S}_j(k_x, y, z) e^{ik_x(x_r - x_s)} dk_x \tag{8.6}$$

with the Fourier Kernel

$$\hat{S}_j(k_x, y, z) = \int\limits_{A_j} \hat{\mathbf{E}}^a(-k_x, y, z) \cdot \left( \frac{\partial \tilde{\sigma}}{\partial \sigma_j} \hat{\mathbf{E}}(k_x, y, z) \right) dA_j. \tag{8.7}$$

where $\hat{\mathbf{E}}$ corresponds to the electric field in wave number domain $\mathbf{k}_x$ generated at the source location and $\hat{\mathbf{E}}^a$ to the adjoint electric field generated at an adjoint source at the receiver position. The term $\frac{\partial \tilde{\sigma}}{\partial \sigma_j}$, where $\tilde{\sigma}$ corresponds to the conductivity tensor is 1 for an isotropic earth and therefore the sensitivities depends on all electric field components. For the sensitivity calculation for all model parameters of any given field component, only the adjoint field $\hat{\mathbf{E}}^a$ needs to be calculated additionally. Considering that for most 2D cases the amount of model parameters n is much larger than the amount of field components p, the solution for the additional adjoint sources p is more time efficient compared with a direct calculation of sensitivities (Key, 2016). In the following modelling studies the sensitivities will be displayed as summation over the column of the Jacobian $\mathbf{J}_{ij}$ normalized over the area of the mesh cells $A_j$ and weighted by the data error $\mathbf{W}$, which reflects the accumulated error-weighted sensitivity of one model parameter with respect to all data points.

$$\mathbf{J}_{\mathbf{W}j} = \frac{1}{A_j} \sum_i |\mathbf{W}_{ii} \mathbf{J}_{ij}|. \tag{8.8}$$

In order to compare sensitivities calculated for different field components, error settings and data transformations, 8.8 is multiplied with the diagonal matrix $\mathbf{W}$ containing the (transformed) data errors.

### 8.1.2. Fast Occam Inversion

In `MARE2DEM` the Occam inversion approach (cp. Equation 3.22) is implemented utilizing the L2 norm of the model gradient (Occam R1)

$$||R(m)||^2 = \int\limits_{\Omega} \nabla m \cdot \nabla m \; d\Omega \tag{8.9}$$

where $\Omega$ is the area of the model domain and $m$ is the model parameter. For an unstructured grid, the gradient can be computed by a summation over the difference in resistivity of all model cells adjacent to the $i-th$ cell with parameter $m_j$ weighted by their respective distance $\Delta r_{ij}$ and the area ratio $\omega_j$ of the total area of all $N_i$ neighbouring cells.

$$\omega_j = \frac{A_j}{\sum_{k=1}^{N_i} A_k} \tag{8.10}$$

It follows that the total roughness can be expressed by

$$||\mathbf{Rm}||^2 = \sum_{i=1}^{n} A_i \left[ \sum_{j=1}^{N_i} \omega_j \left( \frac{\Delta m_{ij}}{\Delta r_{ij}} \right)^2 \right], \tag{8.11}$$

where $\Delta m_{ij} = |m_i - m_j|$ and the distance $r_{ij}$ normally is euclidean distance between the centre of the model cells

$$\Delta r_{ij} = \sqrt{(y_i - y_j)^2 + (z_i - z_j)^2} \tag{8.12}$$

However, this equation can be modified by a horizontal-vertical smoothness factor $\omega_{hv}$ to weight the corresponding roughness penalty. For values of $\omega_{hv} > 1$ horizontal smoothness is achieved, whereas for values $\omega_{hv} < 1$ the vertical smoothness is increased.

$$\Delta r_{ij} = \sqrt{\left( \frac{y_i - y_j}{\omega_{hv}} \right)^2 + (z_i - z_j)^2} \tag{8.13}$$

In the first step, the Occam algorithm tries to find the optimum trade-off parameter $\mu$ which minimizes the data misfit. Since a dynamic search over the parameter $\mu$ (e.g. by the L-curve criterion) is computational costly, the Occam fast implementation search for $\mu$ was adapted. If a better model is found at any step of the minimization search, which reduces the misfit below a certain threshold, the model is accepted without carrying out the full bracketing minimization which can reduce the computational effort considerably (compare Figure 8.1).

In the optimum case, a good model is already found after the first minimization step. If the minimization approach fails to find a better model, a reduced model step is taken. The initial value for the step size is $\alpha = 1$. When the line search fails, $\alpha$ is cut in half each time and the line search starts again with the new model $m_{k+1}$.

$$m'_{k+1} = \alpha m_{k+1} + (1 - \alpha) m_k \tag{8.14}$$

After a model is found, which decreases the misfit to the target misfit, the second part of the minimization algorithm starts. Using interpolation methods, the largest value for $\mu$ within the target misfit is searched, trying to find the smoothest model within the target misfit.

### 8.1.3. Bounds on Model Parameters

Model parameters can reach geological unrealistic values, e.g. very small or high resistivity values respectively, especially, if the dataset is afflicted by noise, voltage shift etc. Therefore, a global bound for all model parameters between 1 and 10000 Ωm was applied. This has additional benefit, that the adaptive mesh refinement scheme does not put too

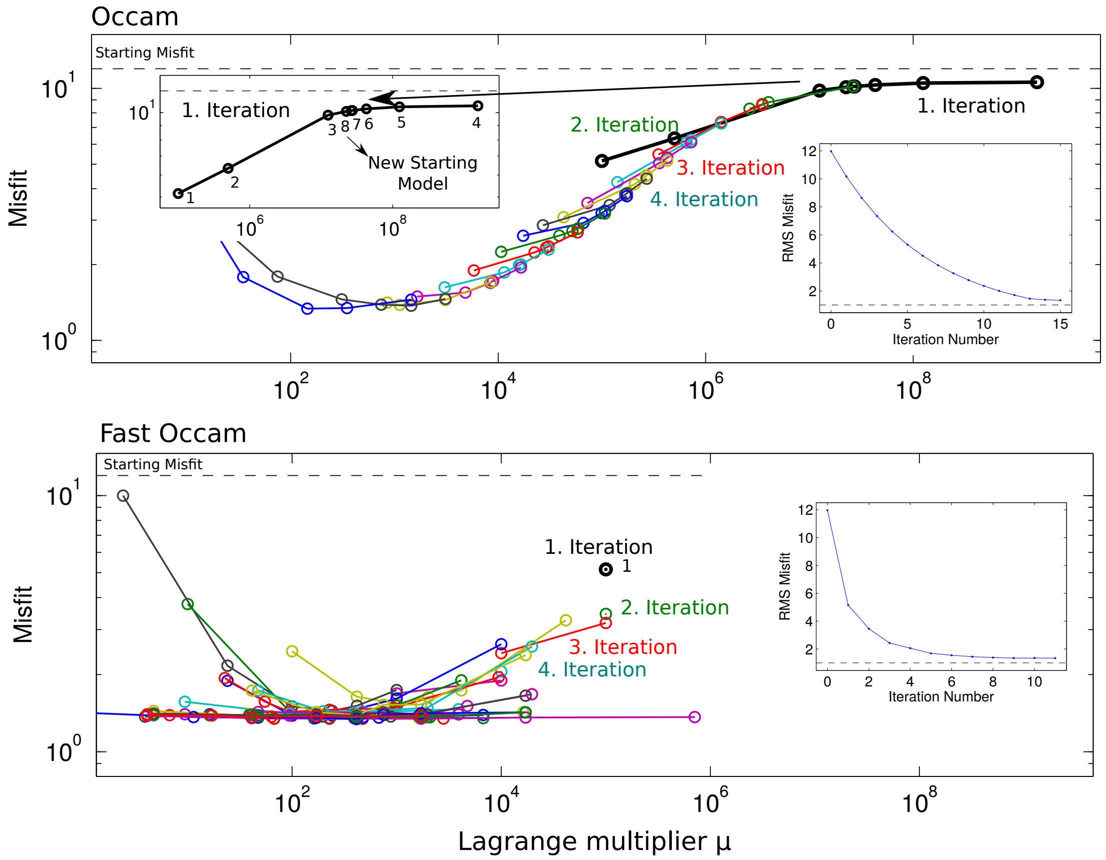

**Figure 8.1.:** Misfit versus Lagrange multiplier for the Occam and fast Occam approach. The Occam approach performs every iteration step a complete bracketing minimization, finding the best trade of parameter between roughness and data fit. For example for the first iteration, 8 forward calculations are needed to find the intercept value $\mu$. The Fast Occam approach only makes 1 forward calculation, since already in the first try a model update with a misfit decrease larger 15 percent is found. The inversion characteristics shown here are based on the inversion of the dataset corresponding to block model 1 introduced in Section 8.2.2.

much computational effort in the discretization of e.g. very high conductivity regions. In order to allow the minimization algorithm to work on a non restricted domain, the model parameters $m$ are transformed in a new transformed model vector $x(m)$, which takes values in the full domain of real numbers.

$$-\infty < x(m) < \infty \tag{8.15}$$

and is defined between the boundaries of the model parameters

$$l \leq m \leq u \tag{8.16}$$

In `MARE2DEM` a band pass transformation is utilized where inside the desired domain (e.g. between 1 and 10000 Ωm) the transformation is close to identity while on the edges the sensitivity of the transformed parameter strongly decay. On the one hand this guarantees that the values are inside the boundaries while on the other hand the smooth decay ensures that close resistivity values near the boundaries are not over or under penalized.

## 8.2. Synthetic Tests with MARE2DEM

In order to deviate suitable inversion and forward modelling parameters for the evaluation of the LOTEM dataset, synthetic modelling studies were performed. The dataset is studied as amplitude in log transformation and phase (cp. Section 6.2.4) rather than real and imaginary part, since inversion of field data in the latter representation did not converge to satisfying results. Wheelock et al. (2015) studied the advantages of logarithmically scaled data for electromagnetic inversion. The authors found, that logarithmically amplitude and phase is a more robust data transformation for inversion than real and imaginary data, utilizing fewer iteration steps in the inversion procedure. In a first step, different inversion meshes are tested to find a good trade off between an accurate model response and computational time for the subsequent modelling studies. Additionally the influence of topography and the extension of the dipole source is considered. Smoothing parameters are adapted, and the effects of error levels are evaluated. Aim of the LOTEM validation study is the derivation of a reference model, which detects EM conductivity anomalies within depth ranges of up to at least 1 km. Therefore, calculated sensitivities are analysed to get insights into the capabilities of the dataset to resolve either conductive or resistive structures with a focus to depths in the range of 1 km. If not noted otherwise, for all tests, real field data geometry is taken, considering the frequency range of the acquired field data. Frequencies are ranging between 1 Hz and 1000 Hz, times between $10^{-3}$ s and 1 s. Offsets for magnetic SQUID data are ranging between 272 m and 2647 m, for electric field data between 307 m and 4921 m. The vertical position of transmitters and receivers is derived from an interpolated elevation model. In order to make sure that `MARE2DEM` can perform a finite conductivity calculation at the receiver location, receivers and transmitters are located 0.1 m below the surface (cp. Figure 8.2). Transmitter positions are indicated with a red circle, electrical receiver stations with a white triangle and magnetic receiver stations with a white diamond marker.

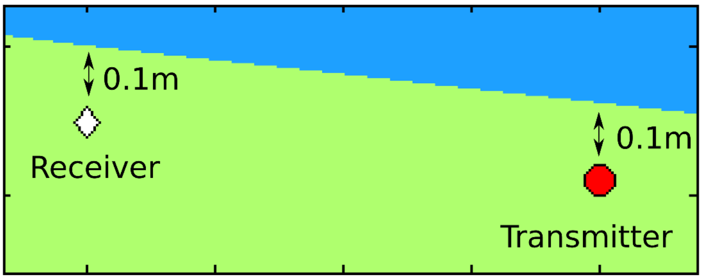

**Figure 8.2:** To ensure that transmitters and receivers are located in an area with finite conductivity, they are located in a small distance to the surface, e.g. in a depth of 10 cm.

The starting model for subsequent inversions were set to 100 Ωm, if not mentioned otherwise. If data is shown in terms of sensitivity, note that always the error-weighted sensitivities are plotted and, if an arsinh transformation was applied, back transformed according to Section 3.8. Since magnetic field data was only processed in frequency domain, the main part of the modelling study will concern resolution capabilities of the field components in frequency domain. However, most of the parameters studied, e.g. grid discretisation, smoothing parameters, effects of the starting model topography are somehow conferrable to time domain, however the relative influence compared to the data parameters may vary. Therefore in the end of this chapter, sensitivities of electrical data towards a deep conductive anomaly are studied in time domain and compared to the frequency domain response.

### 8.2.1. Validation of the FD Response

Since `MARE2DEM` is mainly utilized for marine applications which exhibit a rather high conductive environment, the accuracy of the forward response for the components measured during the field campaign with varying offsets between 100 m and 5000 m and a resistive environment was tested beforehand. Background resistivities of the model were set to 300 Ωm and a conductive layer with 10 Ωm was included in a depth of 500 m. In a first step, the forward solution for a point dipole for $E_x$, $B_y$ and $B_z$ was tested against the 1D forward solution of the `EM1DW` code (cp. Figure 8.3). For the presented forward calculations, 90 wave numbers spaced logarithmically from $10^{-6}$ to $10^{2}$ $\mathrm{m}^{-1}$ are utilized, which proved to deliver an accurate response for the complete frequency range. Misfit in phase and amplitude between the 1D algorithm and `MARE2DEM` are below 1 % and 0.2° respectively for offsets between 100 m and 5000 m. However, the utilized transmitters of the field experiments are approx. 1000 m long. Due to bipole effects, the calculation of a single point dipole will lead to an inaccurate response. Relative differences between the dipole solution and the solution for an extended dipole is increasing up to 100 % for the presented model and short offsets (cp. Figure C.1 in Appendix). Therefore, the forward response was calculated for a predefined number of point dipoles along the transmitter cable. A total number of 9 dipoles were utilized for the results given in Figure 8.4. In the version of `MARE2DEM` currently freely available (Version:10.03.2014) a low-order Gauss-Legendre quadrature rule is used for the approximation of the bipole (Key et al., 2014).

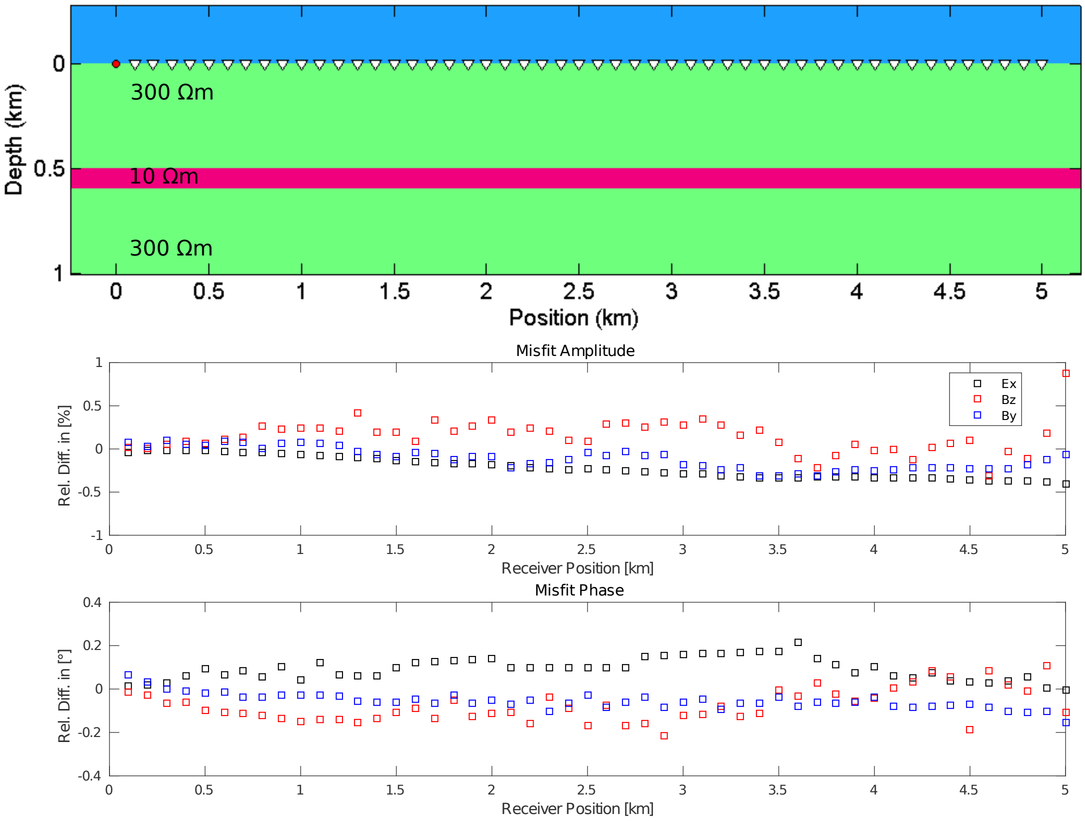

**Figure 8.3.:** The 3-layer case model is displayed in the upper panel. Forward responses for a point dipole transmitter and for electric and magnetic receivers (white triangles) with varying offsets of 100 m to 5000 m to the transmitter (red circle) are calculated. The 1D forward solution of `EM1DW` is compared to the forward solution of `MARE2DEM` in terms of relative differences for amplitude and phase in the lower Panels.

However, as shown in Figure 8.4, the forward response is deviating from the response calculated by the 1D algorithm for short offsets. Haroon et al. (2018) implemented the summation over the nine dipoles along the transmitter cable. Here, we set analogue to the approach of `EM1DW` and `MARTIN`, the location of the nine point dipoles $DP_j$ in the centre $x(j)$ of each of nine equally spaced segments (cp. Eq. 8.17) along the transmitter wire with a length $L$ and summed up in order to achieve the dipole response.

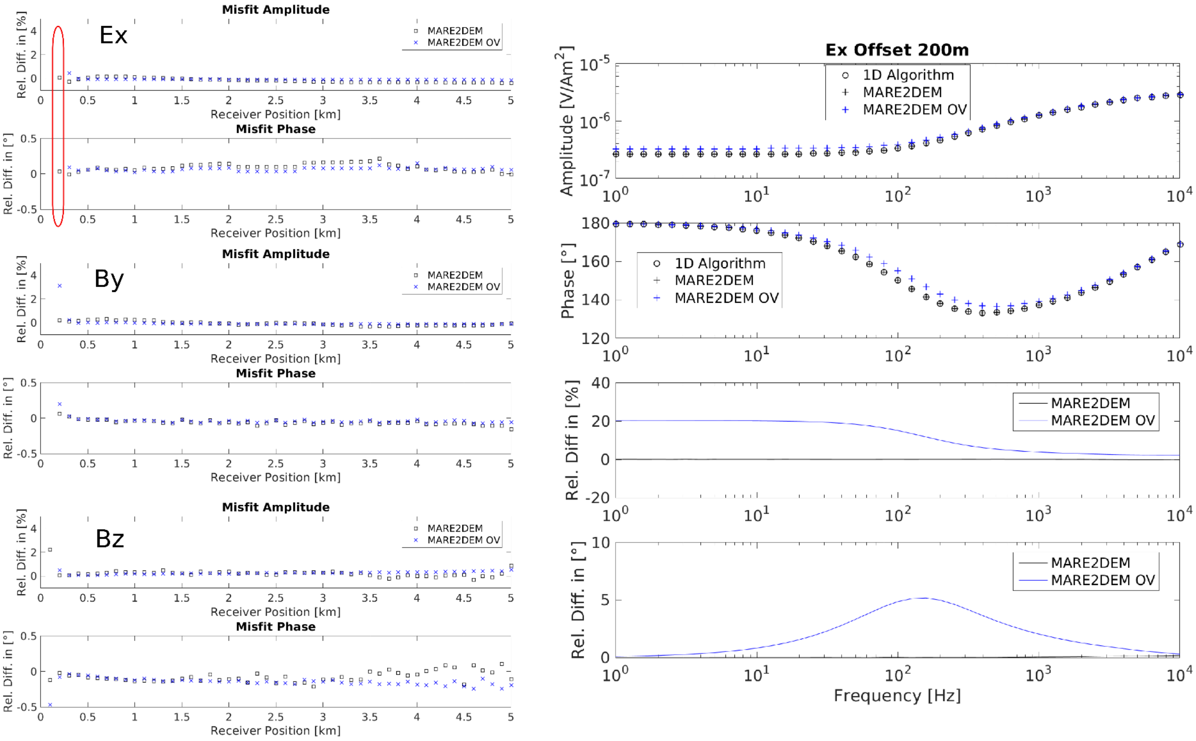

**Figure 8.4.:** Left Panel: Validation of the extended dipole response along the profile for the summation algorithm (MARE2DEM) and the integration via the Gauss-Legendre quadrature rule (MARE2DEM OV) for the three field components displayed as rel. difference towards EM1DW. Right Panel: The $E_x$ field component at a Tx-Rx offset of 200 m is exemplarily displayed over frequency for both algorithms and the 1D solution.

$$x(j) = (j - 0.5)\frac{L}{N} - L/2 \tag{8.17}$$

Results were compared with the 1D algorithm, utilizing 100 segments in order to get a dense discretization of the transmitter cable and therefore an accurate response. For the 2D forward response, such a large number of segments would be inefficient due to the strongly increased computational load. With the summation of single dipoles, accurate responses were achieved for an offset of 200 m and higher. Therefore for inversion of field data the summation algorithm is favoured over the integration utilizing the low-order Gauss-Legendre quadrature rule. For offsets of 100 m, both algorithms exhibited deviations larger than 50 % from the 1D solution. However, field data was recorded within offsets of 272 m to 4921 m. In this range, calculated field responses are well within 1 % deviation to the 1D algorithm for amplitudes and 0.2° for phases for all three components. In order to find a suitable forward mesh during adaptive refinement in less iterations, `MARE2DEM` allows to subdivide transmitters and receivers into smaller groups. However, as shown in Figure 8.5 exemplarily for the $B_z$ component, the accuracy of the response is smaller when the receivers are subdivided in groups for mesh refinement than for a combined mesh search for all 50 receiver stations. Therefore for field data inversion, a high number of receivers and transmitters were grouped together, resulting in less groups.

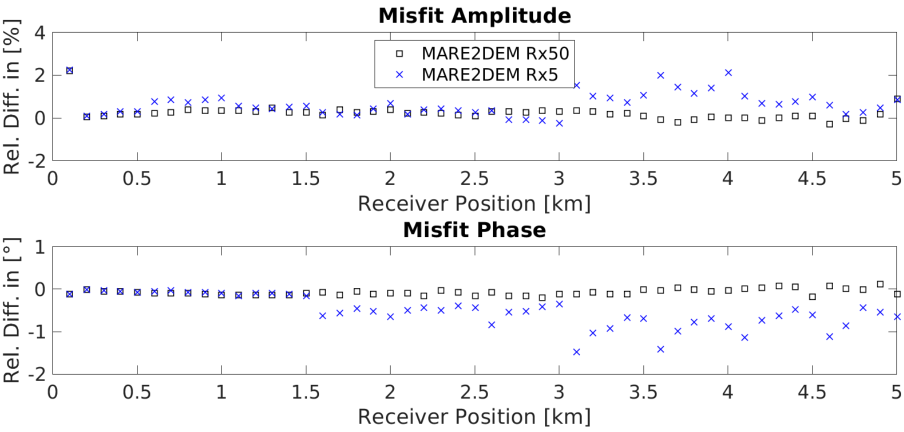

**Figure 8.5.:** Forward response along the profile grouping 5 receivers together during mesh refinement and grouping all 50 receivers together compared to the forwards response of `EM1DW`. Exemplarily shown for the $B_z$ component, which exhibited the highest difference.

## 8.2.2. Creation of the Inversion Mesh

For the forward calculation meshes are generated automatically by the adaptive goal oriented refinement, therefore the user only needs to define the grid for inversion. In the open source `MARE2DEM` package available at https://mare2dem.ucsd.edu/, additional Matlab scripts are provided for the generation of the inversion mesh. In order to assure, that the EM-fields generated at the centre of the mesh are sufficiently attenuated at the boundaries, the model boundaries should be at least several skin depth away from the region of interest. For the following modelling and inversion studies, model boundaries are located ± 100 km from the centre. Conductivity values of the input model are assigned to segment bound polygonal regions.

The geometry of topography in the area of interest can be included before the mesh is generated. The triangulation is generated automatically using constraint Delaunay triangulation, which ensures that no slivers are present in the triangle mesh, exhibiting angles below 25 degrees. All introduced models were divided in 3 regions with deviating triangle size. In an area close to the transmitters and receivers, with a width slightly larger than the profile length of 8.5 km and a depth of 3 km, the smallest triangle size was utilized, since the resolution is the highest in the shallow subsurface. In order to take the decreasing resolution with increasing depth into account and save computational time, in an intermediate region with depth down to 10 km, the triangle size was increased. The outer regions up to the model boundaries, where the resolution is low to zero, were filled with large triangle. Different triangle sizes, and therefore a different total amount of modelling cells will be tested in synthetic modelling studies. During each iteration of the Occam inversion, new adaptively refined meshes are generated during each forward call for the conductivity model. In the survey area, high conductive structures at the surface need to be resolved and at the same time, a reasonable high resolution for deep

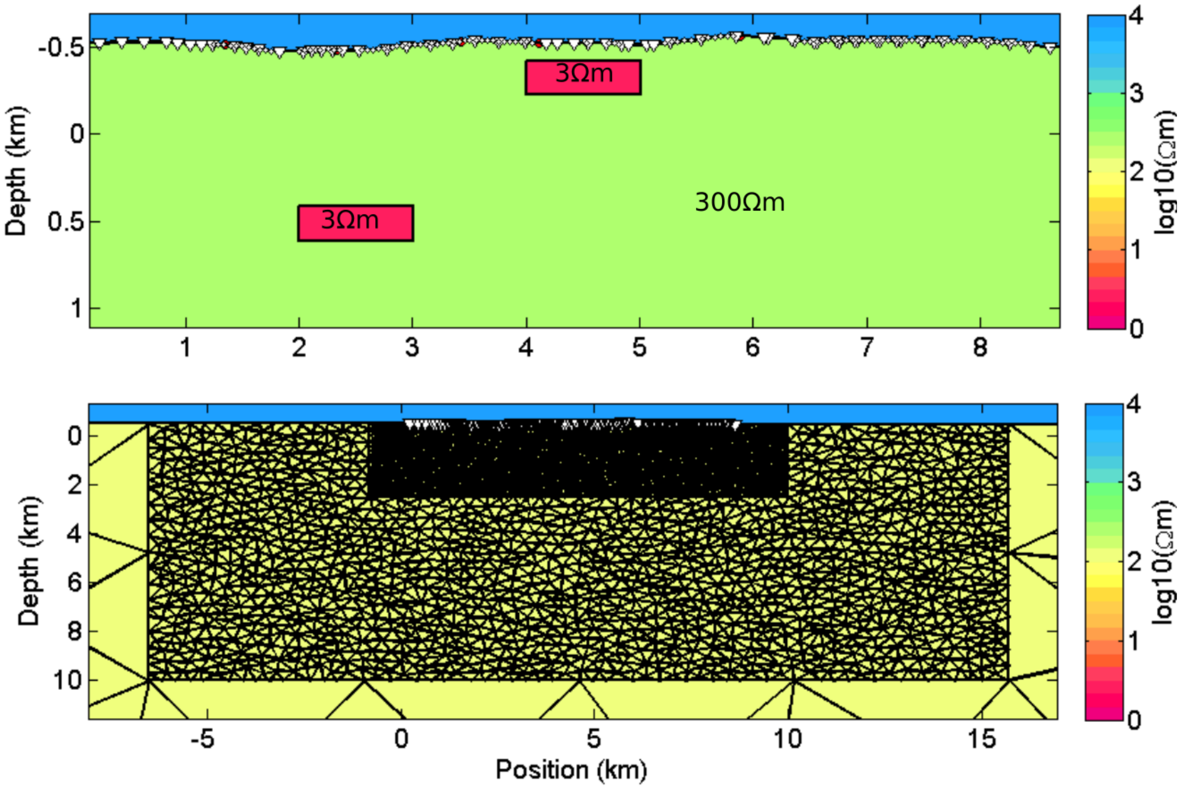

**Figure 8.6.:** Upper Panel: Block model (block model 1) for grid testing. Lower Panel: Example of a coarse inversion mesh. The model space is subdivided in three regions in order to decrease the amount of model parameters. A small triangle length is chosen for the inner region which has a high sensitivity to changes in single model parameters. An intermediate region with increased triangle length where the model shows a lower sensitivity. And an outer region with a very large triangle size, where the sensitivity is close to zero. Receiver and transmitter locations are marked with white triangles and are setup in profile km 0 to 9.

subsurface structures is required. Therefore, a block model (block model 1) exhibiting shallow and deep conductive anomalies as given in Figure 8.6 is created in order to find a good trade off between computational effort and model resolution. For inversion, three different discretised inversion meshes are created. A dense mesh, containing in total 25000 triangles and an triangle length of 75 m in the inner region of the grid. A medium dense mesh, consisting of 15000 model cells and an inner triangle length of 100 m and a rather coarse mesh with 8000 triangles and an inner triangle length of 200 m. Synthetic data was forward modelled for the electric field component at the location of the LOTEM E-field receivers and the vertical magnetic field at the SQUID receiver locations. To the modelled synthetic dataset 5 % Gaussian noise was added to both, amplitude and phase and for inversion subsequently an error floor of 5 % for the amplitudes and a constant error floor of 2.86° for the phases. Resulting inversion models for all three inversion meshes are shown in Figure 8.7. As starting model for the inversion a homogeneous half-space of 100 Ωm was utilized. All three inversions utilizing the different meshes converged to an error-weighted RMS of 1 and can sufficiently reproduce the conductivity structure in shallow and larger depth. However, for the coarse mesh, the large triangle size already affects the shape of the good conducting anomaly. In order to be able to reflect also small scale conductivity structures within in a reasonable calculation time and working memory, a medium grid was utilized for further inversions.

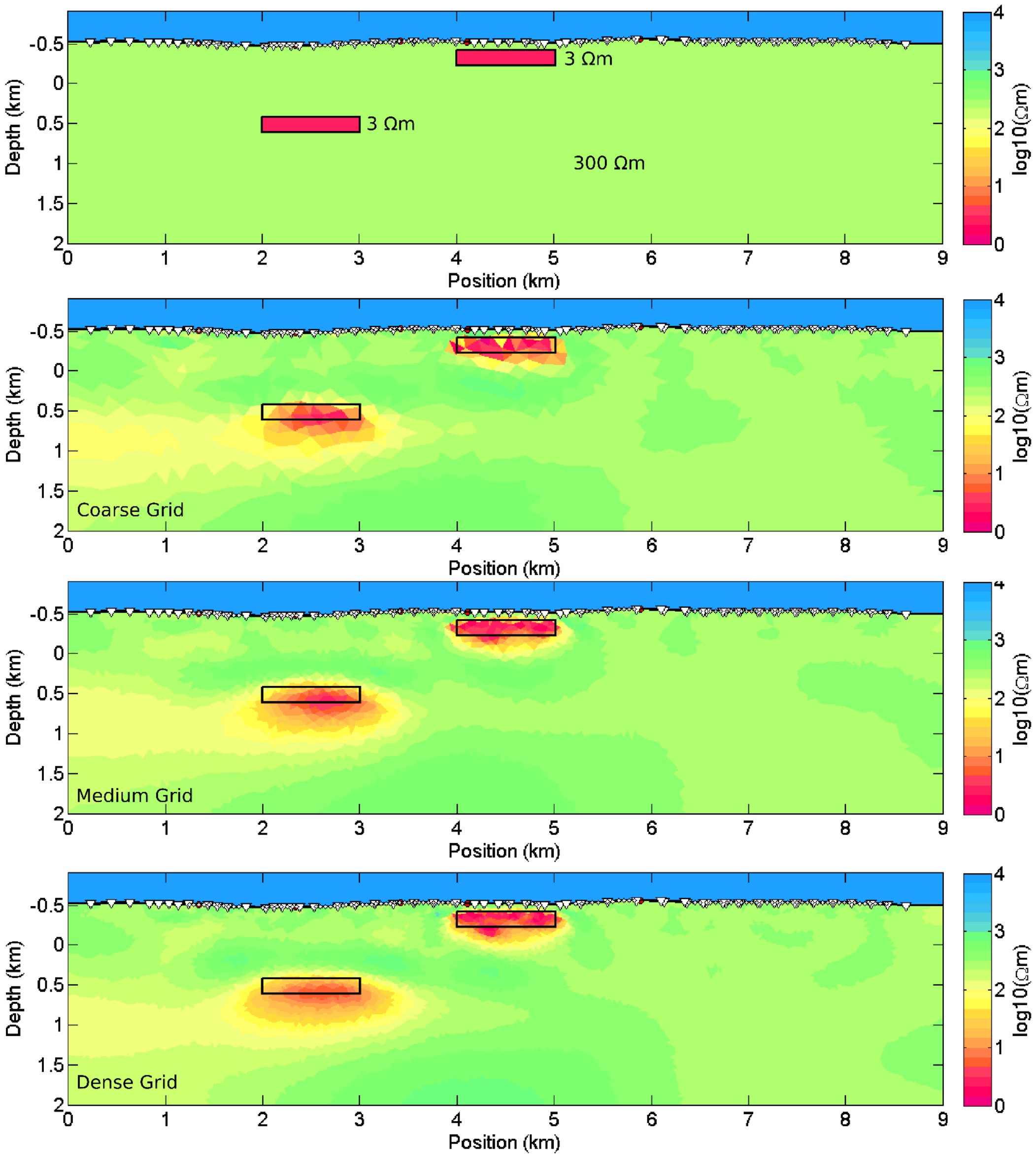

**Figure 8.7.:** The forward model (block model 1) and the inversion results using the $E_x$ and $B_z$ component for the three tested discretisations for the inversion meshes. All three utilized meshes are able to reproduce the conductivity anomaly. Rectangular boxes mark the location of the anomaly. The smoothness factor $\omega_{hv}$ was set to 3.

### 8.2.3. Influence of Topography

One of the advantages of utilizing finite differences is the easy implementation of topography, since a finite difference implementation would now require a very dense grid over a large modelling space. Figure 8.8 gives an image of the influence of topographic effects assuming the geometry of the real dataset: Data was forward calculated for a homogeneous halfspace of 300 Ωm without topography and a model including topography. Along the profile, the topography ranges from 475 m above sea level up to 561 m along the 8.5 km long profile, with a moderate maximum slope angle of 4° around profile 1, 2-3.5, 5-6 km and at the end of the profile (Figure 8.8 b). The slopes in the survey area are therefore only moderate. Figure 8.8 a shows the error-weighted difference between the forward calculated data averaged over all stations over frequency and averaged over all frequencies along the profile. Where the difference in amplitude does not show a clear frequency dependence, phase differences depending strongly on frequencies, exhibiting a larger misfit for higher frequencies, which refer to the more shallow subsurface for all components. The largest misfit between the forward calculated data shows the $B_z$ component.

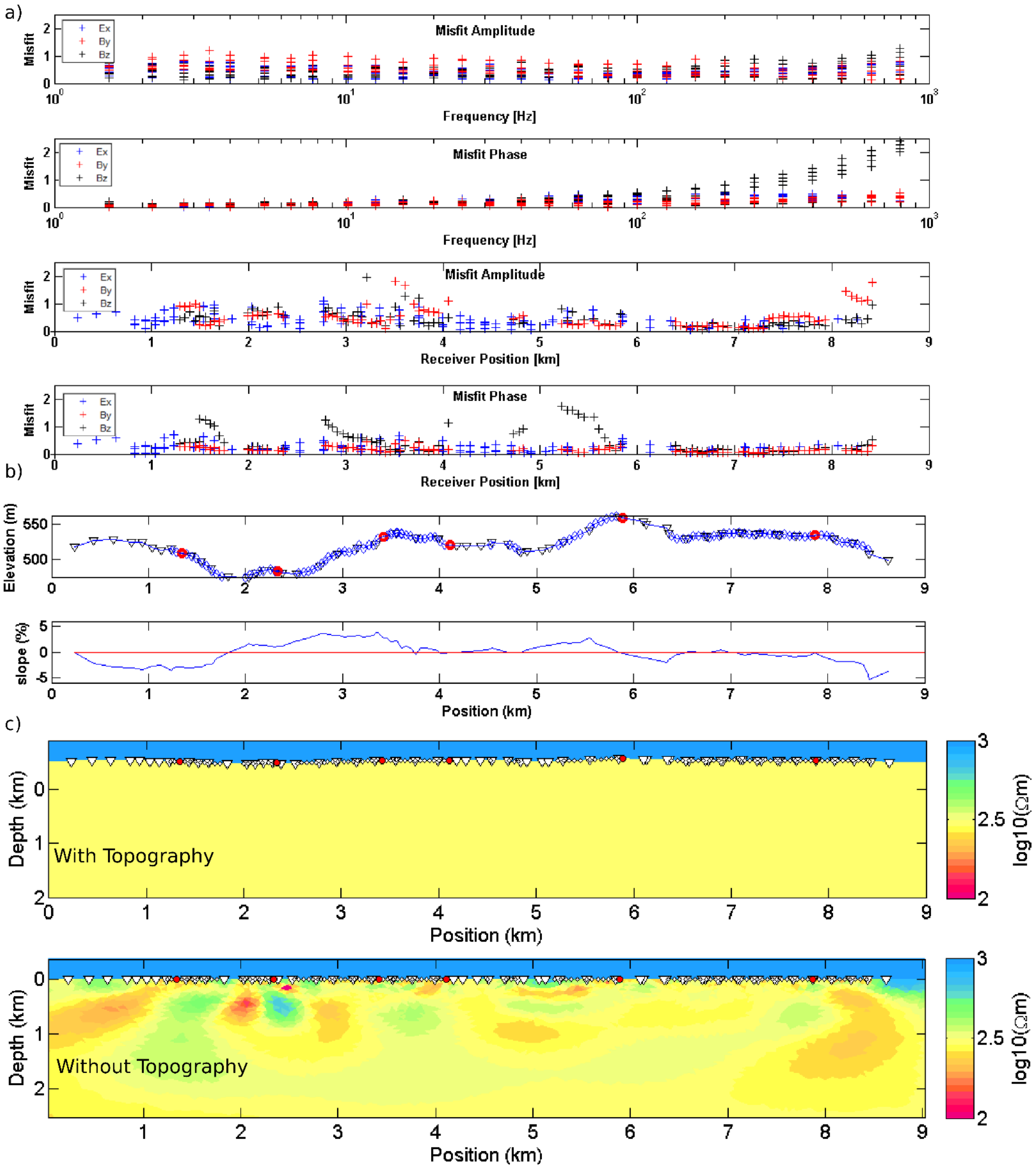

**Figure 8.8.:** a) Relative weighted misfit (assuming 5 % error) averaged over frequency and receiver location respectively for the amplitude and phase of the $E_x$,$B_y$ and $B_z$ component and per transmitter. b) Elevation and slopes around the surface. B-field receiver stations are marked with white diamonds, E-fields with white triangles and transmitters with circles. c) Inversion result utilizing forward calculated data including topography of an inversion model with and without topography. Both models converged to an RMS of 1. Inversion artefacts are present for the inversion model without topography.

Note that for some receiver locations, several receiver stations using multiple transmitters are averaged. Since the sensitivities are the highest under receiver and transmitter location, not only the topography under the receiver but also under the transmitter will influence the result. However, when comparing the frequency-averaged misfit along the profile, regions with the highest misfit correlate weakly with regions with high slopes, i.e. around profile km 1.5, 3, 5-6 for the $B_z$ component. The forward calculated data was then subsequently inverted using a homogeneous halfspace of 100 Ωm and including topography and additionally a homogeneous halfspace of 100 Ωm without topography, assuming a flat surface. Where for the inversion model with topography, the background resistivity of 300 Ωm of the original model could be retrieved, the model without topography exhibits artefacts. The influence is the largest at profile length 1-3 km where relative steep slopes are present. Resistivities here are reaching values between 100 up to 1000 Ωm instead of the 300 Ωm. Note that the artefacts are the strongest in the shallow subsurface up to ≈ 500 m, matching the fact, that the strongest difference is at high to medium frequencies. However, the depth of artefacts can reach up to 1 km, demonstrating, that even for areas with only moderate topography, inclusion of topography in the model is crucial and can produce artefacts not only in the very shallow subsurface.

### 8.2.4. Influence of the Starting Model

As described in Section 3.4, the minimization algorithm can easily get stuck in a local minimum rather than in a global, if the starting model resistivity is strongly deviating from the real model parameters. The impact of the choice of the starting model is depicted in Figure 8.9. The data was forward calculated for block model 1. For subsequent inversion, a starting model a homogeneous halfspace of 1 Ωm and 1000 Ωm is chosen.

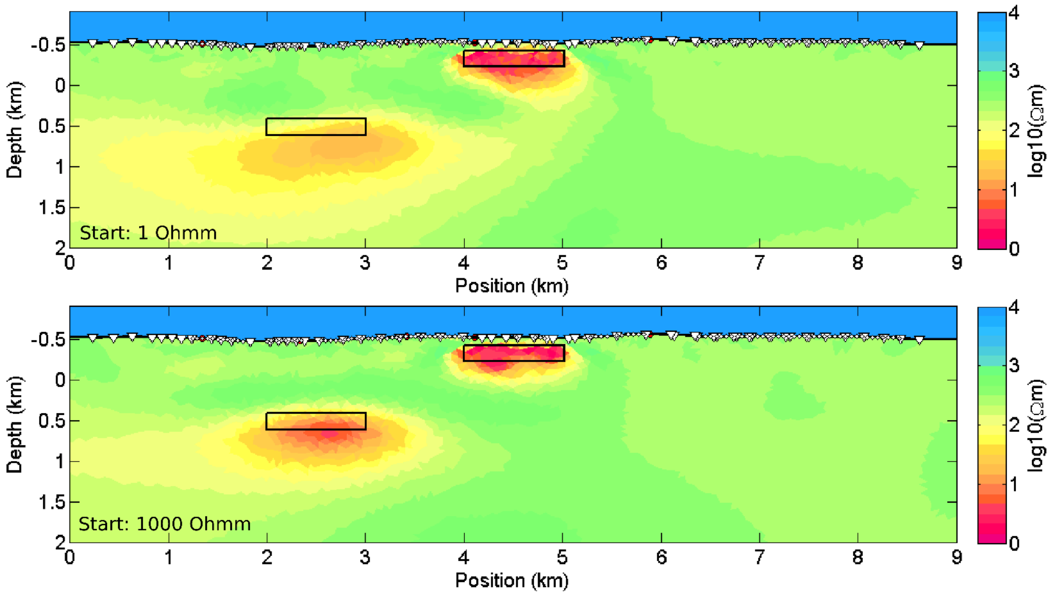

**Figure 8.9.:** Inversion result of forward calculated data from block model 1 for $E_x$ and $B_z$ utilizing different starting models for inversion. Rectangular boxes mark the location of the anomaly. RMS model 1Ωm: 2.2. RMS of model 1000 Ωm: 1.3.

The background resistivities of block model 1 are 300 Ωm, the resistivity of both anomalies 3 Ωm. Both inversion models did not converged to a RMS of 1, but got stuck in a local minimum with a final RMS of 1.3 for the 100 Ωm homogeneous halfspace and 2.2 for a 1000 Ωm homogeneous halfspace as a starting model. Where the background resistivity could be captured well, the resistivity and location of the deeper anomaly at profile km 2-3 was only retrieved poorly for the 1 Ωm starting model, although the starting values are closer to the resistivity of the anomaly. Therefore, for inversion of the real dataset, different starting models should be tested to prevent the convergence to a local minimum rather than to the global minimum. In an ideal case, background resistivities should be retrieved from additional information by geology/geophysics/petrophysics.

### 8.2.5. Influence of Smoothing Parameters

As described in Section 3.4, a horizontal-vertical smoothness factor $\omega_{hv}$ to weight the corresponding roughness penalty can be utilized to favour either smooth horizontal structures for values of $\omega_{hv} > 1$ or smooth vertical structures for values $\omega_{hv} < 1$. To test the influence of the smoothing parameter to the inversion model, a rather high horizontal/vertical smoothing factor of 300 is compared to a rather low $\omega_{hv}$ of 0.3. Figure 8.10 shows the resulting inversion models. For the previous and following synthetic parameter studies a medium value of 3 for $\omega_{hv}$ was utilized, favouring slightly horizontal conductivity structures. A clear influence of the smoothing ration can be observed for the lower anomaly structure, which exhibit due to the larger depth of its location lower sensitivities and is therefore less constrained by the data than the upper anomaly. For the low $\omega_{hv}$ value, the anomaly structure is stretched in the vertical dimension, for the high value the anomaly is stretched in the horizontal dimension. Therefore $\omega_{hv}$ should be fixed based on a priori informations which indicate if e.g. layered structures are expected or dome like vertical structures.

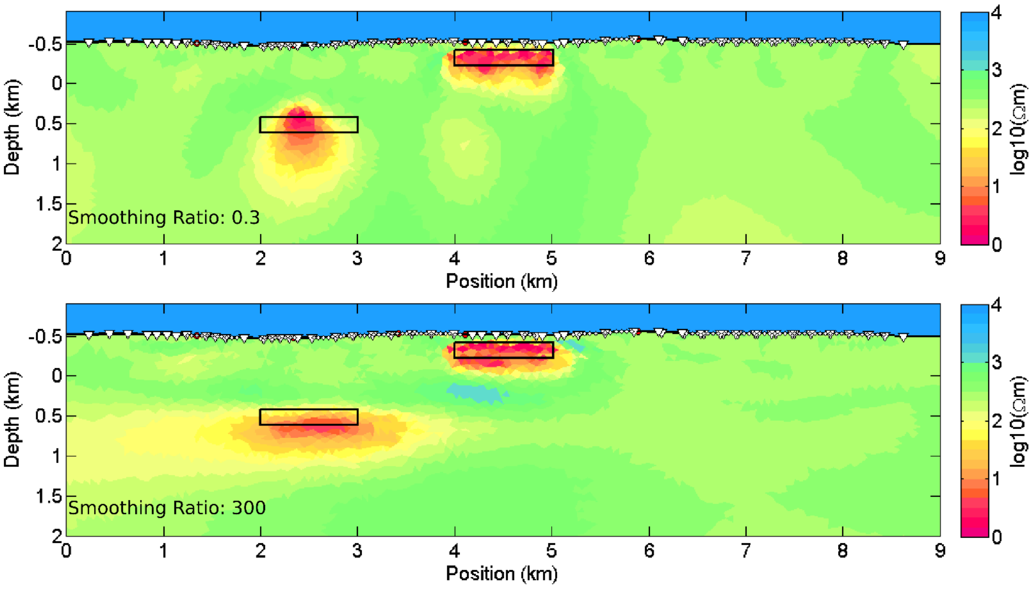

**Figure 8.10.:** Inversion result of forward calculated data for $E_x$ and $B_z$ from block model 1 utilizing a different horizontal to vertical smoothing ratio $\omega_{hv}$ for inversion. The models converged to a final RMS of 1.4 ($\omega_{hv} = 300$) and 1.3 ($\omega_{hv}$=0.3)

### 8.2.6. Resolution of Different Field Components

In the next section, the capability of the EM components resolving a conductive block anomaly in 1 km depth is studied. The block model used for forward calculation of the data consists of a conductive block anomaly with 3 Ωm embedded in an homogeneous halfspace of 300 Ωm with a dimension of 200 m × 1000 m with the upper border located in a depth of 1 km. Prior to inversion, Gaussian error of 5 % was added and a

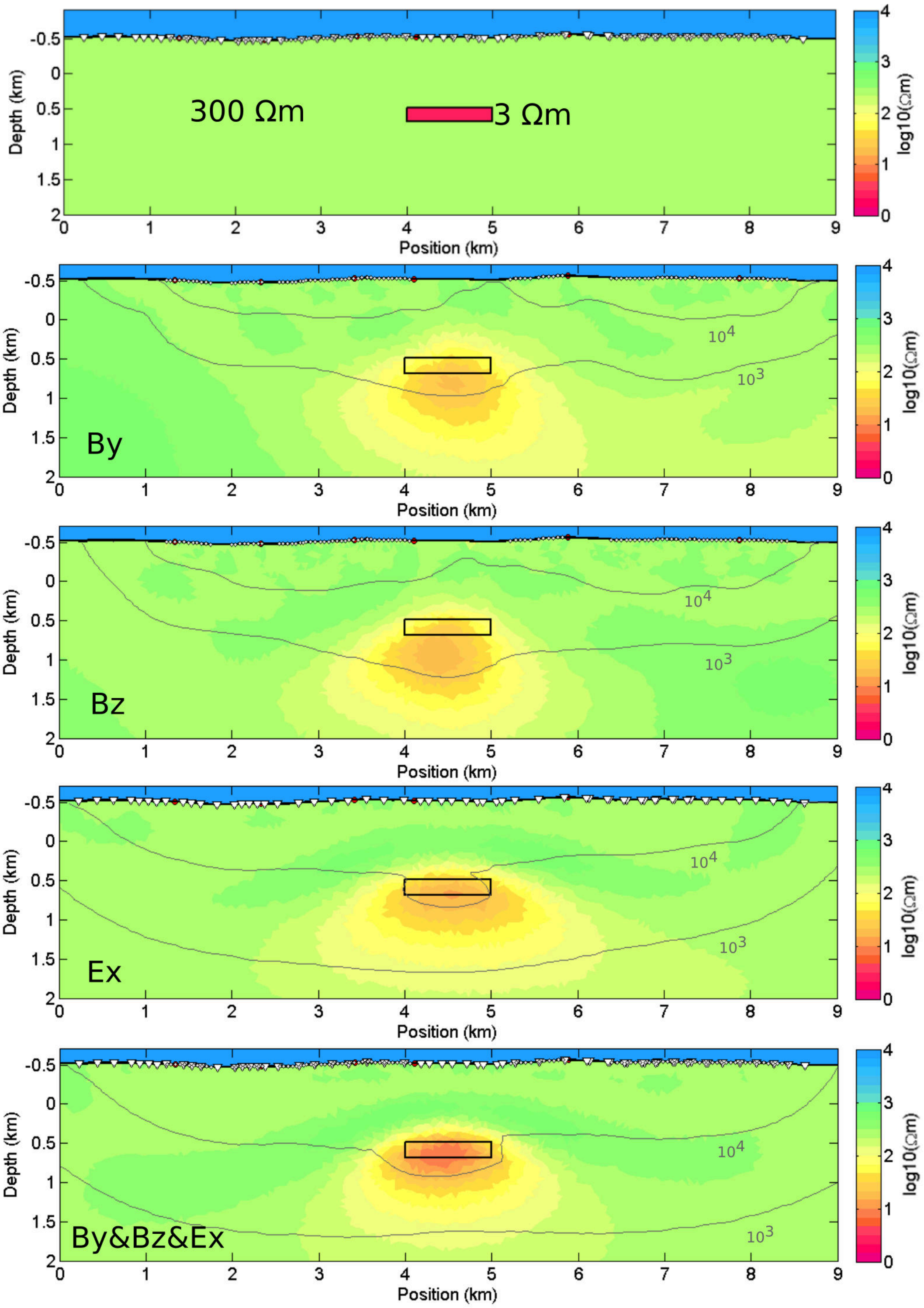

**Figure 8.11.:** Block model 2 and inversion results utilizing different field components. Isolines of $10^4$ and $10^3$ sensitivity. Error floor: 5 % Amplitude and 2.86°. RMS converged to 1 for all inversion models.

corresponding error floors of 5 % and 2.86° was set to the data. Figure 8.11 shows the forward model (block model 2) and the inversion results, utilizing a homogeneous halfspace as a starting model with 100 Ωm electrical resistivity. Sensitivities, here shown as error-weighted sensitivities $\mathbf{J_W}$, are plotted as isolines for sensitivity values of $10^4$ and $10^3$. The sensitivities are summed up over the complete frequency range between 1 Hz and 1 kHz for all components as well as over amplitude and phase. Note, that in order to compare the outcomes of this resolution study later for the inversion of real field data, here, the data geometry of the collected dataset is utilized. Therefore, magnetic field data was calculated at the SQUID receiver stations only (white diamonds) and electric fields only at electric field stations (triangles). For an overview of the transmitter-receiver setup and utilized offsets refer to Figure 6.18.

For the electric field, sensitivities are typical higher in the centre of the profile, since more transmitter combinations cover this area. The electric field component shows values above $10^4$ for the conductivity anomaly. For the $B_z$ and $B_y$ components sensitivities are decreased at profile 4-5 km, due to the lack of magnetic field stations in this area. Note, that the sensitivity for $B_y$ is slightly smaller in the centre than for the $B_z$ component, although the same station distribution is utilized.

While both inversion models underestimate the conductivity amplitude of the anomaly, the shape of the anomaly is better retrieved by the electric field component. As expected, sensitivities are the highest for a combined inversion of all field components jointly and consequently, the shape of the anomaly is retrieved reasonable well, whereas the conductivity of the anomaly is still underestimated. In conclusion, a joint inversion of all components helps to increase the sensitivity of the model towards the conductive anomaly and consequently increases the capabilities to resolve the conductivity structure in 1 km depth. This would hold even more for structures which are not located between profile 4-5 km, where no magnetic field stations are present. Differences in sensitivity and resolution of the block model are therefore not due to differences of the capabilities to resolve resistivity structures between the EM components, but mainly due to differences in the station distribution, amount of stations and field geometry. In addition, to the lack of stations on top of the anomaly, electric fields are setup with an maximal offsets up to approx. 5 km, whereas magnetic field data was only collected within offsets of 2.6 km to the transmitter site. Furthermore, for most electric field stations, several transmitters where utilized. Hence, the maximal exploration depth is higher for electric fields. Comparing the magnetic field components however, the $B_z$ component shows a slightly increased sensitivity at profile 4-5 km compared with the $B_y$ compoment having the same station distribution. This is in accordance with the sensitivity distributions for the individual field components shown in Figure C.3 in the Appendix. For a sensitivity distribution study where the same receiver-transmitter geometry for all components was considered refer to Figure C.4 in the Appendix.

### 8.2.7. Resolution of Resistive Structures

In a next step, the resistivity of the anomaly from block model 2 was changed to a high value of 3000 Ωm compared with its surroundings of 300 Ωm. Data was forward calculated, Gaussian noise of 5 % was added to the dataset and subsequently inverted utilizing a homogeneous halfspace of 100 Ωm. The resulting inversion model is shown in Figure 8.12. The final RMS reached a value of 1, however, the resistive body could not be detected. As expected from an mainly inductive method, the received fields are not sensitive to a small scale resistive structure embedded in a more conductive halfspace. Furthermore, for the utilized broadside geometry, the TE mode dominates and the sensitivity towards resistive structures is decreased compared to an inline configuration. Isolines of sensitivities reflect the low resolution. Where sensitivities in block model 2, assuming a more conductive body, are increased within the location of the anomaly, for a resistive structure, sensitivities are slightly decreased compared with the surrounding area. Sensitivity distribution for the block model shown in Figure 8.12 are displayed in Figure C.2 in the Appendix.

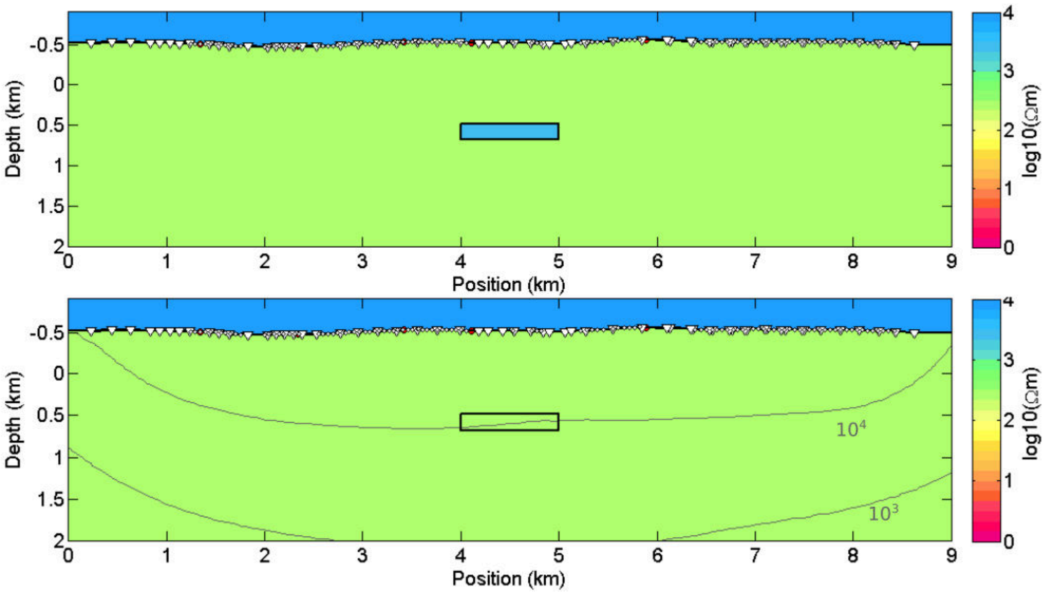

**Figure 8.12.:** Block model 3 used for forward calculation and inversion results. Data was calculated and inverted for all collected field components. Error floor: 5 %. The resistive anomaly could not be resolved. Isolines at $10^4$ and $10^3$.

### 8.2.8. Error Settings

In the following part the influence of different error settings to the resolution of the model structures is studied. Next to the standard error obtained during data processing, different noise sources not considered in the statistical derived standard error must be taken into account: Numerical (approximation) errors, errors due to possible 3D effects and effects which influence the EM response but are not considered in the modelling studies with `MARE2DEM`, e.g. anisotropy and IP. Additional there are geometrical setup errors, i.e. the accuracy of the receiver length and the transmitter length. The offset and the deviation from profile direction and systemic errors due to the receiver data logger and the current clamp for current recording. The standard errors obtained during processing are frequency dependent, but for most offsets and frequencies relative small compared with the influence of the geometrical/geological and systematic errors. IP studies were performed assuming a 1D layered earth in Section 7.3. Relative differences up to several tens of percent for real and imaginary part are obtained. Since inversion of synthetic data showed problems of convergence for the inversion of real and imaginary part, the data and corresponding errors are transformed to log10 amplitude and linear phase. The setting of a frequency independent error floor of 1 % of real and imaginary part would therefore result in an amplitude error of $0.01/\log(10) = 0.0043$ according to Equation 6.17-6.18 and an fixed phase error of $180°/(0.01 \cdot \pi) = 0.5730°$. Note that the phase error was calculated using a constant maximum phase value of 180° and not as percentage of the actual phase value. Therefore the same weighting for small and high phase values is achieved. Figure 8.13

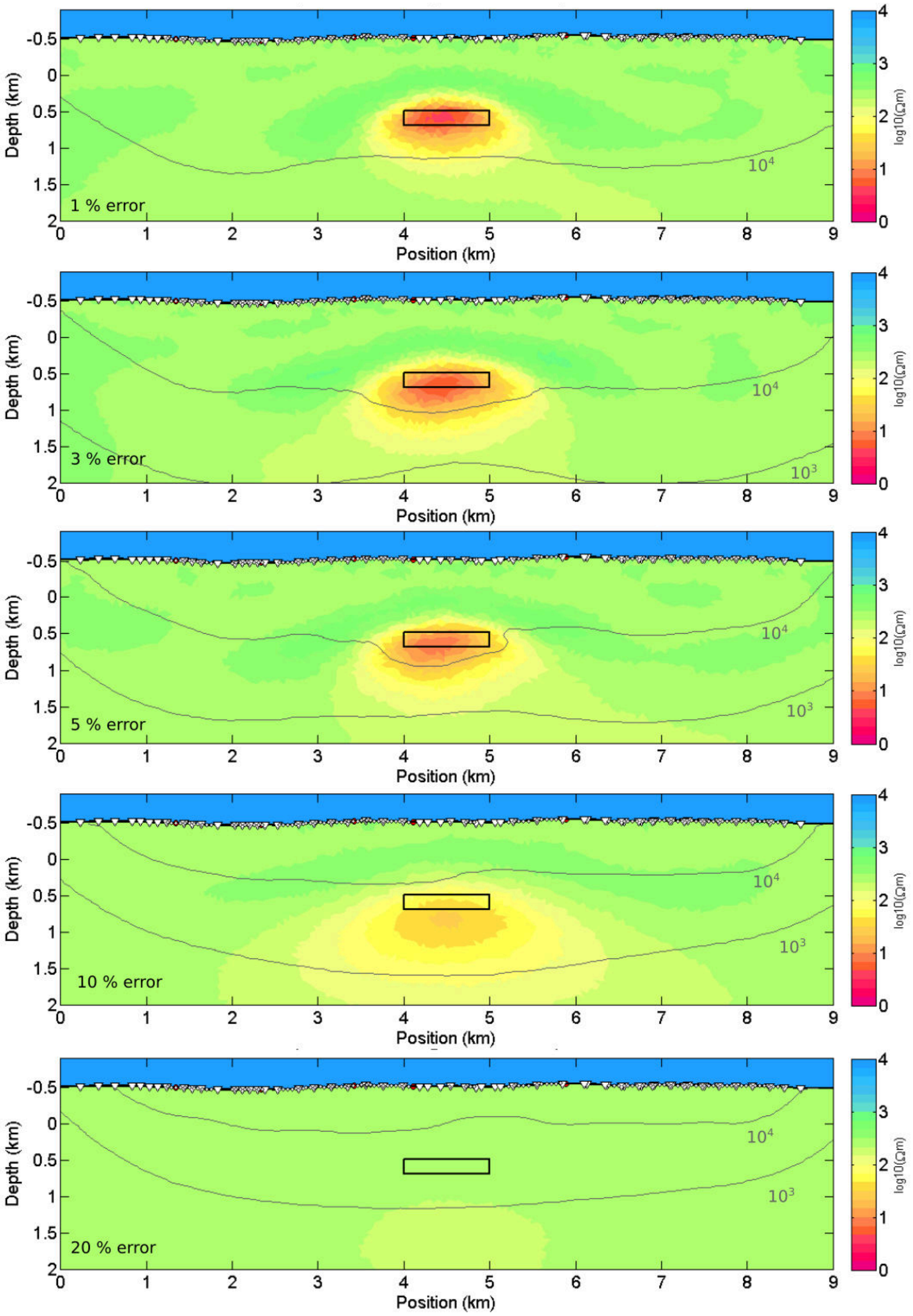

**Figure 8.13.:** Inversion results utilizing different error settings for all collected field components. Isolines of $10^4$ and $10^3$ sensitivity. RMS converged to 1.6 including 1 % error, 1.2 for 3% error and to 1 for higher error levels.

shows the influence of the error level on the resolution of the anomaly and the sensitivity values throughout the inversion model. Errors between 1 % of the amplitude with a corresponding phase error of 0.57° and up to 20 % (11.5°) are set as error floor. Data was forward calculated for the real station distribution utilizing block model 2, calculating the electric $E_x$ component for electric field receivers (triangles) and all magnetic field component for SQUID stations (diamonds). Prior to inversion, Gaussian error in the size of the set error floor was added to the data. Sensitivities are plotted as isolines for values of $10^4$ and $10^3$. For an error level of 1 %, the location and amplitude is well defined and the model shows relative high sensitivities over $10^4$ up to 1.5 km depth. With increasing error level, the error-weighted sensitivity gets smaller and the the amplitude and form of the anomaly is less well retrieved. For an error level of 20 %, neither the location nor the amplitude of the anomaly can be resolved. Note that the resolution of an anomaly depends on the absolute conductivity, the conductivity contrast to surrounding material, the size and the depth. E.g. a high conductive anomaly embedded in a strongly resistive host rock with a large horizontal and vertical extension might still be partly resolved, whereas a small scale conductivity structure in a more shallow subsurface cannot be retrieved. Therefore it is difficult to define a certain threshold, at which an anomaly is either resolved, or not resolved below. However, one can analyse the sensitivity distribution throughout the model and can define regions and bodies with high and low resolution and quantify the influence of the structures at certain depths/locations to the model response. The location and amplitude of the anomaly can be reasonable well detected up to errors of 5 % of the amplitude and phase, showing sensitivities above $10^4$ for the model parameters located at the anomaly.

### 8.2.9. Inversion of Imaginary and Real Part

For CSEM data, `MARE2DEM` allows either the inversion of real and imaginary part as linear values or the inversion of data transformed to amplitude and phase in either linear or log space. Therefore, synthetic data was forward calculated and subsequently inverted for both data types, real and imaginary part (cp. Figure 8.14) and log amplitude and phase respectively for the block model given in Figure 8.11. The block model structure is reasonably well resolved, delivering a comparable result to the inversion of data in terms of amplitude and phase (cp. Figure 8.11). The same relative error floor of 5 % was set for all types of data transformation. However considering that sign reversals can occur in both, real and imaginary part, the error was increased to 100 % for data points around the sign reversal. Considering the noise level in the area, an error floor of $10^{-12}$ [V/Am$^2$] was set.

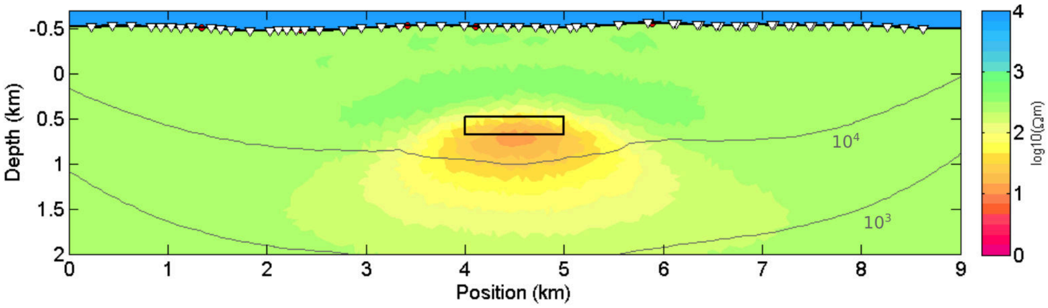

**Figure 8.14.:** Inversion result utilizing electric field data as real and imaginary part. Additionally the sensitivity isolines for $10^3$ and $10^4$ is shown. The global RMS converged to 1.

The global misfit decreased to 1. Figure 8.15 gives an insight about sensitivity distribution for all data representations. While the sensitivity of amplitude, phase and real part exhibit similar sensitivity values as well as a similar distribution throughout the model, the imaginary part shows increased values. As showed in Equation 2.34, the imaginary part is zero in the near zone of the transmitter considering a homogeneous halfspace, whereas the real part scales offset dependent with the background resistivity. Amplitudes of imaginary part for high frequencies are therefore significantly lower compared with the real part.

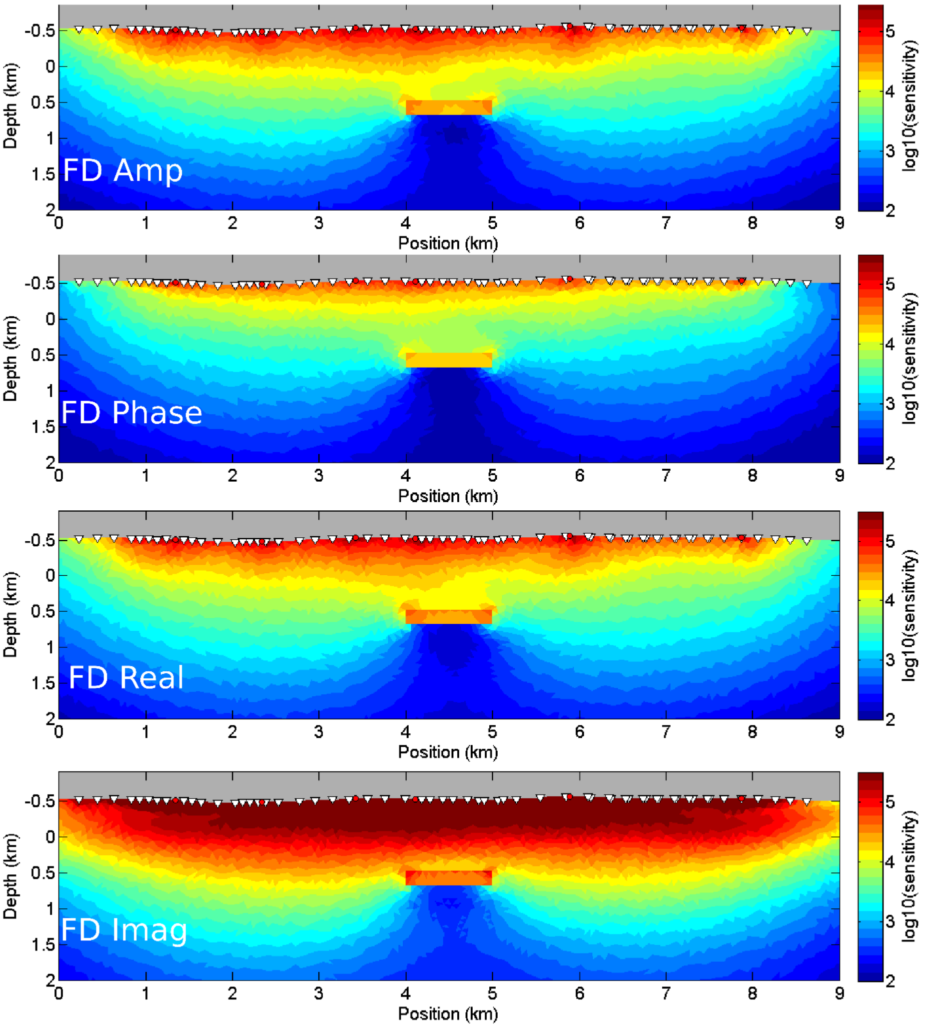

**Figure 8.15.:** Error weighted sensitivities for amplitude and phase, as well as real and imaginary part in frequency domain for the electric field component utilizing real station distribution.

If one considers relative error floors to real and imaginary part independently, and a small absolute error level, the imaginary part exhibits increased sensitivities compared to the real part. Note that real part data typically exhibits larger values than imaginary part data, and therefore amplitude and phase are mainly driven by the sensitivities of the real valued dataset. Therefore, the sensitivity distribution of the transformed values is similar to that of the real part. However, sensitivities of the imaginary part are mainly increased for the shallow subsurface, and the conductivity anomaly is not significantly better resolved than for the inversion of amplitude and phase values. Wheelock et al.

(2015) found, that convergence during inversion is in general improved, if log amplitude and phase are inverted. Furthermore, inversion of data in terms of real and imaginary part failed for the obtained field dataset. For future application, an implementation of an arsinh transformation for real and imaginary part data could possibly improve the convergence during inversion, especially if sign reversals are present in the dataset.

### 8.2.10. Synthetic Tests in Time Domain

Recently, a time domain approach was implemented in `MARE2DEM` by Haroon et al. (2018). In order to retrieve the time domain solution, the frequency domain response is transformed into time domain utilizing a sine or cosine transformation as described in Section 2.3.4, Equations 2.37-2.38. Filter coefficients for the computation of the integrals were taken from Anderson (1975). For transient switch on data, the sine-transformation of the real part is used (Li, 2010). Due to computational reasons (Newman et al., 1986), the step off response is calculated over a cosine transformation of the imaginary part (Eq.2.37) instead of a subsequent calculation of the step off response by subtracting the step on response from the DC response. In order to calculate the integrals given in Equation 2.37 and 2.38, a large number of frequencies is needed. For example for the calculation of 40 time points spanning 4 decades of time, 119 frequencies are calculated. Therefore, the computation of the time domain response is computationally costly compared to the calculation of a frequency domain response. In order to facilitate the fit of sign reversals when inverting step off data, next to the inversion of linear data, an asinh transformation (cp. Section 3.8) of the dataset was implemented.

### 8.2.11. Validation of the TD Response

Since the time domain algorithm was not tested for land based applications before, a comparison with the 1D forward solution of the CSEM time domain implementation of `MARTIN` was carried out utilizing the same 3-layer model used for the validation in frequency domain (cp. Figure 8.3). Wave numbers were ranging from $10^{-6}$ to $10^{2}$ $\text{m}^{-1}$ with a total number of 90 values. The transmitter dipole was discretized in nine segments and the forward response is calculated as summation of single point dipole responses according to Equation 8.17. The calculated data of a time domain step on electric field response are compared to the solution of the 1D algorithm `MARTIN`. The modelled time points ranging between $10^{-4}$ s and 1 s at 41 logarithmically distributed discrete values, which were transformed into 120 frequencies for forward calculation. Since field data was only available for the electrical component, only the solution of the electric field is validated.

The electrical step on response is calculated via a sine transformation of the frequency domain real part response (cp. Eq. 2.38). Therefore, a similar behaviour as demonstrated in Section 8.2.1 is expected regarding the accuracy of the response. The deviations between the 2D and 1D algorithm are below 1 % for offsets of 200 m and larger (Figure 8.16). This leads to the conclusion, that the calculated forward response for an extended transmitter is applicable for the LOTEM survey regarding the high resistive environment, the time range and utilized offsets, if the superposition of point dipoles is calculated according to Equation 8.17.

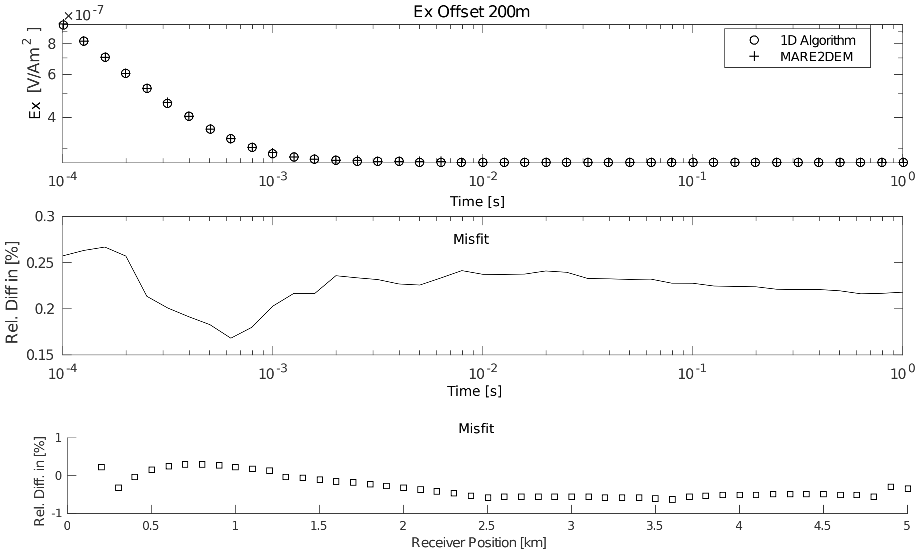

**Figure 8.16.:** Validation of the extended dipole response along the profile for the summation algorithm (MARE2DEM) in TD compared with the 1D solution of `MARTIN`. Upper Panel: $E_x$ response at an offset of 200 m and relative difference to `MARTIN` over time. Lower Panel: Relative difference to `MARTIN` along the Profile.

## 8.2.12. Sensitivities in TD and FD

In order to evaluate the sensitivities of frequency and time domain data for a conductive anomaly and the homogeneous halfspace surrounding the structure, a forward and sensitivity calculation was carried out for block model 2 in both domains. Figure 8.17 shows the comparison of sensitivities for frequency domain amplitude and phase data as well as time domain switch on and switch off data. Since the sensitivities were calculated utilizing a log transformation for frequency domain amplitude data and an arsinh transformation for time domain data, for comparison the error-weighted sensitivities $\mathbf{J_W}$ are displayed. Note, that therefore the Jacobian matrix $\mathbf{J}$ needs to be multiplied by the corresponding weighting factor $\mathbf{W}$ in the correct transformation space, as given in Section 3.8. Errors for all cases were set to 5 % relative error for FD amplitude and TD data, for phases 5 % error of the maximum value. In addition, an absolute time independent minimum error of $10^{-12}$ V/Am$^2$ was applied to the data, based on the measured noise levels in the survey area as discussed in Section 6.1.6. Note, that this mainly downweights the switch off data, since switch off transients for most stations decrease to low values below $10^{-12}$ V/Am$^2$ for late times.

The error-weighted sensitivities for frequency domain amplitude and phase and time domain switch on data only show small scale differences. The overall amplitude and structural behaviour is the same. The similar behaviour of electric field switch on data compared with the real part (cp. Figure 8.17) or the amplitude of frequency domain data are in accordance with the findings of Section 2.3.4. Sensitivities are larger in the centre of the profile and are decreasing at the corners of the profile and with depth. The conductive block structure in the centre exhibits increased sensitivity values. Below the conductive structure, sensitivities are decreased. This can be explained by a shielding effect due to current channelling of the overlying conductive structure. Time domain switch off data shows an overall similar behaviour. Sensitivities are decreasing when going downwards

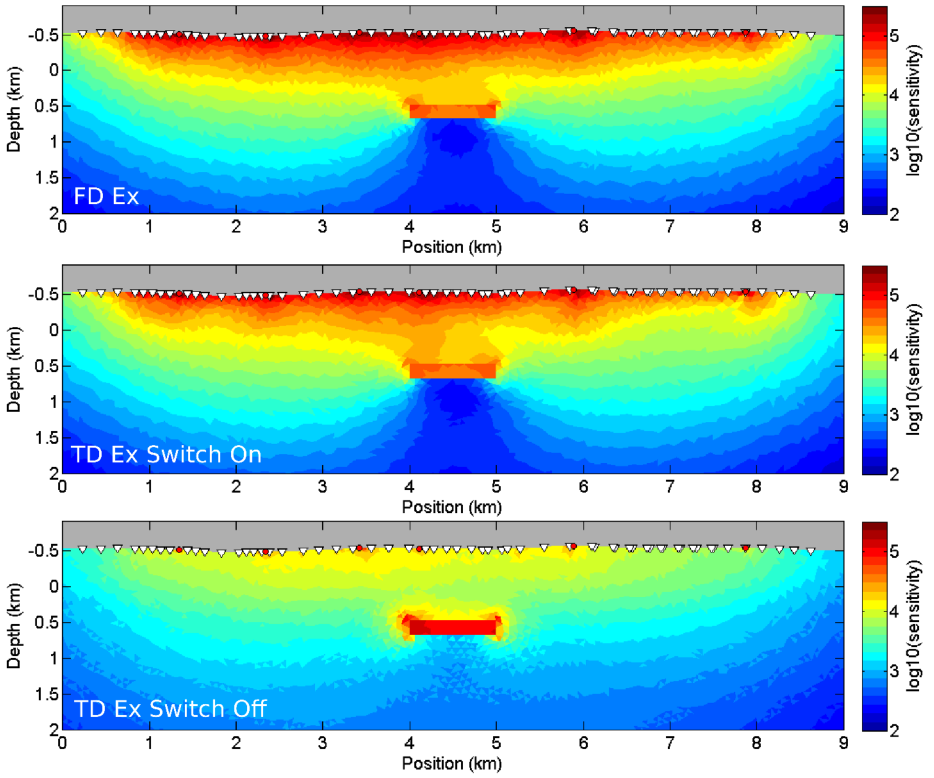

**Figure 8.17.:** Error weighted sensitivities for summed up amplitude and phase in FD, as well as TD switch on and switch off sensitivities for the electric field component.

and outwards, whereas the conductivity structure in the centre shows increased sensitivity values. When comparing TD switch off sensitivities with FD and TD switch on sensitivities, several differences are evident: The overall sensitivity amplitude towards the halfspace is lower. However the conductive structure itself exhibits a sensitivity which is more than half a decade higher than for frequency domain and time domain switch on data. These findings are in accordance to Section 2.3.5. Considering the near field approximation of TD Switch off data, the fields consist only out of an inductive term, which is somewhat similar to the vortex term for real and imaginary part frequency domain data: Switch on data exhibits the same inductive term, but similar to the real part data in FD (and therefore also data in amplitude and phase representation), is superimposed by an additionally DC term. Therefore those components exhibit higher sensitivities to the surrounding halfspace. In conclusion, for the detection of a deep conductive anomaly however, time domain switch off data is more suitable. When studying sensitivities with respect to a relative error, the inductive response is downweighted, in FD and TD switch on data, since the primary field or DC level respectively can be several amplitudes higher. For time domain switch off data, the response is purely inductive. The sensitivities are therefore lower for the halfspace, the conductive body on the other hand exhibits a strong relative inductive response and exhibits therefore high sensitivities.

In a next step, the forward calculated data was inverted, using a homogeneous halfspace of 100 Ωm as a starting model and Gaussian noise was added. Figure 8.18 shows the inversion results for all three data types, including sensitivity isolines for $10^4$ and $10^3$. The resolution of the conductivity anomaly can be well explained by the discussed sensitivity

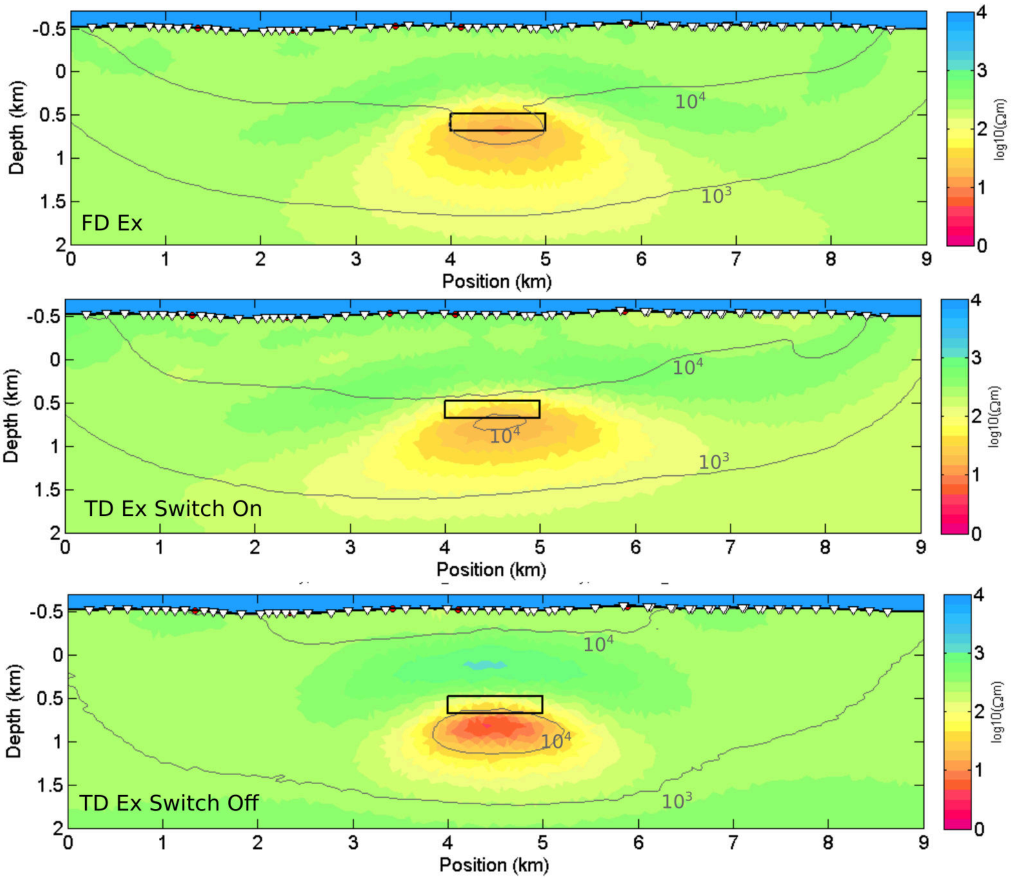

**Figure 8.18.:** Comparison of inversion model and sensitivities of the electric field for frequency domain amplitude and phase and time domain switch on and switch off data respectively. Input in inversion: Forward calculated data based on block model 2. For each dataset a relative error floor of 5 % was set for inversion and Gaussian noise of 5 % was added. Plotted are the isoline of error weighted sensitivity for $10^4$ and $10^3$.

distribution. FD and TD switch on data exhibit a similarly resolved body. A conductive anomaly is visible, however the borders of the structure and the conductivity value are poorly resolved. Especially the lower border of the anomaly is not resolved. For switch off data, both amplitude and borders of the anomaly are reasonable well resolved. Therefore, when the target is the resolution of a deep, high conductive anomaly, TD switch off data is favourable over TD switch on and FD amplitude and phase data, if similar relative error levels are considered.

## 8.3. Summary

Two dimensional studies were conducted in order to study parameters which might affect or hinder the inversion of the field dataset. Additionally resolution studies are carried out for different components, showing which types of resistivity anomaly can be resolved and if certain components or data transform in either time or frequency domain are beneficial to resolve a high conductive structure.

In a first step, the `MARE2DEM` solution was validated against a 1D algorithm. Where the response of point dipoles are calculated sufficiently accurate, the solution for an extended dipole differed for short offsets depending on the integration type used to approximate the transmitter. However, a summation over the response of nine dipoles located in the centre of each segment showed misfits below 1 % and proved to be accurate enough for all offsets and the complete frequency (and time) range.

Since the mesh during forward calculation is defined via an automatically mesh refinement, only the inversion mesh must be defined beforehand and the triangle size should be a trade off between the smallest structure which is resolvable given the utilized frequency range, depth and calculation time. Therefore, a nested grid should be generated, having small triangle size in areas with high sensitivity, i.e. in shallow areas along the profile and an increased triangle size for outer regions. Topography should be considered in any case, because even for only small slopes, as present in the survey area, effects of topography can produce artefacts with in either higher or lower conductivity during inversion.

Frequency domain data can be transformed in phase and amplitude respectively. Sensitivities of the imaginary part are higher compared to the sensitivities of amplitude, phase and real part. Since the imaginary part exhibits typically smaller amplitudes than the real part, a transformation to amplitude and phase will lead to a downweighting of it. Hence, the overall sensitivities are decreased. However amplitudes and phases do not exhibit sign reversals and showed a better convergence behaviour in the resolution study. Additionally amplitudes can be transformed into log space, which increases the stability of the inversion. Therefore, if the inversion of real and imaginary field data does not converge sufficiently, an inversion of phase and amplitude might converge. The implementation of an arsinh transformation for real and imaginary part might improve the convergence properties and should be considered in the future.

In a next step the influence of smoothing constraints to the inversion results is studied. If one expects a strong layering, a rather high horizontal to vertical smoothing ratio should be applied, for dyke structure anomalies a low ratio. However, since we expect a more anticline structure with alternating dipping angles throughout the profile, a rather even adjusted smoothing ratio between 1-3 should be selected. Additionally if the resistivities of the starting model is too far from the true background resistivity, the inversion algorithm might get stuck in a local minima. Therefore a priori information should be taken into account for inversion. Best, different starting models should be tested for the real dataset. Another factor which influences the resolution of structures are the data errors. Since in the survey area several effects which are not accounted for can influence the EM response, e.g. anisotropy and induced polarization effects as well as three dimensional effects, it is reasonable to set an error floor in order to account for this error sources. However consequentially, the resolution capabilities are strongly decreasing, if a high error floor is applied. E.g. the studied block structured high conductivity anomaly introduced in the block model study can be resolved up to an error floor of 3-5 % reasonable well, exhibiting sensitivities above $10^4$ in the area of the anomaly. Assuming an error of 20 % to both amplitude and phase, both location and conductivity of the anomaly could not be retrieved.

CSEM being an inductive method, resistive anomalies exhibit low sensitivities and cannot be detected. Where information of the background resistivity can be well retrieved by studying e.g. frequency domain electric field data or time domain electrical step on data, small scale resistive anomaly structures are practically invisible to EM fields. All modelled EM components exhibit increased sensitivities for conductive structures. However when comparing time domain step on, step off and frequency domain electrical data, the time domain step off response is clearly superior in order to resolve the high conductive anomaly. On the other hand, since step off data does not contain information of the DC level in the near field of the transmitter, the sensitivity towards the background resistivity is decreased compared with frequency domain or step on electric field data.

# CHAPTER 9

# 2D Inversion of Field Data

As demonstrated in Chapter 7, 1D inversion models of LOTEM data as well as inversion models from geophysical pre-investigations (e.g. airborne electromagnetics, Figure 4.3) indicate a multidimensional resistivity distribution. Therefore, the frequency domain 2D inversion algorithm `MARE2DEM` is applied to the acquired dataset. The aim is the derivation of an independent subsurface model, which explains B-field (SQUID) data as well as E-field data collected along the transect for all receiver-transmitter setups jointly. Recently, a time domain approach was implemented in `MARE2DEM` by Haroon et al. (2018), which allows the inversion of the electric LOTEM field dataset in time domain. However, for the derivation of the final CSEM validation model, inversion was performed in frequency domain, since a joint interpretation of the large scale frequency domain SQUID dataset and the electric field dataset improves resolution capabilities of the model. Hence, the focus in this chapter is on the inversion of the dataset in frequency domain.

## 9.1. 2D Inversion of Field Data in FD

Parameters for the introduced inversion models are derived from the modelling study presented in Section 8. A horizontal to vertical smoothness factor $\omega_{hv}$ of 3 was taken for all presented inversions. In order to accelerate the inversion procedure, but simultaneously keeping the inversion grid fine enough to reproduce shallow structures on a smaller scale, different triangle sizes were utilized for the inner and outer part of the mesh (cp. Section 8.2.2). Since the overall aim is the derivation of an independent inversion model, the influence of a priori information is kept small. Therefore, a homogeneous halfspace is taken as starting model. Different starting resistivities were tested, however a value of 300 $\Omega$m led to the fastest convergence during inversion. In order to include bipole effects due to the extended transmitter, the solution was calculated for 9 point dipoles distributed along the transmitter line. The topography was obtained by GPS data and implemented in the model. Therefore, the depth axis of the obtained models refers to the absolute altitude.

The dataset was inverted as amplitude and phase, since it showed an accelerated convergence behaviour compared with the inversion of real and imaginary part. In addition, the latter exhibited problems during convergence due to sign reversals. In order to speed up the inversion process, frequencies and corresponding amplitudes and phases measured for different base frequencies were interpolated to one common logarithmically spaced array containing 10 values per decade. Standard errors derived during processing for the dataset were small (cp. Section B in the Appendix). However, in order to take errors from numerous additional sources into account, e.g. errors due to possible 3D effects, anisotropy, IP, or geometrical errors, a relative data floor was defined. An additional absolute error floor of $10^{-12}$ V/Am$^2$ was set, however amplitudes were well above the error floor. If not stated otherwise, an error floor of 5 % was assigned to the amplitude and a constant error of 2° to the phase. Since small timing errors affect the highest frequencies, frequencies above 1 kHz were excluded from inversion. In the following, sensitivity isolines correspond to error-weighted sensitivities, summed over all frequencies or times respectively and normalized to the area of the model cell (Eq. 8.8). Note that the term RMS applies to the error weighted RMS, as given in Equation 3.8.

### 9.1.1. Single Component Inversion

Before a joint inversion of electric and magnetic field data is performed, the inversion models of individual field components are introduced and the resolution capabilities of each dataset is illuminated by evaluating the sensitivity distribution along the profile and over depth. Figure 9.1 shows the inversion results for the field components $E_x$, $B_y$ and $B_z$ individually. The $B_x$ component will be discussed separately. Data fit for the inversion of individual components is reasonable well for both amplitude and phase (cp. Table 9.1), however the phase exhibits a better data fit. The electric field component exhibits with an RMS of 3.89 the highest misfit. Both magnetic field components are well fitted with an RMS of 1.64 ($B_y$) and 1.34 ($B_z$). The misfit along the profile is given for one selected frequency in Figure 9.2 for each component. Furthermore, data and fit for two selected stations for both, electric and magnetic fields, with their locations marked in Figure 9.1 are displayed.

Obtained magnetic field inversion models exhibit a decreased sensitivity compared with the sensitivities of the $E_x$ inversion model. For the inversion of the magnetic field data measured with the SQUID magnetometer, the same station distribution was utilized for each component. In total 5220 data points were inverted for each model. Due to the poor accessibility around profile 4-5 km, no SQUID data was acquired in this segment. This results in a low sensitivity in this region and the extension of the prominent conductive anomaly is poorly resolved. The sensitivity isolines in all three individual models follow the conductivity distribution. Where sensitivities towards resistive structures are low, e.g. for the $B_y$ component in the region between profile 0-3 km, sensitivities towards conductors are high, if the receiver-transmitter geometry covers the area. Sensitivities directly beneath conductive structures are decreased. When comparing shallow structures in the upper 350 m with high sensitivities (cp. Figure 9.3), magnetic field components show an overall similar resistivity distribution.

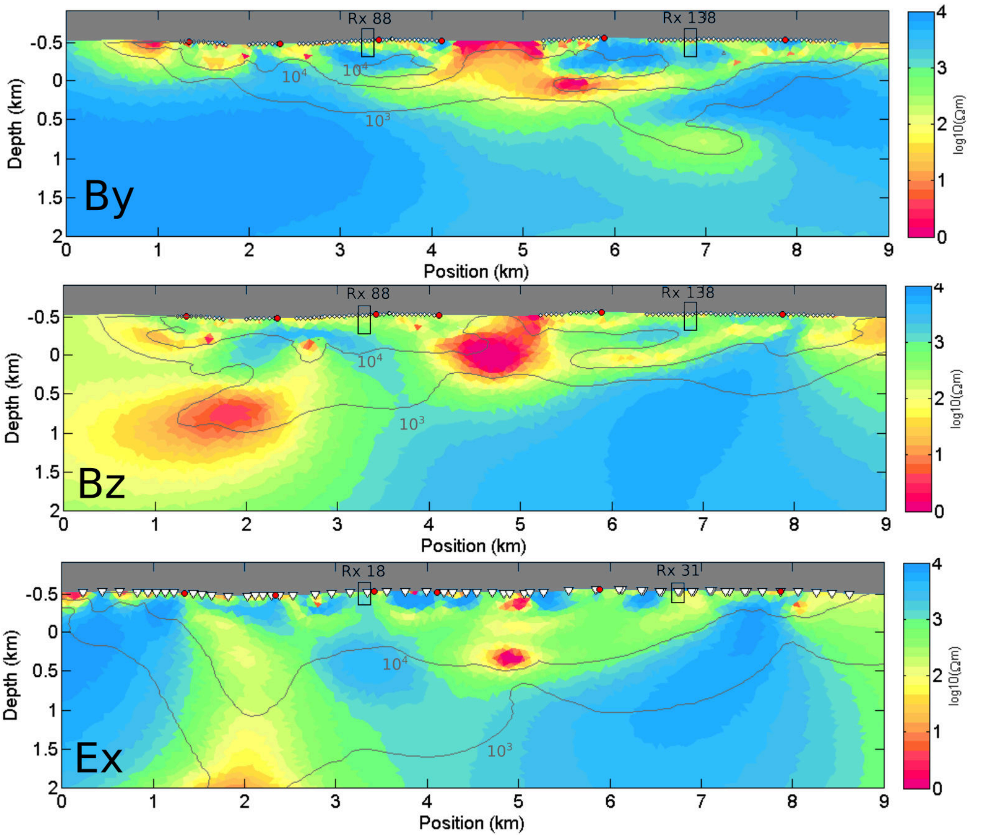

**Figure 9.1.:** Individual inversion results of $B_y$, $B_z$ and $E_x$. As starting model, a homogeneous halfspace of 300 Ωm was used. Grey lines mark the isolines of error weighted sensitivities of $10^4$ and $10^3$.

Considering deep structures, the most prominent difference between the inversion model utilizing $B_y$ and $B_z$ is the high conductive anomaly present in the inversion model of $B_z$ with its center located 1.5 km below the surface at profile 1.5-2 kilometre. For the $B_y$ component, resistivities range in the order of several thousand Ωm in this region. Although overall sensitivities are low at depth for the $B_y$ component, a forward modelling study for the $B_y$ component adding a conductive structure derived from the inversion results of $B_z$ (cp. Figure D.1 in the Appendix) led to an overall misfit increase from 1.64 to 1.94.

**Table 9.1.:** Misfit between modelled and observed data for the $B_x$, $B_y$, $B_z$ and $E_x$. The first column lists, which inversion model from which component was used for the forward calculation. Column 2-5 list the error weighted RMS for each component separately: Amplitude | Phase | Total.

| Model | $B_x$-Comp | $E_x$-Comp | $B_y$-Comp | $B_z$-Comp |
|---|---|---|---|---|
| $E_x$ | 69.8; 31.4; **54.1** | 4.63; 2.98; **3.89** | 5.47; 4.34; **4.94** | 8.51; 9.00; **8.76** |
| $B_y$ | 72.6; 28.6; **55.2** | 24.5; 9.19; **18.5** | 1.88; 1.35; **1.64** | 10.4; 10.1; **10.2** |
| $B_z$ | 63.3; 31.8; **50.1** | 13.7; 6.51; **10.7** | 5.17; 3.08; **4.25** | 1.47; 1.19; **1.34** |

In addition, misfits for each component towards each obtained inversion model can be studied. Table 9.1 gives information about the error weighted RMS for each component and each obtained inversion model for amplitude, phase and the total RMS of both amplitude and phase. Not only the RMS for the corresponding inversion model for each component is given, but also the misfit for forward calculated data from the models

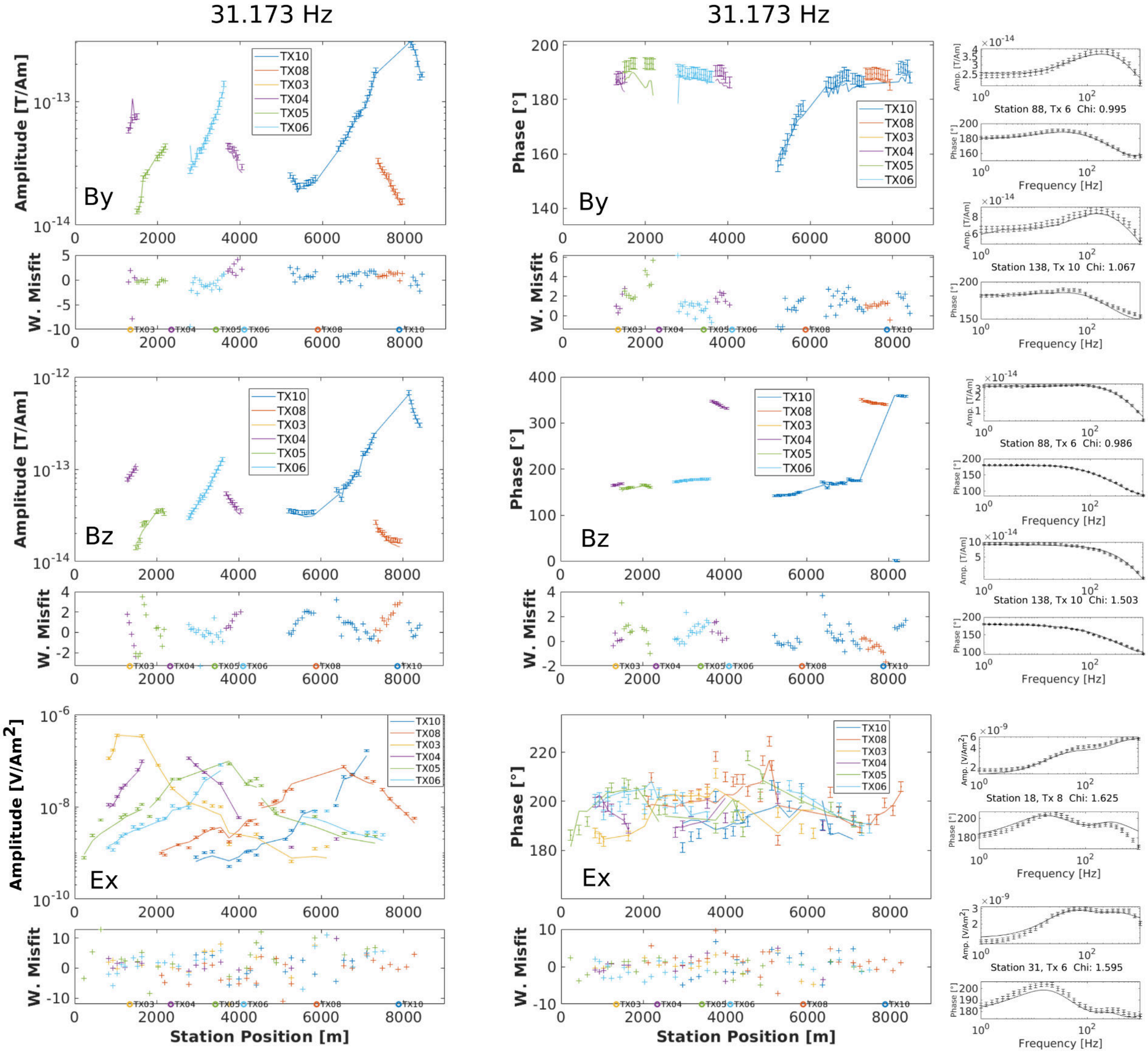

**Figure 9.2.:** Measured data (points), calculated data (lines) and misfit for the inversion results shown in Figure 9.1 for one frequency at 32 Hz for all three components. Measured data and calculated data are shown for two exemplary stations for each inversion model. The location of the exemplary stations along the profile is marked in Figure 9.1. Location of the transmitters are indicated with circles along the x-axis.

obtained by inversion of the other components. For example, the inversion of $B_y$ data converged to a total misfit of 1.64 for the final inversion model. The model obtained by the inversion of the $E_x$ component could fit the $B_y$ dataset with a RMS of 4.94 and the inversion model of the $B_y$ component with a RMS of 4.25. It is evident, that inversion models from the other components can not fit the data sufficiently. This holds for all three components.

The inversion for the electric field component converged to a total RMS of 3.89 and exhibits therefore a slightly decreased data fit compared to the SQUID dataset. An electric field dataset of 7140 data points was utilized. For the $E_x$ dataset, larger offsets are included, most stations exhibited data from different offsets and stations are also located between profile 4-5 km. This leads to higher sensitivities, particular in the centre of the profile and for higher depth as discussed in Section 8.2.6. In addition, stations exist be-

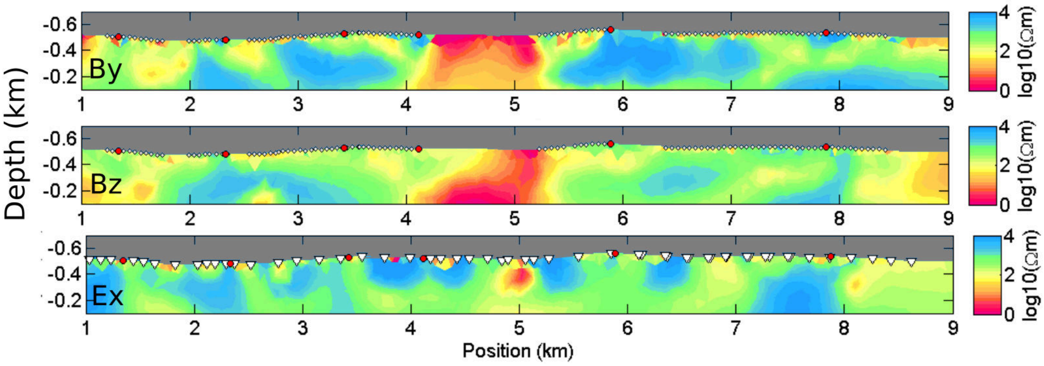

**Figure 9.3.:** Inversion results utilizing the $B_y$, $B_z$ and $E_x$ component for the upper 400 m. For the comparison of the shallow subsurface, triangles were interpolated.

tween profile 0-1 km , whereas in this region no SQUID data exists. Here, structures are poorly resolved by the SQUID dataset and the model parameters are mainly driven by the smoothness constraints, the models differ. This results in the highest misfit of the forward calculated data for the electric field component based on the inversion models obtained by $B_y$ and $B_z$. Misfits listed in Table 9.1 show, that differences in amplitude are higher than in phase utilizing different inversion models for forward calculation. In order to benefit from the better fit of phase data when comparing models from different components, influence of phases are upweighted in the subsequent joint inversion of all components.

### 9.1.2. The $B_x$ Component

An inversion of the $B_x$ dataset did not converge. Where overall data quality was high for the obtained transfer functions (cp. Appendix B), the dataset could not be explained by a 2D subsurface. Figure 9.4 shows the dataset along the profile for one exemplary frequency. The measured $B_x$ component exhibits amplitudes in the range of $10^{-14}$ T/Am. In order to understand which errors might have an high impact on the $B_x$ component, a modelling study was carried out. The impact of deviations of the receiver positions from the profile line is investigated and rotational errors due to misaligned sensors are studied. Measured and calculated data are compared in Figure 9.4.

The red lines in the upper panel of Figure 9.4 indicates forward calculated data based on the $B_z$ inversion model, assuming that receivers are centred in the middle of the transmitter line. Note, that the response is close to zero, which is in accordance with Section 2.3. Deviations can occur due to the finite element approximation utilized in `MARE2DEM`. The black lines in the upper panel of Figure 9.4 denote the forward response calculated for the real survey geometry for the $B_x$ component for the $B_z$ inversion model. The receiver positions of the magnetic field components are depicted in the lower panel of Figure 9.4. Field strengths are correlating with the deviation of the receiver position from the 0-level of the x-axis. However, calculated misfits are still high between calculated and the measured dataset. The total RMS of measured $B_x$ data towards calculated data from inversion models of the other components is given in Table 9.1.

In order to estimate errors due to sensor misalignment, a forward calculation assuming rotated field sensors was conducted. In the upper panel of Figure 9.4, the blue lines denote the forward calculation of inversion model $B_z$ for the $B_x$ component assuming a rotational error of 15°. Misfit between measured and calculated data is significantly decreased. Amplitudes are in a similar range as the measured dataset, however for some parts along the profile, amplitudes are overestimated and for other parts underestimated. A single rotational constant can not be found, which fits the dataset along the profile. A fixed misalignment of sensors during measurements is therefore unlikely. Arbitrary setup errors of the sensors would result in arbitrary errors for each station and are therefore implausible, since obtained data along the profile is rather smoothly varying from station to station. The increased amplitude of $B_x$ is therefore a strong indication for 3D effects.

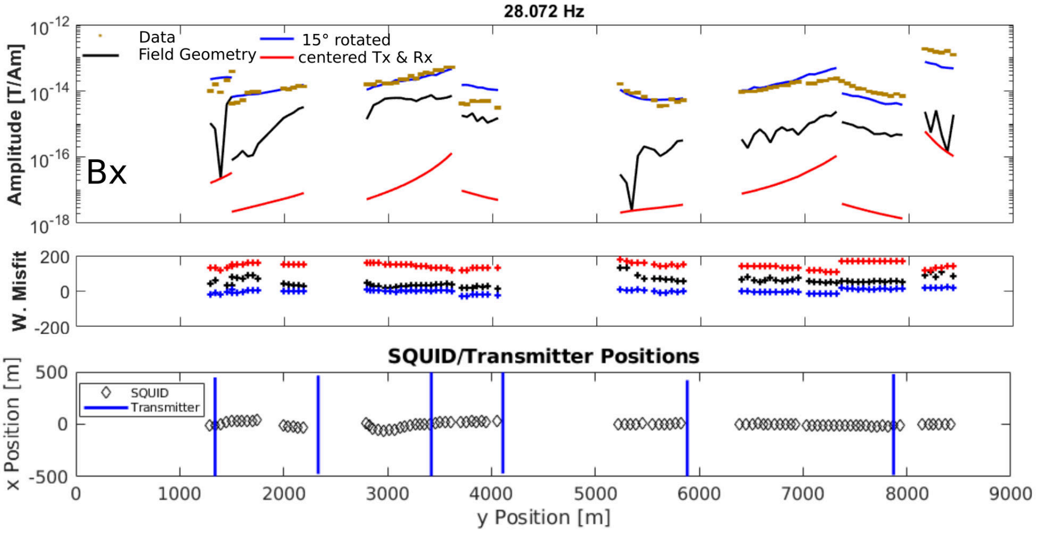

**Figure 9.4.:** Upper Panel: Measured data for the $B_x$ component compared with forward calculated data utilizing the model obtained by inversion of the $B_z$ component and corresponding error weighted misfit between measured and calculated data. The black lines represent data calculated for field data geometry. The red lines represent data calculated setting the location of the receiver at x = 0. The blue lines represent data calculated with a horizontal sensor rotation of 15°. Lower Panel: Location of receivers and transmitter along the profile in x-y view.

## 9.1.3. The CSEM Validation Model

In a next step, a joint inversion of the $E_x$, $B_y$ and $B_z$ component is performed. Considering the high amplitudes of the $B_x$ component, which can not be explained by a 2D subsurface, $B_x$ was excluded from subsequent inversion. Since the misfit between inversion models for different components were almost a factor of two higher for error weighted amplitudes and phases, for the joint inversion the amplitudes were down-weighted. The error floor was increased from 5 % to 10 % in order to account for 3D effects. For the phases, the error floor was kept at 2°, which refers to a relative error floor of 3.5%. Inversions with lower error settings for the amplitude were performed, however the overall relative misfit decrease was higher when amplitudes were downweighted.

**Table 9.2.:** Error weighted RMS between observed and calculated data for the Validation model

| Component | RMS Amplitude | RMS Phase | RMS Total |
|---|---|---|---|
| $E_x$ | 3.524 | 3.033 | 3.288 |
| $B_y$ | 1.250 | 1.911 | 1.615 |
| $B_z$ | 1.554 | 2.042 | 1.814 |

Figure 9.5 shows the final inversion result, which converged after 10 iterations to a global RMS of 2.48. In addition, the corresponding sensitivity distribution is shown. In total 16408 data points were included in the inversion. The error weighted RMS for each component for amplitude and phase is listed in Table 9.2. Magnetic fields exhibit a higher fit than the electric field component.

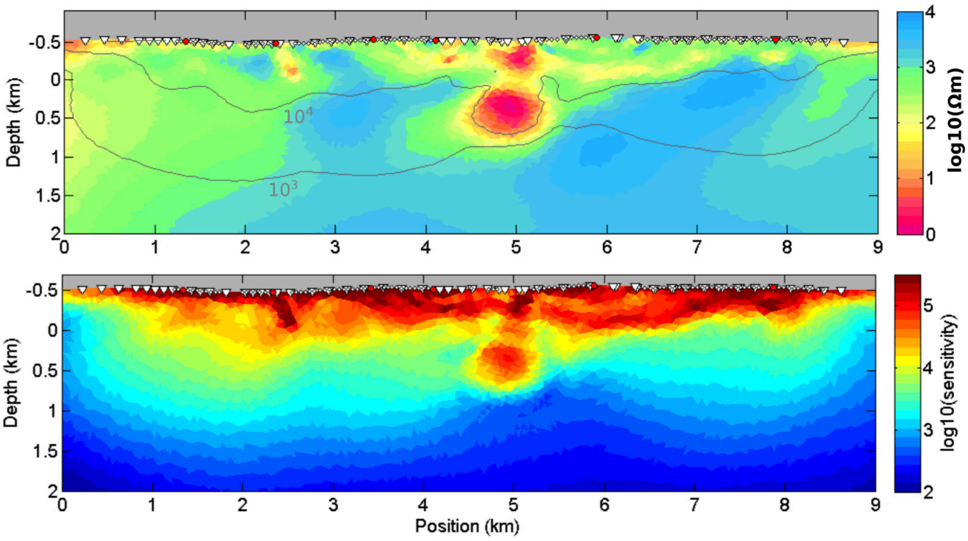

**Figure 9.5.:** Upper Panel: Inversion result utilizing the $B_y$, $B_z$ and $E_x$ dataset jointly. Grey lines mark the isolines of error weighted sensitivities of $10^4$ and $10^3$. Lower Panel: Weighted sensitivities summed up over $B_y$, $B_z$ and $E_x$.

Data fit for one exemplary frequency along the profile and corresponding misfit is given for all components in Figure 9.6. In the lower panel of Figure 9.6, the averaged misfit over frequency for each component is given. Where misfit for frequencies between 1 Hz and 300 Hz are in a similar range, misfit slightly increases for higher frequencies for all components. An overview over data and misfit for each station and component for one exemplary transmitter is given in the Appendix D, Figures D.3 - D.18.

The most prominent conductive structure is located in the centre of the profile between profile 4.5-5 km. It exhibits low resistivities down to 1 Ωm and reaches depth down to 1.2 km below the surface. In addition, several shallow conductivity anomalies are present. Overall the model features high conductivity contrasts between only a few Ωm and several thousand Ωm. Prominent high conductive structures of the CSEM model will be discussed in Chapter 10 in more detail.

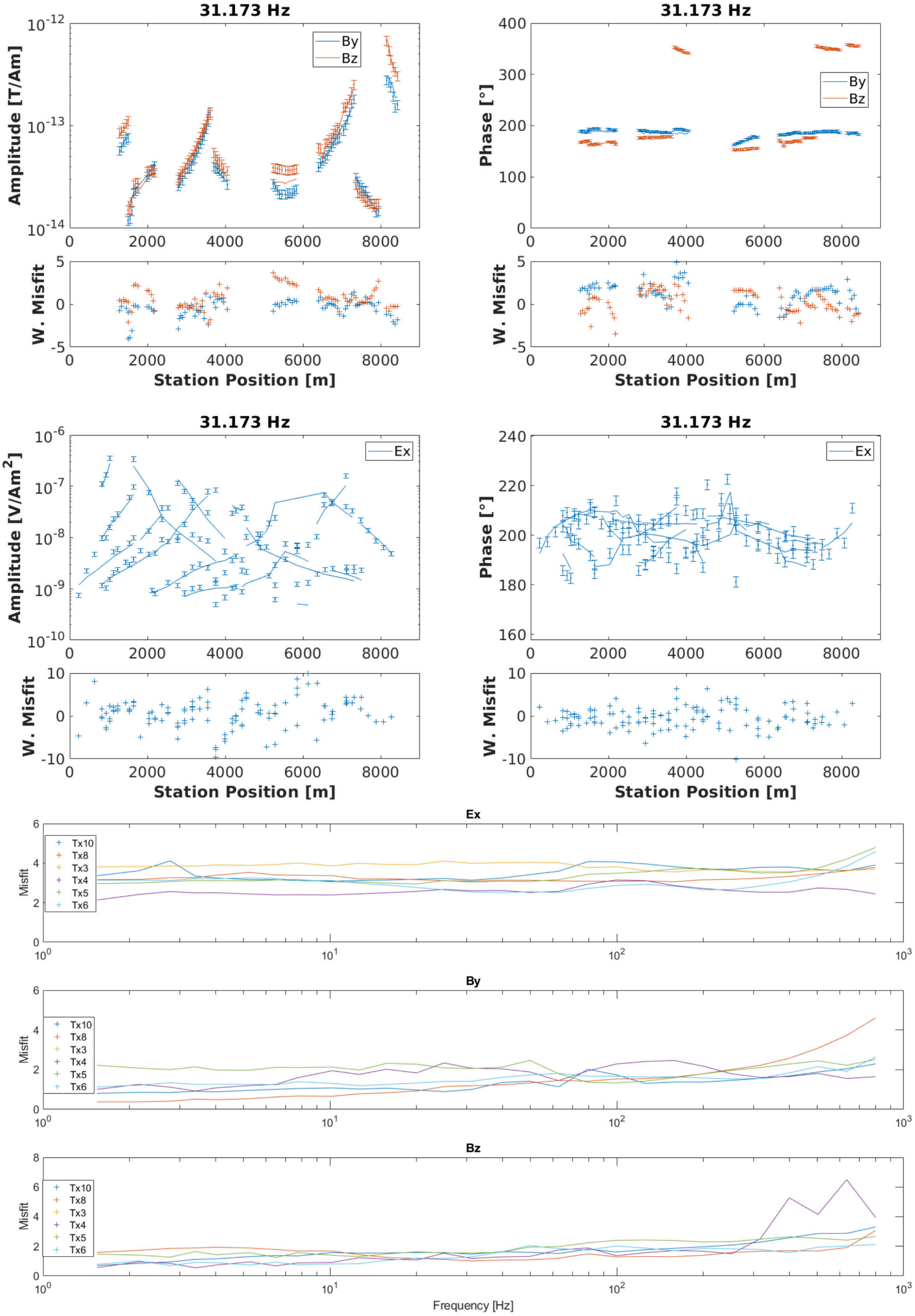

**Figure 9.6.:** Measured data, calculated data and error weighted RMS for the inversion result shown in Figure 9.5 plotted over the profile position of the receiver for the 31 Hz frequency for two magnetic field (upper panels) and one electric field (central panel) component. The solid lines denote the forward response, the measured data is represented as circles. Lower Panel: The error weighted misfit, averaged over all stations for different frequencies is shown for each component separately. Different colours refer to different transmitters.

Sensitivities are as expected higher in the centre part of the profile than at the edges. High sensitivities indicate a resolution of the prominent conductive structure. Sensitivities directly below the anomaly are decreased. The sensitivity distribution for each component of the joint inversion model can be found in Figure D.2 in the Appendix. These results are in agreement with the results obtained by the inversion of the individual field components in Section 9.1.1 and results from the 2D synthetic modelling study in Section 8.2.6. Deep structures and the prominent conductivity anomaly are mainly resolved by the $E_x$ component.

Figure 9.7 introduces a modelling study conducted in order to evaluate, if a deep conductivity structure is needed to explain the data. A forward calculation was conducted replacing the high conductive structure at depth below 500 m with the high resistivities of the surrounding model cells. Misfit between the inversion model and the modified inversion model are compared along the profile and for different components over frequency.

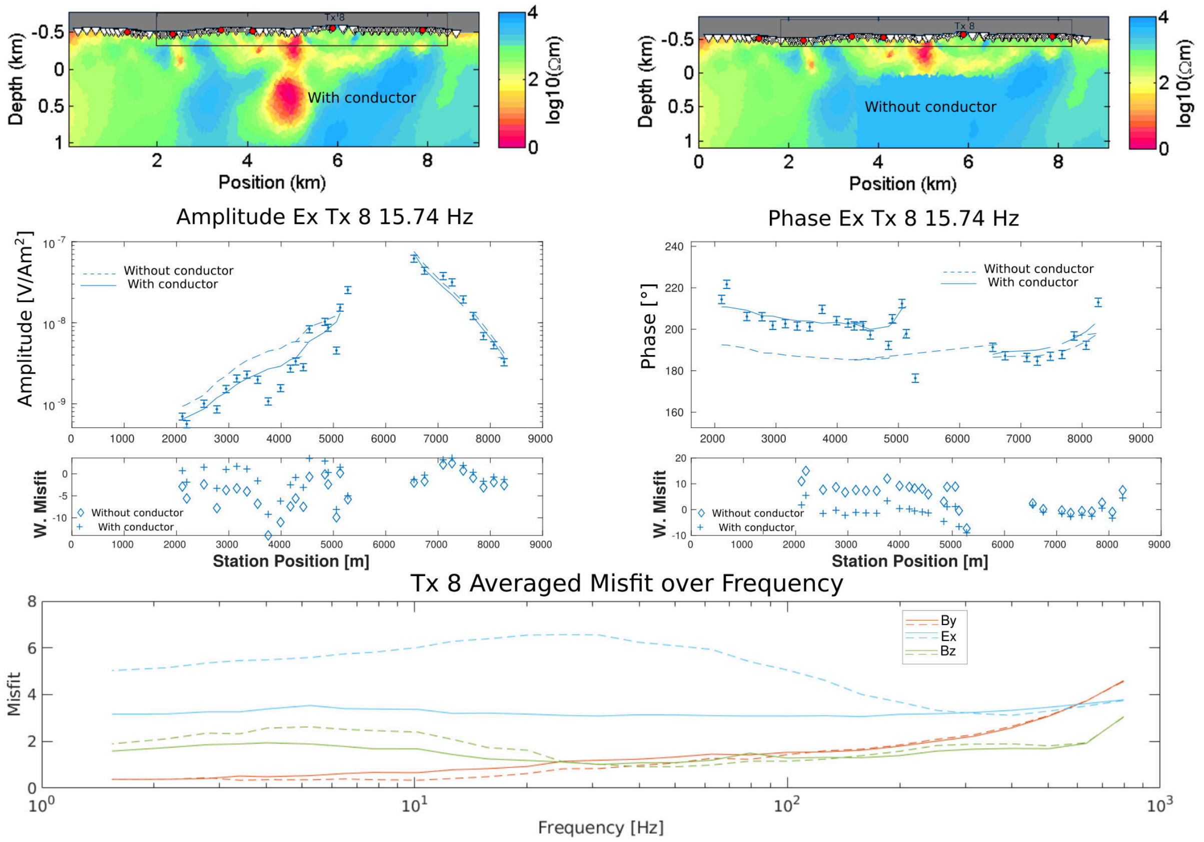

**Figure 9.7.:** Upper Panel: Validation model with deep conductor and modified model without deep conductor. Below, data (points), calculated data (lines) and corresponding misfit for both models is shown exemplarily for one frequency and one transmitter. The corresponding profile section is marked with a black box in the models. Lower Panel: Error weighted misfit utilizing Tx 8, averaged over all stations and displayed over frequency for all components.

Figure 9.7 exemplarily shows the misfit for the model with and without a deep conductor for one frequency along the profile for transmitter Tx 8. Utilized stations cover the part of the transect with high sensitivities towards the conductive anomaly, i.e between profile 2-5 km. Misfits are visibly increased for stations at profile 2-5 km, where the strongest increase in misfit is shown in the phase. The lower panel of Figure 9.7 shows the misfit between modelled and measured data for both models for all components over frequency, averaged over all stations from transmitter 8. Note that SQUID stations for transmitter 8 are located between profile 7-8 km. The SQUID data does not cover the profile section 4-5 km, where the deep anomaly is located. Therefore only a very small increase of misfit is seen for the magnetic field $B_z$ component at frequencies below 20 Hz. For the $B_y$ component, the misfit decreased slightly.

The electric field component shows a strong increase in misfit for frequencies below 300 Hz, with a maximum increase of weighted misfit at a frequency of 30 Hz. If one considers a homogeneous halfspace of 300 Ωm, the corresponding skin depth ( cp. Equation 2.18) for a frequency of 300 Hz is approximately 500 m. Frequencies above 300 Hz can most likely not resolve the conductive structure due to a limited penetration depth. However, for all frequencies below 300 Hz the misfit is significantly increased. The total misfit averaged over all transmitter-receiver configurations and frequencies increased from 2.48 to 3.11 for the model without the deep conductor. We conclude, that the deep conductor is needed to explain the electric field dataset. Magnetic field data shows a lower sensitivity towards the deep conductor, since no transmitter receiver geometry covers the profile between kilometre 4-5, where the conductor is located.

## 9.2. 2D Inversion of $E_x$ in Time Domain

For comparison, the electrical LOTEM field data was inverted utilizing the recently implemented time domain solution of `MARE2DEM`. The same inversion parameters were used as for the frequency domain inversion. In order to facilitate the fitting of sign reversals, an arsinh-transformation was applied to the dataset. As shown in Section 8.2.12, inversion of switch off data is superior in terms of the resolution of a deep conductive structure. However, the inversion of the obtained switch off dataset did not converge. Therefore, electric field data was inverted as switch on transients. Similar to the inversion of the data in frequency domain, an error floor of 5 % was set to the data. Since the dataset is well above the noise level, no additional absolute error floor was applied.

As described in Section 8.2.10, the response for a large number of frequencies is calculated in order to solve the integrals given in Equation 2.37 and 2.38. In addition, the frequency domain solution must be transformed into time domain. Therefore, inversion of time domain data is computational more expensive. For example, for calculation in time domain on the High Performance Computing CHEOPS of the RRZK Cologne, 5 inversion iteration were calculated parallel on 100 processors in 60 hours. In frequency domain, 9 iterations were calculated in the same time using the same resources. For both models identical mesh grouping and an identical number of data points and model cells were used. For later stages of the inversion, in which typically a larger number of forward calls is needed, calculation times increase strongly. Since the wall time per user is limited, inversion was stopped after approximately 10 iterations for time domain modelling, if the misfit decrease was small between subsequent iterations.

In a first step an inversion of the latest time point from each transient was performed and compared to the DC only inversion algorithm `BERT` (Günther and Rücker, 2012). Subsequently, the full dataset was inverted.

### 9.2.1. Inversion of Late Time $E_x$ Data

As a first evaluation step in time domain, a pseudo-DC inversion model is obtained. Transient switch on data was measured in time ranges of 2x$10^{-5}$ up to 0.45 s or 1 s. For the pseudo-DC inversion, only the latest time points of the LOTEM switch on transients were considered for inversion under the assumption, that the inductive response is sufficiently lower than the DC level. In Figure 9.8 the resulting model is compared with a model obtained utilizing the 2D DC algorithm `BERT`. For both models, the same dataset was used. A relative error of 5 % was applied to the dataset prior to the inversion with `MARE2DEM`. For inversion with `BERT`, a relative error of 3 % was set and an absolute error floor of 10 $\mu$V was added.

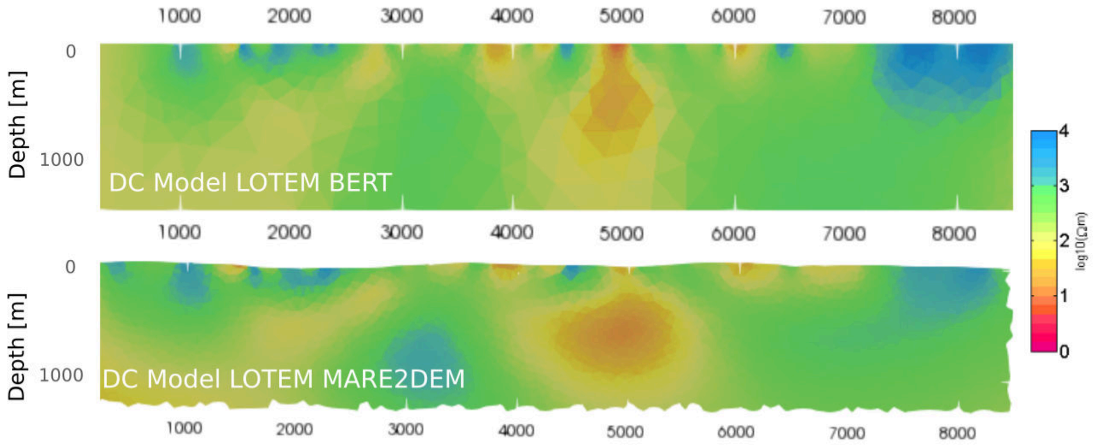

**Figure 9.8.:** Inversion of the last time point of LOTEM $E_x$ transients utilizing the DC code `BERT` (model provided by T. Günther) and the time domain implementation of `MARE2DEM`. Note that for the `BERT` model no topography was considered. For a better comparison, the surface of the `MARE2DEM` model was shifted to the 0-level. The `MARE2DEM` model converged from a starting RMS of 21.78 to a final RMS of 5.75.

Obtained inversion models are well comparable. Note that for the `BERT` model, no topography was considered. Small scale differences which occur are most probable due to topography effects, different inversion parameters, e.g. different horizontal to vertical smoothing parameters and different error floors. For both datasets, data from 137 electric field stations were used. Not all measured electric field stations were included for inversion. Since `BERT` is an DC algorithm, which does not account for inductive EM response, time points were excluded from inversion, which exhibited a slope larger 4 % over the last 100 ms of the transient. A slope in the transients at late times is an indicator for either induced polarisation or inductive response. For most transients, the DC level was approximately reached for late times. In addition, strong outliers were excluded. Since the largest offsets are in the range of 4-5 km, the maximum depth of penetration is roughly 1.2 km.

Similar to the inversion of the frequency domain model utilizing the full frequency range shown in Figure 9.2, a high conductive structure appears in the centre of the profile. However, overall resistivities are closer to the 300 Ωm homogeneous halfspace taken as starting model. This can be explained by the much lower information content in the sparse LOTEM-DC dataset, since the inductive earth response over time is not considered.

From the similarity between the DC model and the EM model, one can conclude that inductive effects are negligible for late time switch on data. Furthermore, the applicability of a computational inexpensive DC algorithm to the late times of the dataset gives the possibility to derive a first 2D inversion model within a short calculation time.

### 9.2.2. Inversion of $E_x$ Data

Subsequently the full LOTEM $E_x$ switch on dataset was inverted. Similar to the error settings for frequency domain amplitudes, an error floor of 5 % was set to the data. Due to an increased calculation time, the inversion progress was stopped after the misfit decrease for subsequent iterations dropped under a certain threshold. Therefore, presented inversion models did not fully converge. However, the models from subsequent iterations did not change significantly.

Yet, a convolution of the early time dataset with a system response is not implemented in `MARE2DEM`. Therefore, early time transient data was neglected. Furthermore, since frequencies above 1 kHz were excluded from inversion in frequency domain, for a better comparability a time range between $10^{-3}$ and 1 s was used. The same parameter settings were applied for both, time and frequency domain inversion. Note that due to time shifts of the transmitter current in 2016, stations were excluded in frequency domain. After the application of time domain processing routines, those time shifts could be reversed. Therefore, the TD dataset exhibits more stations and therefore more data points. A detailed list of stations and applied processing routines in both domains is given in the Appendix A.

Figure 9.9 shows the comparison between time domain and frequency domain inversion models for the $E_x$ component. For all inversions, a similar time-frequency range was inverted, the same inversion parameters were utilized and a homogeneous halfspace of 300 Ωm was used as starting model. For all four cases, next to the inversion models, the inversion progress is displayed. The upper two models show different iterations from the same inversion run in FD. Model a) converged after 20 iterations. For comparison with the TD models shown in Figure 9.9, in addition model b) obtained after 6 iteration steps is shown. For time domain inversion, due to small misfit decrease between subsequent models, inversion was stopped after 9 and 11 iteration steps, respectively. For model c) the full time domain dataset was utilized. Model d) utilizes the same set of stations as in the FD models a) and b). Data fit for model a) and model d) for one exemplary frequency or time respectively is given in Figure 9.10.

While overall structures are similar in the inversion models, differences occur. Model a) converged in 20 iterations to the lowest misfit of 3.88. Misfit of TD model c) and d) are 6.49 and 5.88. However, the starting misfit is higher for both TD models. Model a)

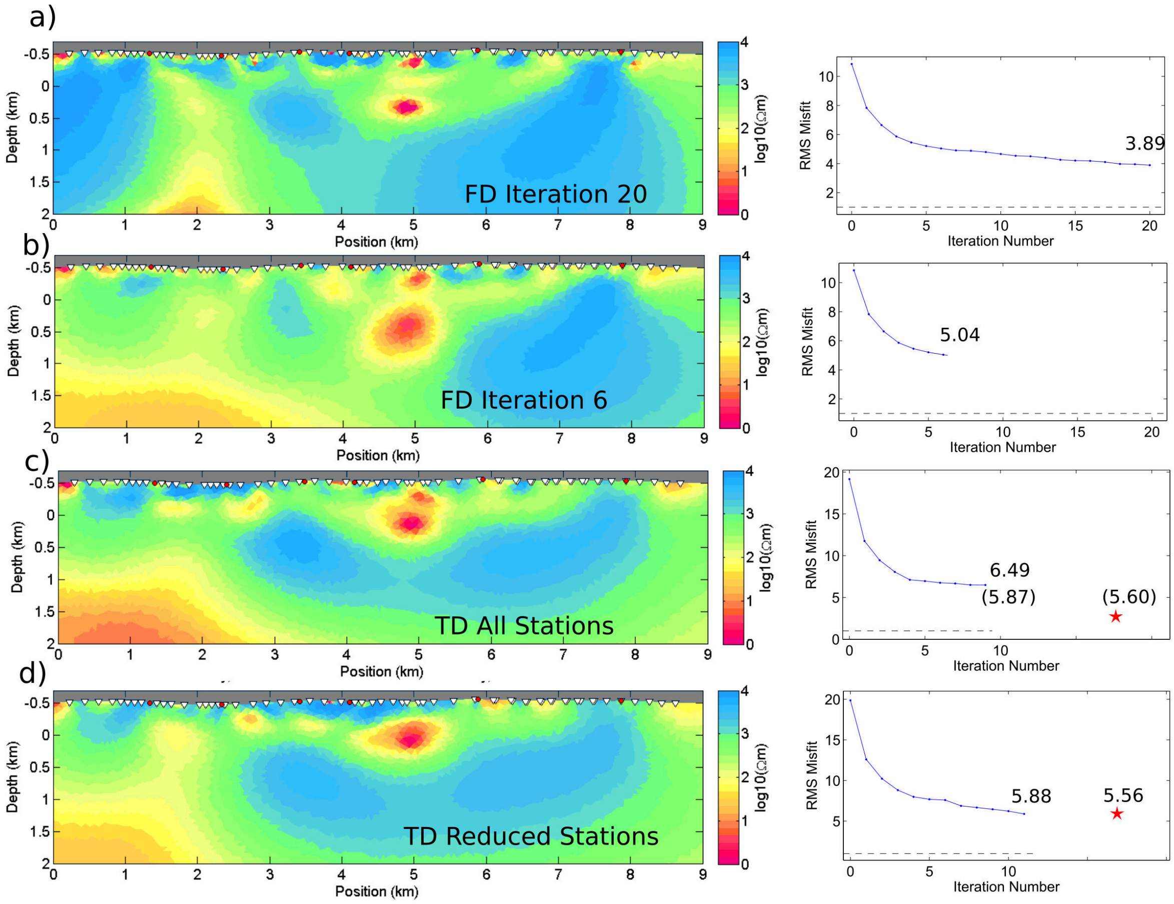

**Figure 9.9.:** FD (a-b) and TD (c-d) inversion models for the $E_x$ component. Next to the inversion model, the inversion progress for each model is given. The final RMS of the last iteration is given. For model c), values in brackets correspond to the overall misfit after the removal of one station with a large misfit from the dataset. The red star indicates the RMS obtained by performing a forward calculation of the inversion model (a) for the corresponding dataset.

exhibits the highest roughness, being in a later stage of inversion. Comparing an earlier stage of the inversion in FD model b) with the TD models, overall similar conductivity structures are contained. High background resistivities in the order of several thousand Ωm and a deep conductive structure around profile km 5 is present in all inversion models. The shape and depth extension of the conductive anomaly however differs. While model a)-c) indicate a bisection of the structure at an absolute height of -200 to 0 meter, model d) shows only one continuous conductive structure.

However, the overall resistivity distribution is similar. Furthermore, a forward calculation of model a) for the TD models c) and d) was conducted. The misfit of the FD model to the time domain dataset is indicated with a red star. The misfit is lower than for the obtained inversion models. Therefore we conclude, that obtained data and models in time and frequency domain are in good agreement.

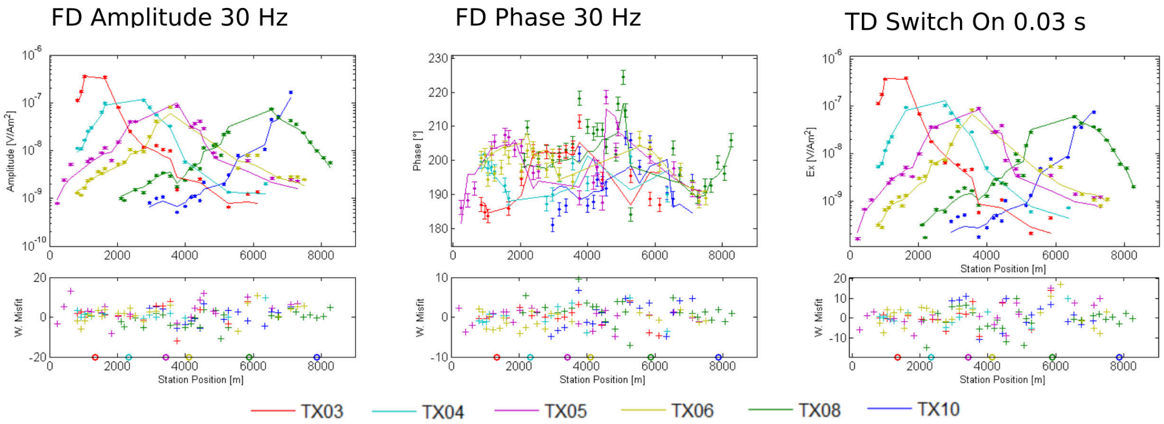

**Figure 9.10.:** Measured data (Points), calculated data (line) and error weighted RMS for the inversion result a) and d) shown in Figure 9.5. In frequency domain, the response for 30 Hz is shown, in TD for 0.03 s. Different colors refer to different transmitters. In the lower Panel, the error weighted misfit along the profile is displayed. Location of the transmitters are indicated with circles along the x-axis.

## 9.3. Summary

Field data was inverted with the 2D algorithm `MARE2DEM`. In a first step, an inversion of the $B_y$, $B_z$ and $E_x$ component in frequency domain was conducted. A comparison of the inversion models obtained by different components indicate, that multidimensional effects are present in the dataset. Differences in the inversion models can only partly be explained by a different sensitivity distribution. Especially the high amplitudes of the $B_x$ component, which can not be modelled by a 2D EM approach, indicate, that the dataset is biased by additional effects. Nevertheless it is evident, that a joint inversion of the different components leads to an higher overall resolution. Especially the large offsets and station distribution of the electric field data deliver constraints for high depth and the prominent conductive anomaly at profile 4.5-5 km. On the other hand, the dense station distribution of the SQUID data constrains the shallow subsurface.

Subsequently, for the derivation of a CSEM validation model, a joint inversion of all components was conducted in frequency domain. Based on the analysis of the inversion of the single components, which exhibit a higher agreement for the phase values, amplitudes were downweighted by adding a higher relative error floor. The RMS did not converged to 1, nevertheless, due to the large dataset, the outcoming inversion model delivers a robust image of the 2D conductivity distribution of the subsurface. A prominent high conductive and deep reaching structure occurs in the centre of the profile. Where B-field data does not exhibit high sensitivities in this section of the profile, the electric field component can partly resolve the structure. A forward calculation replacing the deep part of the conductive anomaly with the background resistivity led to a significantly increased misfit.

Since electric field data was processed in time and frequency domain, inversion was conducted in both domains. As a first step, the last time point of the LOTEM dataset was inverted with `MARE2DEM` and compared to the solution of a DC only code. Inversion models are in a good agreement. This demonstrates, that the time domain solution of `MARE2DEM` delivers reasonable results and furthermore, that the DC level is approximately reached for the last time point of the LOTEM switch on dataset. In a next step, the LOTEM $E_x$

dataset was inverted in TD. An inversion of the dataset as switch off component failed, although an additional absolute error floor was set to the data in order to account for sign reversals and an arsinh transformation was applied to the dataset. The switch on dataset converged after 10 iterations to a RMS of 5.88. Overall structures are similar, but lateral and depth extension of the prominent conductive anomaly in the centre of the profile slightly differs. However, a forward calculation of the obtained frequency domain inversion model could fit the TD dataset reasonably well and led even to a misfit decrease compared with the last iteration obtained in TD. Therefore, data and model agree reasonable well in both domains.

## CHAPTER 10

# Validation of Inversion Results

In Chapter 9 a 2D inversion model of the frequency domain dataset was derived. The most prominent structure is a high conductive anomaly with a depth extension of approximately 1.2 km in the centre of the profile, which is mainly resolved by the electric field data. The obtained LOTEM model can be compared to EM methods detecting the same geophysical parameter, i.e. the electrical resistivity. Being a reference model for the semi-airborne method, this applies foremost to the semi-airborne EM inversion results. Smirnova et al. (2019b) presented first inversion models from semi-airborne measurements in the survey area utilizing a subset of the acquired data from one receiver system.

In addition, for deep structures, Dipole-Dipole measurements from LIAG deliver a robust reference dataset which images the same geophysical parameter. It has an increased sensitivity towards resistive structures compared with inductive methods and therefore delivers complementary information. Moreover, shallow high conductive subsurface structures can be compared to existing inversion models from airborne EM, semi-airborne EM and DC measurements. Considering resistivities derived from petrophysical investigations conducted by BGR and resistivity statistics derived from borehole logs (Geophysica, 2019), obtained resistivities can be correlated to lithological layers. Note, that the derivation of an integrated deposition model and a final geological interpretation is not the objective of this thesis, but rather the derivation of a robust and independent CSEM reference model. Large amount of data for different geophysical parameters were acquired in the framework of DESMEX from different project partners, including magnetics, radiometrics, airborne and semi-airborne EM, direct current methods, induced polarisation measurements and petrophysical investigations. In order to compare data imaging different geophysical parameters, Geophysica (2019) applied statistical methods to detect patterns of resistivity distributions which are subsequently compared with available geological information. An integrated model and a final interpretation of the geological and geophysical subsurface parameters of the survey area will be discussed in future publications of the DESMEX working group.

## 10.1. Comparison with Geophysical Results

Figure 10.1 comprises a comparison of obtained inversion models from different geophysical methods along the LOTEM profile. The airborne (HEM) and DC profiles are measured along the LOTEM transect. Shown are inversion results from HEM 1D models (Steuer et al., 2015), a DC 2D model (Cherevatova et al., 2017) and a cross section from the semi-airborne 3D model (Smirnova et al., 2019b). As in previous sections, topography is included. Therefore the depth axis refers to the absolute altitude of the model.

Airborne data was obtained utilizing a frequency domain transmitter and receiver system. A flight area of in total 445 km$^2$ was covered within a helicopter survey in 2015. 1D results shown in Figure 10.1 are from a flight line running directly along the LOTEM profile (as depicted in Figure 4.3, Flight line 17). Inversion results are obtained by utilizing airborne magnetic field data. Due to the small penetration depth of the HEM method, only a shallow subsurface model is obtained. Therefore in the comparison only the lateral extension of the outcropping structures is compared with the other models rather than the depth extension. Detailed information about the HEM survey can be found in Steuer et al. (2015), information about the system and 1D inversion procedures can be found in Siemon et al. (2011) and Sengpiel and Siemon (2000).

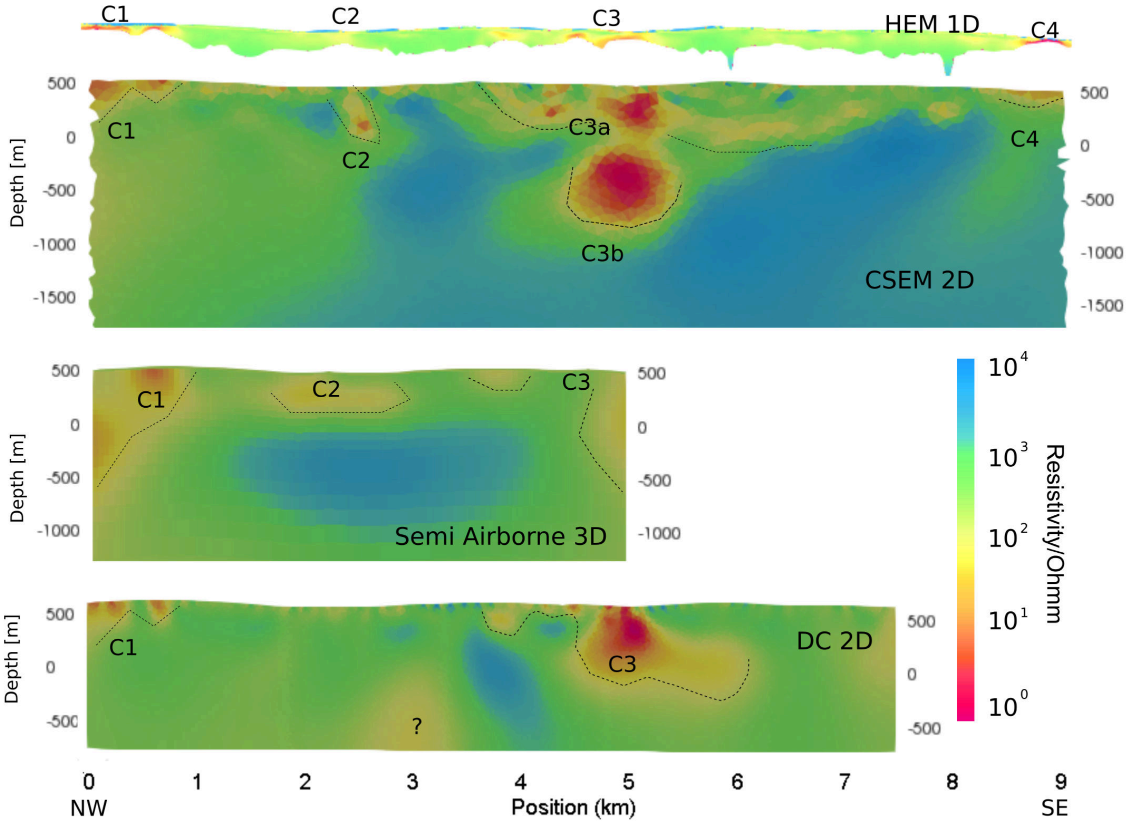

**Figure 10.1.:** Comparison of Inversion results from HEM data, the CSEM Validation model, a 2D cross section of the 3D semi-airborne model and the DC result. Prominent conductivity structures are marked with the labels C1-C4 and outlined with black lines.

DC data was acquired on a transect along the LOTEM profile (Cherevatova et al., 2017). The DC dataset was obtained in two surveys in 2015 and 2016 on two overlapping segments, with a combined profile length of 7.5 km. Inversion was conducted with the DC code `BERT`. Both, field measurements and inversion were conducted by LIAG. As setup configuration a Dipole-Dipole layout was utilized, consisting of 36 electrodes with distance of 125 m each, which results in a total length of 4.375 km per segment. Therefore, the estimated maximal exploration depth of the DC model is roughly 1 km. However, exploration depth is decreased at the profile edges. Note that, contrary to the broadside configuration of the LOTEM survey setup, the DC experiment is in inline configuration, where transmitter and receivers are set up parallel to the profile. Consequently the method has an increased sensitivity towards resistors, when compared with the broadside setup utilized within the LOTEM survey.

The semi-airborne 3D model (Smirnova et al., 2019b) was obtained by inversion of the vertical magnetic $B_z$ component utilizing both, induction coil and fluxgate data from an airborne receiver system. The LOTEM transmitter from the UoC was employed as a source. The cross section shown in Figure 10.1 is a 2D slice interpolated from the 3D semi-airborne model covering a 5×7 km flight area (as depicted in Figure 4.4). As transmitter for the semi-airborne flights, the transmitters Tx 4 and Tx 5 from the LOTEM study were used. As third source, an additional transmitter in inline configuration was set up, located in between the Tx 4 and Tx 5 position parallel to the profile, which was not utilized for the ground based LOTEM measurements. Flight lines were running parallel to and with a spacing of 100 m in the vicinity of the LOTEM profile. Mainly depending on the flight velocity and stacking routines, time series were separated in segments of 5 s each, which correlates to a station spacing of 150 m. A detailed description of the novel concept, the measurement system and the conducted field experiment can be found in Smirnova et al. (2019b).

The presented cross section is located in the centre of the 3D inversion model and matches with the LOTEM profile, however it is only approximately 5 km long. For inversion, 8 selected frequencies between 30 and 1096 Hz were considered (Smirnova et al., 2019b). The base frequency of 30 Hz was used for inversion of the semi-airborne data compared with the lowest frequency of 1 Hz utilised for the CSEM inversion. Offsets up to approximately 2 km were included in the inversion. Considering a higher base frequency (cp. Equation 2.18) and smaller maximum offsets, the exploration depth of the semi-airborne model is lower than for the CSEM validation model. Note that for the shown semi-airborne model, no ground based data was included thus far, however it is planned for future evaluation in the framework of DESMEX.

The location of the most prominent conductive structures are denoted with C1 to C4 in Figure 10.1 for each model. The outline of the anomalies are delineated with black lines. A more detailed comparison of the shallow subsurface structures between geological maps, the CSEM model and the airborne model is presented in Figure 10.3.

The conductive structure C1 in the northwest of the profile occurs in all 4 inversion models depicted in Figure 10.1. While the lateral and depth extension of C1 is similar in the DC and CSEM validation model, the outlines of the anomaly are blurred out in the semi-airborne model. For the semi-airborne model, the indicated depth extension of the conductive body is higher. However, being located at the outer border of the 3D model, the resolution for the structure is low. Furthermore, the semi-airborne model is affected by 3D smoothing, considering the ill-posedness of the 3D problem. Therefore, the resolution in depth of C1 is lower for the semi-airborne model.

The conductive anomaly C2 is present in the airborne, semi-airborne and CSEM validation model, however the lateral extension and depth extension is different between the CSEM and semi-airborne model. In the DC model, no indications for a conductive body C2 is evident.

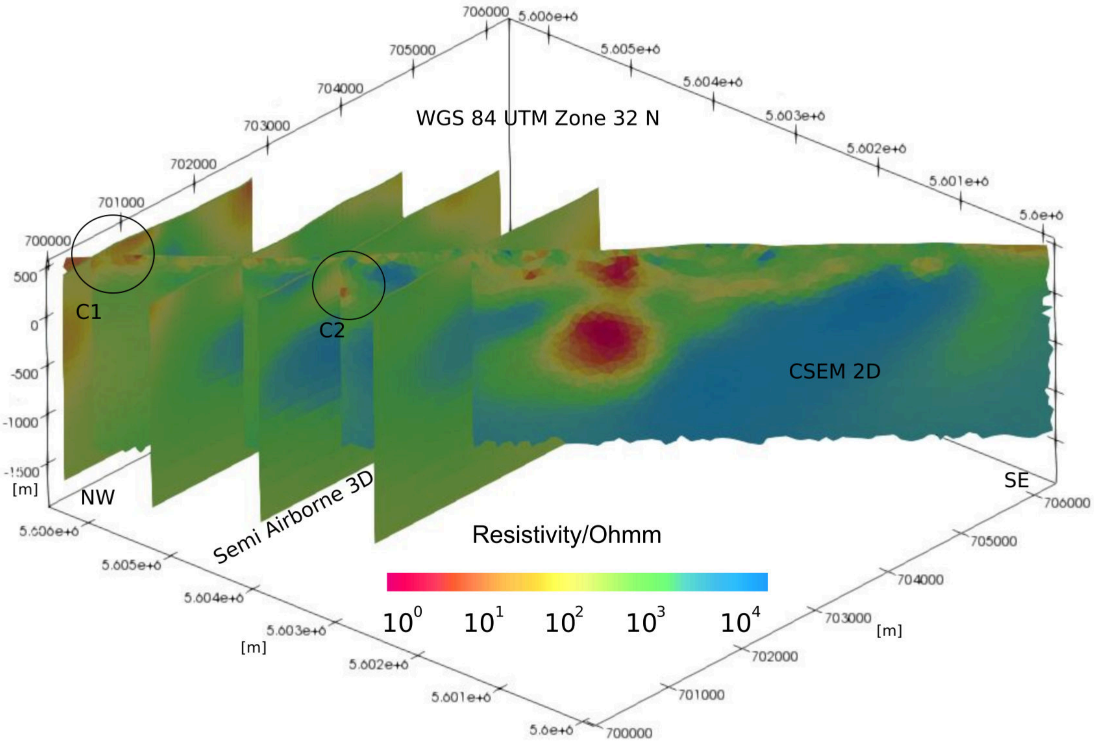

**Figure 10.2.:** 2D slices interpolated from the semi-airborne 3D model in comparison with the CSEM Validation model. Black circles denote the location of the conductivity structures C1 and C2.

The main conductive body C3 is present in all 4 inversion models. A lateral continuation towards southeast is indicated for the CSEM and DC model. Unfortunately, there is no semi-airborne inversion model available between profile 5-9 km. Therefore, the prominent conductive structure C3 is located at the outer edge of the cross section and is only partly imaged. Conductivities are lower for the semi-airborne data, being in the range of approximately 30-100 Ωm. Resistivities of the structure C3 are in the range of 1 to 10 Ωm for the DC and CSEM model. A bi- or trisection respectively of the conductive structure can be observed at the shallow subsurface for the semi-airborne, DC, CSEM and airborne model rather than a continuous conductivity structure between profile 3.5 to 5 km.

The depth extension of the conductive feature varies for the three deep inversion models. For the semi-airborne cross section, the anomaly, with its NW edge located at the end of the profile, is blurred out and no reliable conclusions about the size of the anomaly can be drawn. For the DC model, the lower edge of the anomaly reaches approximately

500-600 m deep, whereas for the CSEM model, the lower edge reaches depth of approximately 1300 m from the surface. For the CSEM model, forward modelling studies were performed in Section 9.1.3. A depth extension of more than 500 m, here denoted as C3b, is needed to explain the electric field dataset.

Only the airborne and CSEM validation model cover the conductive structure C4. Both models show a similar lateral extension. The overall background resistivities are higher in the CSEM and semi-airborne models compared with the DC model. A conductive structure is present in the DC model around profile 3 km, which does not occur in the other models. Given the penetration depth of the DC model, the resolution towards this structure is however questionable.

Figure 10.2 depicts the CSEM validation model in comparison with interpolated 2D cross sections from the semi-airborne model. The prominent shallow conductive structures C1 and C2 are indicated with black circles. Depth extension of resistivity structures and their amplitude match between the different models. Both, the semi-airborne cross sections and the 2D CSEM model exhibit rather high resistivities in the NW part of the profile within 500 - 1000 m below the surface.

## 10.2. Comparison with Geology

Figure 10.3 shows the comparison between the upper 500 m of the CSEM validation model, the 1D inversion result of semi-airborne data along flight line 17 and a geological cross section running parallel to the profile. In Figure 10.3 the layout of the LOTEM setup is depicted on top of a geological outcrop map. The location of the mine "Halber Mond" is marked in all models. The black lines sketch the approximated depth extension of the mining shaft. Due to the rather coarse triangle size and for visual comparison of the shallow subsurface with the airborne model, a parameter shading was conducted for the CSEM validation model. The inversion models and the geological cross section are all displayed 2.5 times exaggerated. Both models show the prominent conductive bodies C1-C4, with a comparable lateral extension between the models. Structures C1, C3, and C4 can be well correlated to the occurrence of the Silurian Graptolite shales (black shales, blue) in the region. Costabel and Martin (2019) measured high conductivities for the Silurian black shales from the survey area down to 2 Ωm, which coincides with high conductivity values obtained in the inversion models. Furthermore, outcropping Devonian shales could be correlated to conductive shallow structures of the 3D semi-airborne model and the HEM 1D models within the flight areas (Smirnova et al., 2019b).

The conductive structure C3 might be also correlated to the occurrence of Devonian Slates (Schwärzschiefer Formation). The conductive structure C3 continues in the CSEM model until depth of 1500 m below the surface. Occurrences of deep Devonian shales between 400-600 m are reported in the south of the survey area (Kunz, 1988). However, typical thickness for Silurian and Devonian black shales are in the range of 20-60 m (Liebe et al., 1912). The source of a conductive anomaly with a high lateral as well as large depth extension as shown in the CSEM model but also in the DC model is therefore not completely clear. Note that graphtolite shales exhibit strong induced polarisation effects which can bias the inversion results and exhibit anisotropy.

The conductive structure C2 is not shown in the outcrop map and does not outcrop to the surface in the obtained models, however it is present in the semi-airborne model, the CSEM model and the airborne model. Slates from the Ordovician group exhibit values between 100 and 1000 Ωm obtained from bore log data (cp. Figure 4.5), which correlate to the background resistivities of the inversion models. However, the CSEM validation model also shows regions with high resistivities exhibiting values of several thousand Ωm, which would correlate to Diabase.

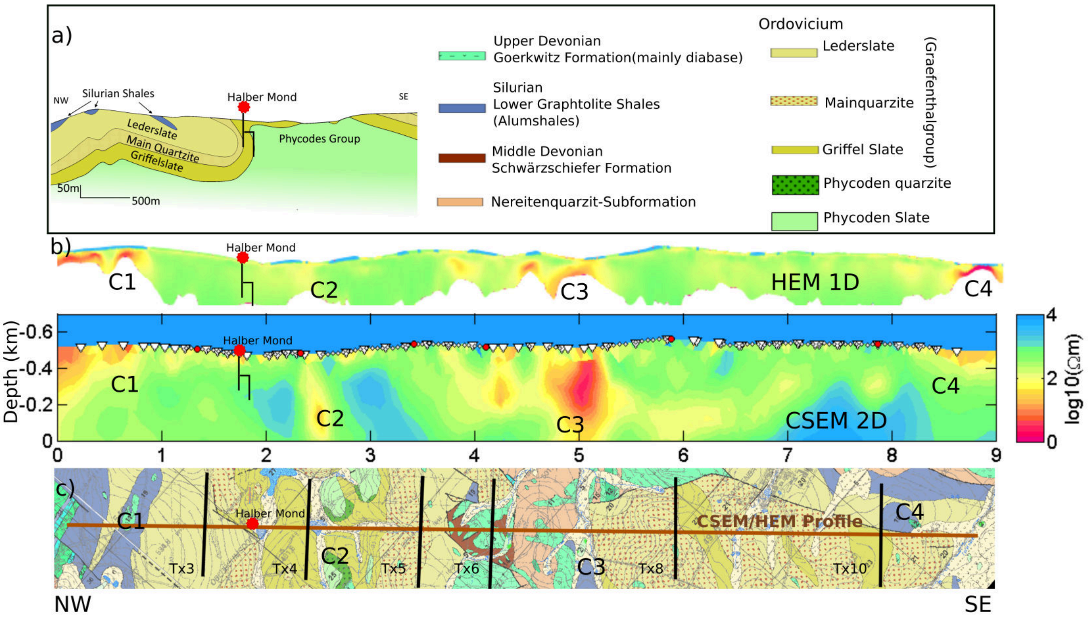

**Figure 10.3.:** a) Cross section, modified after Wagenbreth (1946) and legend. b) Airborne and CSEM model. Cross section and inversion model are exaggerated 2.5 times for better comparison. c) The Geological outcrop map (digital geological map of Thuringia (Germany) 1:25000), location of the LOTEM Profile (brown) and locations of transmitters. The location of the former antimony mine "Halber Mond" (red star) and the two main mine shafts are added in all models. Locations of the most prominent Silurian black shale formations along the LOTEM profile are marked with C1-C4. Inversion model of the HEM flight line and the geological cross section run along the LOTEM profile.

## 10.3. Summary

Existing geophysical, geological and petrophysical information was compared with the obtained CSEM validation model. Along the LOTEM transect, inversion models derived from airborne, semi-airborne and DC measurements give insights into the resistivity distribution with varying exploration depth and resolution. Location and lateral extension of the conducive structures C1-C4 are well comparable between the airborne model and the CSEM validation model. Conductive structures C1 and C3 are present in all inversion models. The semi-airborne model shown here does not cover the full lateral extend of the conductive main anomaly C3. However, conductive structures C1 and C2 as well as background resistivities are well comparable between the CSEM and semi-airborne model.

By comparing the inversion models with geological outcrop map, a geological cross section and petrophysical investigations as well as borehole logs from the area, the detected conductive anomalies C1, C2 and C4 could be correlated to Silurian black shales. Low resistivities of structure C3 might be influenced by both, Silurian black shales and Devonian shales. This correlation is in agreement of the findings from Smirnova et al. (2019b). While the deep anomaly C3b is needed to fit the CSEM data, obtained data in this region might be influenced by induced polarisation effects or anisotropy, which could produce artefacts in the model.

Overall, inversion models from different geophysical methods are matching. Especially the HEM airborne model and the upper few hundred meters of the CSEM model are in a good agreement and match with geological outcrop maps. For comparison with the semi-airborne model, slices from a 3D model were compared with the CSEM result. Considering higher smoothing, inversion of less frequencies and lower offsets, the overall resolution of structures is lower for the 3D model. Nevertheless, overall conductivity structures are similar in all models. In the future, a joint inversion of semi-airborne and ground based data is intended, which improves the resolution and depth extension of the semi-airborne method (Smirnova et al., 2019a; Cai et al., 2019).

# CHAPTER 11

# Conclusion and Outlook

The aim of this thesis was the derivation of an independent multidimensional subsurface model utilizing land based controlled source electromagnetics, which serves as a reference model for the newly developed semi-airborne method. As test area for the novel concept, a former antimony mining area in the Thuringian Slate Mountains was chosen. Where the antimony mineralisation itself can not be detected, present alum shales in the survey area exhibit a high conductivity contrast to the surrounding mostly Ordovician rocks and are therefore a suitable target for the detection of high conductive structures.

In order to provide a robust dataset for subsequent inversion, electric field data and a dense full component SQUID magnetic dataset was collected along an 8.5 km long transect, utilizing 6 different transmitter locations. Large offsets between receiver and transmitter ensured a high penetration depth. For the recording of the electric field component, conventional non polarisable CuCu/SO and AgAg/Cl electrodes were utilized. Since the setup of large loops for the recording of the time derivative of the magnetic field was time consuming, and the application for SQUID sensors for LOTEM application proved to be successful in the first survey, in the second survey magnetic data was solely collected with the SQUID system. Recorded data was afflicted by industrial EM noise, however after the application of robust processing schemes, high quality transient over a large time range could be obtained.

In a first step, data was interpreted utilizing 1D inversion routines. However, the time derivative of the vertical magnetic field exhibited sign reversals, which can not be produced by a 1D model. Since chargeable graptolite shales are present in the survey area which strongly affects the late time behaviour of the step off transient, electric field switch off data could not be fitted by 1D conductivity models. Therefore, time domain step on data was inverted, which is on a relative scale less affected by IP but unfortunately also exhibits a smaller relative inductive response due to the superimposed DC level. However, the resulting stitched inversion models show a multidimensional subsurface and the inversion models contained by different transmitters are not consistent. Hence, a 1D approach is not sufficient to interpret the data.

Geophysical pre-investigations, geological information, petrophysical laboratory measurements and the performed 1D LOTEM inversion results indicate that the survey area has a strongly multidimensional resistivity distribution. Here, a new approach was tested. In order to benefit from the availability of multidimensional open source frequency domain inversion codes and considering the different effect of IP to frequency domain data compared to time domain data, the time domain LOTEM data was transferred into frequency domain. After the application of a univariate robust least square processing scheme, smooth transfer functions could be obtained for the electric field data and the full component SQUID dataset. The electric field transfer functions were subsequently inverted by a 1D frequency domain algorithm. Obtained 1D inversion models of the LOTEM data in frequency domain are well comparable with the time domain step on results and suggest that the LOTEM dataset is suitable for frequency domain evaluation. The analysis of the inversion statistics in terms of SVD and BTSV suggests that the model parameters within the target depth can be well defined in both domains.

For 2D inversion of the dataset in frequency domain, the open source code `MARE2DEM` was utilized. Suitable inversion parameters were derived by synthetic studies. Data was subsequently inverted as amplitude and phase rather than real and imaginary part, since the transformation showed improved convergence behaviour during inversion. During the time frame of this thesis, a time domain implementation for `MARE2DEM` was developed by Haroon et al. (2018). This allowed a 2D study of sensitivity distributions for both domains. If relative errors are considered and the response is above the absolute error floor, the electrical switch off data representation exhibit improved resolution capabilities of a deep conductor in a synthetic study.

A subsequent 2D inversion of the dataset in frequency domain was performed for all receiver transmitter configurations and for each component individually as well as jointly. All inversion models showed overall similar structures, with a high conductive structure in the centre of the profile as most striking feature. However in detail, the individual inversion models for each component differed. Moreover, the $B_x$ component could not be fitted, since measured amplitudes were up to two decades higher than the forward calculation of the inversion model obtained using $B_z$. Since strong $B_x$ field components can not be modelled under the assumption of a 2D resistivity distribution, the $B_x$ component was excluded from the subsequent joint inversion of all components.

Furthermore, the code was applied to the electric field dataset in time domain. The SQUID dataset was not yet evaluated in time domain, however a future inversion in time domain might increase resolution capabilities. While inversion of electric field data in both domains delivered similar structures, the final CSEM validation model was derived from frequency domain data only. The frequency domain algorithm is superior in terms of calculation time. In addition, the obtained FD model exhibits an increased data fit and was therefore chosen as validation model for the semi-airborne method.

The final inversion model exhibited several conductive anomalies. The high conductive structure C3 in the centre of the profile has a depth extension of at least several hundred meters. The sensitivity of the dataset towards the deep conductive structure could be confirmed by sensitivity studies and forward modelling. Shallow conductive structures are correlated to the alum shales, which agrees well with other geophysical results and geological background information. The derived model exhibits high sensitivities within depth larger than 1 km and is therefore suitable as reference model for deep conductive targets. However, due to the strong indications of a 3D subsurface, the application of a 3D time or frequency domain algorithm for inversion is recommended and impacts of IP effects to all EM components must be studied and estimated beforehand.

Evaluation of the LOTEM field data and modelling studies identified several points, which can be considered for future applications. In general, LOTEM, or CSEM is a suitable and frequently applied tool for the detection of deep conductive structures associated with deep mineral deposits. However, in a more complex geological and geoelectrical subsurface, integrative methods are required for the deduction of a mineral deposit model. Furthermore, considering the large footprint of the LOTEM method, the application of 1D inversion algorithms is not suitable. In a complex setting 2D or even 3D inversion routines should be applied. In order to provide a dataset suitable for 3D inversion, data should be either collected over a wider area, not only a single transect or inverted jointly with e.g. semi-airborne data. In addition, data collected with inline and broadside configuration delivers complimentary information about the resistivity distribution. Therefore both configurations should be combined. Since conventional magnetotelluric data loggers provided by the GIPP proved to be suitable for time domain applications, a large pool of LOTEM equipment is available for the collection of dense LOTEM datasets suitable for 3D inversion in the future. Non commercial multidimensional inversion tools for EM exist, more for frequency domain applications and less for time domain applications. However, there is currently no inversion tool which can be applied without restriction to a 3D dataset and which can integrate complimentary geophysical data, e.g. from seismics, magnetic or gravimetry. An open source electromagnetic modelling tool for time and frequency domain applications was developed recently (Rochlitz et al., 2019; Seidel, 2019), which allows the computation of EM fields for arbitrary transmitter geometry and topography. It has the potential to be further adapted to an integrative inversion tool for different geophysical methods, and could be a beneficial tool for LOTEM applications in a more complex resistivity distribution. It was shown in 1D modelling studies, that IP effects have the potential to strongly distort the purely inductive EM response. One future focus should therefore be either on the extraction of IP parameters from LOTEM/CSEM data or on the joint interpretation of both, EM and IP. Since ore deposits often exhibit a strong IP response, a joint interpretation of LOTEM/CSEM and IP is a powerful tool to identify possible deep mineral deposits.

Nevertheless, resolution capabilities of the CSEM method for deep resistivity structures are high and CSEM delivers valuable information also as stand alone method for more complex 2D resistivity distributions. The possibility to evaluate data in both, time and frequency domain results in a larger choice of available multidimensional inversion routines. Even more, equipment and survey settings typically used for time domain applications, are also suitable for subsequent frequency domain evaluation. Hence, a decision in which domain data is evaluated can be made after the conduction of the survey and a first evaluation of collected data, as long as the current function is recorded continuously. Relative responses in the evaluated data representations differ, even if the information content of the dataset is not changed by the application of a Fourier transformation. Therefore evaluation in one domain or the other might be beneficial. For example, although transient switch off data exhibits an increased sensitivity towards conductors, evaluation in frequency domain might be preferable, if IP is superimposing the late time EM response.

# Bibliography

Airo, M.-L., 2015. Geophysical signatures of mineral deposit types in Finland. Geological survey of Finland.

Anderson, W. L., 1975. Improved digital filters for evaluating fourier and hankel transform integrals. Tech. rep., US Geological Survey.

Archie, G. E., et al., 1942. The electrical resistivity log as an aid in determining some reservoir characteristics. Transactions of the AIME 146 (01), 54–62.

Asten, M. W., Duncan, A. C., 2012. The quantitative advantages of using B-field sensors in time-domain EM measurement for mineral exploration and unexploded ordnance search. Geophysics 77 (4), WB137–WB148.

Cai, J., Tezkan, B., Li, Y., 2018. Effects of the sea floor topography on the 1D inversion of time-domain marine controlled source electromagnetic data. Geophysical Prospecting 66 (8), 1602–1624.

Cai, J., Tezkan, B., Yogeshwar, P., Mörbe, W., Cherevatova, M., Becken, M., Steuer, A., 2019. 1D joint inversion of HEM, LOTEM, and Semi-Airborne CSEM data - weighting and resolution analysis. In: In Protokoll über die 79. Jahrestagung der Deutschen Geophysikalischen Gesellschaft, Braunschweig.

Chave, A. D., Jones, A. G., 2012. The magnetotelluric method: Theory and practice. Cambridge University Press.

Cherevatova, M., Nittinger, C., Becken, M., Günther, T., 2017. 3D Inversion of the Semi-airborne Electromagnetic Data from Schleiz, Germany. In: Second European Airborne Electromagnetics Conference.

Cherevatova, M., Nittinger, C., Becken, M., Yogeshwar, P., Mörbe, W., Tezkan, B., Rochlitz, R., Günther, T., Petersen, H., Meyer, U., et al., 2018. Three-dimensional inversion of the semi-airborne data collected over ancient antimony mine in eastern Germany. In: EGU General Assembly Conference Abstracts. Vol. 20. p. 12143.

Chwala, A., Smit, J., Stolz, R., Zakosarenko, V., Schmelz, M., Fritzsch, L., Bauer, F., Starkloff, M., Meyer, H., 2011. Low temperature SQUID magnetometer systems for geophysical exploration with transient electromagnetics. Superconductor Science and Technology 24 (12), 125006.

Chwala, A., Stolz, R., Schmelz, M., Zakosarenko, V., Meyer, M., Meyer, H.-G., 2015. SQUID systems for geophysical time domain electromagnetics (TEM) at IPHT Jena. IEICE Transactions on Electronics 98 (3), 167–173.

Cole, K. S., Cole, R. H., 1941. Dispersion and absorption in dielectrics I. Alternating current characteristics. The Journal of chemical physics 9 (4), 341–351.

Commer, M., 2003. Three-dimensional inversion of transient-electromagnetic data: A comparative study. Ph.D. thesis, University of Cologne.

Constable, S. C., Parker, R. L., Constable, C. G., 1987. Occam's inversion: A practical algorithm for generating smooth models from electromagnetic sounding data. Geophysics 52 (3), 289–300.

Costabel, S., Martin, T., 2019. Petrophysikalische Untersuchungen zum Befliegungsgebiet Schleiz/Greiz im Rahmen des BMBF-geförderten Projektes DESMEX. Tech. rep., Bundesanstalt für Geowissenscheften und Rohstoffe, Hannover.

Dill, H. G., 1993. Die Antimonvorkommen der mitteleuropäischen Alpiden und Varisziden. Z Dtsch Geol Ges 144, 434–450.

Druskin, V., 1988. A spectral semi-discrete method for numerical solution of 3-D nonstationary problems in electrical prospecting. Phys. Sol. Earth 24, 641–648.

Edwards, R. N., 1997. On the resource evaluation of marine gas hydrate deposits using sea-floor transient electric dipole-dipole methods. Geophysics 62 (1), 63–74.

Egbert, G. D., Booker, J. R., 1986. Robust estimation of geomagnetic transfer functions. Geophysical Journal of the Royal Astronomical Society 87 (1), 173–194.

Farquharson, C., Oldenburg, D., 1996. Approximate sensitivities for the electromagnetic inverse problem. Geophysical Journal International 126 (1), 235–252.

Geophysica, 2019. Interpretation von Bohrlochmessdaten aus Bohrungen im Bereich des Bergaer Sattels – Thüringen.

Gräbe, R., Schlegel, G., Wiefel, H., 1996. Digitale geologische Karte von Thüringen 1:25000, Blatt 5436 Schleiz. Thüringer Landesanstalt für Umwelt und Geologie, Jena, Germany.

Grayver, A. V., Streich, R., Ritter, O., 2013. Three-dimensional parallel distributed inversion of CSEM data using a direct forward solver. Geophysical Journal International 193 (3), 1432–1446.

Günther, T., Rücker, C., 2012. Boundless electrical resistivity tomography (BERT) v. 2.0 open access software for advanced and flexible imaging. C. Herve, A. Adler, and B. Lionhart, eds 100, 177–180.

Hansen, P. C., O'Leary, D. P., 1993. The use of the l-curve in the regularization of discrete ill-posed problems. SIAM Journal on Scientific Computing 14 (6), 1487–1503.

Hanstein, T., Eilenz, H., Strack, K., 1986. Einige Aspekte der Aufbereitung von LOTEM Daten. In: Protokoll über das 11. Kolloquium 'Elektromagnetische Tiefenforschung'. pp. 319–328.

Haroon, A., 2016. Development of novel time-domain electromagnetic methods for offshore groundwater studies: A data application from bat yam, israel. Ph.D. thesis, University of Cologne.

Haroon, A., Adrian, J., Bergers, R., Gurk, M., Tezkan, B., Mammadov, A., Novruzov, A., 2015. Joint inversion of long-offset and central-loop transient electromagnetic data: Application to a mud volcano exploration in perekishkul, azerbaijan. Geophysical Prospecting 63 (2), 478–494.

Haroon, A., Hölz, S., Weymer, B., Tezkan, B., Jegen, M., 2018. Calculating Time-Domain Controlled Source Electromagnetic Signals with MARE2DEM. In: 3rd Applied Shallow Marine Geophysics Conference.

Hauser, J., Yogeshwar, P., Tezkan, B., 2016. Radiomagnetotellurische Messungen zur Erkundung der oberflächennahen Leitfähigkeitsstruktur bei Schleiz/ Thüringen. In: Protokoll über die 76. Jahrestagung der Dt. Geophys. Gesellschaft, Münster, Germany.

Hoheisel, A., 2000. Untersuchung des Einflusses von Induzierter Polarisation (IP) auf, Long-Offset Transient Electromagnetics (LOTEM). Master's thesis, University of Cologne, Institute for Geophysics and Meteorology.

Hoheisel, A., Hördt, A., Hanstein, T., 2004. The influence of induced polarization on long-offset transient electromagnetic data. Geophysical prospecting 52 (5), 417–426.

Hördt, A., 1992. Interpretation transient elektromagnetischer tiefensondierungen für anisotrop horizontal geschichtete und für dreidimensionale leitfähigkeitsstrukturen. Ph.D. thesis, Institute for Geophysics and Meteorology, University of Cologne.

Hördt, A., Dautel, S., Tezkan, B., Thern, H., 2000. Interpretation of long-offset transient electromagnetic data from the Odenwald area, Germany, using two-dimensional modelling. Geophysical Journal International 140 (3), 577–586.

Kaufman, A. A., Keller, G. V., 1983. Frequency and transient soundings. Chi-Yu King Roberto Scarpa 207, 7.

Key, K., 2016. MARE2DEM: a 2-D inversion code for controlled-source electromagnetic and magnetotelluric data. Geophysical Journal International 207 (1), 571–588.

Key, K., Du, Z., Mattsson, J., McKay, A., Midgley, J., 2014. Anisotropic 2.5 D inversion of Towed Streamer EM data from three North Sea fields using parallel adaptive finite elements. In: 76th EAGE Conference and Exhibition 2014.

Key, K., Ovall, J., 2011. A parallel goal-oriented adaptive finite element method for 2.5-D electromagnetic modelling. Geophysical Journal International 186 (1), 137–154.

Kingman, J. E., Halverson, M., Garner, S. J., 2004. Stacking of controlled source electrical geophysical data: Terrigena technical white paper number 20040328.0101(e).

Krolop, P., Burisch, M., Richter, L., Fritzke, B., Seifert, T., 2019. Antimoniferous vein-type mineralization of the Berga Antiform, Eastern-Thuringia, Germany: A fluid inclusion study. Chemical Geology 508, 47–61.

Kroner, U., Hahn, T., Romer, R. L., Linnemann, U., 2007. The Variscan orogeny in the Saxo-Thuringian zone-heterogenous overprint of Cadomian/Paleozoic Peri-Gondwana crust. Special Papers - Geological Society of America 423, 153.

Kunz, I., 1988. Lithologisch-geochemische bearbeitung der bohrungen demausel 1/63 und bernsgrün 1/63. Archive of Federal Institute for Geosciences and Natural Resources, Hannover, Germany.

Levenberg, K., 1944. A method for the solution of certain non-linear problems in least squares. Quarterly of applied mathematics 2 (2), 164–168.

Li, Y.-G., 2010. Transient electromagnetic in shallow water: insights from 1D modeling. Chinese J. Geophys 53, 737–742.

Liebe, K. T., Zimmermann, E., Kaiser, E., Weise, E., 1912. Digitale geologische Karte von Thüringen 1:25000, Blatt 5437 Mühltroff. Thüringer Landesanstalt für Umwelt und Geologie, Jena, Germany.

Lippert, K., 2015. Detektion eines submarinen aquifers vor der küste israels mittels mariner long offset transient-elektromagnetischer messung. Ph.D. thesis, University of Cologne.

Martin, R., 2009. Development and application of 2d and 3d transient electromagnetic inverse solutions based on adjoint green functions: A feasibility study for the spatial reconstruction of conductivity distributions by means of sensitivities. Ph.D. thesis, University of Cologne.

Martin, T., Flores-Orozco, A., Günther, T., Dahlin, T., 2018. Comparison of TDIP and SIP measurements in the field scale. In: 5th International Workshop on Induced Polarization.

Meju, M. A., 1994. Geophysical data analysis: understanding inverse problem theory and practice. Society of Exploration Geophysicists.

Menke, W., 2018. Geophysical data analysis: Discrete inverse theory. Academic press.

Müller, F., 2018. Tectonic 3D-model of the Berga antiform. Master's Thesis, University Freiberg.

Nabighian, M. N., Macnae, J. C., 1991. Time Domain Electromagnetic Prospecting Methods. In: Nabighian, M. N. (Ed.), Electromagnetic Methods in Applied Geophysics. Vol. 2. Society of Exploration Geophysicists, Ch. 6.

Newman, G. A., Hohmann, G. W., Anderson, W. L., 1986. Transient electromagnetic response of a three-dimensional body in a layered earth. Geophysics 51 (8), 1608–1627.

Nittinger, C., Cherevatova, M., Becken, M., Rochlitz, R., Günther, T., Martin, T., Matzander, U., 2017. Novel semi-airborne CSEM system for the exploration of mineral resources. In: EGU General Assembly Conference Abstracts. Vol. 19. p. 15439.

Oldenburg, D. W., Haber, E., Shekhtman, R., 2012. Three dimensional inversion of multisource time domain electromagnetic data. Geophysics 78 (1), E47–E57.

Ossen, D., 2017. Evaluation of TEM Data from Schleiz, Thuringia: 1D Inversion and 2D Modelling. Master's Thesis, University of Cologne.

Ovall, J. S., 2006. Asymptotically exact functional error estimators based on superconvergent gradient recovery. Numerische Mathematik 102 (3), 543–558.

Pankratov, O. V., Geraskin, A. I., 2010. On processing of controlled source electromagnetic (CSEM) data. Geologica acta 8 (1), 31–49.

Preugschat, B., 2019. Technischer Bericht: Erstellung eines integrierten 3D Untergrundmodells und Auswertung geophysikalischer Messungen mithilfe von künstlichen neuronalen Netzen anhand von geowissenschaftlichen Untersuchungen in Schleiz/Greiz in Thüringen. In: Report, BGR Hannover.

Rochlitz, R., Mörbe, W., Nittinger, C., Martin, T., Tezkan, B., 2017. DESMEX –Deep Electromagnetic Soundings for Mineral Exploration, Part II –Recent Results.

Rochlitz, R., Queitsch, M., Yogeshwar, P., Günther, T., Chwala, A., Janser, S., Kukowski, N., Stolz, R., 2018. Capability of low-temperature squid for transient electromagnetics under anthropogenic noise conditions. Geophysics 83 (6), E371–E383.

Rochlitz, R., Skibbe, N., Günther, T., 2019. custEM: Customizable finite-element simulation of complex controlled-source electromagnetic data. Geophysics 84 (2), F17–F33.

Schiffler, M., Chwala, A., Kukowski, N., Meyer, H. G., Meyer, M., Meyer, U., Stolz, R., 2017. Development of new magnetic field sensors for electromagnetic mineral exploration in the desmex project.

Schlegel, G., Wiefel, H., 1998. Erläuterungen zur Geologischen Karte 1 : 25.000 von Thüringen.

Scholl, C., 2001. Die Periodizität von Sendesignalen bei LOTEM. Diploma Thesis, University of Cologne.

Scholl, C., 2005. The influence of multidimensional structures on the interpretation of lotem data with one-dimensional models and the application to data from israel. Ph.D. thesis, University of Cologne.

Scholl, C., Edwards, R. N., 2007. Marine downhole to seafloor dipole-dipole electromagnetic methods and the resolution of resistive targets. Geophysics 72 (2), WA39–WA49.

Seidel, M., 2019. A 3D Time Domain CSEM Forward Modeling Code using custEM and FEniCS. Ph.D. thesis, University of Cologne.

Sengpiel, K.-P., Siemon, B., 2000. Advanced inversion methods for airborne electromagnetic exploration. Geophysics 65 (6), 1983–1992.

Siemon, B., Steuer, A., Ullmann, A., Vasterling, M., Voß, W., 2011. Application of frequency-domain helicopter-borne electromagnetics for groundwater exploration in urban areas. Physics and Chemistry of the Earth, Parts A/B/C 36 (16), 1373–1385.

Smirnova, M., Juhojuntti, N., Becken, M., Smirnov, M., Yogeshwar, P., Steuer, A., Rochlitz, R., Schiffler, M., 2019a. Combined 3D Inversion of Ground and Airborne Electromagnetic Data over Iron Ore in Kiruna. In: 25th European Meeting of Environmental and Engineering Geophysics.

Smirnova, M. V., Becken, M., Nittinger, C., Yogeshwar, P., Mörbe, W., Rochlitz, R., Steuer, A., Costabel, S., Smirnov, M. Y., Group, D. W., et al., 2019b. A novel semi-airborne frequency-domain CSEM system. Three-dimensional inversion of semi-airborne data from the flight experiment over an ancient mining area near Schleiz, Germany. Geophysics.

Spagnoli, G., Hannington, M., Bairlein, K., Hördt, A., Jegen, M., Petersen, S., Laurila, T., 2016. Electrical properties of seafloor massive sulfides. Geo-Marine Letters 36 (3), 235–245.

Spies, B. R., 1989. Depth of investigation in electromagnetic sounding methods. Geophysics 54 (7), 872–888.

Steuer, A., Siemon, B., Pielawa, J., Petersen, H., Vob, V., Balzer, H. U., Plath, C., 2015. Zwischenbericht hubschraubergeophysik befliegung desmex teil 1. Tech. rep., Bundesanstalt für Geowissenscheften und Rohstoffe, Hannover.

Stolz, R., 2015. SQUIDS in geophysics, in applied superconductivity: Handbook on devices and applications. John Wiley & Sons.

Strack, K.-M., 1992. Exploration with deep transient electromagnetics. Vol. 373. Elsevier Amsterdam.

Strack, K.-M., Lüschen, E., Kötz, A., 1990. Long-offset transient electromagnetic (LOTEM) depth soundings applied to crustal studies in the Black Forest and Swabian Alb, Federal Republic of Germany. Geophysics 55 (7), 834–842.

Streich, R., 2016. Controlled-source electromagnetic approaches for hydrocarbon exploration and monitoring on land. Surveys in Geophysics 37 (1), 47–80.

Streich, R., Becken, M., Matzander, U., Ritter, O., 2011. Strategies for land-based controlled-source electromagnetic surveying in high-noise regions. The Leading Edge 30 (10), 1174–1181.

Telford, W. M., Telford, W., Geldart, L., Sheriff, R. E., Sheriff, R., 1990. Applied geophysics. Vol. 1. Cambridge university press.

Tikhonov, A. N., Arsenin, V. I., 1977. Solutions of ill-posed problems. Vol. 14. Winston, Washington, DC.

Wagenbreth, O., 1946. Die Antimon Lagerstätte der Grube Halber Mond bei Oberböhmsdorf bei Schleiz.

Ward, S., 1990. Resistivity and induced polarization methods geotechnical and environment geophysics. vol. 1, hal. 147. Tulsa. SEG.

Ward, S. H., Hohmann, G. W., 1988. Electromagnetic theory for geophysical applications. In: Electromagnetic Methods in Applied Geophysics: Voume 1, Theory. Society of Exploration Geophysicists, pp. 130–311.

Weidelt, P., 1986. Einführung in die elektromagnetische Tiefenforschung. Lecture Technische Universät Braunschweig.

Wheelock, B., Constable, S., Key, K., 2015. The advantages of logarithmically scaled data for electromagnetic inversion. Geophysical Journal International 201 (3), 1765–1780.

Witherly, K., 2000. The quest for the Holy Grail in mining geophysics: A review of the development and application of airborne EM systems over the last 50 years. The Leading Edge 19 (3), 270–274.

Yogeshwar, P., 2014. A resistivity-depth model of the central Azraq basin area, Jordan: 2D forward and inverse modeling of time domain electromagnetic data. Ph.D. thesis, University of Cologne.

Yogeshwar, P., Tezkan, B., Haroon, A., 2013. Investigation of the Azraq sedimentary basin, Jordan using integrated geoelectrical and electromagnetic techniques. Near Surface Geophysics 11 (4), 381–389.

Zhdanov, M. S., 2002. Geophysical inverse theory and regularization problems. Vol. 36. Elsevier.

Zhdanov, M. S., 2010. Electromagnetic geophysics: Notes from the past and the road ahead. Geophysics 75 (5), 75A49–75A66.

Ziolkowski, A., Hobbs, B. A., Wright, D., 2007. Multitransient electromagnetic demonstration survey in France. Geophysics 72 (4), F197–F209.

Ziolkowski, A., Slob, E., 2019. Introduction to Controlled-source Electromagnetic Methods: Detecting Subsurface Fluids. Cambridge University Press.

# Appendix

# A. Survey Setup

In this section, setup specific information will be given. Survey parameters for both, transmitter and receivers are listed. Figure A.1 shows the setup of the LOTEM study with corresponding names of the receiver stations and transmitters along the profile. The zero point of the profile hereby corresponds to the definitions as utilized in the 2D inversion setup files. Tables A.1-A.2 list the location of each transmitter and receiver station in terms of latitude and longitude as well as relative position along the profile for the electric field dataset and induction coil data, if available. Tables A.3-A.8 list survey parameters in detail for each electric field (+ induction coil) station per transmitter. Furthermore, the tables list, if processing was performed in time or frequency domain or both. Additional information is given in the comment section, e.g. if the time series exhibits a time shift or a high noise level. Information about the SQUID dataset is given in table A.9. Since SQUID data was recorded using only one transmitter per station, all information is comprised in one list. Influence of the transmitter ramp in frequency domain (cp. Figure A.2) and influence of the sampling rate to transient recording (cp. Figure A.3) is shown afterwards.

## A.1. Overview over Transmitter and Receiver Stations

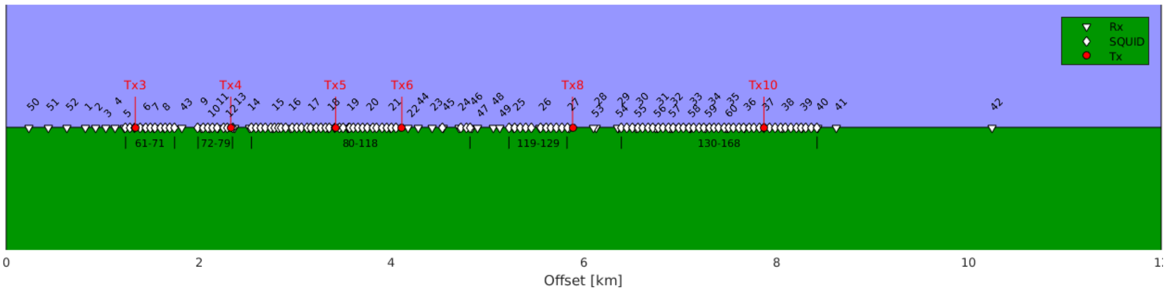

**Figure A.1.:** Receiver and transmitter locations and corresponding names along the profile

**Table A.1.:** Location and dipole length of utilized transmitters

| Transmitter | Latitude | Longitude | Profile x | Profile y | Length |
|---|---|---|---|---|---|
| Tx 5 | 50,55233 | 11,8586 | 29 | 3422 | 1052 |
| Tx 4 | 50,55997 | 11,84898 | -4 | 2333 | 947 |
| Tx 3 | 50,56694 | 11,8402 | -34 | 1340 | 970 |
| Tx 6 | 50,54751 | 11,86471 | 48 | 4111 | 1043 |
| Tx 8 | 50,535945 | 11,882025 | -51 | 5885 | 949 |
| Tx 10 | 50,52207 | 11,89968 | -3 | 7872 | 970 |

**Table A.2.:** Location of electric field receiver stations. Whether additional induction coil data is present and which transmitters were utilized is listed in column 6 and 7.

| Rx | Latitude | Longitude | Profile x | Profile y | Add. dBz/dt | Tx |
|---|---|---|---|---|---|---|
| 1 | 50.570554 | 11.835667 | -50 | 826 | ✓ | 3,4,5,6 |
| 2 | 50.569636 | 11.836292 | -18 | 933 | X | 3,4,6 |
| 3 | 50.569106 | 11.837501 | -44 | 1033 | X | 3,4,5,6 |
| 4 | 50.568226 | 11.83804 | -10 | 1132 | X | 4,5,6 |
| 5 | 50.567724 | 11.839226 | -38 | 1229 | X | 4,5,6 |
| 6 | 50.566302 | 11.841104 | -36 | 1436 | ✓ | 4,5,6 |
| 7 | 50.565352 | 11.841539 | 9 | 1536 | X | 4,5,6 |
| 8 | 50.564665 | 11.842544 | 4 | 1640 | X | 3,4,5,6 |
| 9 | 50.561884 | 11.84595 | 22 | 2032 | X | 3,4,5,6 |
| 10 | 50.561438 | 11.846861 | 5 | 2112 | X | 3,5,6,8 |
| 11 | 50.56093 | 11.847751 | -7 | 2196 | ✓ | 3,5,6,8 |
| 12 | 50.560188 | 11.848557 | 3 | 2295 | X | 3,5,6 |
| 13 | 50.559454 | 11.848938 | 36 | 2375 | X | 3,5,6 |
| 14 | 50.558634 | 11.850701 | 0 | 2525 | X | 3,5,6,8 |
| 15 | 50.556696 | 11.852487 | 44 | 2772 | ✓ | 3,4,5,6,8 |
| 16 | 50.556398 | 11.855786 | -113 | 2948 | X | 3,4,5,6,8,10 |
| 17 | 50.554484 | 11.856712 | -24 | 3153 | X | 3,6,8,10 |
| 18 | 50.553249 | 11.858662 | -40 | 3347 | X | 3,4,6,8,10 |
| 19 | 50.551359 | 11.85965 | 43 | 3552 | ✓ | 3,4,6,8 |
| 20 | 50.550048 | 11.861614 | 31 | 3754 | X | 3,4,5,6,8,10 |
| 21 | 50.54818 | 11.863322 | 74 | 3990 | ✓ | 3,4,5,8,10 |
| 22 | 50.54707 | 11.865355 | 45 | 4178 | X | 3,4,5,8,10 |
| 23 | 50.545613 | 11.868057 | 4 | 4425 | X | 3,4,5,8,10 |
| 24 | 50.543397 | 11.870123 | 53 | 4708 | ✓ | 3,4,5,6,8,10 |
| 25 | 50.539329 | 11.874996 | 83 | 5276 | ✓ | 3,4,5,6,8,10 |
| 26 | 50.537239 | 11.876995 | 126 | 5545 | X | 4,6,10 |
| 27 | 50.535334 | 11.880031 | 100 | 5846 | ✓ | 3,4,5,6,10 |
| 28 | 50.533304 | 11.882439 | 117 | 6128 | X | 4,6 |
| 29 | 50.531688 | 11.884579 | 118 | 6363 | X | 4,5,6 |
| 30 | 50.530304 | 11.886344 | 123 | 6562 | X | 5,6 |
| 31 | 50.528875 | 11.888119 | 130 | 6764 | X | 5,6 |
| 32 | 50.528071 | 11.88991 | 91 | 6915 | ✓ | 5,6 |
| 33 | 50.526686 | 11.891739 | 93 | 7116 | X | 5,6 |
| 34 | 50.525077 | 11.892897 | 146 | 7306 | X | 5,6 |
| 35 | 50.523739 | 11.894592 | 151 | 7497 | ✓ | 5,6 |

| Rx | Latitude | Longitude | Profile x | Profile y | Add. dBz/dt | Tx |
|---|---|---|---|---|---|---|
| 36 | 50.52341 | 11.8978 | 2 | 7672 | X | 8 |
| 37 | 50.521856 | 11.899223 | 37 | 7869 | X | 8 |
| 38 | 50.520527 | 11.901058 | 34 | 8066 | X | 8 |
| 39 | 50.519286 | 11.903095 | 14 | 8264 | X | 8 |
| 40 | 50.518384 | 11.905048 | -26 | 8431 | X | failed |
| 41 | 50.516713 | 11.90616 | 34 | 8623 | X | 8,10 |
| 42 | 50.505942 | 11.921519 | -18 | 10242 | X | 10 |
| 43 | 50.563253 | 11.843926 | 32 | 1823 | X | 5,8 |
| 44 | 50.546669 | 11.866813 | -5 | 4278 | X | 5,8,10 |
| 45 | 50.544781 | 11.869051 | 11 | 4541 | X | 5,8,10 |
| 46 | 50.542969 | 11.872165 | -26 | 4838 | X | 5,8 |
| 47 | 50.542674 | 11.872986 | -49 | 4900 | X | 5,8 |
| 48 | 50.541383 | 11.874032 | -13 | 5058 | X | 8,10 |
| 49 | 50.540625 | 11.874177 | 34 | 5129 | X | 5,8,10 |
| 50 | 50.574313 | 11.829684 | 1 | 233 | X | 5 |
| 51 | 50.572938 | 11.831535 | 0 | 435 | X | 5 |
| 52 | 50.571586 | 11.833355 | 0 | 633 | X | 5 |
| 53 | 50.533172 | 11.881545 | 174 | 6098 | X | 10 |
| 54 | 50.53249 | 11.885712 | -1 | 6347 | X | 10 |
| 55 | 50.53115 | 11.887464 | 1 | 6541 | X | 8,10 |
| 56 | 50.529778 | 11.889316 | 0 | 6743 | X | 8,10 |
| 57 | 50.528704 | 11.890756 | 0 | 6900 | X | 8,10 |
| 58 | 50.52734 | 11.89256 | 1 | 7098 | X | 8,10 |
| 59 | 50.526181 | 11.894124 | 0 | 7268 | X | 8 |
| 60 | 50.524719 | 11.896083 | 0 | 7482 | X | 8 |

**Table A.3.:** Settings for obtained electric field stations utilizing transmitter 3. Column 5 gives the dipole length of the electric field receiver. Column 6 gives the offset to the transmitter. Column 7 and 8 give information, if the data was processed in time (TD) and/or frequency domain (TF). If additional transient magnetic field data is obtained is given in column 10. SR=Sign reversal in transient.

| Name | $T_{switch}$ | DC | I[A] | dl[m] | Offset[km] | TD | TF | Comment | $dB_z/dt$ |
|---|---|---|---|---|---|---|---|---|---|
| 1 | 1050 | 50% | 10 | 58.5 | 0.514 | ✓ | ✓ | | Loop, SR |
| 2 | 1050 | 50% | 10 | 60.3 | 0.408 | ✓ | ✓ | | |
| 3 | 1050 | 50% | 10 | 59.6 | 0.307 | ✓ | ✓ | | |
| 8 | 1050 | 50% | 9 | 58.5 | 0.303 | ✓ | ✓ | | |
| 9 | 1050 | 50% | 9 | 58.7 | 0.694 | ✓ | ✓ | | |
| 10 | 1050 | 50% | 10 | 40 | 0.773 | ✓ | X | Time Shift | |
| 11 | 1050 | 50% | 10 | 59 | 0.856 | ✓ | X | | Loop, SR |
| 12 | 1050 | 50% | 10 | 40 | 0.956 | ✓ | ✓ | | |
| 13 | 1050 | 50% | 9 | 59.7 | 1.037 | ✓ | ✓ | | |
| 14 | 1050 | 50% | 10 | 60 | 1.186 | ✓ | X | Time Shift | |
| 15 | 1050 | 50% | 9 | 40.3 | 1.433 | ✓ | ✓ | | |
| 16 | 1050 | 50% | 10 | 40 | 1.610 | ✓ | X | Time Shift | |
| 17 | 1050 | 50% | 10 | 39.9 | 1.813 | ✓ | ✓ | | |
| 18 | 1050 | 50% | 10 | 40 | 2.007 | ✓ | ✓ | | |
| 19 | 1050 | 50% | 9 | 10.7 | 2.213 | ✓ | ✓ | | Loop, SR |
| 20 | 1050 | 50% | 10 | 63 | 2.414 | ✓ | ✓ | | |
| 21 | 1050 | 50% | 10 | 64.5 | 2.652 | ✓ | ✓ | | Loop, SR |
| 22 | 1050 | 50% | 10 | 41 | 2.838 | ✓ | X | Time Shift | |
| 23 | 1050 | 50% | 9 | 36.9 | 3.085 | ✓ | ✓ | | |
| 24 | 1050 | 50% | 9 | 58.5 | 3.368 | ✓ | ✓ | | Coil, SR |
| 25 | 1050 | 50% | 10 | 56.5 | 3.937 | ✓ | ✓ | | Coil, SR |
| 26 | 1050 | 50% | 9 | 59.7/35.7 | 4.207 | X | X | Time Shift | |
| 27 | 1050 | 50% | 10 | 59 | 4.507 | ✓ | ✓ | Power Line | |
| 28 | 1050 | 50% | 10 | 59.6 | 4.790 | X | X | Power Line | |

**Table A.4.:** Settings for obtained electric field stations utilizing transmitter 4. Column 5 gives the dipole length of the electric field receiver. Column 6 gives the offset to the transmitter. Column 7 and 8 give information, if the data was processed in time (TD) and/or frequency domain (TF). If additional transient magnetic field data is obtained is given in column 10. SR=Sign reversal in transient.

| Name | $T_{switch}$ | DC | I[A] | dl[m] | Offset[km] | TD | TF | Comment | $dB_z/dt$ |
|---|---|---|---|---|---|---|---|---|---|
| 1 | 1000 | 50% | 16 | 58.5 | 1.508 | ✓ | ✓ | | Loop, SR |
| 2 | 1050 | 50% | 16 | 60.3 | 1.401 | ✓ | ✓ | | |
| 3 | 1050 | 50% | 18 | 59.6 | 1.301 | ✓ | ✓ | | |
| 4 | 1050 | 50% | 16 | 59.8 | 1.201 | ✓ | ✓ | | |
| 5 | 1050 | 50% | 18 | 60.8 | 1.105 | ✓ | ✓ | | |
| 6 | 1000 | 50% | 16 | 58.2 | 0.898 | ✓ | ✓ | | |
| 7 | 1050 | 50% | 18 | 40 | 0.797 | ✓ | ✓ | | |
| 8 | 1050 | 50% | 18 | 58.5 | 0.693 | ✓ | ✓ | | |
| 9 | 1050 | 50% | 18 | 58.7 | 0.302 | ✓ | X | Time Shift | |
| 15 | 1050 | 50% | 18 | 40.3 | 0.441 | ✓ | ✓ | | Loop, SR |
| 16 | 1050 | 50% | 18 | 40.4 | 0.624 | ✓ | ✓ | | |
| 17 | 1050 | 50% | 16 | 39.9 | 0.82 | ✓ | X | | |
| 18 | 1050 | 50% | 16 | 39.9 | 1.014 | ✓ | X | | |
| 19 | 1050 | 50% | 16 | 10.7 | 1.220 | ✓ | ✓ | | Loop, SR |
| 20 | 1050 | 50% | 16 | 63 | 1.421 | ✓ | X | Time Shift | |
| 21 | 1000 | 50% | 16 | 64.5 | 1.659 | ✓ | ✓ | | Loop, SR |
| 22 | 1050 | 50% | 18 | 41 | 1.845 | ✓ | ✓ | | |
| 23 | 1050 | 50% | 18 | 36.9 | 2.091 | ✓ | X | Time Shift | |
| 24 | 1000 | 50% | 16 | 58.5 | 2.375 | ✓ | ✓ | | Loop, SR |
| 25 | 1000 | 50% | 16 | 56.5 | 2.944 | ✓ | ✓ | | Coil |
| 26 | 1000 | 50% | 16 | 59.7/35.7 | 3.214 | ✓ | X | No GPS | |
| 27 | 1000 | 50% | 16 | 59 | 3.513 | ✓ | X | Time Shift | |
| 28 | 1000 | 50% | 16 | 59.6 | 3.796 | ✓ | X | No GPS | |
| 29 | 1050 | 50% | 18 | 61.7 | 4.031 | ✓ | X | No Tx file | |

**Table A.5.:** Settings for obtained electric field stations utilizing transmitter 5. Column 5 gives the dipole length of the electric field receiver. Column 6 gives the offset to the transmitter. Column 7 and 8 give information, if the data was processed in time (TD) and/or frequency domain (TF). If additional transient magnetic field data is obtained is given in column 10. SR=Sign reversal in transient.

| Name | $T_{switch}$ | DC | I[A] | dl[m] | Offset[km] | TD | TF | Comment | $dB_z/dt$ |
|---|---|---|---|---|---|---|---|---|---|
| 1 | 500 | 100% | 11 | 58.5 | 2.597 | ✓ | X | Time Shift | Loop, SR |
| 3 | 500 | 50% | 10 | 59.6 | 2.390 | ✓ | X | Time Shift | |
| 4 | 1050 | 50% | 9.5 | 59.8 | 2.290 | ✓ | ✓ | | |
| 5 | 500 | 50% | 10 | 60.8 | 2.194 | ✓ | ✓ | 25 kHz | |
| 6 | 1050 | 50% | 9.5 | 58.2 | 1.987 | ✓ | X | Time Shift | |
| 7 | 1050 | 50% | 9.5 | 41 | 1.886 | ✓ | ✓ | | |
| 8 | 1050 | 50% | 9.5 | 58.5 | 1.781 | ✓ | ✓ | | |
| 9 | 1050 | 50% | 9.5 | 58.7 | 1.389 | ✓ | ✓ | | |
| 10 | 1050 | 50% | 9.5 | 40 | 1.310 | ✓ | ✓ | | |
| 11 | 500 | 100% | 22 | 59 | 1.227 | ✓ | X | Time Shift | Loop, SR |
| 12 | 1050 | 50% | 9.5 | 40 | 1.127 | ✓ | X | Time Shift | |
| 13 | 1050 | 50% | 9.5 | 59.7 | 1.047 | ✓ | ✓ | | |
| 14 | 1050 | 50% | 9.5 | 60 | 0.897 | ✓ | ✓ | | |
| 15 | 500 | 50% | 10 | 40.3 | 0.650 | ✓ | X | Time Shift | |
| 16 | 1050 | 50% | 9.5 | 40.4 | 0.495 | ✓ | X | Time Shift | |
| 20 | 1050 | 50% | 9.5 | 63 | 0.332 | ✓ | ✓ | | |
| 21 | 500 | 100% | 22 | 64.5 | 0.570 | ✓ | X | Time Shift | Loop, SR |
| 22 | 1050 | 50% | 9.5 | 41 | 0.756 | ✓ | ✓ | | |
| 23 | 1050 | 50% | 9.5 | 36.9 | 1.003 | ✓ | ✓ | | |
| 24 | 500 | 50% | 10 | 58.5 | 1.286 | ✓ | ✓ | 25 kHz | Coil |
| 25 | 500 | 50% | 11 | 56.5 | 1.854 | ✓ | X | | |
| 27 | 810 | 50% | 7 | 59 | 2.424 | ✓ | ✓ | TX 2000m | Loop, SR |
| 29 | 500 | 50% | 11 | 61.7 | 2.942 | ✓ | X | Time Shift | |
| 30 | 500 | 50% | 10 | 58.4 | 3.141 | ✓ | ✓ | | |
| 31 | 500 | 50% | 11 | 56.7 | 3.343 | ✓ | X | Time Shift | |
| 32 | 500 | 100% | 22 | 59.4 | 3.493 | ✓ | X | Time Shift | Loop, SR |
| 33 | 500 | 50% | 10 | 60.5 | 3.694 | ✓ | ✓ | | |
| 34 | 500 | 50% | 10 | 57.8 | 3.885 | ✓ | ✓ | | |
| 35 | 500 | 100% | 22 | 53.1 | 4.076 | ✓ | X | Time Shift | Loop, SR |
| 43 | 810 | 50% | 12 | 61.7 | 1.598 | ✓ | ✓ | | |
| 44 | 810 | 50% | 12 | 60.4 | 0.857 | ✓ | ✓ | | |
| 45 | 810 | 50% | 12 | 44.4 | 1.119 | ✓ | ✓ | | |
| 46 | 810 | 50% | 12 | 62.5 | 1.416 | ✓ | ✓ | | |
| 47 | 810 | 50% | 12 | 45 | 1.480 | ✓ | ✓ | | |
| 48 | 810 | 50% | 7 | 48.7 | 1.636 | ✓ | ✓ | TX 2000m | |
| 49 | 810 | 50% | 12 | 48.7 | 1.706 | ✓ | ✓ | | |
| 50 | 810 | 50% | 12 | 58.3 | 3.188 | ✓ | ✓ | | |
| 51 | 810 | 50% | 12 | 57.4 | 2.987 | ✓ | ✓ | | |
| 52 | 810 | 50% | 12 | 59 | 2.789 | ✓ | ✓ | | |

**Table A.6.:** Settings for obtained electric field stations utilizing transmitter 6. Column 5 gives the dipole length of the electric field receiver. Column 6 gives the offset to the transmitter. Column 7 and 8 give information, if the data was processed in time (TD) and/or frequency domain (TF). If additional transient magnetic field data is obtained is given in column 10. SR=Sign reversal in transient.

| Name | $T_{switch}$ | DC | I[A] | dl[m] | Offset[km] | TD | TF | Comment | $dB_z/dt$ |
|---|---|---|---|---|---|---|---|---|---|
| 1 | 1000 | 50% | 11 | 58.5 | 3.285 | ✓ | ✓ |  | Loop, SR |
| 2 | 1050 | 50% | 13 | 60.3 | 3.178 | ✓ | ✓ |  |  |
| 3 | 1050 | 50% | 12 | 59.6 | 3.078 | ✓ | ✓ |  |  |
| 4 | 1050 | 50% | 13 | 59.8 | 2.978 | ✓ | ✓ |  |  |
| 5 | 1050 | 50% | 12 | 60.8 | 2.882 | ✓ | ✓ |  |  |
| 6 | 1050 | 50% | 12 | 58.2 | 2.676 | ✓ | ✓ |  | Loop, SR |
| 7 | 1050 | 50% | 13 | 41 | 2.574 | ✓ | ✓ |  |  |
| 8 | 1050 | 50% | 12 | 58.5 | 2.470 | ✓ | ✓ |  |  |
| 9 | 1050 | 50% | 12 | 58.7 | 2.078 | ✓ | ✓ |  |  |
| 10 | 1050 | 50% | 12 | 40 | 1.999 | ✓ | X | time shift |  |
| 11 | 1000 | 50% | 11 | 59 | 1.915 | ✓ | ✓ |  | Loop, SR |
| 12 | 1050 | 50% | 12 | 40 | 1.815 | ✓ | X | time shift |  |
| 13 | 1050 | 50% | 12 | 59.7 | 1.735 | ✓ | X | no sync |  |
| 14 | 1050 | 50% | 12 | 60 | 1.586 | ✓ | ✓ |  |  |
| 15 | 1050 | 50% | 12 | 40.3 | 1.339 | ✓ | ✓ |  | Loop, SR |
| 16 | 1050 | 50% | 13 | 40.4 | 1.173 | ✓ | ✓ |  |  |
| 17 | 1050 | 50% | 13 | 39.9 | 0.960 | ✓ | ✓ |  |  |
| 18 | 1050 | 50% | 13 | 39.9 | 0.769 | ✓ | X | time shift |  |
| 19 | 1050 | 50% | 13 | 10.7 | 0.558 | ✓ | ✓ |  | Loop, SR |
| 20 | 1050 | 50% | 13 | 63 | 0.357 | ✓ | X | time shift |  |
| 24 | 1050 | 50% | 13 | 58.5 | 0.597 | ✓ | ✓ |  | Coil, SR |
| 25 | 500 | 50% | 12.5 | 56.5 | 1.166 | ✓ | X | time shift | Coil, SR |
| 26 | 1000 | 50% | 11 | 35.7 | 1.436 | ✓ | ✓ |  |  |
| 27 | 1000 | 50% | 11 | 59 | 1.735 | ✓ | ✓ |  | Loop, SR |
| 28 | 1000 | 50% | 11 | 59.6 | 2.018 | ✓ | ✓ |  |  |
| 29 | 500 | 50% | 12.5 | 61.7 | 2.253 | ✓ | ✓ |  |  |
| 30 | 1050 | 50% | 12 | 58.4 | 2.452 | ✓ | X |  |  |
| 31 | 500 | 50% | 12.5 | 56.7 | 2.654 | ✓ | ✓ |  |  |
| 32 | 1000 | 50% | 11 | 59.4 | 2.804 | ✓ | ✓ |  | Loop, SR |
| 33 | 1000 | 50% | 11 | 60.5 | 3.005 | ✓ | ✓ |  |  |
| 34 | 500 | 50% | 12.5 | 57.8 | 3.196 | ✓ | ✓ |  |  |
| 35 | 500 | 50% | 12.5 | 53.1 | 3.387 | ✓ | ✓ |  | Loop, SR |

**Table A.7.:** Settings for obtained electric field stations utilizing transmitter 8. Column 5 gives the dipole length of the electric field receiver. Column 6 gives the offset to the transmitter. Column 7 and 8 give information, if the data was processed in time (TD) and/or frequency domain (TF). If additional transient magnetic field data is obtained is given in column 10. SR=Sign reversal in transient.

| Name | $T_{switch}$ | DC | I[A] | dl[m] | Offset[km] | TD | TF | Comment |
|---|---|---|---|---|---|---|---|---|
| 10 | 810 | 50% | 13 | 58.5 | 3.773 | ✓ | ✓ | |
| 11 | 810 | 50% | 13 | 55.2 | 3.689 | ✓ | ✓ | |
| 14 | 810 | 50% | 13 | 54.7 | 3.359 | ✓ | ✓ | |
| 15 | 810 | 50% | 13 | 49.7 | 3.114 | ✓ | ✓ | |
| 16 | 810 | 50% | 13 | 44.4 | 2.937 | ✓ | ✓ | |
| 17 | 810 | 50% | 13 | 46 | 2.732 | ✓ | ✓ | |
| 18 | 810 | 50% | 13 | 32.7 | 2.537 | ✓ | ✓ | |
| 19 | 810 | 50% | 13 | 60.4 | 2.334 | ✓ | ✓ | |
| 20 | 810 | 50% | 13 | 56.7 | 2.132 | ✓ | ✓ | |
| 21 | 810 | 50% | 13 | 58 | 1.898 | ✓ | ✓ | |
| 22 | 810 | 50% | 13 | 38.8 | 1.710 | ✓ | ✓ | |
| 23 | 810 | 50% | 13 | 72.3 | 1.461 | ✓ | ✓ | |
| 24 | 810 | 50% | 13 | 52.1 | 1.182 | ✓ | ✓ | |
| 25 | 810 | 50% | 13 | 58.6 | 0.624 | ✓ | ✓ | |
| 36 | 810 | 50% | 13 | 62 | 1.787 | ✓ | ✓ | |
| 37 | 810 | 50% | 13 | 57.3 | 1.985 | ✓ | ✓ | |
| 38 | 810 | 50% | 13 | 58.1 | 2.181 | ✓ | ✓ | |
| 39 | 810 | 50% | 13 | 59.7 | 2.379 | ✓ | ✓ | |
| 40 | 810 | 50% | 13 | - | 2.545 | Failed | - | |
| 41 | 810 | 50% | 13 | 57.8 | 2.738 | ✓ | ✓ | |
| 43 | 810 | 50% | 13 | 61.7 | 4.061 | ✓ | X | |
| 44 | 810 | 50% | 13 | 60.4 | 1.607 | ✓ | ✓ | |
| 45 | 810 | 50% | 13 | 44.4 | 1.345 | ✓ | ✓ | |
| 46 | 810 | 50% | 13 | 62.5 | 1.048 | ✓ | ✓ | |
| 47 | 810 | 50% | 13 | 45 | 0.985 | ✓ | ✓ | |
| 48 | 810 | 50% | 13 | 35.2 | 0.828 | ✓ | ✓ | |
| 49 | 810 | 50% | 13 | 48.7 | 0.761 | ✓ | ✓ | |
| 55 | 810 | 50% | 13 | 58.1 | 0.658 | ✓ | ✓ | |
| 56 | 810 | 50% | 13 | 56.8 | 0.859 | ✓ | ✓ | |
| 57 | 810 | 50% | 13 | 60 | 1.015 | ✓ | ✓ | |
| 58 | 810 | 50% | 13 | 60 | 1.214 | ✓ | ✓ | |
| 59 | 810 | 50% | 13 | 60 | 1.383 | ✓ | ✓ | |
| 60 | 810 | 50% | 13 | 59.1 | 1.597 | ✓ | ✓ | |

**Table A.8.:** Settings for obtained electric field stations utilizing transmitter 10. Column 5 gives the dipole length of the electric field receiver. Column 6 gives the offset to the transmitter. Column 7 and 8 give information, if the data was processed in time (TD) and/or frequency domain (TF). If additional transient magnetic field data is obtained is given in column 10. SR=Sign reversal in transient.

| Name | $T_{switch}$ | DC | I[A] | dl[m] | Offset[km] | TD | TF | Comment |
|---|---|---|---|---|---|---|---|---|
| 16 | 810 | 50% | 22.4-22.9 | 44.4 | 4.921 | ✓ | ✓ | |
| 17 | 810 | 50% | 22.4-22.9 | 46 | 4.717 | ✓ | ✓ | |
| 18 | 810 | 50% | 22.4-22.9 | 32.7 | 4.523 | ✓ | ✓ | |
| 19 | 450 | 50% | 21 | 60.4 | 4.317 | X | ok | noisy |
| 20 | 450 | 50% | 21 | 56.7 | 4.116 | ✓ | ✓ | |
| 21 | 450 | 50% | 21 | 58 | 3.880 | ✓ | ✓ | |
| 22 | 450 | 50% | 21 | 38.8 | 3.692 | ✓ | ✓ | |
| 23 | 810 | 50% | 21 | 72.3 | 3.445 | ✓ | ✓ | |
| 24 | 810 | 50% | 21 | 52.1 | 3.163 | ✓ | ✓ | |
| 25 | 810 | 50% | 21 | 58.6 | 2.596 | ✓ | ✓ | |
| 26 | 810 | 50% | 21 | 57 | 2.329 | ✓ | ✓ | |
| 27 | 810 | 50% | 21 | 56,5 | 2.028 | ✓ | X | |
| 41 | 450 | 50% | 21 | 57.8 | 0.751 | ✓ | ✓ | |
| 42 | 810 | 50% | 22.4-22.9 | 47.3 | 2.369 | ✓ | ✓ | |
| 44 | 810 | 50% | 21 | 60.4 | 3.592 | ✓ | ✓ | |
| 45 | 810 | 50% | 21 | 44.4 | 3.329 | ✓ | ✓ | |
| 48 | 810 | 50% | 21 | 35.2 | 2.813 | ✓ | ✓ | |
| 49 | 810 | 50% | 21 | 48.7 | 2.742 | ✓ | ✓ | |
| 53 | 810 | 50% | 21 | 29.6 | 1.781 | ✓ | ✓ | |
| 54 | 810 | 50% | 22.4-22.9 | 56.1 | 1.524 | ✓ | ✓ | |
| 55 | 810 | 50% | 22.4-22.9 | 58.1 | 1.330 | ✓ | ✓ | |
| 56 | 810 | 50% | 22.4-22.9 | 56.8 | 1.129 | ✓ | ✓ | |
| 57 | 450 | 50% | 21 | 60 | 0.972 | X | X | |
| 58 | 810 | 50% | 22.4-22.9 | 60 | 0.773 | ✓ | ✓ | |

**Table A.9.:** Location of SQUID receiver stations, the utilized transmitter, switching time, current amplitude and offset to the corresponding transmitter. The last column lists if a transfer function (TF) was obtained.

| Rx | Latitude | Longitude | x | y | Tx | $T_{switch}$ | I[A] | Offset[km] | TF |
|---|---|---|---|---|---|---|---|---|---|
| 61 | 50.56751 | 11.839099 | -15 | 1241 | - | 1050 | 18 | 1.092 | no Tx File |
| 62 | 50.567169 | 11.839526 | -14 | 1290 | Tx4 | 1050 | 18 | 1.043 | ✓ |
| 63 | 50.56683 | 11.839915 | -10 | 1336 | Tx4 | 1050 | 18 | 0.997 | ✓ |
| 64 | 50.566426 | 11.840338 | -4 | 1390 | Tx4 | 1050 | 18 | 0.943 | ✓ |
| 65 | 50.565884 | 11.840611 | 21 | 1448 | Tx4 | 1050 | 18 | 0.885 | ✓ |
| 66 | 50.565473 | 11.840913 | 34 | 1497 | Tx4,Tx5 | 1050 | 18 | 0.837/1.924 | ✓ |
| 67 | 50.565107 | 11.841383 | 35 | 1550 | Tx5 | 500 | 10 | 1.872 | ✓ |
| 68 | 50.564758 | 11.84182 | 37 | 1599 | Tx5 | 500 | 10 | 1.822 | ✓ |
| 69 | 50.564429 | 11.842311 | 34 | 1650 | Tx5 | 500 | 10 | 1.772 | ✓ |
| 70 | 50.564092 | 11.842766 | 34 | 1699 | Tx5 | 500 | 10 | 1.722 | ✓ |
| 71 | 50.563719 | 11.843175 | 39 | 1749 | Tx5 | 500 | 10 | 1.672 | ✓ |
| 72 | 50.562344 | 11.845947 | -11 | 1993 | Tx5 | 500 | 10 | 1.429 | ✓ |
| 73 | 50.562033 | 11.846452 | -16 | 2043 | Tx5 | 500 | 10 | 1.380 | ✓ |
| 74 | 50.56172 | 11.846963 | -21 | 2093 | Tx5 | 500 | 10 | 1.330 | ✓ |
| 75 | 50.561434 | 11.847501 | -30 | 2141 | Tx5 | 500 | 10 | 1.282 | ✓ |
| 76 | 50.56113 | 11.847927 | -31 | 2187 | Tx5 | 500 | 10 | 1.236 | ✓ |
| 77 | 50.560666 | 11.848523 | -29 | 2253 | Tx5 | 500 | 10 | 1.170 | ✓ |
| 78 | 50.560292 | 11.848872 | -21 | 2301 | Tx5 | 500 | 10 | 1.122 | ✓ |
| 79 | 50.559933 | 11.84929 | -18 | 2351 | Tx5 | 500 | 10 | 1.072 | ✓ |
| 80 | 50.558229 | 11.850435 | 44 | 2548 | Tx5 | 1000 | 11 | 0.874 | no Tx File |
| 81 | 50.557917 | 11.85092 | 40 | 2596 | Tx5 | 1200 | 11 | 0.826 | no Tx File |
| 82 | 50.557588 | 11.851364 | 40 | 2645 | Tx5 | 500 | 11 | 0.777 | ✓ |
| 83 | 50.557268 | 11.851844 | 37 | 2694 | Tx5 | 500 | 11 | 0.728 | ✓ |
| 84 | 50.556941 | 11.852363 | 33 | 2745 | Tx5 | 450 | 11 | 0.677 | no Tx File |
| 85 | 50.556776 | 11.85305 | 8 | 2791 | Tx6 | 1000 | 11 | 1.320 | ✓ |
| 86 | 50.556663 | 11.85356 | -12 | 2824 | Tx6 | 1000 | 11 | 1.288 | ✓ |
| 87 | 50.556622 | 11.85421 | -44 | 2857 | Tx6 | 1000 | 11 | 1.257 | ✓ |
| 88 | 50.55633 | 11.854724 | -50 | 2905 | Tx6 | 1000 | 11 | 1.209 | ✓ |
| 89 | 50.556004 | 11.855459 | -67 | 2966 | Tx6 | 1000 | 11 | 1.150 | ✓ |
| 90 | 50.555581 | 11.85587 | -58 | 3021 | Tx6 | 1000 | 11 | 1.094 | ✓ |
| 91 | 50.555186 | 11.856209 | -48 | 3070 | Tx6 | 1000 | 11 | 1.045 | ✓ |
| 92 | 50.554776 | 11.856552 | -37 | 3121 | Tx6 | 1000 | 11 | 0.993 | ✓ |
| 93 | 50.554385 | 11.856815 | -23 | 3166 | Tx6 | 1000 | 11 | 0.947 | ✓ |
| 94 | 50.553984 | 11.857184 | -14 | 3217 | Tx6 | 1000 | 11 | 0.896 | ✓ |
| 95 | 50.553561 | 11.85749 | 0 | 3267 | Tx6 | 1000 | 11 | 0.845 | ✓ |
| 96 | 50.553238 | 11.857992 | -3 | 3317 | Tx6 | 1000 | 11 | 0.795 | ✓ |

| Rx | Latitude | Longitude | x | y | Tx | $T_{switch}$ | I[A] | Offset[km] | TF |
|---|---|---|---|---|---|---|---|---|---|
| 97 | 50.552932 | 11.858366 | -2 | 3360 | Tx6 | 1000 | 11 | 0.752 | ✓ |
| 98 | 50.552593 | 11.858855 | -3 | 3411 | Tx6 | 1000 | 11 | 0.701 | ✓ |
| 99 | 50.552184 | 11.859106 | 13 | 3458 | Tx6 | 1000 | 11 | 0.654 | ✓ |
| 100 | 50.551858 | 11.859486 | 16 | 3503 | Tx6 | 1000 | 11 | 0.609 | ✓ |
| 101 | 50.551462 | 11.859974 | 18 | 3559 | Tx6 | 1000 | 11 | 0.553 | ✓ |
| 102 | 50.551124 | 11.860422 | 18 | 3608 | Tx6 | 1000 | 11 | 0.504 | ✓ |
| 103 | 50.544682 | 11.868672 | 38 | 4532 | Tx5 | 500 | 11 | 1.110 | ✓ |
| 104 | 50.55189 | 11.859458 | 15 | 3499 | Tx4 | 1000 | 16 | 1.165 | ✓ |
| 105 | 50.551412 | 11.859998 | 20 | 3564 | Tx4 | 1000 | 16 | 1.231 | ✓ |
| 106 | 50.543318 | 11.870367 | 45 | 4725 | Tx5 | 1000 | 11 | 1.303 | ✓ |
| 107 | 50.551195 | 11.860523 | 8 | 3606 | Tx4 | 1000 | 16 | 1.273 | ✓ |
| 108 | 50.5429 | 11.870767 | 54 | 4779 | Tx6 | 1000 | 11 | 0.668 | X |
| 109 | 50.550811 | 11.860856 | 17 | 3654 | Tx4 | 1000 | 16 | 1.321 | ✓ |
| 110 | 50.542601 | 11.871072 | 59 | 4819 | Tx6 | 1000 | 11 | 0.708 | X |
| 111 | 50.55045 | 11.861249 | 22 | 3703 | Tx4 | 1000 | 16 | 1.370 | ✓ |
| 112 | 50.550097 | 11.861723 | 22 | 3754 | Tx4 | 1000 | 16 | 1.421 | ✓ |
| 113 | 50.549679 | 11.862076 | 33 | 3806 | Tx4 | 1000 | 16 | 1.473 | ✓ |
| 114 | 50.549447 | 11.862654 | 19 | 3852 | Tx4 | 1000 | 16 | 1.519 | ✓ |
| 115 | 50.549033 | 11.862992 | 30 | 3903 | Tx4 | 1000 | 16 | 1.570 | ✓ |
| 116 | 50.548761 | 11.863538 | 21 | 3951 | Tx4 | 1000 | 16 | 1.618 | ✓ |
| 117 | 50.548297 | 11.863846 | 37 | 4004 | Tx4 | 1000 | 16 | 1.671 | ✓ |
| 118 | 50.547976 | 11.864301 | 36 | 4052 | Tx4 | 1000 | 16 | 1.719 | ✓ |
| 119 | 50.54018 | 11.875426 | -1 | 5224 | Tx10 | 450 | 21 | 2.647 | ✓ |
| 120 | 50.539765 | 11.875996 | -2 | 5285 | Tx10 | 450 | 21 | 2.586 | ✓ |
| 121 | 50.539421 | 11.876476 | -3 | 5336 | Tx10 | 450 | 21 | 2.534 | ✓ |
| 122 | 50.538986 | 11.876942 | 3 | 5394 | Tx10 | 450 | 21 | 2.476 | ✓ |
| 123 | 50.538551 | 11.87744 | 8 | 5454 | Tx10 | 450 | 21 | 2.417 | ✓ |
| 124 | 50.537893 | 11.878369 | 5 | 5552 | Tx10 | 450 | 21 | 2.318 | ✓ |
| 125 | 50.537535 | 11.878913 | 2 | 5608 | Tx10 | 450 | 21 | 2.263 | ✓ |
| 126 | 50.537153 | 11.879401 | 3 | 5662 | Tx10 | 450 | 21 | 2.208 | ✓ |
| 127 | 50.536759 | 11.87989 | 5 | 5718 | Tx10 | 450 | 21 | 2.152 | ✓ |
| 128 | 50.536362 | 11.88035 | 9 | 5773 | Tx10 | 450 | 21 | 2.098 | ✓ |
| 129 | 50.535989 | 11.880842 | 9 | 5827 | Tx10 | 450 | 21 | 2.043 | ✓ |
| 130 | 50.532171 | 11.88607 | 3 | 6391 | Tx10 | 810 | 21 | 1.480 | ✓ |
| 131 | 50.531791 | 11.886621 | 0 | 6448 | Tx10 | 810 | 21 | 1.423 | ✓ |
| 132 | 50.531356 | 11.88713 | 4 | 6509 | Tx10 | 810 | 21 | 1.363 | ✓ |
| 133 | 50.530957 | 11.887633 | 6 | 6565 | Tx10 | 810 | 21 | 1.306 | ✓ |

| Rx | Latitude | Longitude | x | y | Tx | $T_{switch}$ | I[A] | Offset[km] | TF |
|---|---|---|---|---|---|---|---|---|---|
| 134 | 50.530629 | 11.88812 | 3 | 6616 | Tx10 | 810 | 21 | 1.256 | ✓ |
| 135 | 50.530302 | 11.888624 | 0 | 6666 | Tx10 | 810 | 21 | 1.205 | ✓ |
| 136 | 50.529905 | 11.889087 | 3 | 6721 | Tx10 | 810 | 21 | 1.150 | ✓ |
| 137 | 50.529514 | 11.889595 | 4 | 6778 | Tx10 | 810 | 21 | 1.093 | ✓ |
| 138 | 50.529185 | 11.890071 | 2 | 6828 | Tx10 | 810 | 21 | 1.044 | ✓ |
| 139 | 50.528829 | 11.890553 | 2 | 6880 | Tx10 | 810 | 21 | 0.991 | ✓ |
| 140 | 50.528485 | 11.89106 | 0 | 6932 | Tx10 | 810 | 21 | 0.939 | ✓ |
| 141 | 50.528144 | 11.891569 | -3 | 6985 | Tx10 | 810 | 21 | 0.887 | ✓ |
| 142 | 50.52781 | 11.892103 | -8 | 7037 | Tx10 | 810 | 21 | 0.834 | ✓ |
| 143 | 50.527456 | 11.892579 | -8 | 7089 | Tx10 | 810 | 21 | 0.782 | ✓ |
| 144 | 50.527101 | 11.893072 | -9 | 7142 | Tx10 | 810 | 21 | 0.729 | ✓ |
| 145 | 50.526734 | 11.893554 | -9 | 7195 | Tx10 | 810 | 21 | 0.676 | ✓ |
| 146 | 50.526366 | 11.894038 | -8 | 7249 | Tx10 | 810 | 21 | 0.623 | ✓ |
| 147 | 50.526016 | 11.894529 | -9 | 7301 | Tx10 | 810 | 21 | 0.571 | ✓ |
| 148 | 50.52568 | 11.895015 | -11 | 7352 | Tx8 | 810 | 13 | 1.466 | ✓ |
| 149 | 50.525334 | 11.895469 | -11 | 7402 | Tx8 | 810 | 13 | 1.516 | ✓ |
| 150 | 50.52497 | 11.895954 | -11 | 7455 | Tx8 | 810 | 13 | 1.570 | ✓ |
| 151 | 50.524636 | 11.896457 | -14 | 7506 | Tx8 | 810 | 13 | 1.621 | ✓ |
| 152 | 50.524258 | 11.896892 | -10 | 7558 | Tx8 | 810 | 13 | 1.673 | ✓ |
| 153 | 50.523923 | 11.897404 | -14 | 7610 | Tx8 | 810 | 13 | 1.725 | ✓ |
| 154 | 50.523611 | 11.897945 | -20 | 7661 | Tx8 | 810 | 13 | 1.776 | ✓ |
| 155 | 50.523212 | 11.898412 | -17 | 7717 | Tx8 | 810 | 13 | 1.831 | ✓ |
| 156 | 50.522831 | 11.898829 | -12 | 7768 | Tx8 | 810 | 13 | 1.883 | ✓ |
| 157 | 50.522488 | 11.899391 | -17 | 7823 | Tx8 | 810 | 13 | 1.937 | ✓ |
| 158 | 50.522093 | 11.899768 | -9 | 7874 | Tx8 | 810 | 13 | 1.988 | ✓ |
| 159 | 50.521674 | 11.900291 | -7 | 7933 | Tx8 | 810 | 13 | 2.048 | ✓ |
| 160 | 50.52131 | 11.900843 | -11 | 7990 | Tx8 | 810 | 13 | 2.104 | ✓ |
| 161 | 50.520876 | 11.901278 | -3 | 8046 | Tx8 | 810 | 13 | 2.161 | ✓ |
| 162 | 50.520494 | 11.901711 | 1 | 8099 | Tx8 | 810 | 13 | 2.213 | ✓ |
| 163 | 50.520145 | 11.902188 | 1 | 8150 | Tx10 | 810 | 21 | 0.278 | ✓ |
| 164 | 50.519778 | 11.902725 | -2 | 8206 | Tx10 | 810 | 21 | 0.334 | ✓ |
| 165 | 50.519411 | 11.903139 | 2 | 8256 | Tx10 | 810 | 21 | 0.384 | ✓ |
| 166 | 50.519063 | 11.903681 | -2 | 8310 | Tx10 | 810 | 21 | 0.438 | ✓ |
| 167 | 50.518693 | 11.904191 | -3 | 8365 | Tx10 | 810 | 21 | 0.493 | ✓ |
| 168 | 50.518263 | 11.904691 | 2 | 8424 | Tx10 | 810 | 21 | 0.553 | ✓ |

## A.2. Influence of Transmitter Ramp Time

Figure A.2 shows the influence of an increased transmitter ramp time in frequency domain. The transmitter signal was first calculated as rectangular shaped 50 % duty cycle with a zero ramp time, second including a ramp time of 500 $\mu$s and third including a ramp time of 1 ms. The amplitude of high order odd harmonics is decreased for longer ramp times.

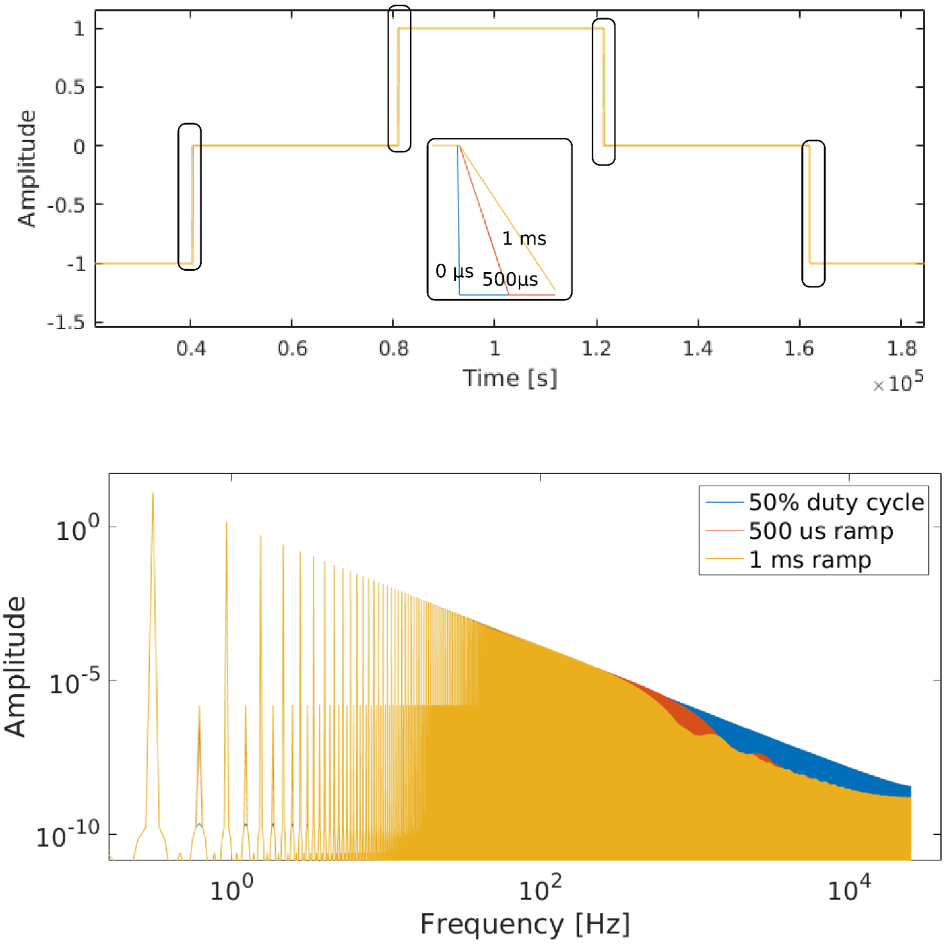

**Figure A.2.:** Influence of length of ramp time to the corresponding Fourier transformed spectrum. Upper panel: Synthetic signal in time domain. Lower panel: Synthetic signal transformed into frequency domain.

## A.3. Early Time Oscillations

Figure A.2 shows the influence of sampling rates on early time oscillations in the recorded transients. Oscillations affecting a longer time range and are stronger if a lower sampling rate is utilized. The influence of the oscillations can be taken into account to some extend, if the same sampling rate is used for current recording and therefore for the measurement of the system response. However, since the system response can only be measured accurately to some extend, a reasonably high sampling frequency would be recommendable. This holds especially for Loop-TEM measurements, were one is more interested in the early time information and typically shorter ramp times are realized, which results in a stronger gradient in the measured transient response and therefore exhibit stronger oscillations.

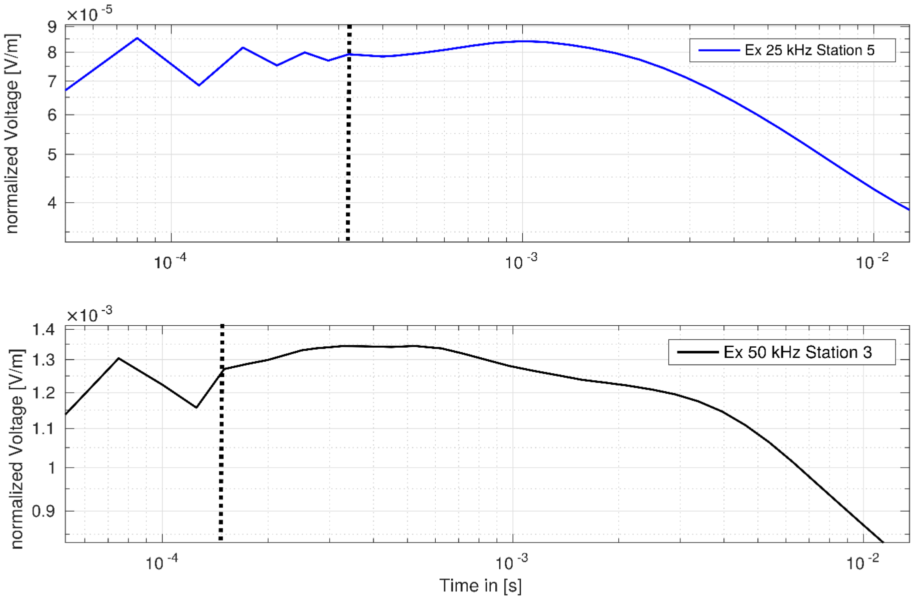

**Figure A.3.:** Transient data for two stations utilizing the same transmitter signal (Rx 3, Rx 5, Tx 5 DC: 50 %. Stations recorded with 25 kHz sampling rate exhibit a longer influence of oscillations

# B. Data Processing

In the following, additional information about data processing and the post processed dataset is given. In the first Figure B.1, the influence of different window types for the Fourier transformation is shown. The error calculation for phase and amplitude errors is derived in the next section. Exemplary LOTEM B-Field transients utilizing the Loop and TEM-3 sensor are shown in Figure B.2. All obtained transfer functions and transients are displayed colour coded in Figure B.3-B.29 in terms of real and imaginary part over the frequency or switch on and switch off over time along the profile.

## B.1. Fourier Transformation: Different Window Types

Figure B.1 shows the influence for different window types utilized for Fourier transformation. The Hanning window is compared with the Parzen and rectangular window. Relative misfits are calculated with respect to the transfer function calculated with the Hanning window. Where differences between a rectangular window and the Hanning window are small, differences utilizing the Parzen window are larger. However, except for the lowest frequency, misfits are mostly increased around the sign reversals. Since the Hanning window has only a moderate impact on the spectral resolution and amplitude resolution, it was utilized for subsequent Fourier transformation of the obtained dataset. However, given the periodicity of the signal, a rectangular shaped window function would result in a similar result, if the window length is an integer number multiple of the period in sample points.

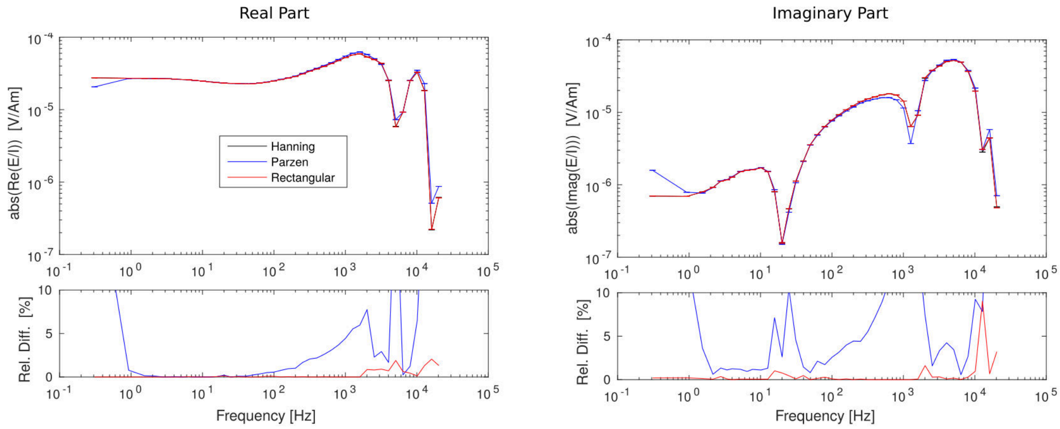

**Figure B.1.:** Transfer functions of an exemplary electric field component obtained utilizing different window types for the Fourier transformation. The lower panel depicts the relative difference of the transfer function with Parzen (blue) and rectangular (red) window compared with the Hanning window.

## B.2. Magnetic Field Transients

Exemplary magnetic field transients acquired with loop sensor and coil sensor for two different offsets. Note, that data was recorded at different stations, therefore the transients can not be compared directly to each other. However, the response at early times can be compared, since it is mostly influenced by the system response. The loop shows a large inertia with an voltage increase in the first ms. Therefore, the system response with a length of 150 $\mu$ s, recorded with the current clamp at the transmitter site is not suitable, since it does not take the sensor specific system response of the loop sensor into account. Furthermore, most of the datasets exhibited sign reversal, an indication for multidimensional effects. Magnetic field data recorded by the TEM 3 induction coil shows the typical overshoot of the transmitted current at early times.

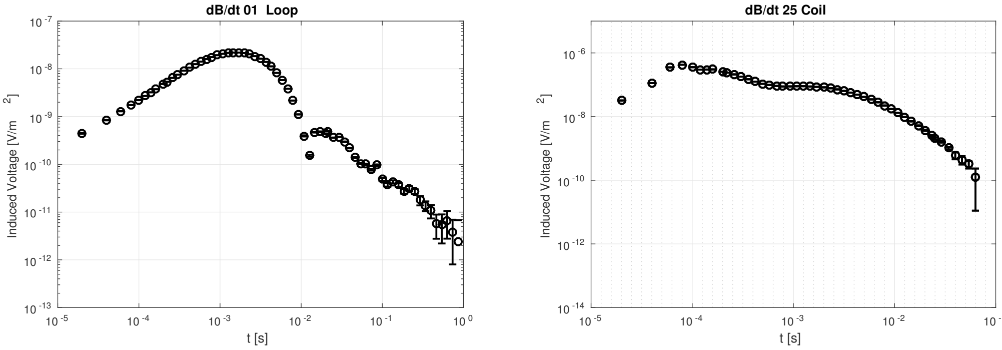

**Figure B.2.:** The time derivative of the vertical magnetic field component measured at station 1 with the loop sensor (left) and station 24 with the coil sensor (right). The dataset obtained at station 25 was cut for times later 80 ms due to high data errors.

## B.3. Error Propagation Data Transform Amplitude and Phase

The transformation from real and imaginary part to amplitude and phase writes

$$A = \sqrt{\Re^2 + \Im^2} \tag{B.1}$$

$$\varphi = \tan^{-1}\left(\frac{\Im}{\Re}\right) \tag{B.2}$$

The corresponding data errors are calculated by estimating the sum of the contributing error sources and follow the $L_1$ norm (cp. Section 3.2) error propagation

$$\begin{aligned} \Delta A &= \frac{\partial A}{\partial \Re}\Delta\Re + \frac{\partial A}{\partial \Im}\Delta\Im \\ &= \frac{\Re\Delta\Re + \Im\Delta\Im}{A} \end{aligned}$$

Since the errors obtained during the data processing only reflect the statistical behaviour of the dataset, an error floor containing estimations of systematic errors (e.g. uncertainty of receiver length, angular uncertainty, geological noise and correlated noise affecting the data) must be added to the dataset before inversion. Since static errors affect the real and imaginary part in the same way, the error floor is set to an identical value $\varepsilon$ for both, imaginary and real part. If $\Delta\Re/\Re = \Delta\Im/\Im = \varepsilon$ holds, the equation simplifies to:

$$\frac{\Delta A}{A} = \varepsilon \tag{B.4}$$

For the phase it holds

$$\begin{aligned}\Delta\varphi &= \frac{\partial\varphi}{\partial\Re}\Delta\Re + \frac{\partial\varphi}{\partial\Im}\Delta\Im \\ &= \frac{\Delta\Re}{1+\frac{\Im^2}{\Re^2}}\frac{\Im}{\Re^2} + \frac{\Delta\Im}{1+\frac{\Im^2}{\Re^2}}\frac{1}{\Re} \\ &= \frac{\Delta\Re/\Re}{\Re/\Im + \Im/\Re} + \frac{\Delta\Im/\Im}{\Im/\Re + \Re/\Im}.\end{aligned}$$

Again, considering the same error with $\Delta\Re/\Re = \Delta\Im/\Im = \varepsilon$, this leads to:

$$\Delta\varphi = \frac{2\varepsilon}{\Re/\Im + \Im/\Re} \tag{B.6}$$

Note that the error in phase is *absolute* (in radian), but depends close to linearity to the *relative* error of the imaginary and real part. It follows that the error is between 0 for $\Im \gg \Re$ or $\Re \gg \Im$ and $\varepsilon$ for $\Im = \Re$. In order to avoid errors close to zero, which could hinder convergence during inversion and to get the same absolute error and therefore an equal weighting over the frequency range independent of the ratio between imaginary and real part, the maximum error value of $\varepsilon$ is set for the phase error for all frequencies.
For example, let's consider an error floor of 5 percent for both, real and imaginary part. For the amplitude, the relative error writes $\Delta A = 0.05 * A$. For the phase, the absolute error in radian writes $\Delta\varphi = \frac{180}{\pi} * 0.05 = 2.8°$

## B.4. The Dataset

In the following the measured voltages are plotted colour coded under the corresponding receiver station over the position on the profile for both, time and frequency. For electric field data, the dataset is displayed in time domain as switch on and switch off. All datasets were levelled before stacking to DC resulting in appropriate error levels for switch on representation. In the following figures, only for stations corresponding to transmitter Tx 8 appropriate errors were calculated for the switch off depiction. Therefore, for the other transmitters, only the switch on errors are presented as comparison. Red markers indicate the location of sign reversals. Below the normalized voltages, errors achieved from the robust processing routine are displayed for each data point.

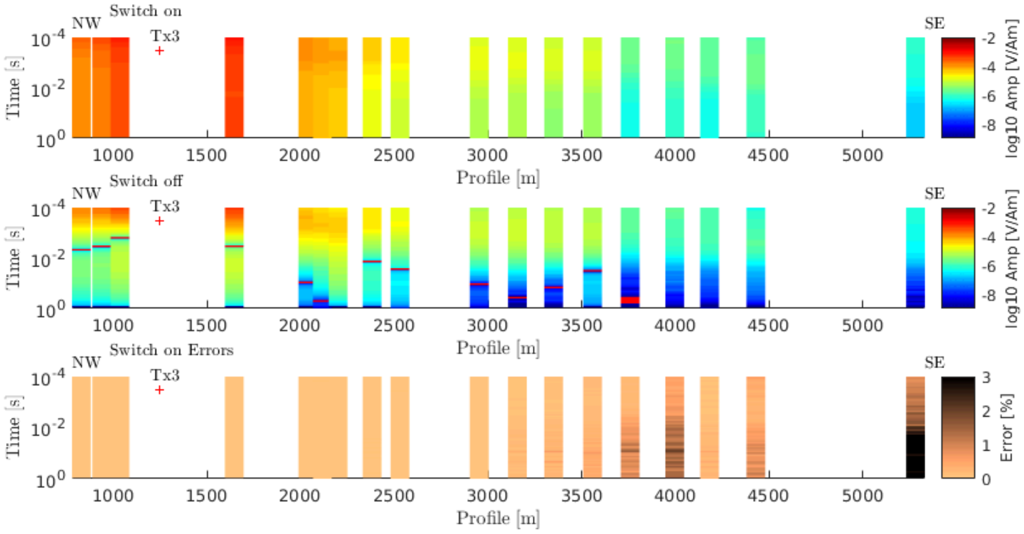

**Figure B.3.:** Normalized electric field voltages measured along Tx 3 for switch on and switch off plotted over time. Lower Panel: Processing errors for switch on data.

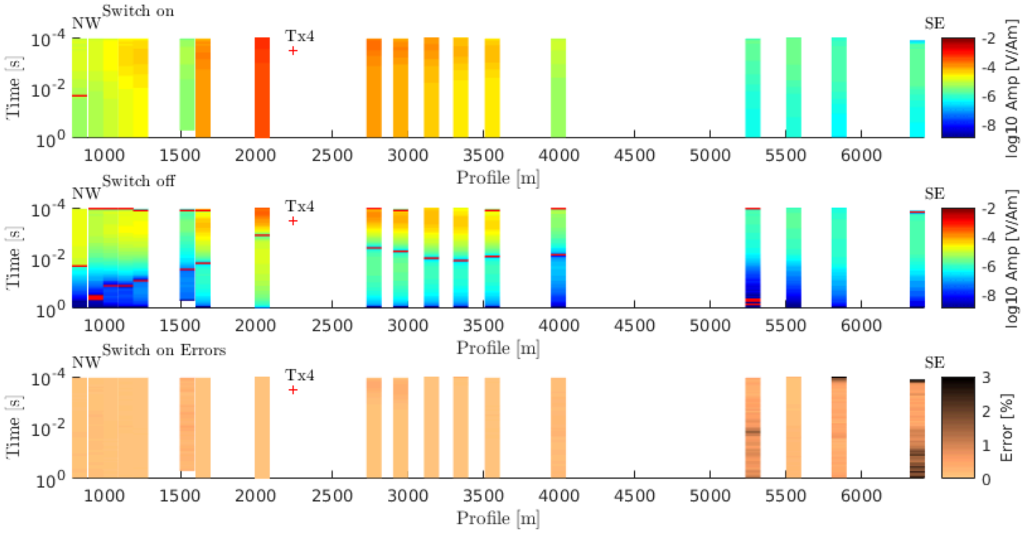

**Figure B.4.:** Normalized electric field voltages measured along Tx 4 for switch on and switch off plotted over time. Lower Panel: Processing errors for switch on data.

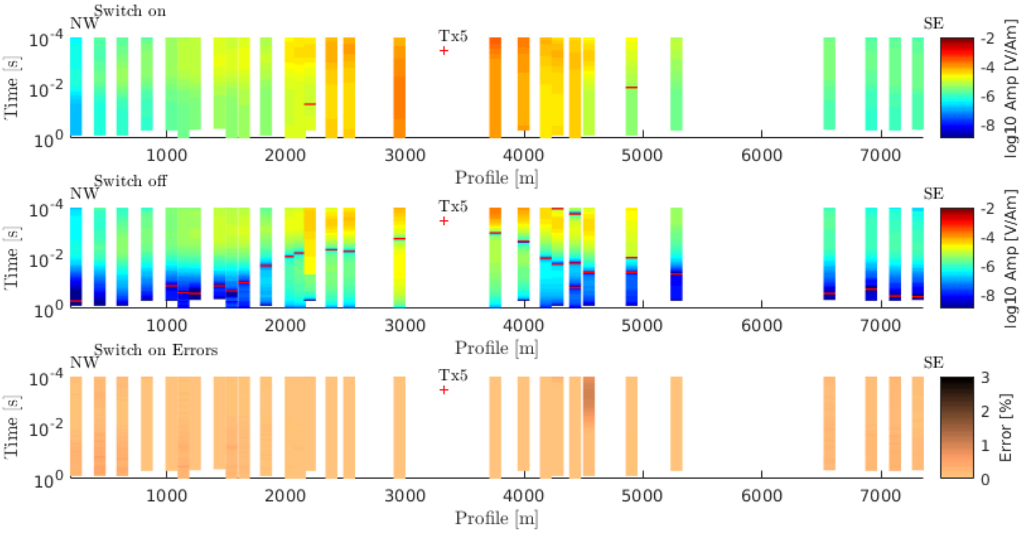

**Figure B.5.:** Normalized electric field voltages measured along Tx 5 for switch on and switch off plotted over time. Lower Panel: Processing errors for switch on data.

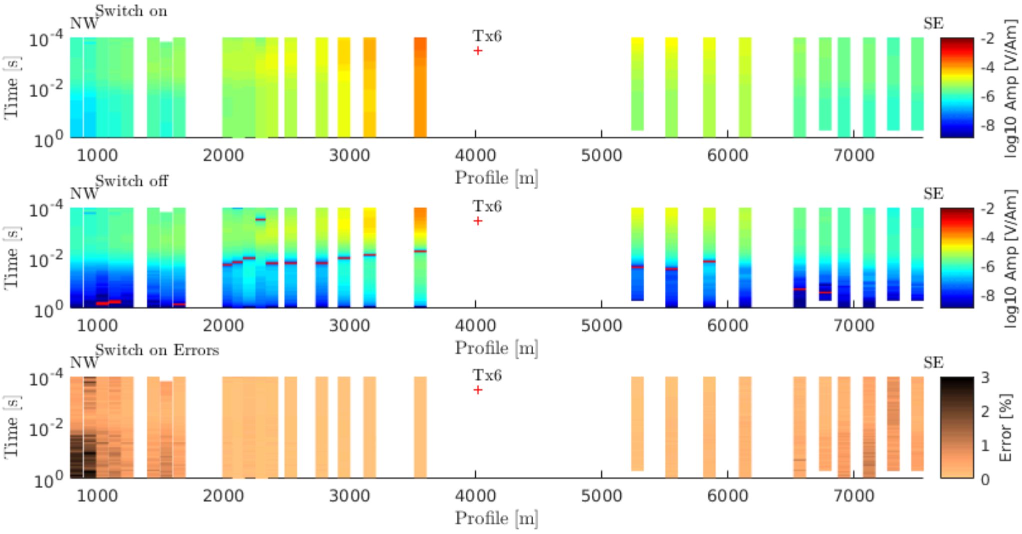

**Figure B.6.:** Normalized electric field voltages measured along Tx 6 for switch on and switch off plotted over time. Lower Panel: Processing errors for switch on data.

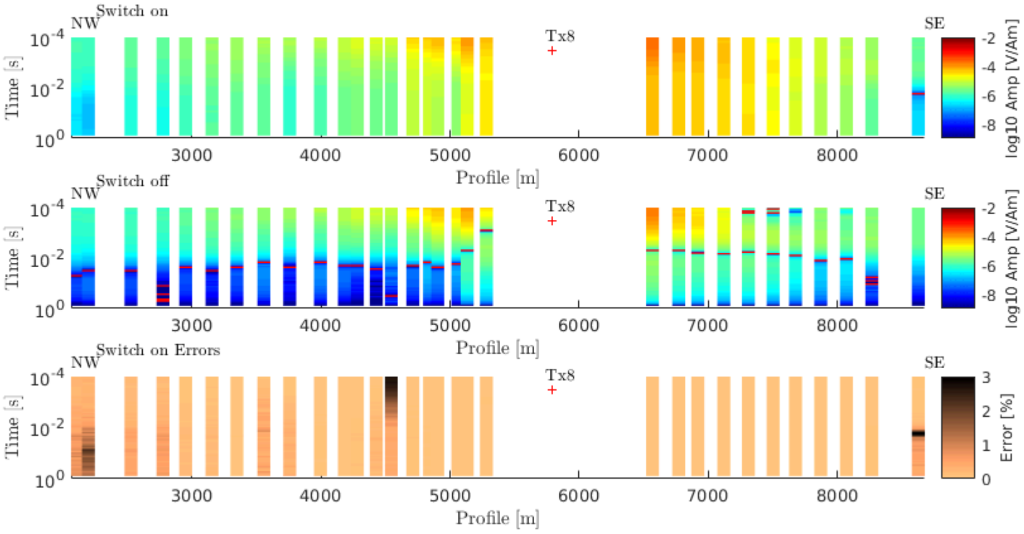

**Figure B.7.:** Normalized electric field voltages measured along Tx 8 for switch on and switch off plotted over time. Lower Panel: Processing errors for switch on data.

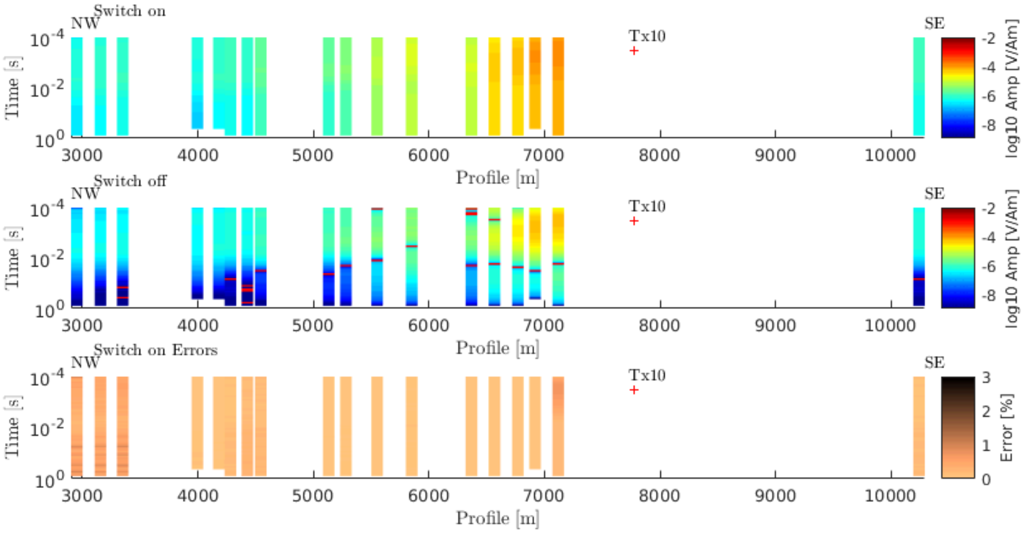

**Figure B.8.:** Normalized electric field voltages measured along Tx 10 for switch on and switch off plotted over time. Lower Panel: Processing errors for switch on data.

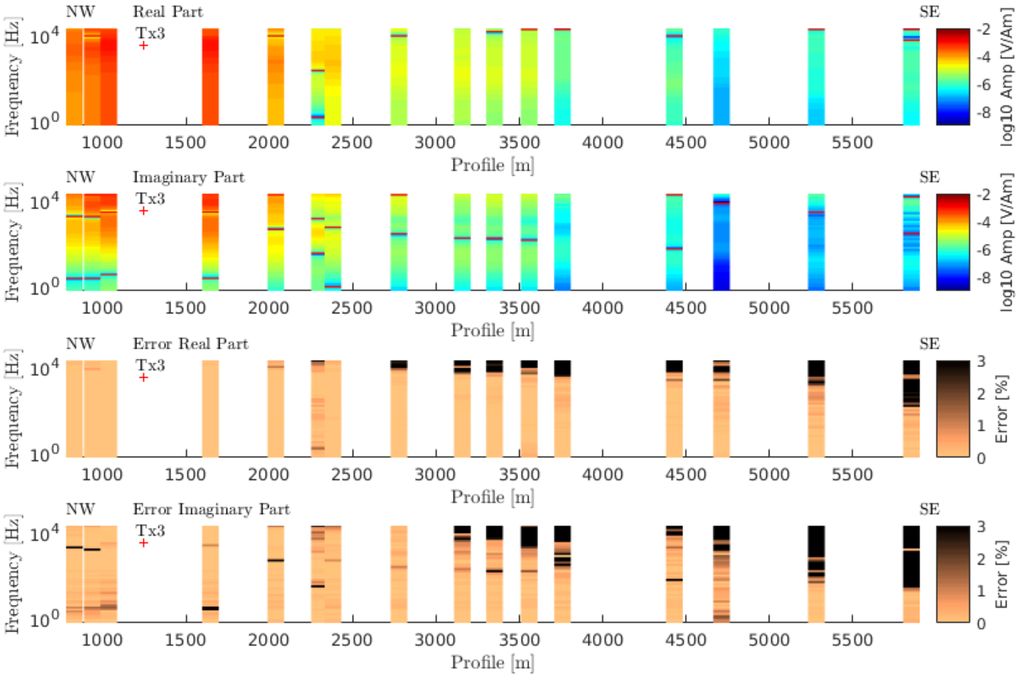

**Figure B.9.:** Normalized electric field voltages measured along Tx 3 for real and imaginary part plotted over frequency. Lower Panels: Processing errors of real and imaginary part.

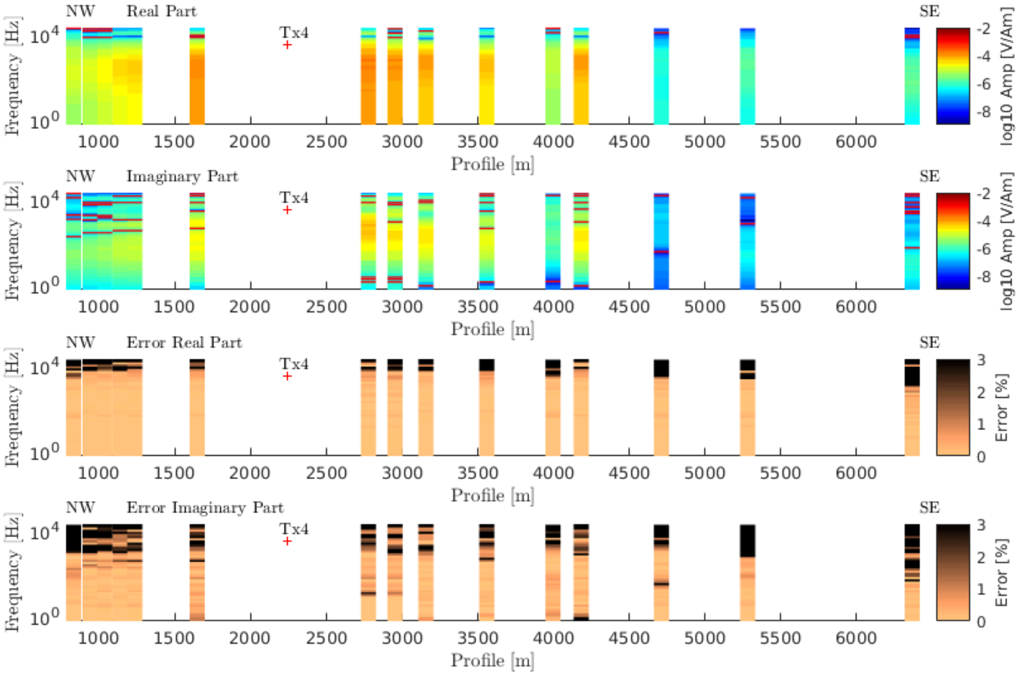

**Figure B.10.:** Normalized electric field voltages measured along Tx 4 for real and imaginary part plotted over frequency. Lower Panels: Processing errors of real and imaginary part.

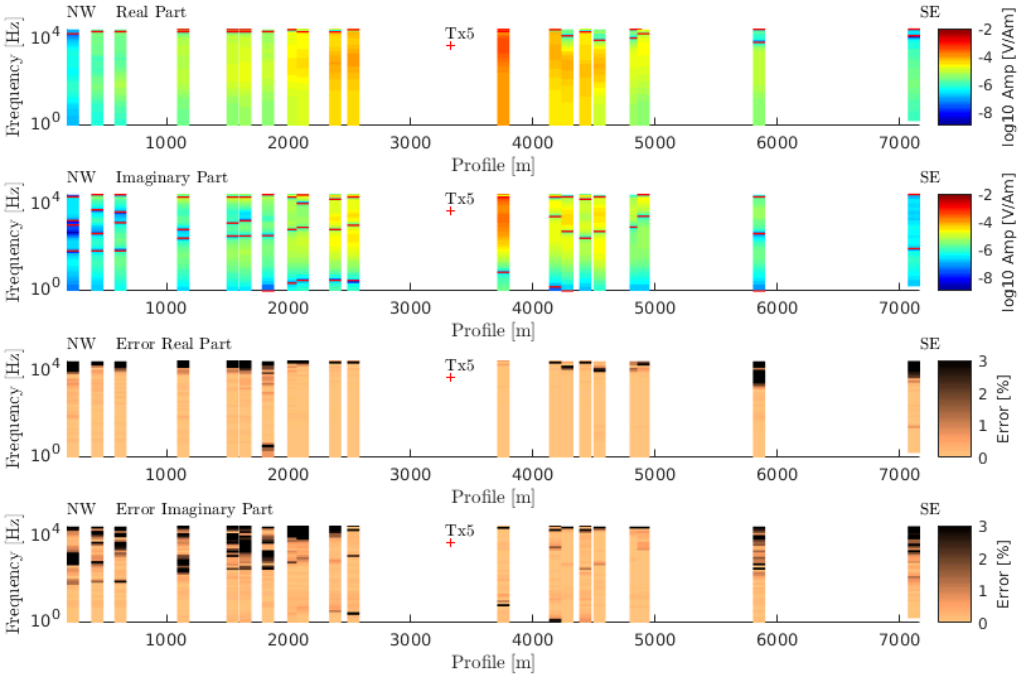

**Figure B.11.:** Normalized electric field voltages measured along Tx 5 for real and imaginary part plotted over frequency. Lower Panels: Processing errors of real and imaginary part.

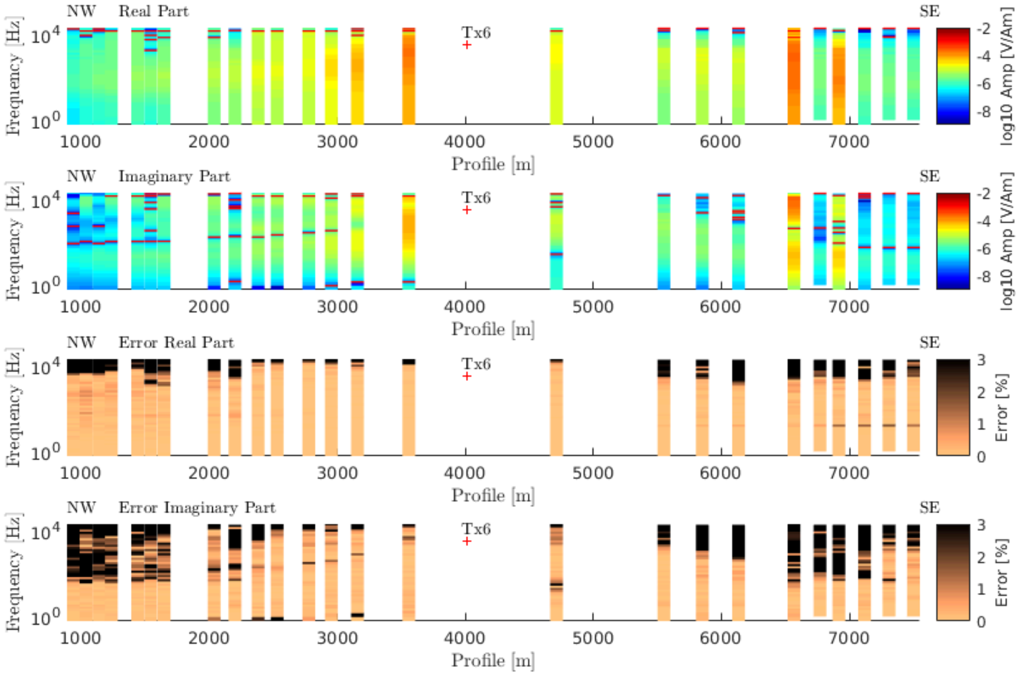

**Figure B.12.:** Normalized electric field voltages measured along Tx 6 for real and imaginary part plotted over frequency. Lower Panels: Processing errors of real and imaginary part.

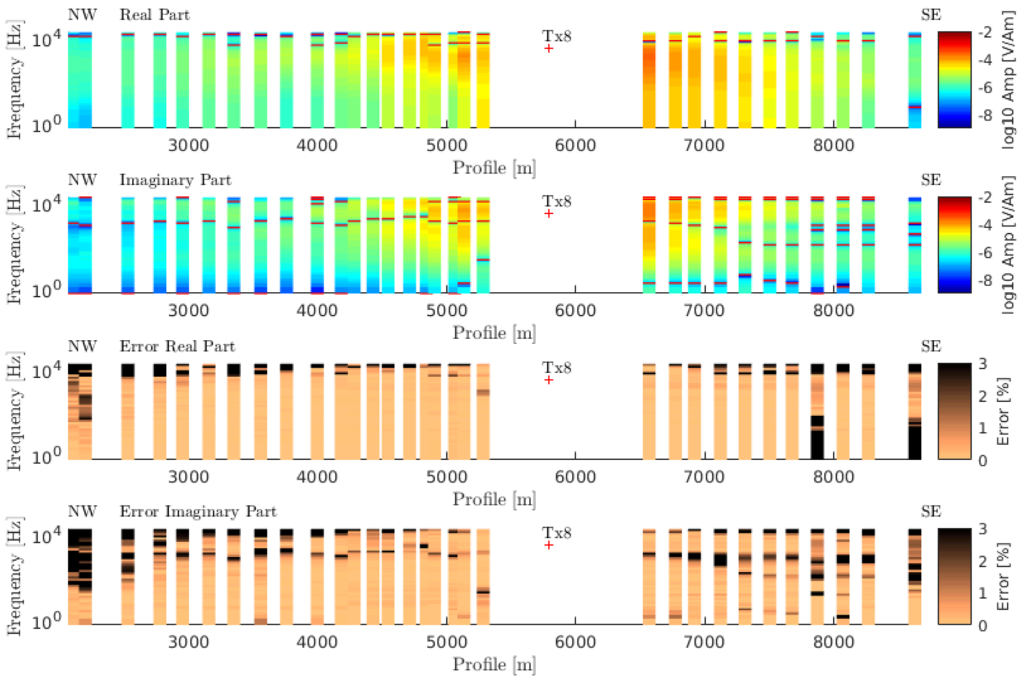

**Figure B.13.:** Normalized electric field voltages measured along Tx 8 for real and imaginary part plotted over frequency. Lower Panels: Processing errors of real and imaginary part.

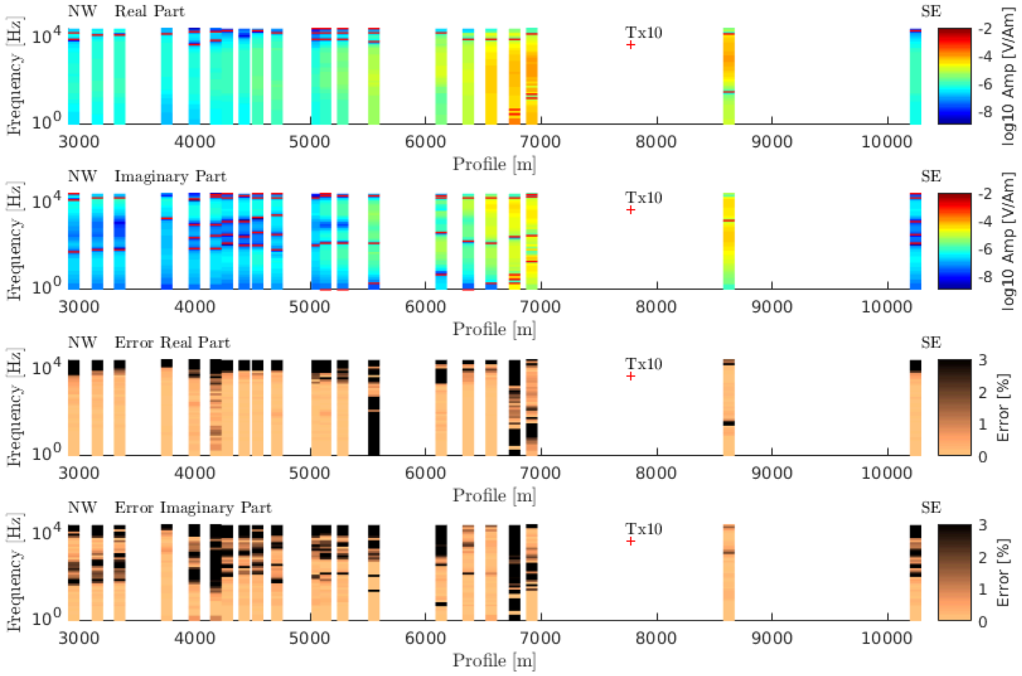

**Figure B.14.:** Normalized electric field voltages measured along Tx 10 for real and imaginary part plotted over frequency. Lower Panels: Processing errors of real and imaginary part.

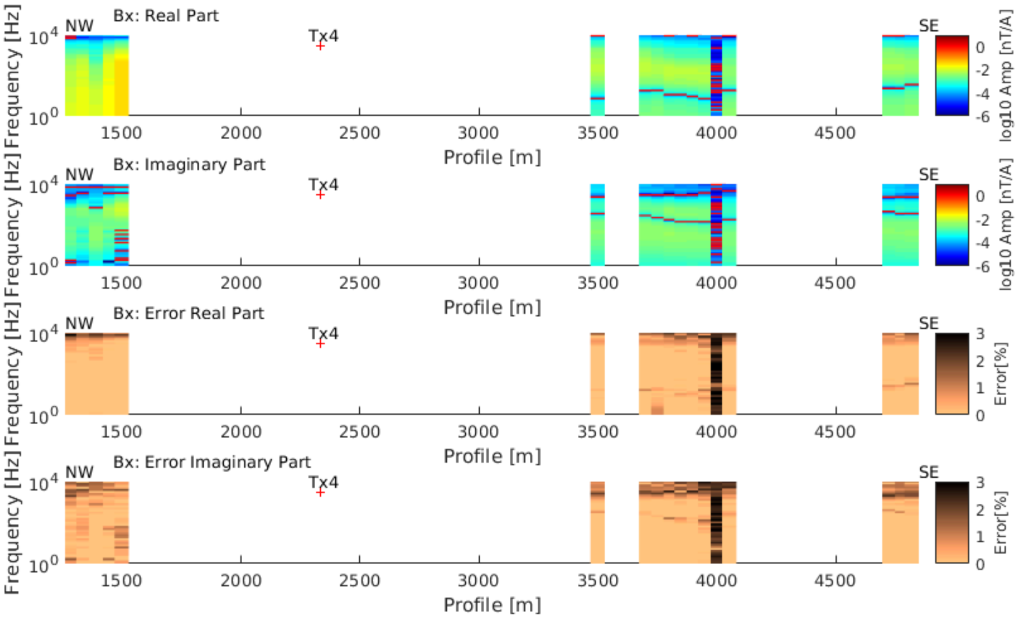

**Figure B.15.:** Normalized magnetic field of the $B_x$ component measured by SQUID sensors along Tx 4 for real and imaginary part plotted over frequency. The dataset is normalized to the current.

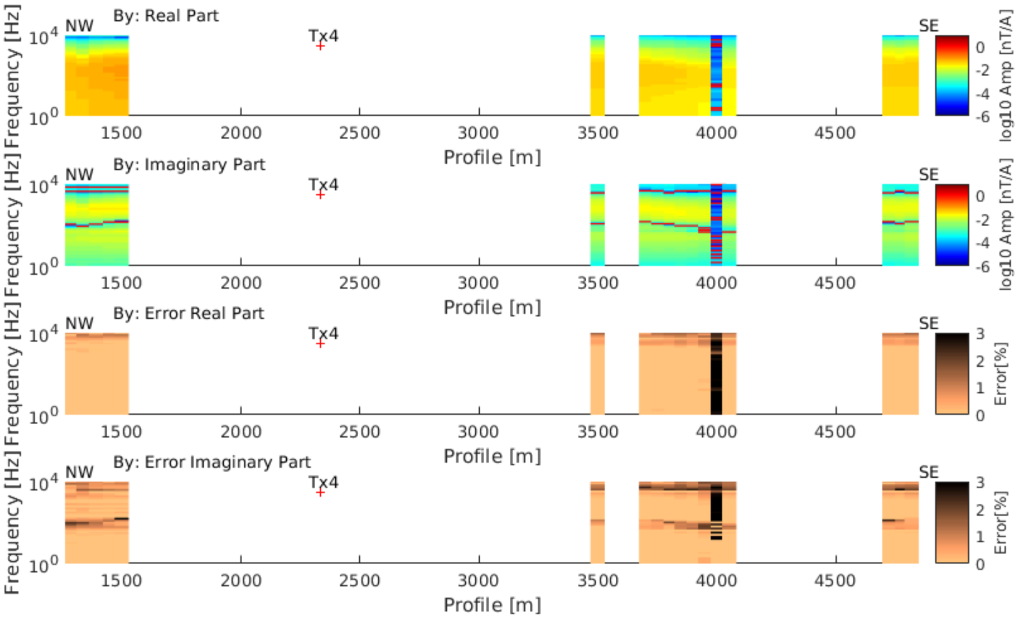

**Figure B.16.:** Normalized magnetic field of the $B_y$ component measured by SQUID sensors along Tx 4 for real and imaginary part plotted over frequency. The dataset is normalized to the current.

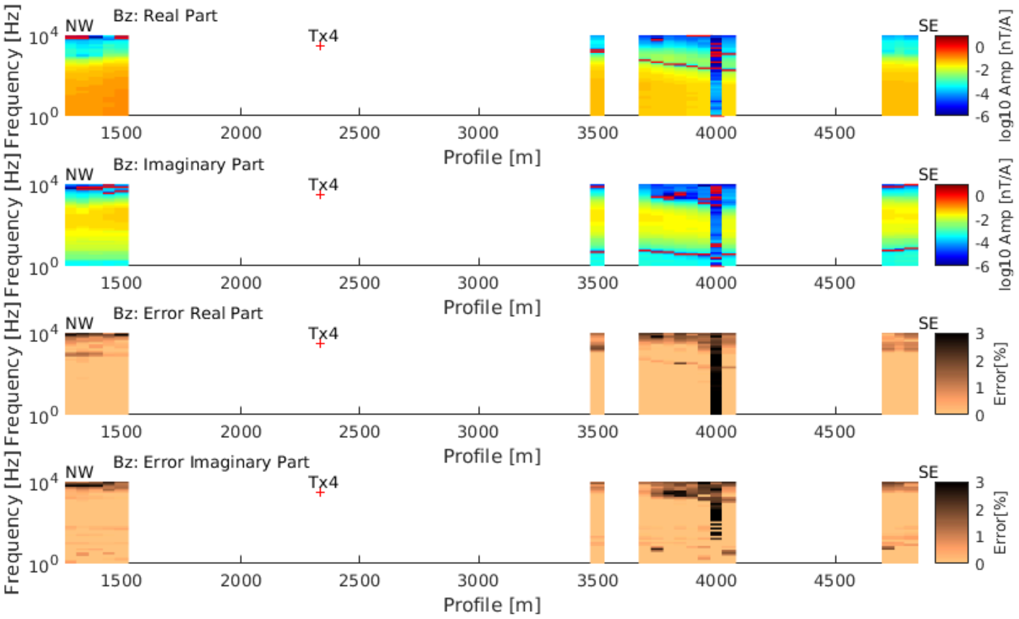

**Figure B.17.:** Normalized magnetic field of the $B_z$ component measured by SQUID sensors along Tx 4 for real and imaginary part plotted over frequency. The dataset is normalized to the current.

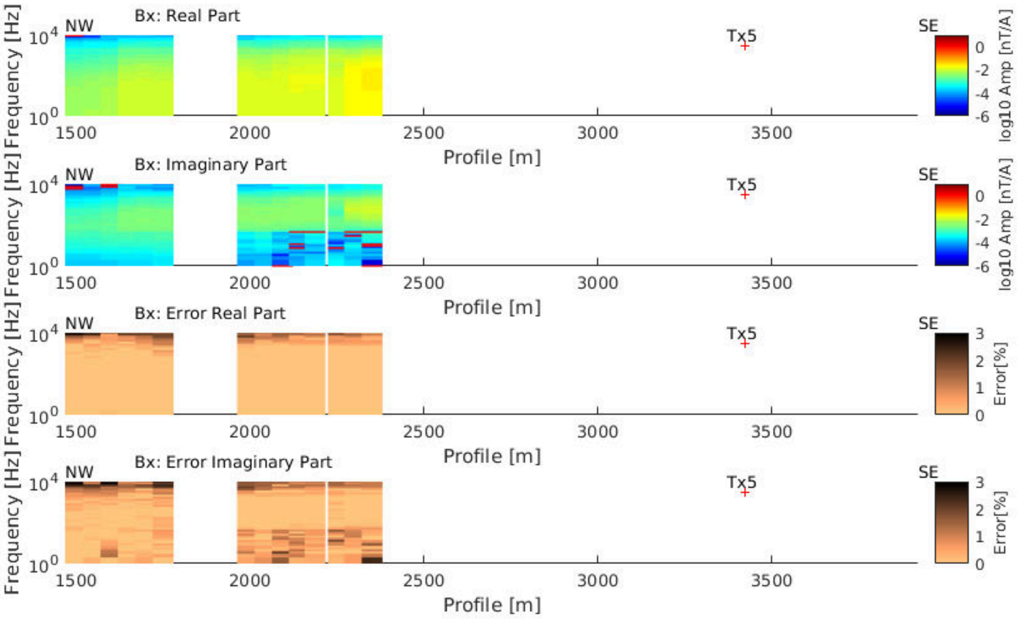

**Figure B.18.:** Normalized magnetic field of the $B_x$ component measured by SQUID sensors along Tx 5 for real and imaginary part plotted over frequency. The dataset is normalized to the current.

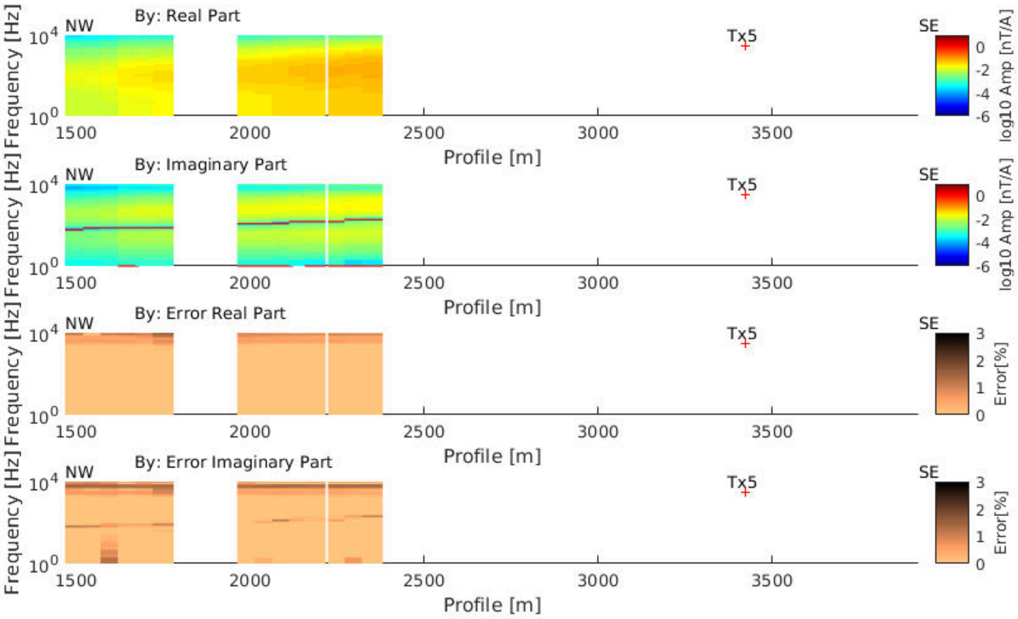

**Figure B.19.:** Normalized magnetic field of the $B_y$ component measured by SQUID sensors along Tx 5 for real and imaginary part plotted over frequency. The dataset is normalized to the current.

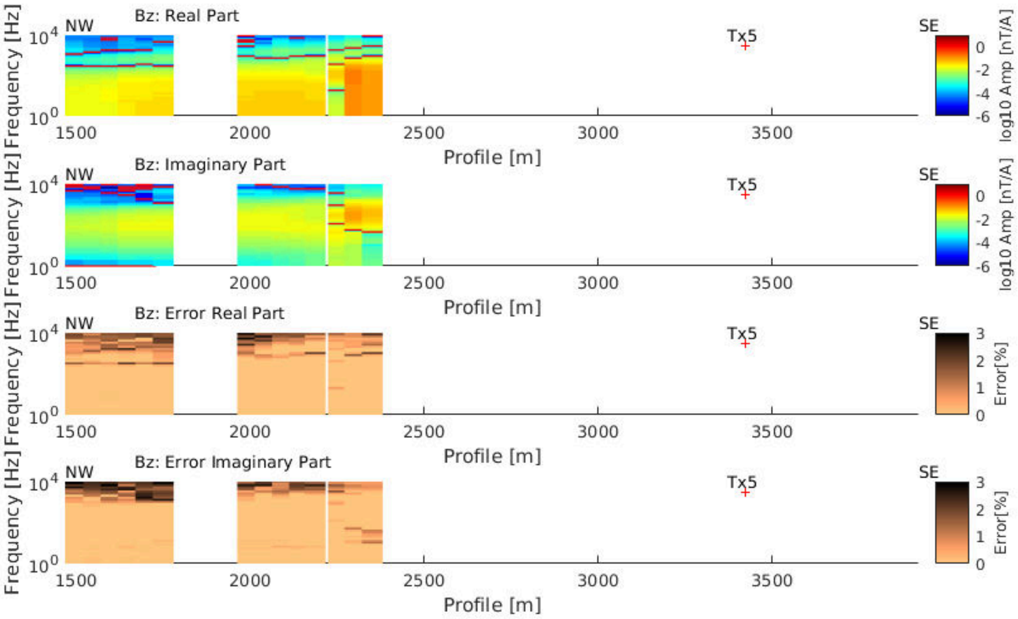

**Figure B.20.:** Normalized magnetic field of the $B_z$ component measured by SQUID sensors along Tx 5 for real and imaginary part plotted over frequency. The dataset is normalized to the current.

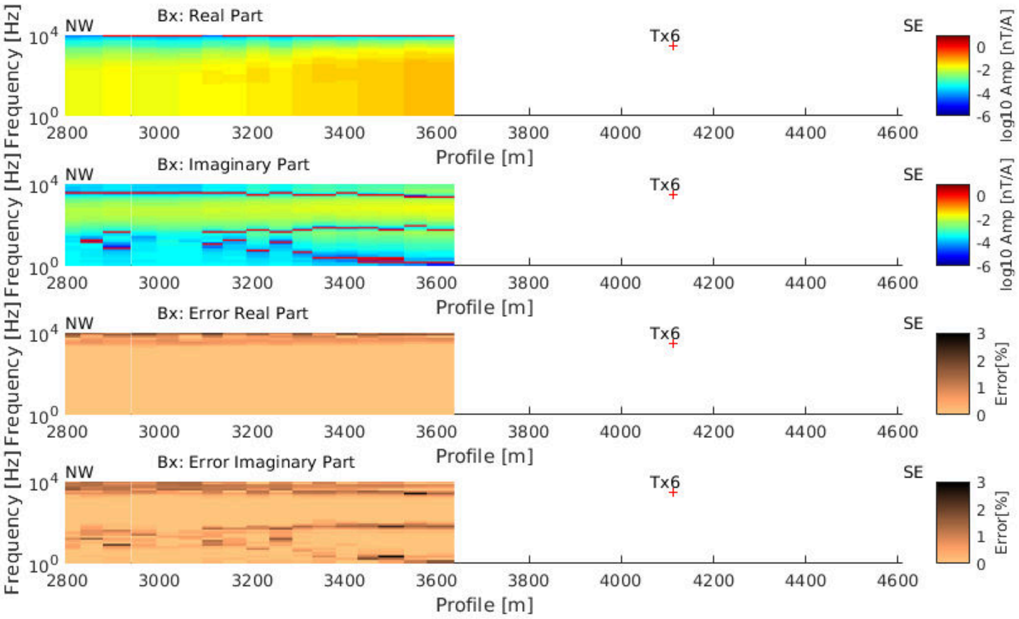

**Figure B.21.:** Normalized magnetic field of the $B_x$ component measured by SQUID sensors along Tx 6 for real and imaginary part plotted over frequency. The dataset is normalized to the current.

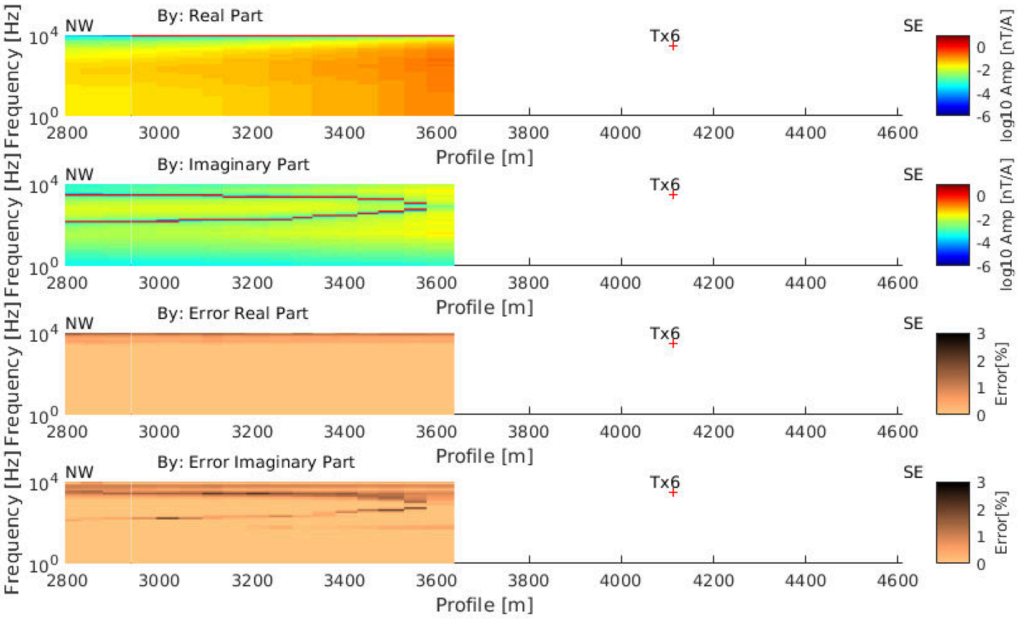

**Figure B.22.:** Normalized magnetic field of the $B_y$ component measured by SQUID sensors along Tx 6 for real and imaginary part plotted over frequency. The dataset is normalized to the current.

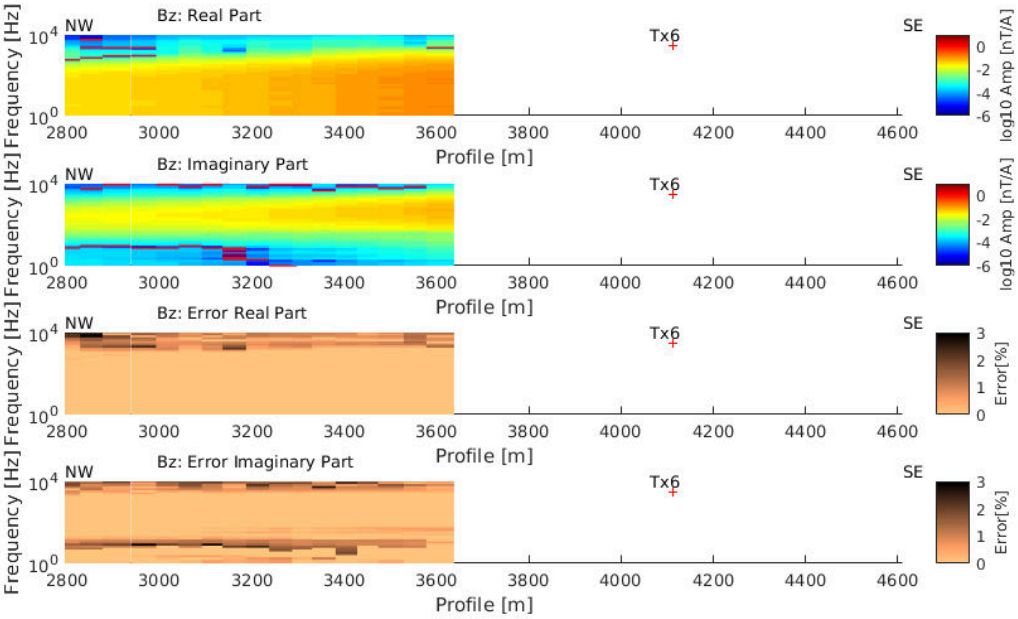

**Figure B.23.:** Normalized magnetic field of the $B_z$ component measured by SQUID sensors along Tx 6 for real and imaginary part plotted over frequency. The dataset is normalized to the current.

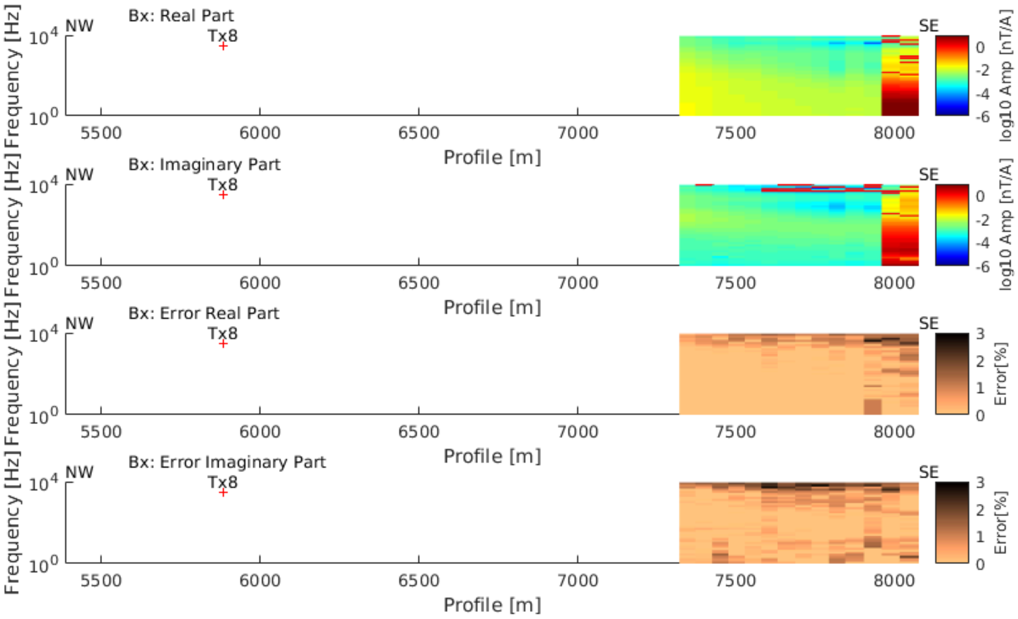

**Figure B.24.:** Normalized magnetic field of the $B_x$ component measured by SQUID sensors along Tx 8 for real and imaginary part plotted over frequency. The dataset is normalized to the current.

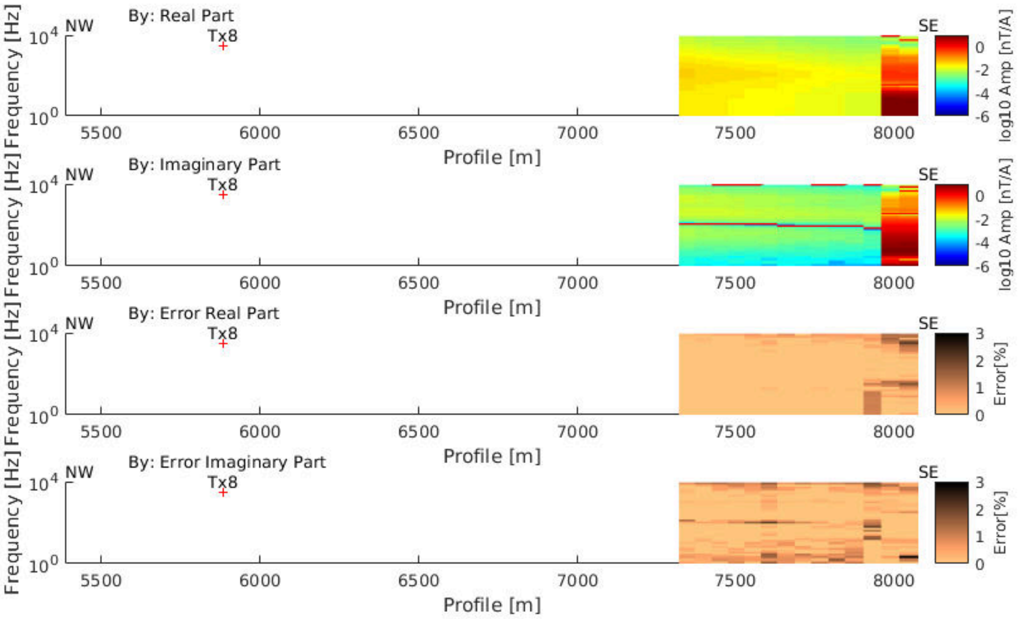

**Figure B.25.:** Normalized magnetic field of the $B_y$ component measured by SQUID sensors along Tx 8 for real and imaginary part plotted over frequency. The dataset is normalized to the current.

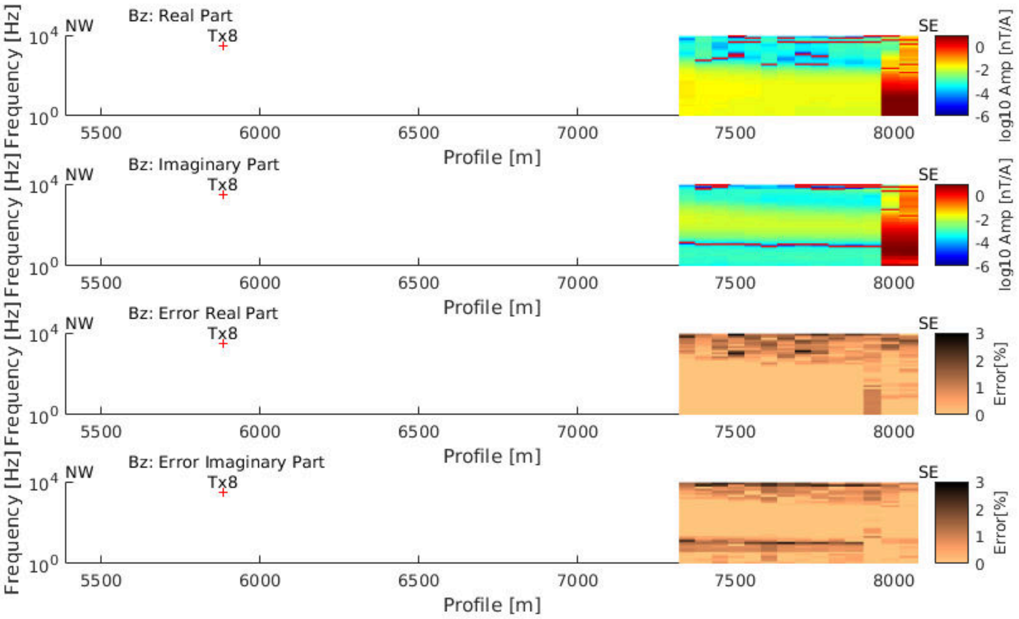

**Figure B.26.:** Normalized magnetic field of the $B_z$ component measured by SQUID sensors along Tx 8 for real and imaginary part plotted over frequency. The dataset is normalized to the current.

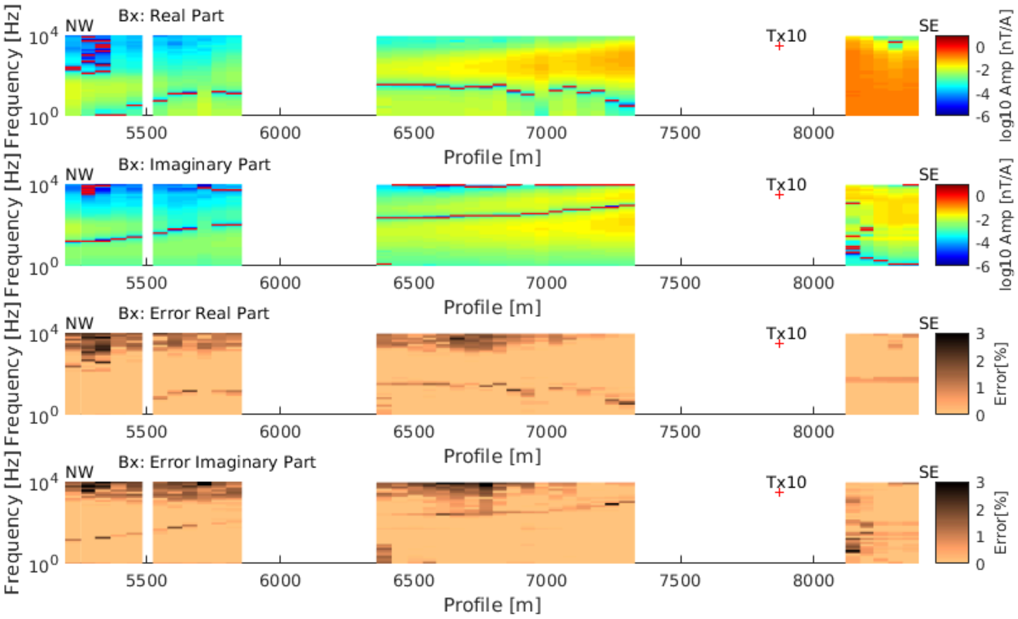

**Figure B.27.:** Normalized magnetic field of the $B_x$ component measured by SQUID sensors along Tx 10 for real and imaginary part plotted over frequency. The dataset is normalized to the current.

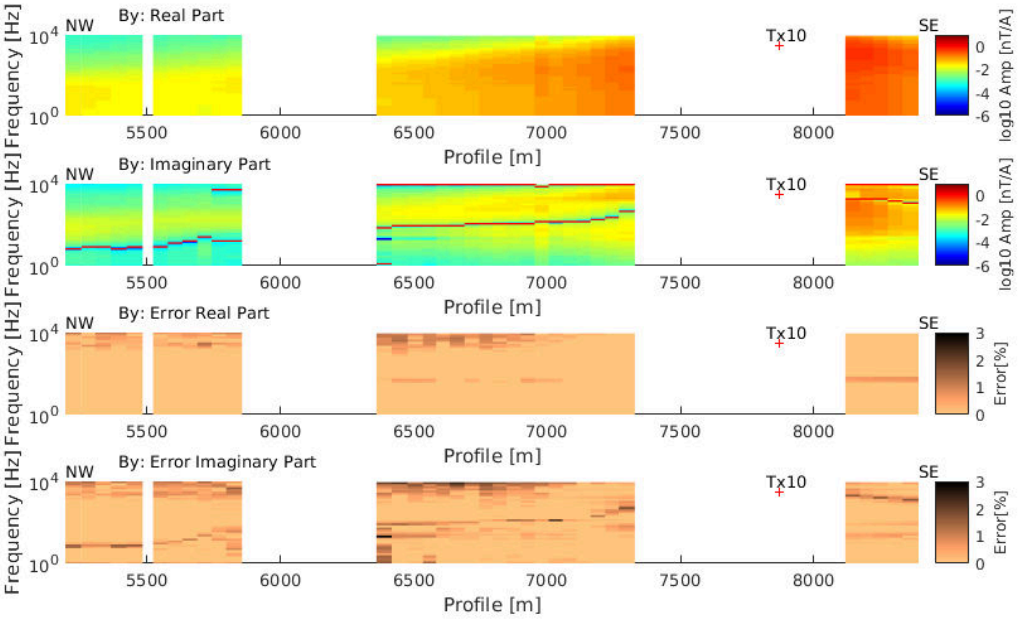

**Figure B.28.:** Normalized magnetic field of the $B_y$ component measured by SQUID sensors along Tx 10 for real and imaginary part plotted over frequency. The dataset is normalized to the current.

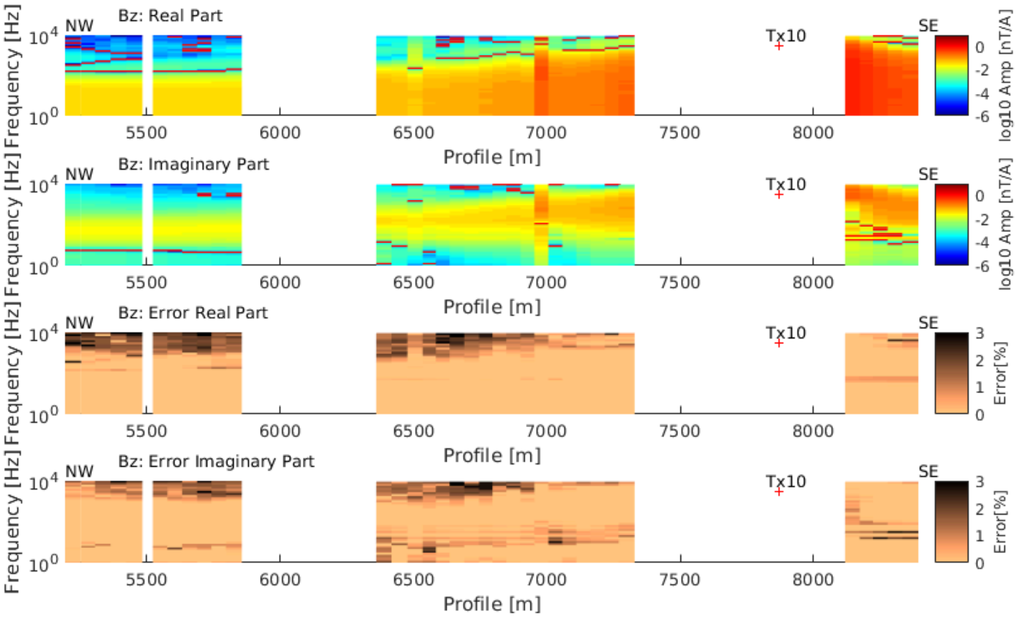

**Figure B.29.:** Normalized magnetic field of the $B_z$ component measured by SQUID sensors along Tx 10 for real and imaginary part plotted over frequency. The dataset is normalized to the current.

# C. Synthetic 2D Studies

In the following, additional information on the synthetic modelling study performed in Chapter 8 is given. Figure C.1 shows the difference between a point dipole source and an extended transmitter. 2D sensitivity studies are shown in Figure C.2 and Figure C.4.

## C.1. Point Dipole Solution vs. Extended Dipole

Figure C.1 shows the relative difference for the electric and magnetic field components utilizing a point dipole and an extended dipole as transmitter. The extended dipole was calculated as summation of the solution from 9 point dipoles along a 1 km long wire. Relative differences for short offsets of 100 m are around 100 %.

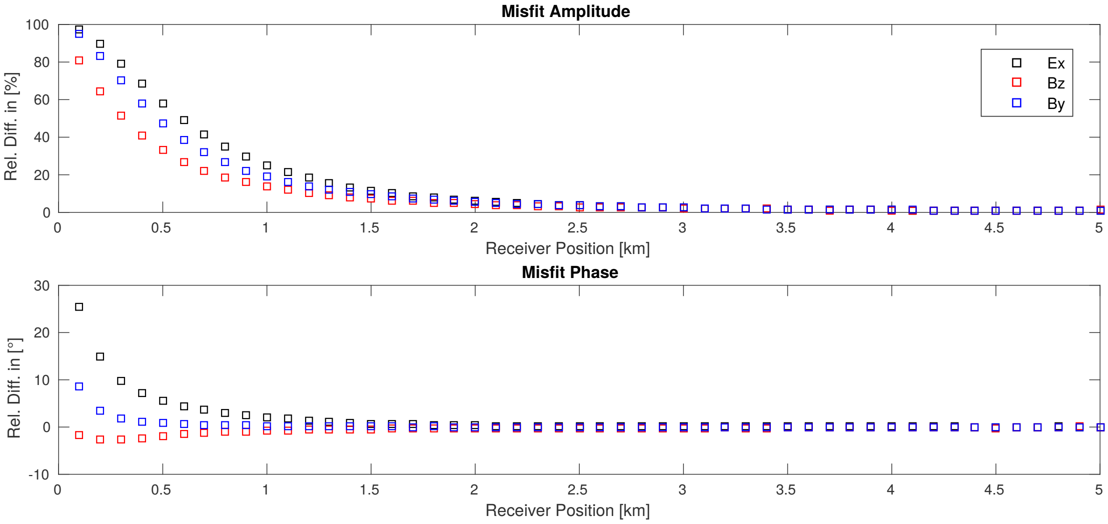

**Figure C.1.:** Relative difference in amplitude and phase for the $E_x$,$B_z$ and $B_y$ component between the forward solution of an extended dipole with 1 km length and a single point dipole as transmitter for the utilized frequency range. As forward model, a background resistivities of 500 Ωm and a conductive layer with 10 Ωm in a depth of 500 m was assumed.

## C.2. Sensitivities 2D

In Figure C.2 the error weighted sensitivities of the $E_x$ component towards a resistor is shown. Displayed are summed sensitivities $J_W$ (cp. Eq. 8.8) for amplitude and phase in frequency domain and for switch on and switch off transients in time domain. The corresponding forward model corresponds to the block model 2, however the anomaly exhibits high resistivities of 3000 Ωm compared to the surrounding resistivity of 300 Ωm. Sensitivities are low, which is in accordance to results obtained in 8.2.7, showing that the resistive anomaly can not be resolved.

Figure C.3 shows the weighted sensitivity distribution for block model 2. Corresponding inversion results are shown in Section 8.2.6. In comparison, it is obvious that sensitivities

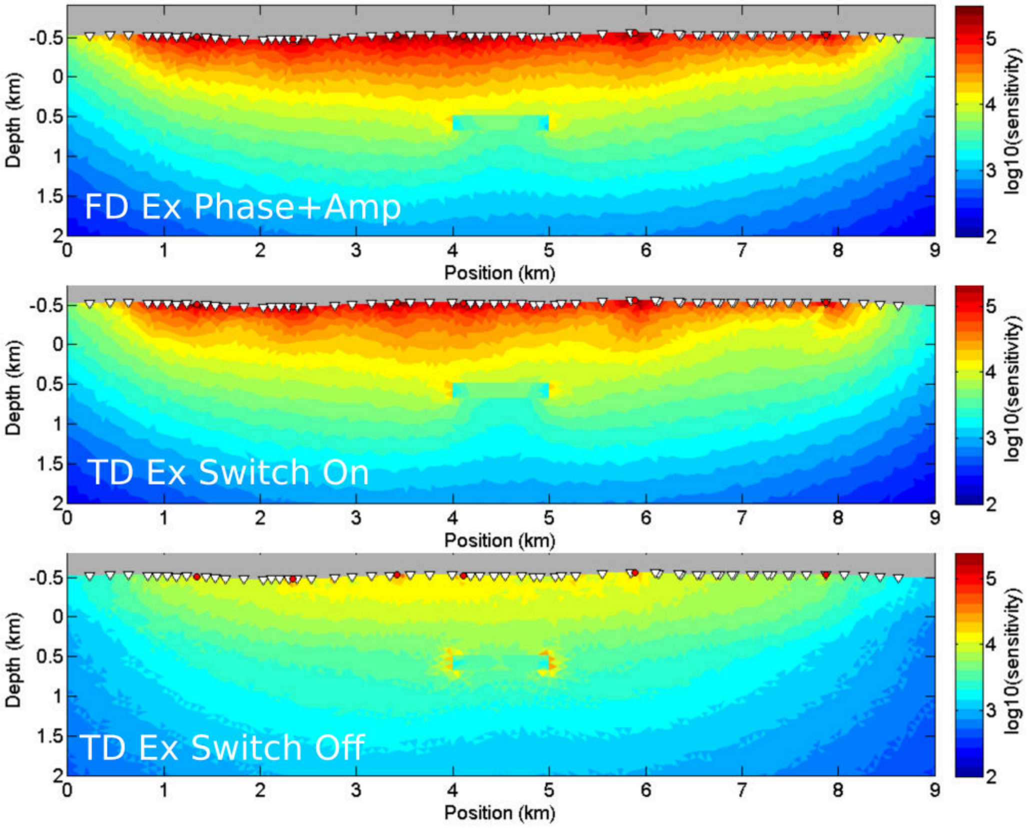

**Figure C.2.:** Sensitivities of electric field component in FD towards a resistor. Forward model is block model 2, however the conductive structure was exchanged by a resistive structure.

are reduced for the magnetic field component due to a reduced number of stations on top of the anomaly structure. In addition, utilized offsets for SQUID data are shorter, which results in a decreased resolution for deep structures.

Figure C.4 shows the weighted sensitivities for the $B_y$, $B_z$ and $E_x$ components for block model 2. In comparison to the block model study shown in Section 8.2.6 and sensitivities shown in Figure C.3, the same receiver transmitter geometry was utilized here for all components. Therefore, sensitivities between different components can be compared directly to each other. All components show increased sensitivities towards the conductor.

'71

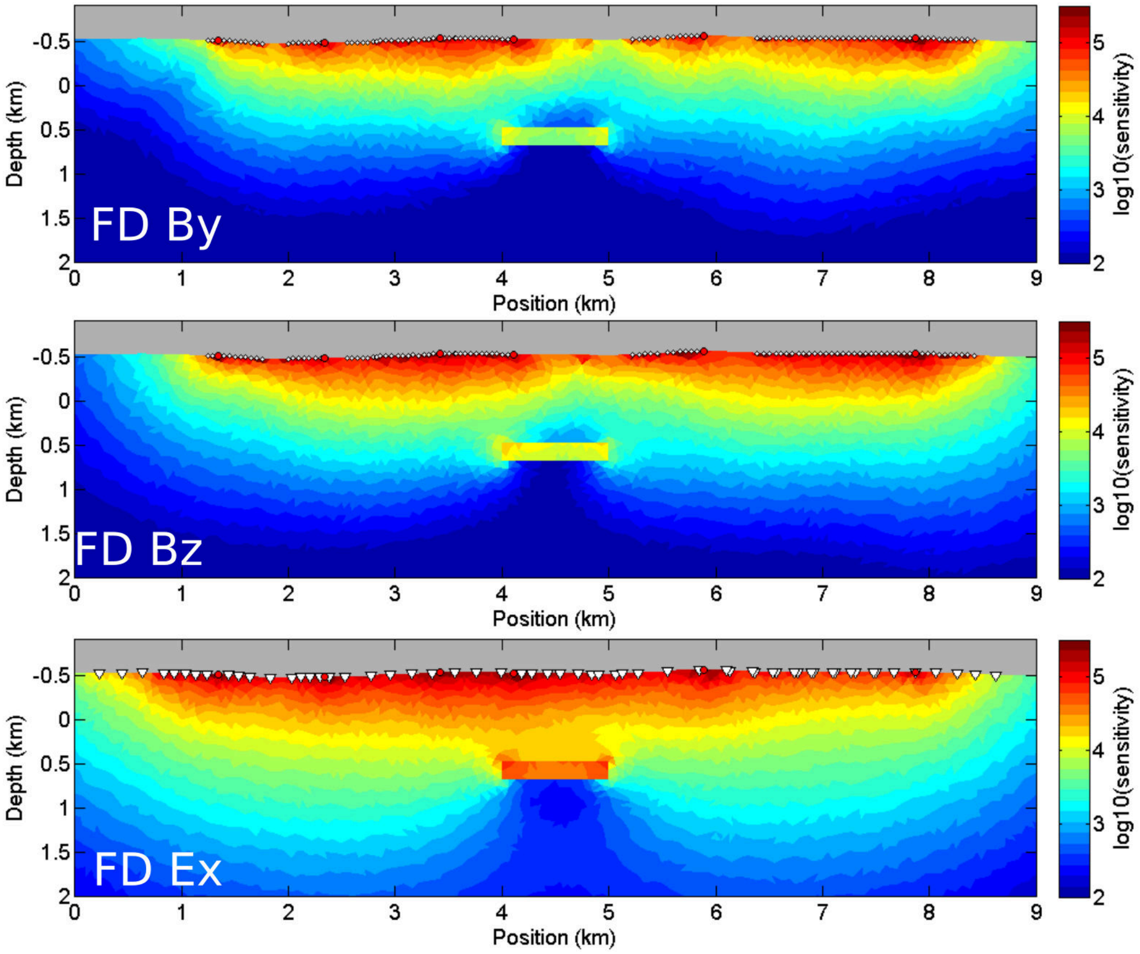

**Figure C.3.:** Comparison of sensitivities of the utilized components $B_y$, $B_z$ and $E_x$. The real station geometry was considered. The used forward model is block model 2.

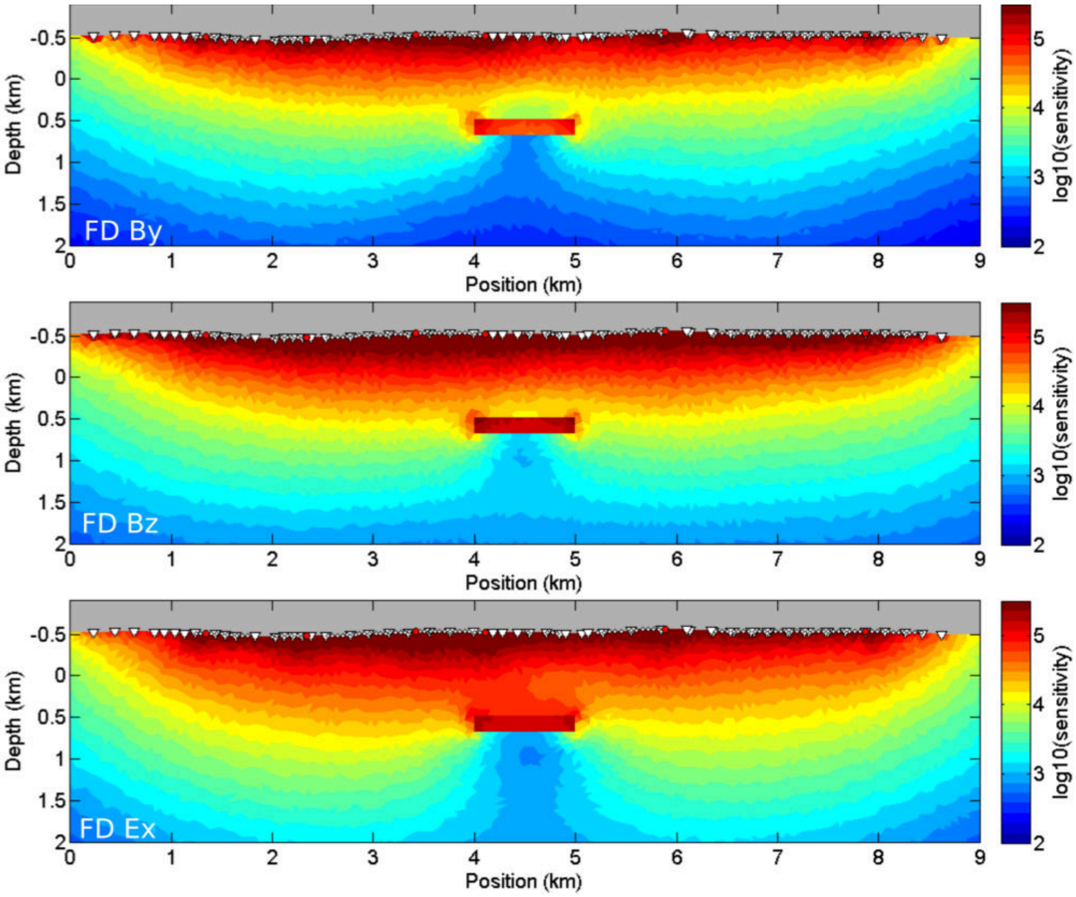

**Figure C.4.:** Comparison of sensitivities of the utilized components $B_y$, $B_z$ and $E_x$. For all components the sensitivities for the same Tx-Rx distribution and frequency range was summed up and normalized over the area. The used forward model is block model 2.

# D. 2D Inversion

In the following, additional content regarding the performed 2D inversion modelling studies is given. In Figure D.1, the sensitivity of $B_y$ towards a high conductive structure is investigated. Figure D.2 shows sensitvities for the CSEM validation for each component individually. Data and fit for one exemplary transmitter is shown in Section D.

## D.1. Forward Modelling of $B_y$

Based on the inversion result of the $B_z$ component, the sensitivities with respect to a deep conductive structure for the $B_y$ component is studied. In Figure D.1, next to the inversion result of $B_y$, a modified forward model is depicted, including a deep conductive structure at profile 1.5-2 kilometre. The misfit between calculated and measured $B_y$ data decreased for the modified model from 1.64 to 1.94.

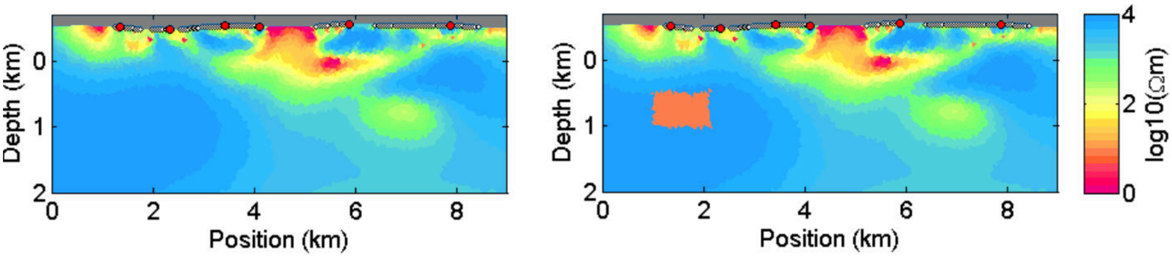

**Figure D.1.:** Left Panel: Inversion model obtained utilising the $B_y$ component. Right Panel: Modified forward model including a deep high conductive structure.

## D.2. Sensitivities of the CSEM Validation Model

Error weighted sensitivities for the CSEM validation model for each component are displayed in Figure D.2.

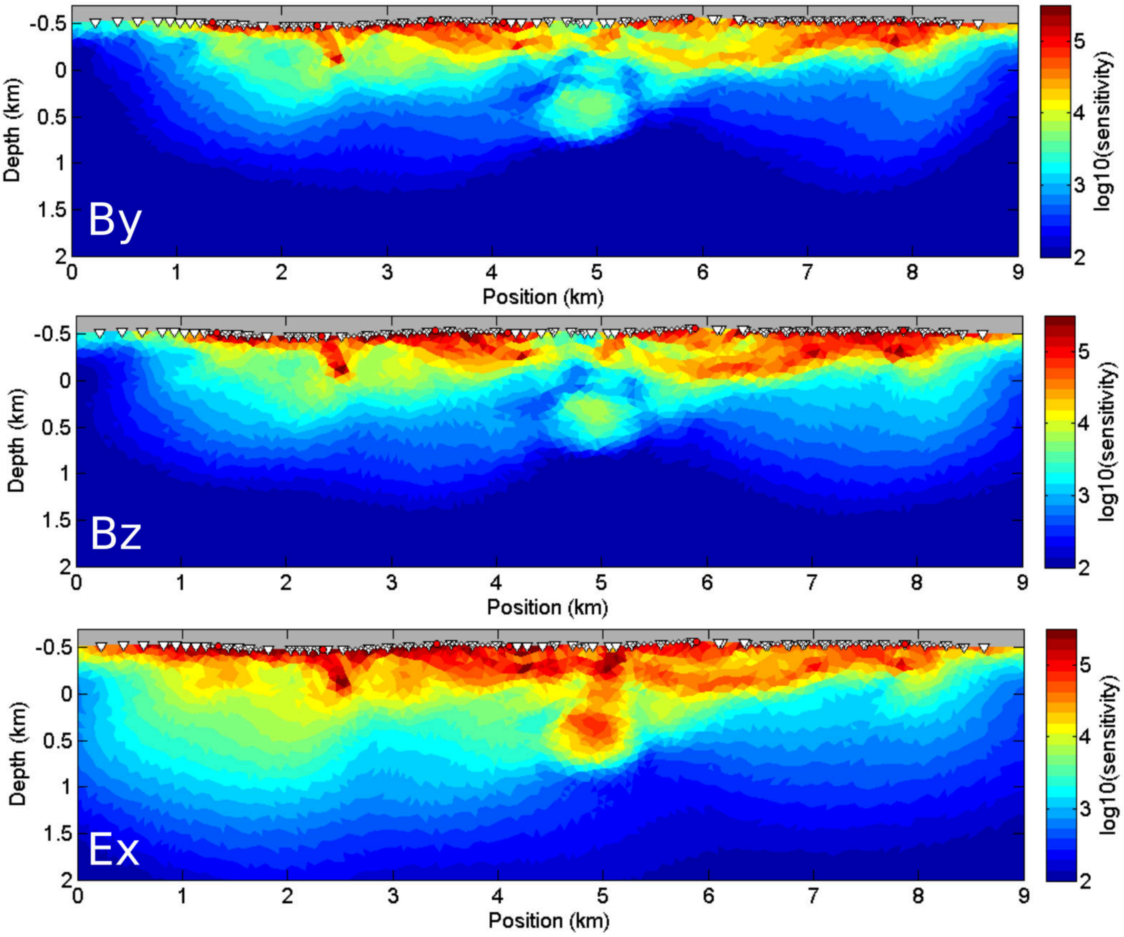

**Figure D.2.:** Error weighted sensitivities for the CSEM validation model.

## D.3. Data and Fit for Tx 10

In the following, measured and calculated transfer functions for the CSEM Validation model are shown exemplarily for Tx 10. Transfer functions for all utilized components ($B_y$, $B_z$ and $E_x$) are displayed as amplitude and phase. The global weighted misfit for the dataset from Tx 10 is 3.53 for the $E_x$ component, 1.35 for the $B_y$ component and 1.81 for the $B_z$ component.

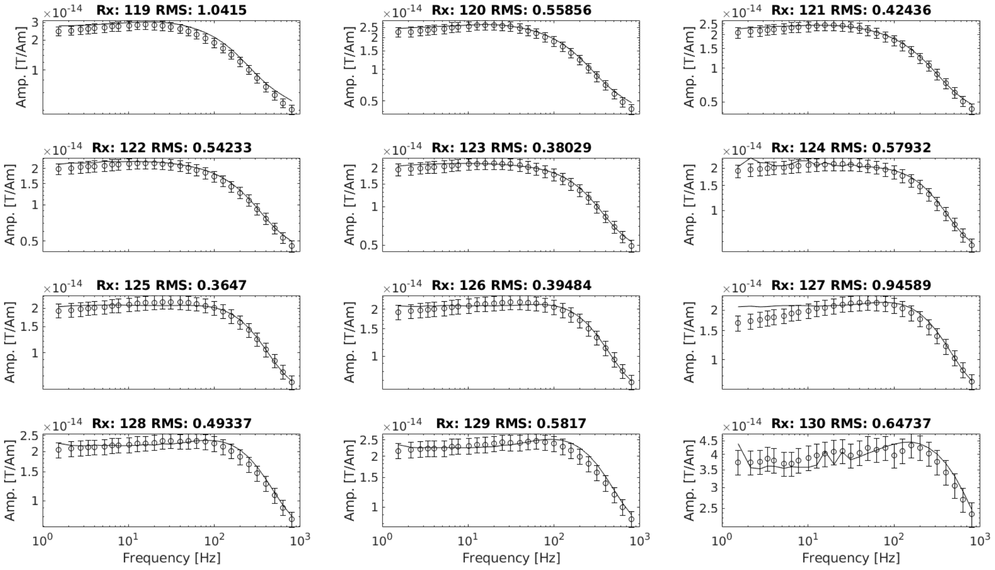

**Figure D.3.:** CSEM Validation Model: Measured amplitude data (circles) and calculated amplitude data (solid line) for the $B_y$ component, stations 119-130 utilizing Tx 10.

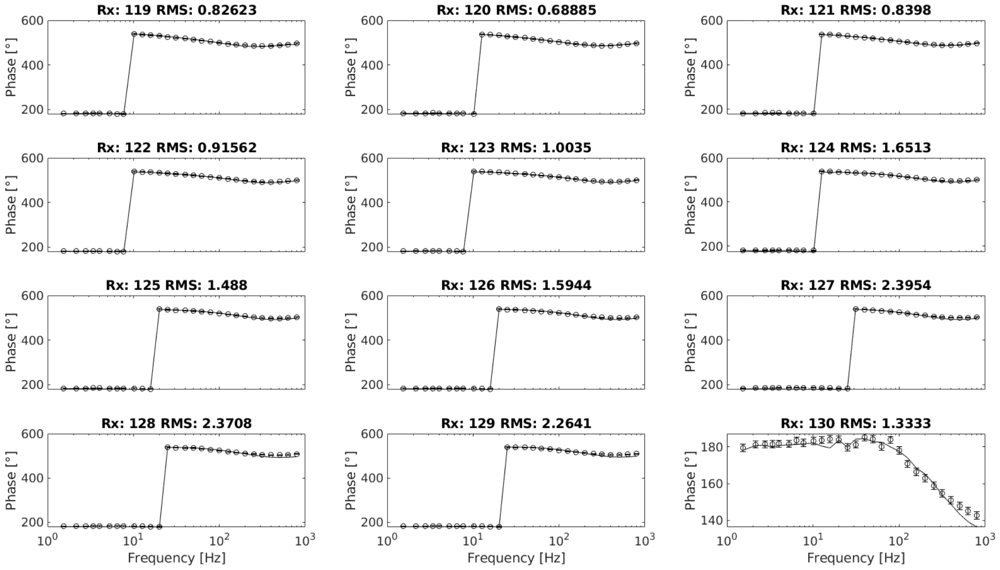

**Figure D.4.:** CSEM Validation Model: Measured phase data (circles) and calculated phase data (solid line) for the $B_y$ component, stations 119-130 utilizing Tx 10.

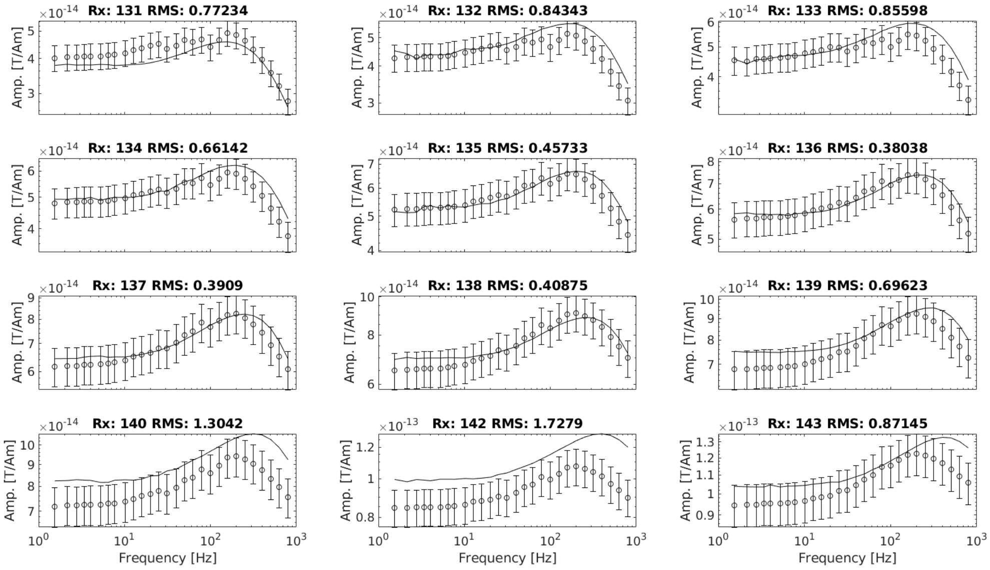

**Figure D.5.:** CSEM Validation Model: Measured amplitude data (circles) and calculated amplitude data (solid line) for the $B_y$ component, stations 131-143 utilizing Tx 10.

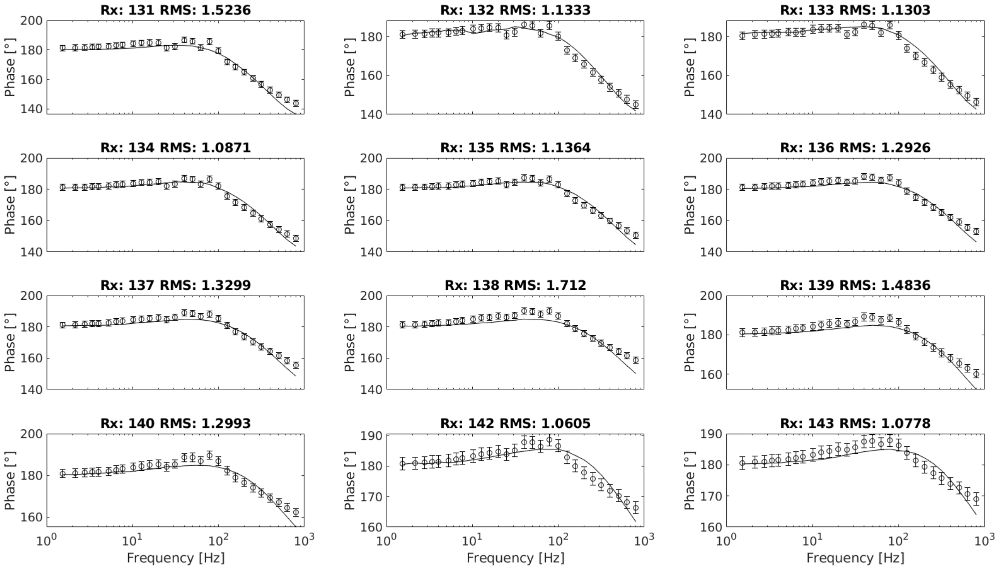

**Figure D.6.:** CSEM Validation Model: Measured phase data (circles) and calculated phase data (solid line) for the $B_y$ component, stations 131-143 utilizing Tx 10.

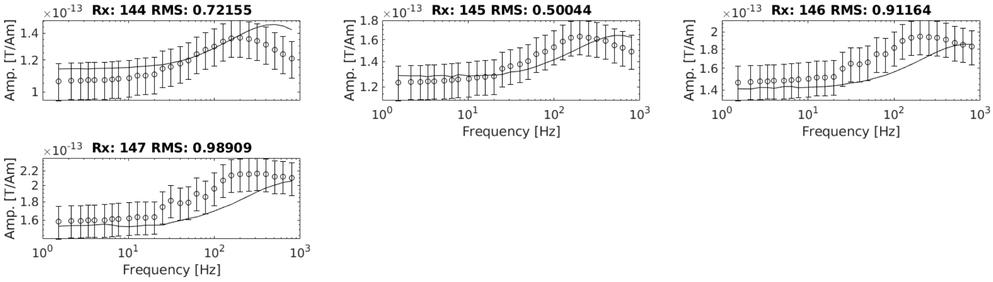

**Figure D.7.:** CSEM Validation Model: Measured amplitude data (circles) and calculated amplitude data (solid line) for the $B_y$ component, stations 144-147 utilizing Tx 10.

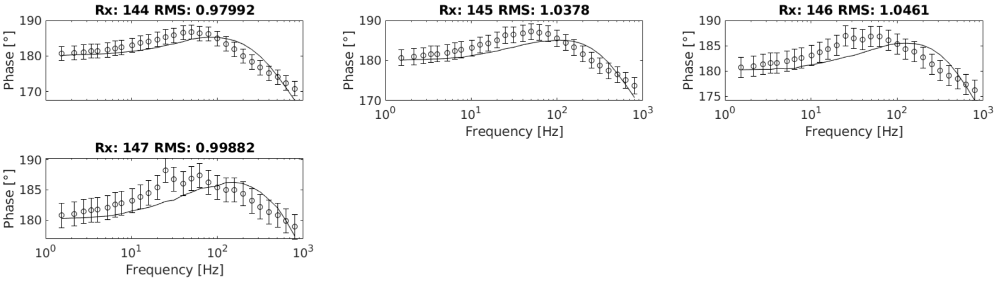

**Figure D.8.:** CSEM Validation Model: Measured phase data (circles) and calculated phase data (solid line) for the $B_y$ component, stations 144-147 utilizing Tx 10.

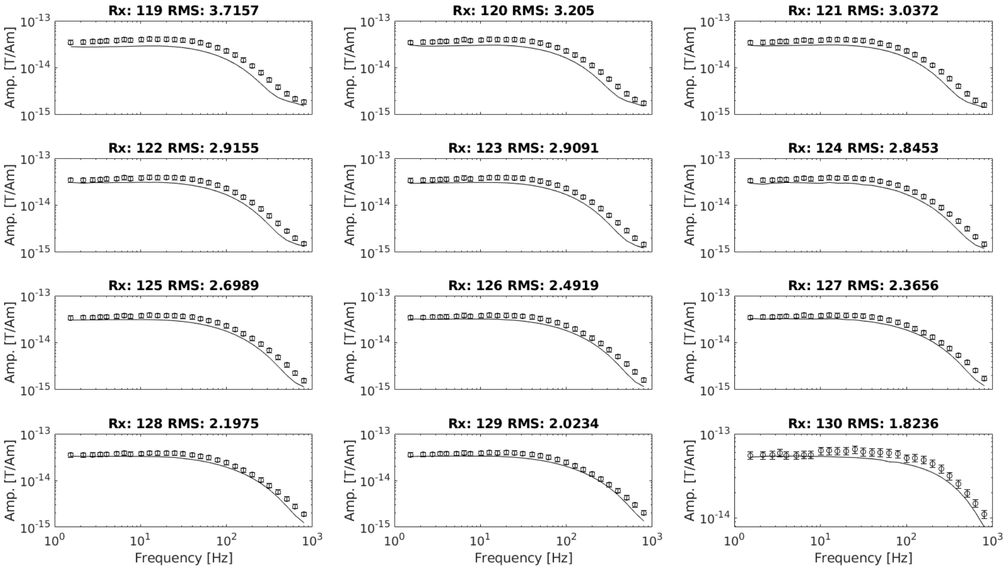

**Figure D.9.:** CSEM Validation Model: Measured amplitude data (circles) and calculated amplitude data (solid line) for the $B_z$ component, stations 119-130 utilizing Tx 10.

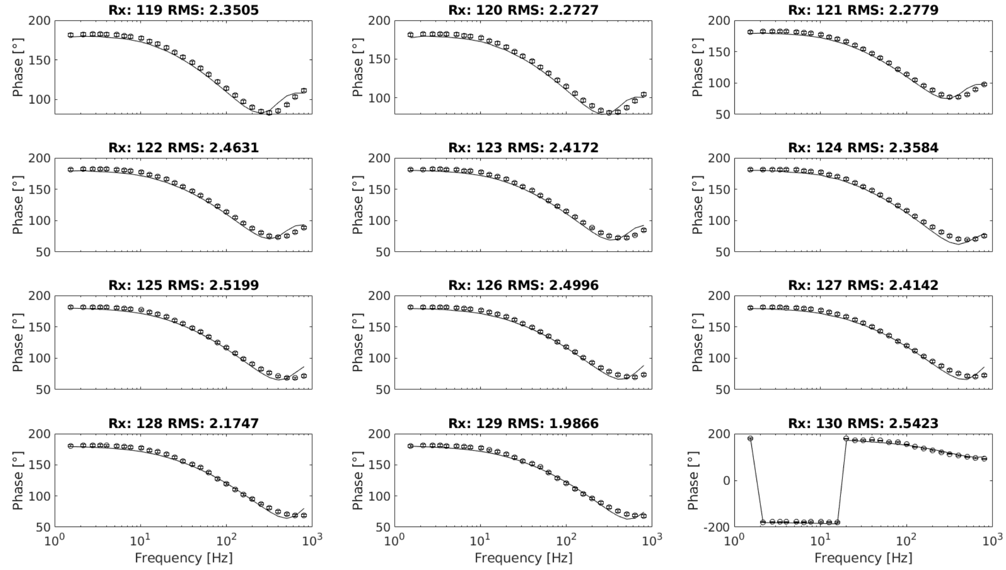

**Figure D.10.:** CSEM Validation Model: Measured phase data (circles) and calculated phase data (solid line) for the $B_z$ component, stations 119-130 utilizing Tx 10.

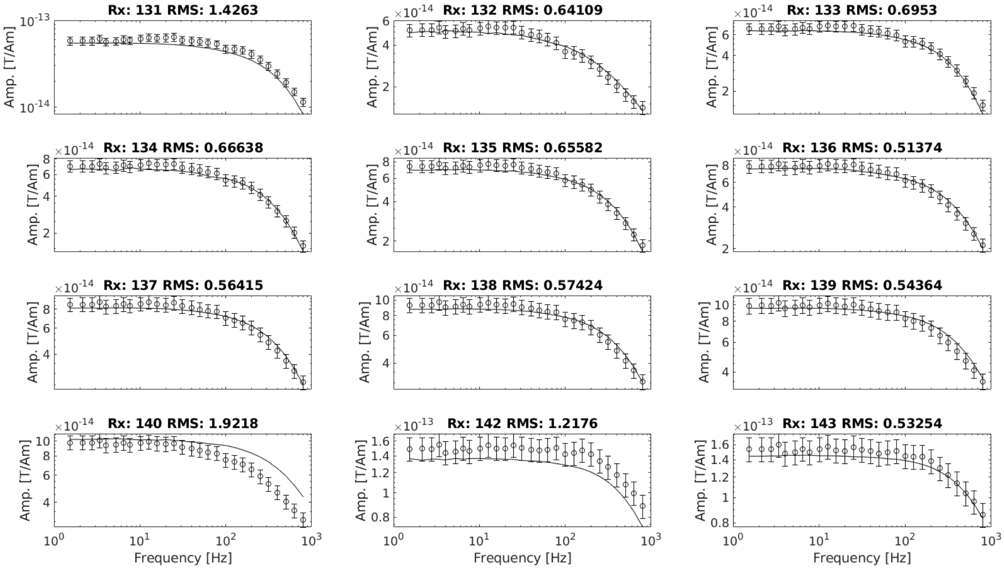

**Figure D.11.:** CSEM Validation Model: Measured amplitude data (circles) and calculated amplitude data (solid line) for the $B_z$ component, stations 131-143 utilizing Tx 10.

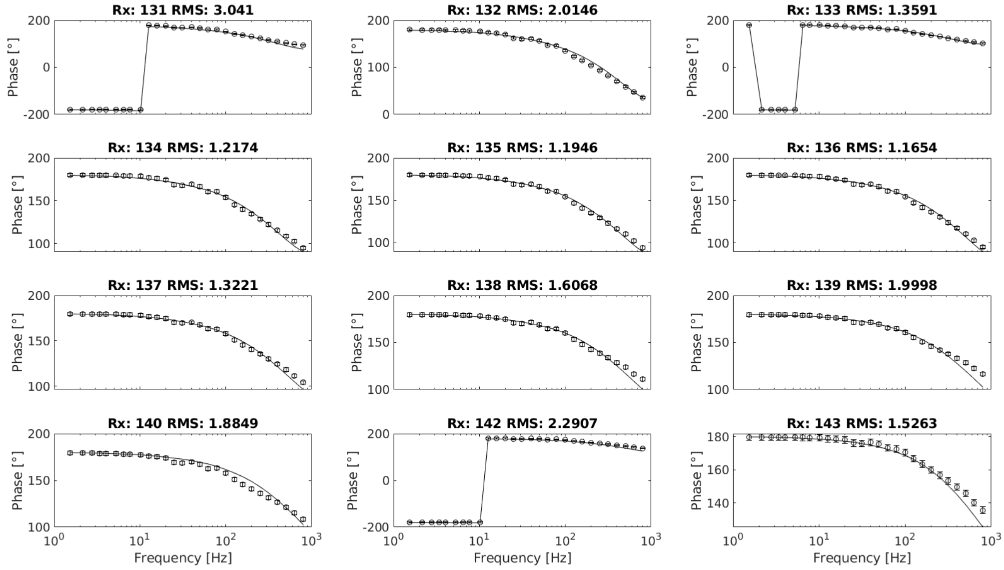

**Figure D.12.:** CSEM Validation Model: Measured phase data (circles) and calculated phase data (solid line) for the $B_z$ component, stations 131-143 utilizing Tx 10.

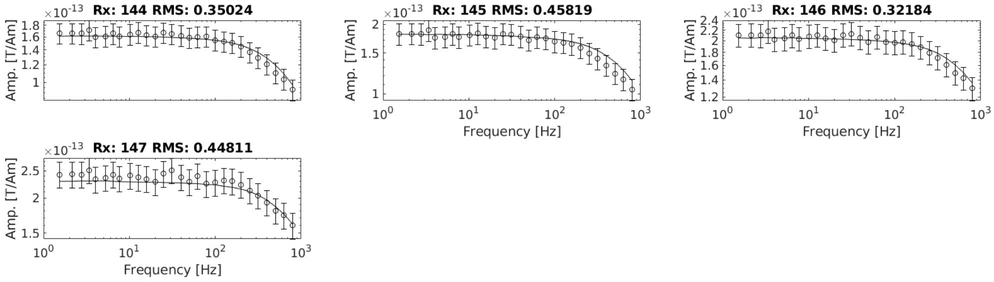

**Figure D.13.:** CSEM Validation Model: Measured amplitude data (circles) and calculated amplitude data (solid line) for the $B_z$ component, stations 144-147 utilizing Tx 10.

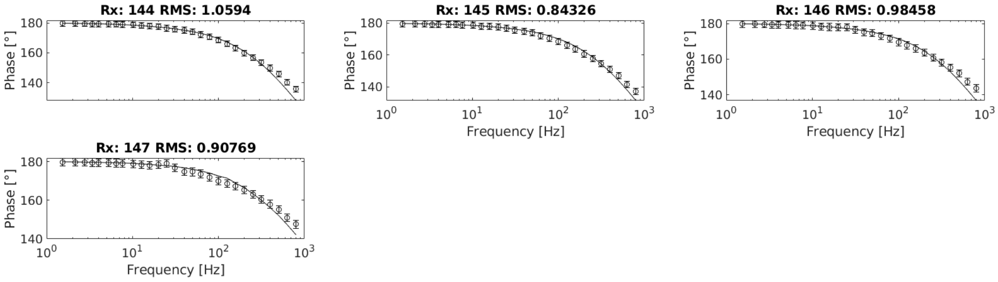

**Figure D.14.:** CSEM Validation Model: Measured phase data (circles) and calculated phase data (solid line) for the $B_z$ component, stations 144-147 utilizing Tx 10.

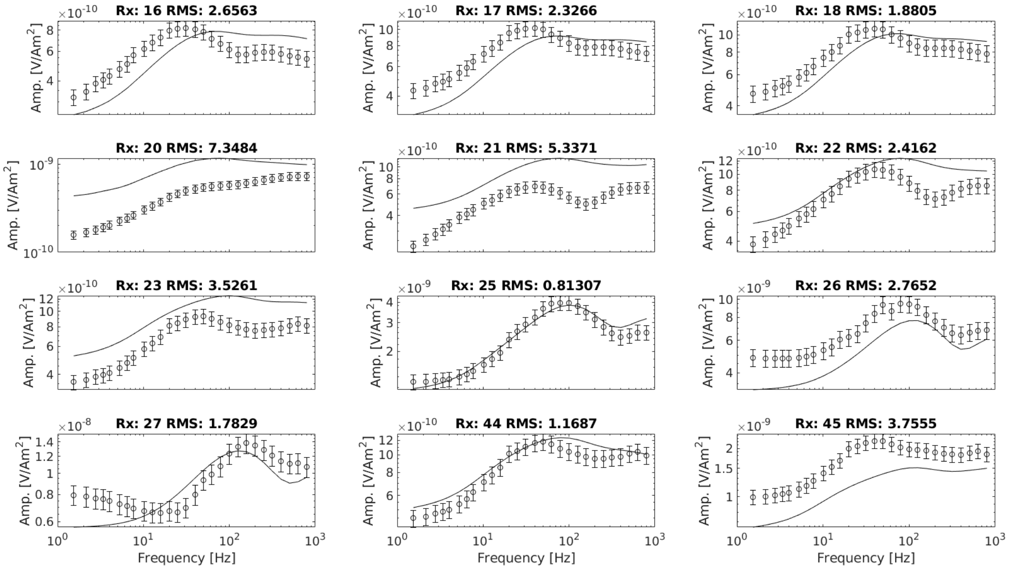

**Figure D.15.:** CSEM Validation Model: Measured amplitude data (circles) and calculated amplitude data (solid line) for the $E_x$ component, stations 16-45 utilizing Tx 10.

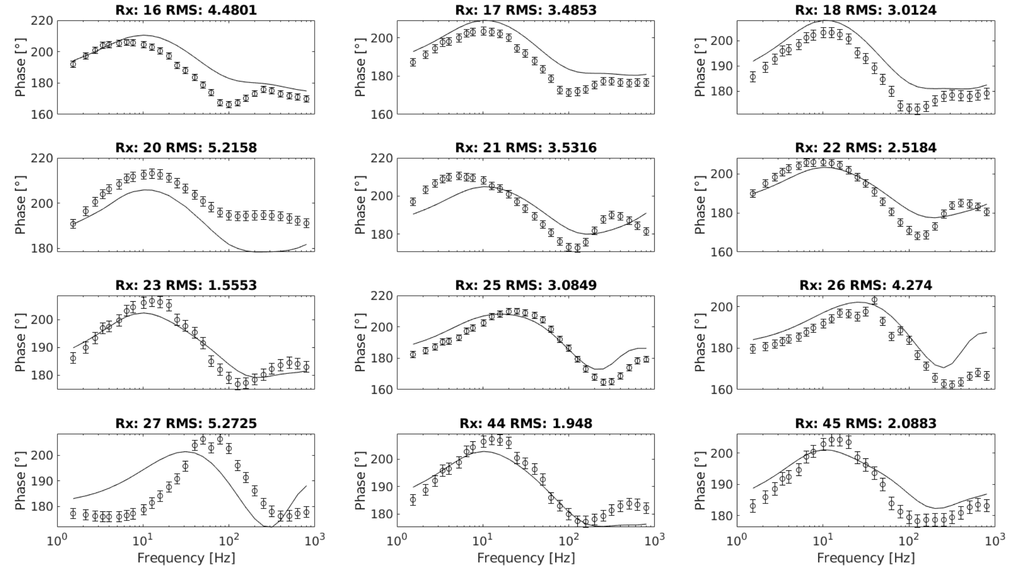

**Figure D.16.:** CSEM Validation Model: Measured phase data (circles) and calculated phase data (solid line) for the $E_x$ component, stations 16-45 utilizing Tx 10.

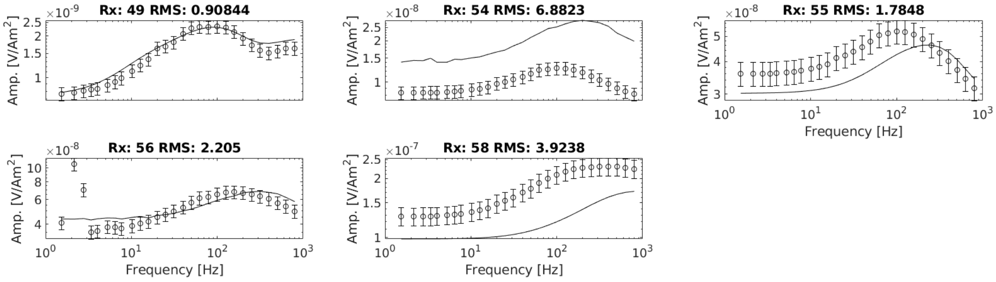

**Figure D.17.:** CSEM Validation Model: Measured amplitude data (circles) and calculated amplitude data (solid line) for the $E_x$ component, stations 49-58 utilizing Tx 10.

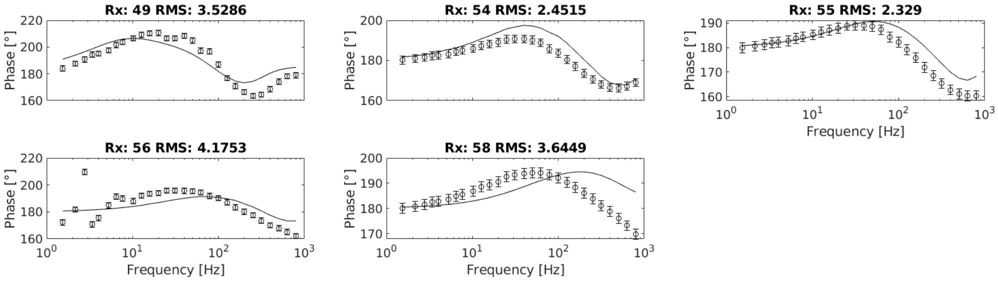

**Figure D.18.:** CSEM Validation Model: Measured phase data (circles) and calculated phase data (solid line) for the $E_x$ component, stations 49-58 utilizing Tx 10.

# Acknowledgements

Here, I want to express my gratitude to

- Prof. Dr. Bülent Tezkan for the supervision of the work and the advice and support in the past years.
- Prof. Dr. Andreas Hördt for appraising this thesis
- Dr. Pritam Yogeshwar for all the successful collaboration, fruitful discussions and advise during the past years
- Dr. Amir Haroon for many helpful discussions and advice. In addition, for the support and provision of the time domain version of MARE2DEM
- Tilman Hanstein for countless advice regarding the KMS acquisition unit, LOTEM data processing and many fruitful discussion about EM in general
- Prof. Dr. Michael Becken for the provision of the magnetotelluric processing scheme EMTS, advice about CSEM data processing and the provision of the 1D inversion algorithm EM1DW
- Dr. Ronny Stolz, Dr. Markus Schiffler, Dr. Matthias Queitsch and Raphael Rochlitz for the provision of the SQUID dataset
- All those, who took part in the LOTEM field campaigns 2016 and 2017: Alex, Burak, Cai Ji, Diego, Felix, Imamal, Jan, Janine, Johanna H., Johanna K., Klaus, Marc, Mira, Nadine, Natalie, Sascha, Stephan, Volker and the team from the DESMEX main experiment
- Andreas Busse and Rainer Bergers for the support in all technical issues regarding the LOTEM system
- Mira Küpper, Stephan Schlegel, Dr. Amir Haroon, Barbara Blanco and Dr. Pritam Yogeshwar for proof-reading this thesis
- The complete Ageo working group for creating a friendly working atmosphere
- The DESMEX WG
- The RRZK for the possibility to use CHEOPS
- The Geophysical Instrument Pool Potsdam (GIPP) for the provision of the SPAM Mk IV System (grant number 201608 and 201716)
- DESMEX is funded by the Federal Ministry of Education and Research (BMBF) under BMBF grant033R130
- And last, thanks to my family and Stephan, who supported me all along.

## Erklärung zur Dissertation

Ich versichere, dass ich die von mir vorgelegte Dissertation selbständig angefertigt, die benutzten Quellen und Hilfsmittel vollständig angegeben und die Stellen der Arbeit einschließlich Tabellen, Karten und Abbildungen , die anderen Werken im Wortlaut oder dem Sinn nach entnommen sind, in jedem Einzelfall als Entlehnung kenntlich gemacht habe; dass diese Dissertation noch keiner anderen Fakultät oder Universität zur Prüfung vorgelegen hat; dass sie abgesehen von unten angegebenen Teilpublikationen noch nicht veröffentlicht worden ist, sowie, dass ich eine solche Veröffentlichung vor Abschluss des Promotionsverfahrens nicht vornehmen werde. Die Bestimmungen der Promotionsordnung sind mir bekannt. Die von mir vorgelegte Dissertation ist von Prof. Dr. B. Tezkan betreut worden.

Köln, Februar 2020